# Catalyst Particles for Fluid Catalytic Cracking Visualized at the Individual Particle Level by Micro-Spectroscopy

*Katalysatordeeltjes voor Gefluïdiseerd Katalytisch Kraken Gevisualiseerd op Individueel Deeltjesniveau met Micro-Spectroscopie*

*(met een samenvatting in het Nederlands)*

**Proefschrift**

ter verkrijging van de graad van doctor aan de Universiteit Utrecht
op gezag van de rector magnificus, prof. dr. G. J. van der Zwaan,
ingevolge het besluit van het college voor promoties in het openbaar
te verdedigen op maandag 5 december 2011 des ochtends te 10.30 uur

door

**Inge Loes Charlotte Buurmans**

geboren op 9 oktober 1983 te Amstelveen

Promotor: prof. dr. ir. B. M. Weckhuysen

This thesis was accomplished with financial support from Albemarle Catalysts B.V.

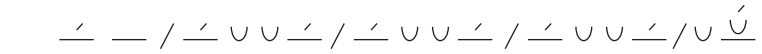

*Tu ne quaesieris, scire nefas, quem mihi, quem tibi*
*finem di dederint, Leuconoe, nec Babylonios*
*temptaris numeros. ut melius, quidquid erit, pati,*
*seu pluris hiemes seu tribuit Iuppiter ultimam,*
*quae nunc oppositis debilitat pumicibus mare*
*Tyrrhenum: sapias, vina liques, et spatio brevi*
*spem longam reseces. dum loquimur, fugerit invida*
*aetas: carpe diem, quam minimum credula postero.*

*Quintus Horatius Flaccus*
*65 BC - 8 BC*
*Book I, Ode XI*
*Oxford University Press, 1963*

*White-Thoughted One,*
*do not ask how you or I will end, or when,*
*or lend credence*
*to horoscopes and Babylonian astrologers:*
*tomorrow is tomorrow,*
*today is today.*
*Whatever the gods are pleased to send your way*
*embrace:*
*many winters more,*
*or the blue sea*
*hurled against pumice never again.*
*Life is like this hill wine,*
*clear today,*
*but will it keep?*
*While we sit here, talking,*
*the hours run by.*
*Another day,*
*another week,*
*another year won't bring another moment*
*like this.*

*translated by Michael Taylor*
*The Greenwood Press, 1992*

Buurmans, Inge Loes Charlotte

Title: Catalyst Particles for Fluid Catalytic Cracking Visualized at the Individual Particle Level by Micro-Spectroscopy

ISBN: 978-90-8891-348-8

Printed by: Proefschriftmaken.nl || Printyourthesis.com

The work described in this thesis was carried out at the Faculty of Science, Inorganic Chemistry and Catalysis group, Utrecht University, The Netherlands.

*Cover microphotograph (4-chlorostyrene drying and reacting on a zeolite pellet) taken by the author.*

## Contents

# Chapter 1

## General Introduction

## 1. Zeolites, some history and their use in catalysis

Zeolites are very important heterogeneous catalysts in chemical industry for a wide variety of reactions. Their physicochemical properties, such as Brønsted acidity, shape selectivity and high surface area make them suitable materials for all kinds of catalytic processes. The history of zeolites started with the discovery of the first mineral of this class, stilbite, by the Swedish mineralogist Axel Cronstedt in 1756, as shown in the timeline in Figure 1.1.[1] Cronstedt found out that stilbite would lose a significant amount of water during heating and called the mineral 'zeolite'. The word is derived from the Greek words ζέω (zeo) and λίθος (lithos), which mean 'boiling stone'. Starting in the late 1700s, scientists described the properties of zeolites, such as their adsorption capabilities, dehydration and reversible cation exchange, in more detail. The idea that dehydrated zeolites act as sponges with an open framework that can absorb liquids was developed by Georges Friedel in 1896.[2-3] Thirteen years later François Grandjean added a variety of gases, such as ammonia, air and hydrogen, to the list of compounds that could be adsorbed by zeolitic materials.[4] In 1925 Oskar Weigel and Eduard Steinhoff were the first to publish a molecular sieve effect for the zeolite chabazite with different organic vapors.[5] All these research efforts led to a significant knowledge of zeolites and their properties, such as adsorption, molecular sieve effects, structural properties and ion exchange capabilities by the mid-1930s. Around that time already some efforts had been made as well to produce synthetic versions of natural zeolitic minerals, but the reproducibility of these experiments was low and the characterization of the materials incomplete.

The first definite synthesis of zeolites, among which mordenite, was described in 1948 by Richard Barrer (Figure 1.1).[6] Some commercially significant zeolites, namely zeolites A, X and Y, were discovered in the years 1949-1954 by Robert Milton and Donald Breck. The Union Carbide company recognized that these materials could be applied for separation and purification purposes and implemented their use in the drying of gas in 1954. In 1967-1969 the syntheses of zeolites Beta and ZSM-5 were introduced by Mobil Oil.[7] In the period since the 1980s the discovery of new compositions and structures of zeolites increased tremendously: in the first edition of the Atlas of Zeolite Structure Types from 1978 only 38 structure types were described. Already in the second edition (1987) this amount increased to 64 and today in the online 2011 edition 197 different zeolitic framework types are known.

Around the 1980s Wilson and Flanigen described a new class of materials: the microporous crystalline aluminophosphates (AlPOs, Figure 1.1).[8-9] These zeotype materials are formed by the substitution of framework silicon atoms by phosphorus atoms and are used as membranes,

heterogeneous catalysts and adsorbents.[10-12] Such substitutions allow the formation of larger ring structures. The thermal stability of the resulting materials is lower, but they display an improved accessibility and diffusivity in comparison to the conventional zeolite frameworks. One example of such a zeolite-like material, VPI-5, was discovered by Davis and his team in 1987.[13] The largest zeolites known before the synthesis of VPI-5 consisted of rings containing 12 or less oxygen atoms, which gave rise to pore sizes below 10 Å. VPI-5, an aluminophosphate, displays rings that contain 18 oxygen atoms, which build up pores with a diameter of 13 Å. This material does not contain potential active sites for catalytic reactions, but upon isomorphous substitution by elements such as Ti, Co, Cu, Mg or V in the framework it is possible to generate acid, basic or redox-active sites. Furthermore, VPI-5 is very suitable for the adsorption of significant amounts of bulky sorbates.[14] The framework type with the largest pores found so far is the gallophosphate cloverite.[15] It contains rings of 20 oxygen atoms, leading to supercages with a 30 Å pore diameter and displays a three-dimensional framework. Another interesting feature of cloverite is that terminal hydroxyl groups are present within the structure, increasing its potential for functionalization. Recently, Corma and co-workers reported the synthesis of another large pore zeolite, the germano(alumino)silicate ITQ-40.[16] ITQ-40 has the lowest framework density reported up to now for zeolitic materials and displays rings of 15 and 16 oxygen atoms. Such low framework density materials will expand the possibilities for the use of zeolites in catalysis, controlled delivery of chemicals and diagnostic treatment, since their pore volume is very large.

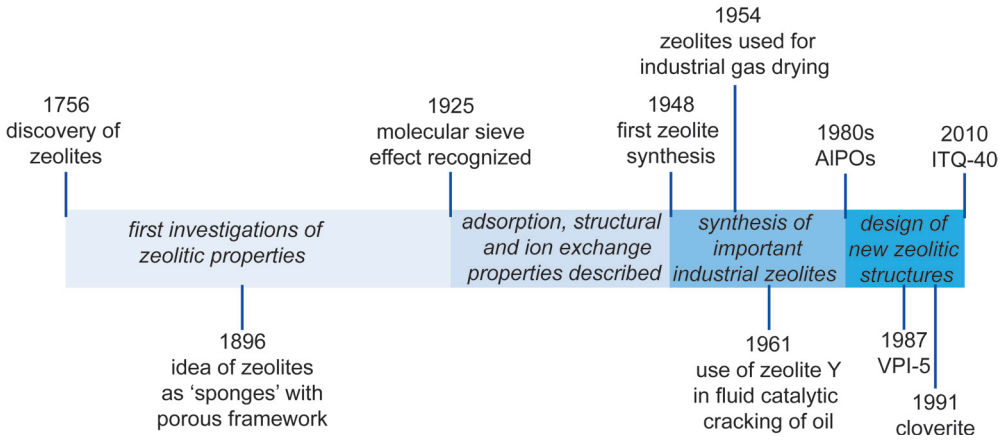


**Figure 1.1.** History of the discovery of zeolites, their properties and applications.

A recently published computational study revealed that over 2.6 million possible ways exist to arrange atoms into a stable zeolite structure for which it is likely that it can be synthesized.[17] Furthermore, a prediction

of the physical and chemical properties of all these zeolite structures has been conducted. About 15% of the investigated zeolite structures displays topological, geometrical and diffraction characteristics that are comparable to the properties of known zeolites. The large number of zeolites that still has to be discovered, produced and applied reflects their bright future for numerous processes.

Zeolites are microporous crystalline aluminosilicates that are built up from $SiO_4$ and $AlO_4$ tetrahedra, which share their oxygen atoms to form a three-dimensional framework. The obtained regular microporous network, with its molecularly sized pores, provides shape selectivity. For that reason zeolites are also called molecular sieves. Since the silicon ($Si^{4+}$) and aluminum ($Al^{3+}$) atoms are differently charged, the resulting framework will display a negative charge, which is compensated by positively charged counter ions. These counter ions, such as $Na^+$ and $NH_4^+$, can be exchanged. Protons as counter ions will introduce Brønsted acidity in the zeolite structure.

The market for synthetic zeolites and molecular sieves has grown significantly over the years. In 2008 the amount used annually was as high as 1.8 million ton.[18] The global synthetic zeolite industry today is worth about US$1.9 billion a year[19] and the most important applications of zeolites are as adsorbents, catalysts and ion-exchange materials. Although the use as a catalyst is only the second-largest application in volume (17%), it covers 55% of the total market value of zeolites.

The application of synthetic zeolites in oil refining and petrochemicals caused their real breakthrough as catalysts.[20] Fluid Catalytic Cracking, the process in which vacuum gas oils or oil residues are converted into transportation fuels, consumes about 95% of the total zeolite amount used in catalysis.

Two different types of zeolites are very important for the catalytic cracking of oil: zeolite Y and ZSM-5.[21-22] Zeolite Y is the synthetic version of the naturally occuring zeolite faujasite (FAU). Its structure is built up by sodalite cages that are connected to each other through hexagonal prisms (double six-rings) as depicted in Figure 1.2.[23-25] The resulting structure displays 12-membered ring openings that lead to large so-called supercages. These supercages are 13 Å in internal diameter, while the pore openings have a diameter of 7.4 Å.[26-27] The channels allow diffusion of molecules in three dimensions and account for the large effective surface area of the zeolite. The ZSM-5 framework can be built from five-rings and displays the so-called MFI (Mobil Five) framework, which consists of intersecting straight and zigzag pores (Figure 1.3).[23] Both types of pores consist of 10-membered rings with an elliptical shape and are 5.1 x 5.5 Å (straight pores) and 5.3 x 5.6 Å (zigzag pores) in diameter.[25] The channel-like structure combined with the fact that ZSM-5 is, in contrast to the large pore zeolite Y, a medium pore zeolite, gives rise to a higher

shape selectivity of the zeolite in petrochemical reactions.[28]

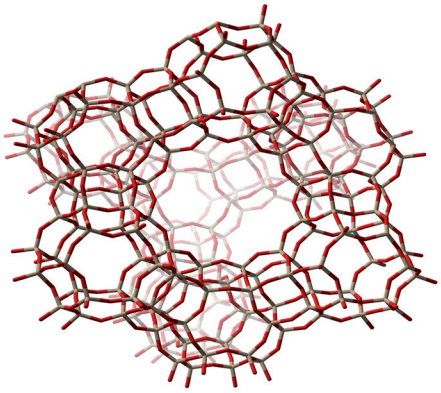

**Figure 1.2.** Sodalite cages and hexagonal prisms are the building blocks of the FAU framework with large supercages.

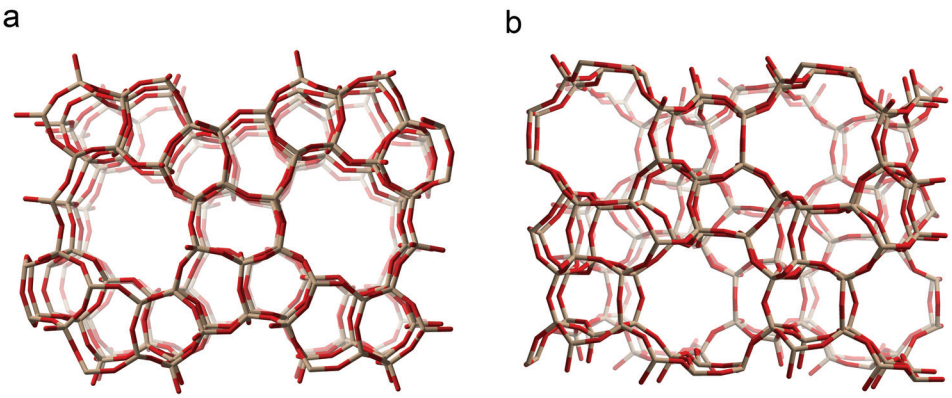


**Figure 1.3.** The MFI framework, which consists of interconnected straight and zigzag pores, as seen **(a)** down the straight ten-ring channels and **(b)** down the zig-zag ten-ring channels.

## 2. The Fluid Catalytic Cracking process

Fluid Catalytic Cracking (FCC) is the major conversion process in oil refineries to produce gasoline and other hydrocarbons from crude oil fractions.[20,29-31] About 40-45% of the gasoline produced worldwide is manufactured through FCC.[32] Since the demand for oil-based products worldwide is ever-increasing, there has been ongoing research for decades to improve the FCC process and the spherical catalyst particles that perform the cracking reaction. In 1966 the world's catalytic cracking capacity was approximately 500000 tons per day.[33] In 2008 this amount had increased to 1.6 million tons per day.[31]

Already in 1916 research showed that it was possible to crack oil in the presence of an aluminum chloride catalyst.[33] In these first years catalytic cracking was not very succesful, but this changed with Eugene Houdry's finding that the molecular weight of hydrocarbons could be decreased using acid-treated natural clays as catalyst materials.[34-36] The first application of this new invention took place in 1936 for oil cracking in a fixed-bed process.[37] In 1942 the process underwent further optimization by using a fluid-bed catalytic cracking unit and since that time many improvements in FCC technology have been made to tune the yield and product distribution.

At quite an early stage scientists observed that not only natural clays, but also synthetic materials based on silica and alumina were suitable catalysts for cracking reactions.[33] The discovery made in 1961 that addition of the synthetic version of faujasite, zeolite Y, to some active matrix components significantly increased catalyst activity, while the amount of coke formed stayed constant or even decreased slightly, constituted another important development step in the FCC process.[37-38] With a typical $SiO_2$-$Al_2O_3$ catalyst used until the 1960s about 30% of gasoline could be produced. This amount was increased to around 45% with the introduction of a stabilized form of zeolite Y.[39] Attempts were also made to use pure zeolite in the cracking of oil. However, in those cases a very high formation of light gas products and coke was reported. Charles Plank and Edward Rosinski developed and patented the idea of diluting the zeolite in a matrix to reduce overcracking and high coke formation.[40]

Nowadays, the catalyst for the FCC process consists of spray-dried porous microspheres with an average diameter of 70 μm that are complex mixtures of several materials. Figure 1.4 shows a scanning electron microscopy (SEM) image of an FCC catalyst particle as well as a schematic representation of its chemical composition and internal structure. Typically the catalyst particles contain 20-40% ultrastable zeolite Y (USY) and a binder. USY is obtained by a hydrothermal treatment of zeolite Y, which causes partial dealumination of the zeolite framework. By this treatment a more silicon-rich zeolite with higher hydrothermal stability is obtained.[41-

[42] Furthermore, during the process mesopores are created that enhance the accessibility of the zeolite. It has also been observed that partially dealuminated zeolite Y materials exhibit higher acid site strength than their parent samples.[28] Additionally, the FCC catalyst particles embody a catalytically active, acidic matrix.[31,43] The major roles of the matrix are to act as a binder for the zeolite particulates, to prevent attrition of the catalyst bodies and to act as a diffusion medium and pre-cracking agent for the oil molecules.[29] The matrix converts some of the bulkiest molecules, but the zeolite is the main active component in the cracking process. Zeolite Y enables cracking of the alkanes and alkylaromatics in the feed as well as cracking of the alkenes that are formed as intermediates after pre-cracking by the matrix. It is assumed that the same acid-catalyzed pathways that have been observed for the conversion of model compounds are the main routes during the FCC process. Since the general view is that cracking is initiated by protonation of oil molecules on Brønsted acid sites inside FCC particles, the acidity of the FCC components influences the overall cracking activity of the catalyst.

Catalyst particles containing zeolite ZSM-5 instead of USY are co-fed in the FCC unit to increase the yield of light olefins. These products are mainly formed at the cost of gasoline yield, but in this process there is a gain in gasoline octane.[44-46] Furthermore, a slight decrease in the deposition of deactivating carbonaceous species on the catalyst is observed due to the addition of ZSM-5.[39]

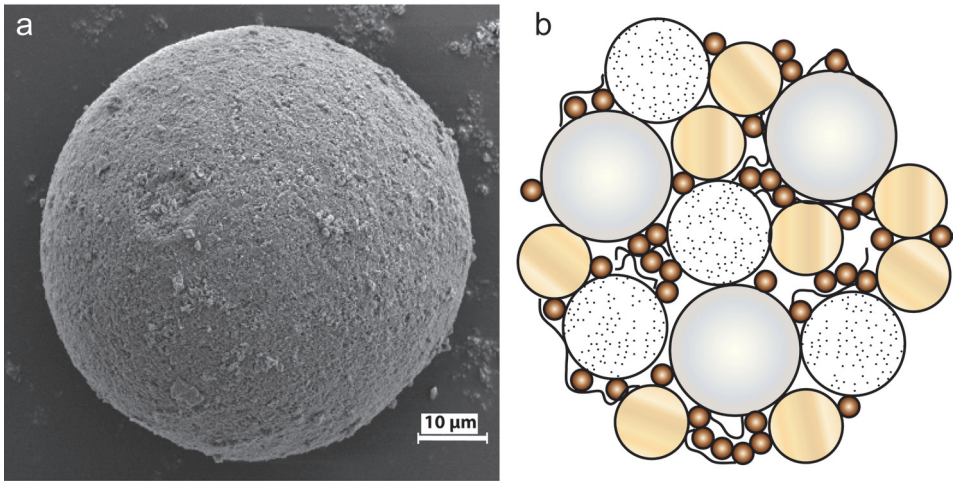


**Figure 1.4. (a)** Scanning Electron Microscopy image of a Fluid Catalytic Cracking (FCC) catalyst particle. **(b)** Schematic representation of the chemical composition and internal structure of an FCC catalyst particle.

Figure 1.5 shows a photograph and a schematic representation of the FCC reactor, which consists of two coupled operations, namely feedstock cracking and catalyst regeneration. The cracking reaction is an endothermic process in which the number of moles increases. For that reason it is favorable to perform the reaction at high temperature and low pressure.[20] Typically the capacity of an FCC unit is about 7 tons of oil per minute, while the catalyst circulation rates are in the order of 40 tons per minute.[21] This means that the catalyst-to-oil ratio lies around 6. The pre-heated catalyst (> 900 K) is mixed with a stream of heavy oil feedstock at pressures of 2-3 bars at the bottom of a so-called riser reactor, in which most of the cracking takes place. The contact time between catalyst and oil is in the order of fractions of seconds to a few seconds.[30,32] The temperature of the feed is normally between 400 and 640 K. After the cracking reaction the riser outlet temperatures are in the range of 770 to 830 K. The products leave the reactor through the cyclone separator, while the catalyst proceeds downwards into the so-called stripper. Here, hydrocarbons adsorbed on the catalyst particles are desorbed from the external surface and the pores by steam.

Due to coke-formation during the cracking process, the activity of the catalyst decreases.[47] These carbonaceous species, mostly aromatics, are highly condensed hydrocarbons which remain in the pore structure of the catalyst, thereby blocking its accessibility and thus reactivity towards new cracking reactions.[30,48] The amount of coke formed depends on the reactions conditions, the feedstock and the catalyst composition.[31] The coke is burnt off in the regenerator at temperatures between 920 and 1030 K to restore activity. The pressure in the regenerator is usually slightly higher than in the riser reactor, because a higher pressure favors the combustion rate.[30] Heat, which is released during the regeneration, is used to provide heat necessary for the endothermic cracking reactions.

After regeneration the catalyst can be re-used and is recycled into the riser reactor. During every cycle some catalyst is lost due to attrition and degradation of the particles. The so-called bleed stream of spent catalyst is for that reason compensated by addition of fresh catalyst particles in every cycle. This is done by feeding catalyst in the regenerator. By doing so a stable conversion level is maintained in the FCC unit. The periodic addition of fresh catalyst leads to a mixture of catalyst particles with a broad age distribution in the FCC unit and as a consequence of this also a wide variation in properties.[31,49] The oldest fractions have undergone a large amount of reaction-stripping-regeneration cycles and consequently suffer from surface area loss, metal deposition and aging, which is reflected in a lower catalytic activity in comparison to younger FCC fractions. The mixture that is present in a real FCC unit is for that reason called an equilibrium catalyst (Ecat).

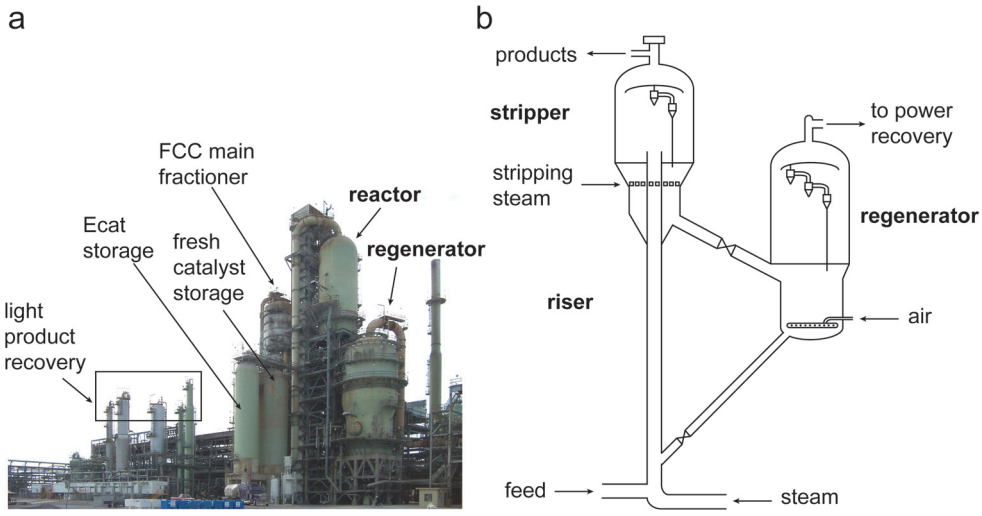


**Figure 1.5. (a)** Photograph and **(b)** schematic representation of an FCC cracking unit.

Not only is the catalyst deactivated due to coke formation and attrition in the cracking unit, but also some other reaction conditions have a detrimental effect on the catalyst particles and their properties. The main deactivating factors are: hydrothermal conditions and metal deposition.[48,50]

The presence of steam in the stripper and the formation of steam during the coke burning in the regenerator can alter the structure of the catalyst. It is known that steam, in combination with high temperatures, can lead to dealumination of the zeolite component and destruction of a part of the microporous zeolitic structure. A standard USY zeolite, which is the main active component in FCC particles, has a framework silicon-to-aluminum (Si/Al) ratio of 5.[48] In a typical Ecat this ratio can be as high as 20, which means that a significant amount of aluminum atoms and thus acid sites has been removed from the framework. The removal of acid sites will lower the overall reactivity of the catalyst. Furthermore, removal of aluminum from the framework can lead to the formation of *extra*-framework aluminum species, such as $Al^{3+}$, $AlO^{+}$, $Al(OH)_2^{+}$, $AlO(OH)$ and $Al(OH)_3$.[48] These components have been proven to act as Lewis acid sites,[51-52] which promote dehydrogenation reactions that lead to an increased coke and gas formation.[28]

As indicated, another very important deactivating factor in the FCC process is the presence of metal ions in the oil feed. Especially nickel and vanadium, mostly found as metal porphyrins in crude oil,[53] damage the zeolite structure and also favor dehydrogenation reactions and thus coke formation.[48,54] While cycling between the reducing atmosphere in

the riser reactor and the oxidative environment in the regenerator, the oxidation states of the nickel and vanadium ions change, which greatly enhances their mobility and favors metal interactions. Initially metals are deposited on the external surface of the catalyst, but as the catalyst ages, the metals migrate to the interior of the catalyst.[21] Over time the initial egg-shell distribution of metal species thus changes into a more homogeneous distribution throughout the whole catalyst body. The dehydrogenation activity of vanadium is about one-quarter to half that of nickel. However, a very deactivating role of vanadium species is the destruction of zeolite surface area, which causes a loss of catalytic activity. It is generally accepted that vanadium oxides can, in the presence of steam in the regenerator, be converted into vanadic acid ($H_3VO_4$) vapor.[55-56] Subsequently, vanadic acid is able to destroy the zeolite structure via acid hydrolysis of framework aluminum atoms. Further research has indicated that sodium, which is also present in the oil feed, can act as a partner of vanadium in the destruction of zeolites.[57-58] The vanadic acid in this mechanism catalyzes the formation of NaOH, which causes dissolution of the zeolite framework.

To study the influence of hydrothermal conditions, coke formation and metal deposition on the activity and structure of FCC catalyst particles, several laboratory deactivation techniques have been developed to simulate these factors. Catalyst manufacturers apply such protocols to deactivate freshly prepared catalyst particles, after which their catalytic activity is evaluated in catalytic cracking tests. Some of the most widely used deactivation techniques are steaming (ST)[59], two-step cyclic deactivation (CD)[60-64] and Mitchell impregnation-steam deactivation (MI).[65] Steaming is a procedure in which the catalyst sample is exposed to severe hydrothermal conditions (100% steam at 1061 K) for 20 h. Two-step cyclic deactivation involves a combination of mild hydrothermal treatment with 20 cycles of cracking-regeneration. The cracking reactions are performed with a real vacuum gas oil, which is spiked with vanadium and nickel naphthenates in order to mimic both the influence of coke formation and metal deposition. The Mitchell impregnation-steam deactivation procedure consists of an incipient wetness impregnation of the catalyst with nickel and vanadium naphthenates, followed by a severe hydrothermal treatment. Mitchell impregnation-steam deactivation overestimates the deactivating influence of metals, while steaming does not mimic metal deposition at all. Two-step cyclic deactivation, on the other hand, mimics the influence of metal deposition relatively well.[61]

After application of one of the deactivation protocols, the performance of the catalyst in terms of activity and selectivity can be tested in a so-called Fluid Simulation Test (FST). This small-scale single batch cracking unit simulates the product yield of a commercial FCC reactor (without regeneration) by injecting a small sample mass of gas

oil into a narrow closed-end cylinder containing a single charge (< 10 g) of fluidized laboratory deactivated catalyst. The products of the cracking reaction are analyzed by gas chromatography to obtain information about the selectivity.

## 3. Characterization of FCC catalysts

In literature a wide variety of analysis techniques has been applied to obtain a better understanding of the structure, composition, activity and chemical properties of FCC catalyst particles. A concise summary of these methods is given in Table 1.1. It can be concluded that most of the characterization methods focus on the investigation of the activity, metal distribution, coke formation and morphology of FCC catalyst materials. Mostly these characterization studies evaluate bulk properties of FCC catalysts.

**Table 1.1.** Main techniques described in literature for the analysis of FCC catalyst particles, in alphabetical order.

| Acronym | Full name | Type of information | Ref. |
|---|---|---|---|
| AAS | atomic absorption spectroscopy | elemental analysis after dissolution | [66] |
| AFM | atomic force microscopy | surface topology | [67] |
| DCR | Davison circulating riser | cracking activity and selectivity | [66,68] |
| EPMA | electron probe microanalysis | metals distribution across catalyst particle | [21,62,69] |
| EPR | electron paramagnetic resonance spectroscopy | chemical identity of coke components | [48,70-71] |
| ESCA | electron spectroscopy for chemical analysis | reaction product analysis | [66] |
| EXAFS | extended X-ray absorption fine structure | local coordination and bond distances of deposited metals | [69,72] |
| GC | gas chromatography | chemical identity of coke components | [48,70] |
| ICP-AES | inductively coupled plasma atomic emission spectroscopy | full chemical analysis after dissolution | [21,66] |
| IR | infrared spectroscopy | chemical identity of coke components | [48,70] |

| Acronym | Full name | Type of information | Ref. |
|---|---|---|---|
| (MAS) NMR | (magic angle spinning) nuclear magnetic resonance | $^{27}$Al: identification of aluminum types; | [69] |
| | | $^{29}$Si: surroundings of silicon atoms, degree of aluminum isolation; | [69] |
| | | $^{13}$C: chemical identity of coke components and other organics | [66,73] |
| MAT | microactivity test | cracking activity and selectivity | [66,74] |
| MS | mass spectrometry | chemical identity of coke components | [73] |
| $N_2$ physis. | nitrogen physisorption | pore volume and micro/ mesopore surface area; pore size distribution | [66] |
| Raman | Raman spectroscopy | chemical identity of coke components | [75] |
| SEM | scanning electron microscopy | morphology and surface topology | [21,69] |
| SEM-EDS | scanning electron microscopy – X-ray energy dispersive spectroscopy | morphology and surface topology, combined with elemental analysis | [21,62,66] |
| SIMS | secondary ion mass spectroscopy | characterization of deposited metals | [76-77] |
| STEM | scanning transmission electron microscopy | structures within catalyst material | [69] |
| TEM | transmission electron microscopy | structures within catalyst material | [66,69] |
| TGA | thermo-gravimetric analysis | reaction/adsorption – desorption monitored by weight changes | [21,69] |
| TPD | temperature-programmed desorption | acid site strength and number | [69,78-79] |
| TPR | temperature-programmed reduction | reductive stability | [69] |
| UV-Vis | ultraviolet – visible spectroscopy | chemical identity of coke components | [48,80-81] |
| XPS | X-ray photo-electron spectroscopy | coke location and characterization; | [73] |
| | | oxidation state of metals | [82-83] |

| Acronym | Full name | Type of information | Ref. |
|---|---|---|---|
| XRD | X-ray diffraction | zeolite unit cell size; structure, composition and amounts of crystalline material | [21,66] |
| XRF | X-ray fluorescence spectroscopy | chemical analysis | [21,66] |

## 4. Scope and outline of this PhD thesis

In this PhD research the investigation of the reactivity and acidity of Fluid Catalytic Cracking catalysts at the level of an individual catalyst particle is described.

**Chapter 2** reviews recently performed micro- and nano-spectroscopic work on the investigation of both model catalysts and industrially relevant catalytic materials. In this chapter the added value of micro-spectroscopic analysis tools becomes clear: *inter*- and *intra*particle heterogeneities within a large variety of catalyst materials can be evaluated using such approaches. Several catalytic systems are discussed, divided into structured porous oxides and supported metal (oxide) nanoparticles. For both classes of catalyst materials the available analysis techniques, together with the main research findings, are highlighted.

**Chapter 3** gives an overview of the reactivity of the main catalytic ingredients of FCC catalyst particles: zeolites H-ZSM-5 and H-Y. As a probe reaction the Brønsted acid-catalyzed oligomerization reaction of 4-fluorostyrene is selected and the reaction products are analyzed in time by UV-Vis micro-spectroscopy. By investigating the reactivity of the zeolite powders as a function of Si/Al ratio, insight in the reactivity as a function of Brønsted acidity is obtained. The formation of different reaction products in the pores of H-ZSM-5 and H-Y is explained by the differences in pore system and is rationalized using density functional theory calculations.

In **Chapter 4** the investigation of the styrene oligomerization reaction in combination with UV-Vis micro-spectroscopy is extended to individual FCC catalyst particles with the aim to study their reactivity and Brønsted acidity. Inspired by the staining approaches applied in life sciences for the visualization of distinct cellular features using fluorescence microscopy, a comparable method is applied in this thesis. When the FCC catalyst particles are examined after the styrene oligomerization (staining) reaction by confocal fluorescence microscopy, the fluorescent products can be visualized in a spatially resolved way in different layers of the catalyst particles. Inhomogeneously distributed fluorescent (zeolite) domains are observed within the catalyst bodies. This approach is not only applied for

fresh catalyst particles, but also for laboratory deactivated samples in order to study the influence of hydrothermal treatment, coke formation and metal deposition on the reactivity / Brønsted acidity of the catalyst in different life stages. A statistical evaluation of the fluorescence data enables comparison of the different catalyst samples and their acidity.

In order to link the space-resolved reactivity data to the structure of FCC catalyst particles, integrated laser and electron microscopy (iLEM) experiments, described in **Chapter 5**, have been performed. The iLEM setup enables correlative fluorescence microscopy / transmission electron microscopy measurements, by which the fluorescence patterns can be linked to structural features within the catalyst particles. Since the same Brønsted acid catalyzed 4-fluorostyrene oligomerization reaction is used in this study, the iLEM approach allows a structural characterization of both the Brønsted acidic and non-reactive areas within individual FCC catalyst particles with nanometer resolution.

A complementary confocal fluorescence study using thiophene oligomerization as a staining probe for Brønsted acidity is described in **Chapter 6**. The reactivity of different thiophene derivatives is assessed using both UV-Vis micro-spectroscopy and confocal fluorescence microscopy. Comparable results are obtained as with the styrene oligomerization reaction, indicating the suitability of thiophene derivatives for the evaluation of Brønsted acidity within FCC catalyst particles.

A statistical examination of the fluorescence intensities of fresh and laboratory deactivated catalyst particles upon reaction with thiophene is reported in **Chapter 7**. This thorough analysis reveals the same decreasing trend as the styrene oligomerization study in Chapter 4. The Brønsted acidity trend is furthermore compared to cracking activity data obtained with Fluid Simulation Tests and supported further by bulk analysis techniques (temperature-programmed desorption of ammonia, infrared spectroscopy after pyridine adsorption and X-ray powder diffraction in combination with a calculation of the unit cell size). As a showcase of the wide applicability of the developed statistical confocal fluorescence approach, an industrial equilibrium catalyst sample has been analyzed in the same manner. This analysis reveals a large *inter*particle heterogeneity that reflects the age range within an equilibrium catalyst.

**Chapter 8** provides an in-depth study of the structural features as well as the acidity of FCC catalyst particles at the single particle level using synchrotron-based infrared micro-spectroscopy. Both fresh and laboratory deactivated catalyst particles have been used for this investigation. The infrared spectra of the catalyst particles as such were used to study structural changes upon deactivation, while spectra after pyridine adsorption shed light on the Brønsted and Lewis acidity of individual FCC catalyst particles. Furthermore, individual particles within an equilibrium catalyst sample are analyzed using the same approach.

**Chapter 9** summarizes the main findings and conclusions of the preceding chapters. This chapter furthermore contains some perspectives for future research. The possibility to use a combination of focused ion beam milling with scanning electron microscopy for a structural investigation of the porosity and the internal structure of FCC catalyst particles is described on the basis of recently obtained results.

**Acknowledgement**

Karen Hemelsoet (Ghent University, Belgium) is acknowledged for the composition of the zeolite structures in Figures 1.2 and 1.3.

**References**

[1] A. F. Cronstedt *Akad. Handl. Stockholm* **1756**, *18*, 120-123.
[2] G. Friedel *C. R. Acad. Sci., Paris* **1896**, *122*, 948-951.
[3] G. Friedel *Bull. Soc. Fr. Mineral. Cristalogr.* **1896**, *19*, 363-390.
[4] F. Grandjean *C. R. Acad. Sci., Paris* **1910**, *149*, 866-868.
[5] O. Weigel; E. Steinhoff *Z. Kristallogr.* **1925**, *61*, 125-154.
[6] R. M. Barrer *J. Chem. Soc.* **1948**, 2158-2163.
[7] E. M. Flanigen *Stud. Surf. Sci. Catal.* **2001**, *137*, 11-35.
[8] E. M. Flanigen; B. M. Lok; R. L. Patton; S. T. Wilson *Stud. Surf. Sci. Catal.* **1986**, *28*, 103-112.
[9] S. T. Wilson *Stud. Surf. Sci. Catal.* **1991**, *58*, 137-151.
[10] J. M. Thomas; R. Raja; G. Sankar; R. G. Bell *Nature* **1999**, *398*, 227-230.
[11] B. M. Weckhuysen; R. R. Rao; J. A. Martens; R. A. Schoonheydt *Eur. J. Inorg. Chem.* **1999**, 565-577.
[12] M. E. Davis *Nature* **2002**, *417*, 813-821.
[13] M. E. Davis; C. Saldarriaga; C. Montes; J. Garces; C. Crowder *Nature* **1988**, *381*, 295-298.
[14] J. Jiang; J. Yu; A. Corma *Angew. Chem. Int. Ed.* **2010**, *49*, 3120-3145.
[15] M. Estermann; L. B. McCusker; C. Baerlocher; A. Merrouche; H. Kessler *Nature* **1991**, *352*, 320-323.
[16] A. Corma; M. J. Díaz-Cabañas; J. Jiang; M. Afeworki; D. L. Dorset; S. L. Soled; K. G. Strohmaier *Proc. Natl. Acad. Sci.* **2010**, *107*, 13997-14002.
[17] R. Pophale; P. A. Cheeseman; M. W. Deem *Phys. Chem. Chem. Phys.* **2011**, *13*, 12407-12412.
[18] S. Davis; Y. Inoguchi *CEH Marketing Research Report: Zeolites* **2009**, SRI Consulting
[19] M. M. Bomgardner *Chem. Eng. News* **2011**, *89*, 20-21.
[20] W. Vermeiren; J.-P. Gilson *Top. Catal.* **2009**, *52*, 1131-1161.
[21] W.-C. Cheng; E. T. Habib; K. Rajagopalan; T. G. Roberie; R. F. Wormsbecher; M. S. Ziebarth In *Handbook of Heterogeneous Catalysis*; 2nd ed.; G. Ertl, H. Knözinger, F. Schüth, J. Weitkamp, Eds.; Wiley-VCH: Weinheim **2008**; *6*, 2741-2778.
[22] J. Hagen *Industrial Catalysis: A Practical Approach*; Wiley-VCH: Weinheim **1999**, 225-247.
[23] C. Baerlocher; L. B. McCusker, Database of Zeolite Structures: http://www.iza-structure.org/databases/.
[24] R. W. Broach In *Zeolites in Industrial Separation and Catalysis*; S. Kulprathipanja, Ed.; Wiley-VCH: Weinheim **2010**, 27-59.
[25] P. A. Wright; G. M. Pearce In *Zeolites and Catalysis: Synthesis, Reactions and Applications*; J. Čejka, A. Corma, S. I. Zones, Eds.; Wiley-VCH: Weinheim **2010**; *1*,

171-207.
[26] W. H. Baur *Am. Mineral.* **1964**, *49*, 697-704.
[27] B. Sivasankar *Engineering Chemistry*; S. Jha, D. Dey, Eds.; Tata McGraw-Hill Publishing Company Limited: New Delhi **2008**, 155-202.
[28] A. Humphries; D. H. Harris; P. O'Connor In *Fluid Catalytic Cracking: Science and Technology*; J. S. Magee, M. M. Mitchell, Jr., Eds.; Elsevier Science Publishers B.V.: Amsterdam **1993**, 41-82.
[29] S. Bhatia *Catalytic Applications of Zeolites in Industrial Processes* CRC Press, Inc.: Boca Raton **1989**.
[30] H. F. Rase *Handbook of Commercial Catalysts*; CRC Press, Inc.: Boca Raton **2000**, 362-391.
[31] M. Rigutto In *Zeolites and Catalysis: Synthesis, Reactions and Applications*; J. Čejka, A. Corma, S. I. Zones, Eds.; Wiley-VCH: Weinheim **2010**; *2*, 547-584.
[32] S. F. Abdo In *Zeolites in Industrial Separation and Catalysis* S. Kulprathipanja, Ed.; Wiley-VCH: Weinheim **2010**, 535-569.
[33] L. E. L. Brouwer *The Petroleum Handbook*; 5th ed. Balding & Mansell Limited: London **1966**.
[34] E. J. Houdry **1931**; US 1837963.
[35] E. J. Houdry **1934**; US 1957648.
[36] E. J. Houdry **1934**; US 1957649.
[37] R. von Balmoos; D. H. Harris; J. S. Magee In *Handbook of Heterogeneous Catalysis*; 1st ed.; G. Ertl, H. Knözinger, J. Weitkamp, Eds.; Wiley-VCH: Weinheim **1997**; *4*, 1955-1983.
[38] *Zeolites for Cleaner Technologies*; M. Guisnet; J.-P. Gilson, Eds.; World Scientific Publishing Company: London **2002**.
[39] R. Gläser; J. Weitkamp In *Basic Principles in Applied Catalysis*; M. Baerns, Ed.; Springer-Verlag: Heidelberg **2004**, 161-212.
[40] C. J. Plank; E. Rosinski **1966**; US 3271418.
[41] P. K. Maher; C. V. McDaniel **1976**; US 3966882.
[42] C. V. McDaniel; P. K. Maher **1976**; US 3449070.
[43] J. Scherzer *Catal. Rev. Sci. Eng.* **1989**, *31*, 215-354.
[44] T. F. Degnan; G. K. Chitnis; P. H. Schipper *Microporous Mesoporous Mater.* **2000**, *35-36*, 245-252.
[45] S. J. Yanik; E. J. Demmel; A. P. Humphries; R. Campagna *Oil Gas J.* **1985**, *83*, 108-117.
[46] N. Y. Chen; T. F. Degnan Jr.; C. M. Smith *Molecular Transport and Reaction in Zeolites* John Wiley & Sons, Inc.: New York **1994**.
[47] M. Guisnet; P. Magnoux *Appl. Catal. A.- Gen.* **2001**, *212*, 83-96.
[48] H. S. Cerqueira; G. Caeiro; L. Costa; F. R. Ribeiro *J. Mol. Catal. A: Chem.* **2008**, *292*, 1-13.
[49] R. Quintana-Solórzano; A. Rodríguez Hernández; R. García-de-León; E. Terrés *Top. Catal.* **2011**, *54*, 547-560.
[50] F. Hernández; R. García-de-León; E. Mogica; J. C. Moreno; R. González; E. Garcia-Figuero *Stud. Surf. Sci. Catal.* **1997**, *111*, 455-462.
[51] D. Coster; A. L. Blumenfeld; J. J. Fripiat *J. Phys. Chem.* **1994**, *98*, 6201-6211.
[52] T. Chen; A. Men; P. Sun; J. Zhou; Z. Yuan; Z. Guo; J. Wang; D. Ding; H. Li *Catal. Today* **1996**, *30*, 189-192.
[53] N. I. Shilonosova; O. V. Serebrennikova; L. V. Ryadovaya *Chem. Technol. Fuels Oil* **1986**, *22*, 295-297.
[54] A. S. Escobar; F. V. Pinto; H. S. Cerqueira; M. M. Pereira *Appl. Catal. A. - Gen.* **2006**, *315*, 68-73.
[55] R. F. Wormsbecher; A. W. Peters; J. M. Maselli *J. Catal.* **1986**, *100*, 130-137.
[56] S. K. Park; H. J. Jeon; K. S. Jung; S. I. Woo *Ind. Eng. Chem. Res.* **2003**, *42*, 736-742.
[57] M. Xu; X. Liu; R. J. Madon *J. Catal.* **2002**, *207*, 237-246.

[58] D. V. Cristiano-Torres; Y. Osorio-Perez; L. A. Palomeque-Forero; L. E. Sandoval-Diaz; C. A. Trujillo *Appl. Catal. A. - Gen.* **2008**, *346*, 104-111.
[59] E. Rautiainen; R. Pimenta; M. Ludvig; C. Pouwels *Catal. Today* **2009**, *140*, 179-186.
[60] M. Bendiksen; E. Tangstad; T. Myrstad *Appl. Catal. A. - Gen.* **1995**, *129*, 21-31.
[61] A. C. Psarras; E. F. Iliopoulou; K. Kostaras; A. A. Lappas; C. Pouwels *Microporous Mesoporous Mater.* **2009**, *120*, 141-146.
[62] A. A. Lappas; L. Nalbandian; D. K. Iatridis; S. S. Voutetakis; I. A. Vasalos *Catal. Today* **2001**, *65*, 233-240.
[63] L. A. Gerritsen; H. N. J. Wijngaards; J. Verwoert; P. O'Connor *Catal. Today* **1991**, *11*, 61-72.
[64] A. C. Psarras; E. F. Iliopoulou; L. Nalbandian; A. A. Lappas; C. Pouwels *Catal. Today* **2007**, *127*, 44-53.
[65] B. R. Mitchell *Ind. Eng. Chem. Prod. Res. Dev.* **1980**, *19*, 209-213.
[66] G. M. Woltermann; J. S. Magee; S. D. Griffith *Stud. Surf. Sci. Catal.* **1993**, *76*, 105-144.
[67] M. L. Occelli; S. A. C. Gould; G. D. Stucky *Stud. Surf. Sci. Catal.* **1994**, *84*, 485-492.
[68] G. W. Young *Stud. Surf. Sci. Catal.* **1993**, *76*, 257-292.
[69] A. W. Peters *Stud. Surf. Sci. Catal.* **1993**, *76*, 183-222.
[70] H. S. Cerqueira; C. Sievers; G. Joly; P. Magnoux; J. A. Lercher *Ind. Eng. Chem. Res.* **2005**, *44*, 2069-2077.
[71] H. G. Karge; J.-P. Lange; A. Gutse; M. Laniecki *J. Catal.* **1988**, *114*, 144-152.
[72] D. J. Sajkowski; S. A. Roth; L. E. Iton; B. L. Meyers; C. L. Marshall; T. H. Fleisch; W. N. Delgass *Appl. Catal.* **1989**, *51*, 255-262.
[73] K. Qian; D. C. Tomczak; E. F. Rakiewicz; R. H. Harding; G. Yaluris; W.-C. Cheng; X. Zhao; A. W. Peters *Energ. Fuel.* **1997**, *11*, 596-601.
[74] E. L. Moorehead; J. B. McLean; W. A. Cronkright *Stud. Surf. Sci. Catal.* **1993**, *76*, 223-255.
[75] D. Espinat; H. Dexpert; E. Freund; G. Martino *Appl. Catal.* **1985**, *16*, 343-354.
[76] K. J. Chao; L. H. Lin; Y. C. Ling; J. F. Hwang; L. Y. Hou *Appl. Catal. A. - Gen.* **1995**, *121*, 217-229.
[77] E. L. Kugler; D. P. Leta *J. Catal.* **1988**, *109*, 387-395.
[78] L. Forni *Catal. Rev. Sci. Eng.* **1973**, *8*, 65-115.
[79] A. Auroux; Y. S. Yin; J. C. Vedrine; L. Benoist *Appl. Catal.* **1988**, *36*, 323-330.
[80] H. G. Karge *Stud. Surf. Sci. Catal.* **1991**, *58*, 531-570.
[81] C. Li; P. C. Stair *Catal. Today* **1997**, *33*, 353-360.
[82] T. F. Petti; D. C. Tomczak; C. J. Pereira; W.-C. Cheng *Appl. Catal. A. - Gen.* **1998**, *169*, 95-109.
[83] R. H. Nielsen; P. K. Doolin *Stud. Surf. Sci. Catal.* **1993**, *76*, 339-384.

# Chapter 2

## Observation of Dynamic Processes in Heterogeneous Catalysis at the Individual Particle Level

**Abstract**

This chapter reviews recent studies on spatiotemporal heterogeneities within catalytic solids at the individual particle level. Two different types of catalysts, namely structured porous oxides and supported metal (oxide) nanoparticles, are discussed. From the highlighted examples one can infer that this lively field of research has provided great advances in monitoring such heterogeneities in a variety of heterogeneous catalysts. It is clear that the widespread occurrence of physicochemical varieties at both the *intra*- and *inter*particle level will impact catalyst performance and that a better understanding of such heterogeneities could lead to strategies for the synthesis of new and improved catalyst materials.

This work is based on the following manuscript: I. L. C. Buurmans and B. M. Weckhuysen, *in preparation.*

## 1. Introduction

Catalysts are vital ingredients of everyday life processes: organisms do not function without enzymes, while for the production of food and many other materials, such as plastics and transportation fuels, catalysts are used. For that reason there has always been an enormous interest to understand and improve catalytic processes.[1-2] Solid materials used as heterogeneous catalysts are of crucial importance to pharmaceutical, (petro-)chemical and environmental industries: the fabrication of more than 85% of all fuels and chemicals involves catalytic materials. Many of the catalysts utilized in these processes consist of porous solid materials with a high surface area that provide the active sites on which chemical reactions are facilitated. By investigating the activity and selectivity of such solids, already major improvements and adjustments have been made in the design of catalyst materials that meet specific industrial needs.

Although many properties and the dynamic behavior of catalysts can be explained by macroscopic phenomena, a thorough insight into the nanoscale structure is required in order to fully understand the role of the active sites. At this scale the physicochemical properties are often very heterogeneous. For this purpose a range of analysis techniques has been developed,[3] among which spectroscopic approaches are often the most informative.[4] Such characterization studies have led to fundamental knowledge of active sites and their dynamics,[5] which facilitates a more profound and clever catalyst synthesis. The application of micro- and nano-spectroscopic techniques to heterogeneous catalysts has emerged as a powerful approach to understand catalysts at the single particle and/or single molecule level.

The aim of this chapter is to show the implications of catalyst heterogeneities as observed by modern micro- and nanoscopic methods. Several catalytic systems will be discussed, divided into structured porous oxides and supported metal (oxide) nanoparticles. For both classes of catalytic solids the available analysis techniques, together with the main research findings, will be highlighted. The chapter describes recent advances within the field and is limited to studies that apply optical techniques, implying that electron and scanning probe microscopy approaches will not be considered. Examples of such approaches can be found in a recent text book[6] and two review articles.[7-8]

An important conclusion of the studies covered is that, even at the single particle level, catalysts display heterogeneities in terms of structure, composition and reactivity. Within individual catalyst particles, even for simple model systems, structural and compositional differences clearly exist and these *intra*particle heterogeneities largely impact the overall performance of a catalyst material. Within a catalyst batch, *inter*particle reactivity heterogeneities complicate matters even more.

## 2. Spatiotemporal heterogeneities in catalytic solids

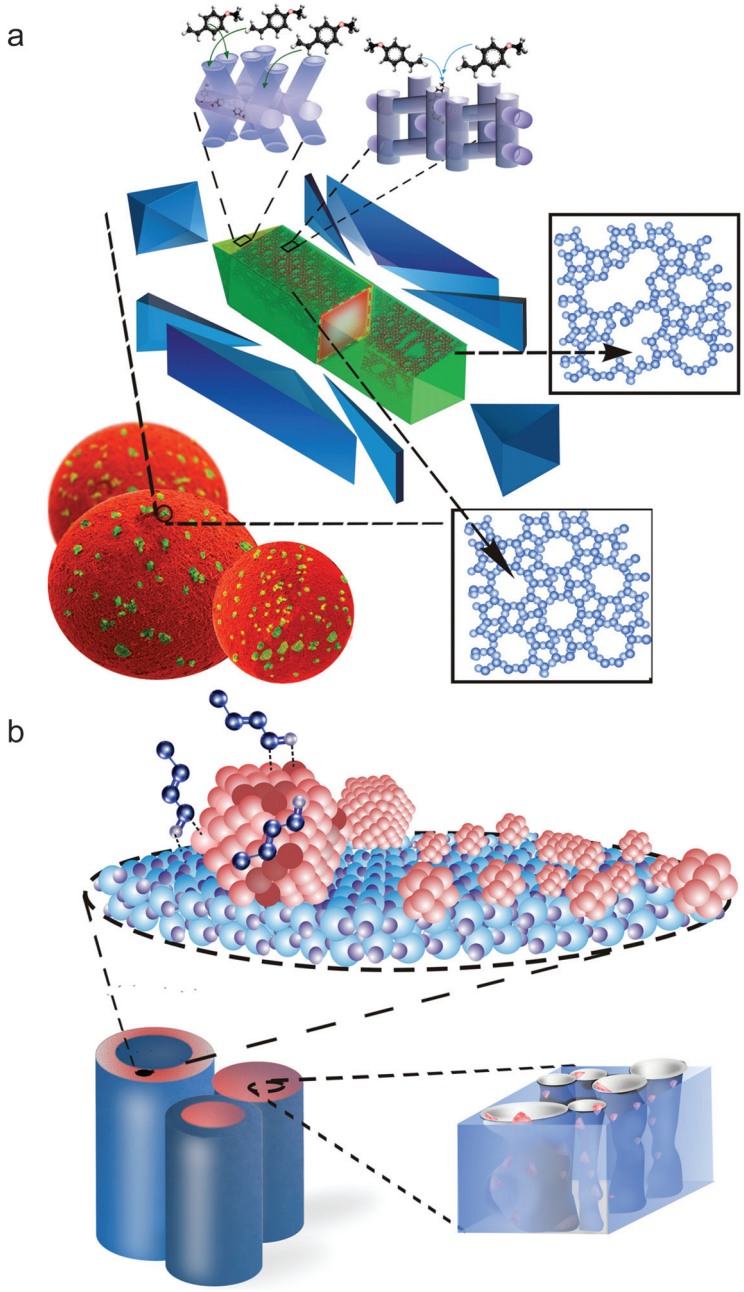


**Figure 2.1.** Schematic representation of spatial heterogeneities found in **(a)** structured porous oxide catalysts and **(b)** supported metal (oxide) nanoparticle catalyst materials.

Figure 2.1 illustrates the complexity of heterogeneous catalysts for two dominant types often employed in industrial processes. A catalyst is an intricate compound. Depending on the reactor type chosen the catalytic ingredient, either a structured porous oxide (Figure 2.1a) or supported metal (oxide) nanoparticles (Figure 2.1b), is dispersed within one or more binders or supports. These compounds are then shaped as either mm-sized (fixed bed reactor) or µm-sized (fluid bed reactor) catalyst pellets.

It is evident that each dispersed catalytically active ingredient within the matrix displays distinct catalytic performance. Due to the interplay of molecular diffusion, adsorption-desorption at the active site and chemical conversion substantial gradients in reagents and reaction products occur, leading *e.g.* to distinct catalytic performances at different positions in the reactor bed as well as in the catalyst pellet. As a result of their structural and compositional complexity additional spatial heterogeneities may occur. Such spatiotemporal heterogeneities can be organized according to the following lines of thought:

* **Active sites**. The spatiotemporal distribution and the nature of active sites in a catalytic material can display heterogeneity. Active site densities may differ from region to region, while differences in the nature of the active sites and their location within the material might cause variations in reactivity, immobilization time of reactants / products, product selectivity and catalyst stability.
* **Accessibility**. Some regions within a catalyst can, at a given moment, be more accessible towards reactants, thus facilitating a higher reaction rate in distinct areas of the catalytic material. Furthermore, within a catalyst batch, catalyst particles of different sizes may be present. Size differences cause fluctuations in the external surface / volume ratio, diffusion rates as well as in the reactivity.

In what follows both aspects will be discussed for the structured porous oxides, while the examples of supported metal (oxide) nanoparticles focus on variations in active sites. No micro- or nanoscopic studies on accessibility are available for this type of catalytic solid so far. Since in most cases the catalyst bodies containing supported metal (oxide) nanoparticles are composed of an amorphous matrix, such as alumina and silica, the macroporous structure implies less diffusion limitations. Most probably the fact that accessibility to the active sites is less restricted explains why this topic has so far not been discussed in literature.

## 3. Structured porous oxides

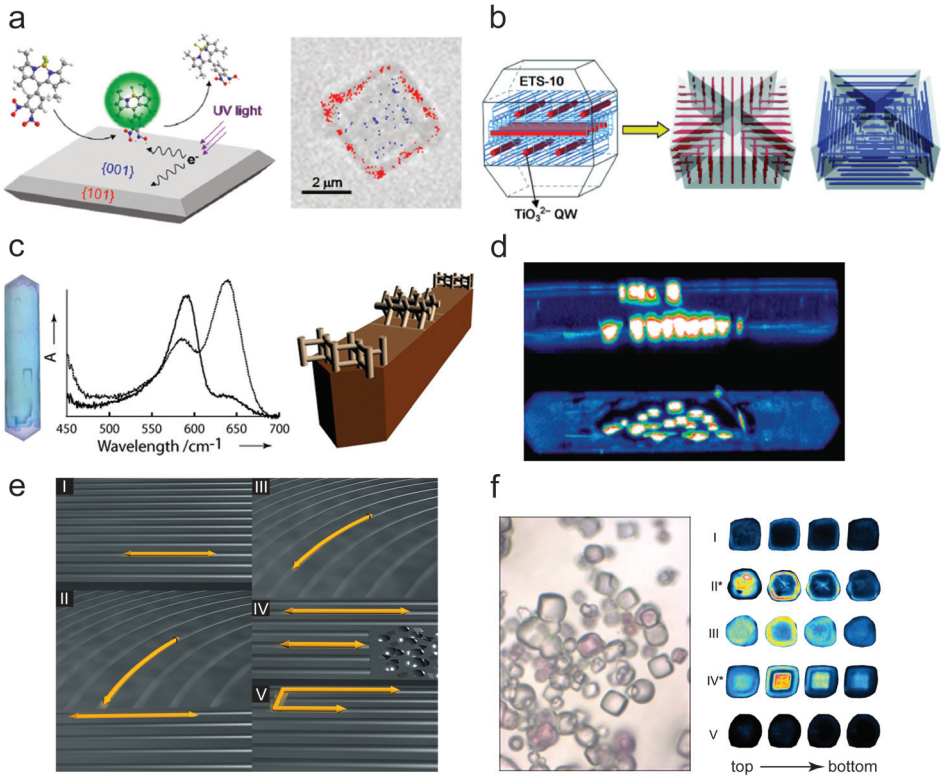


**Figure 2.2.** Selected examples from literature on the presence of spatiotemporal heterogeneities within structured porous oxides. **(a)** Photocatalytic reaction rates within a $TiO_2$ crystal, as revealed by single-molecule, single-particle fluorescence imaging, are higher at the 101 crystal plane compared to the 001 plane[9]; **(b)** Quantum wires are distributed in an organised pattern within the titanosilicate molecular sieve ETS-10[10]; **(c)** The distinct pore orientation in the edges and main body of large ZSM-5 crystals leads to differences in product formation, as exemplified by the corresponding UV-Vis micro-spectroscopy data[11-12]; **(d)** Inclusion of large fluorescent dye molecules in ZSM-5 crystals selectively visualizes the larger external voids that are created upon intentionally damaging the crystals[13]; **(e)** The channel system in different parts of a mesoporous silica film displays very large varieties in shape and tortuosity (schematic representation, reproduced from Zürner *et al.*[14]); **(f)** Heterogeneities in the reactivity of distinct SSZ-13 zeolite crystals towards styrene oligomerization are observed both at the *inter*particle level (left, optical microphotograph) and *intra*particle level (right, confocal fluorescence microscopy images) after alkaline treatment.[15]

### Active sites

Heterogeneities in the density and distribution of active sites within structured porous oxides can be divided into two different types. First, the presence of distinct crystal planes influences the reactivity of such materials, even at the individual crystal level. For example, Roeffaers

and colleagues have performed a single turnover analysis of individual layered double hydroxide (LDH) crystals with single molecule fluorescence microscopy during the transesterification of 5-carboxyfluorescein diacetate with 1-butanol, which revealed *intra*particle heterogeneities in terms of reactivity.[16-17] A higher reaction rate was observed at the 1010 crystal plane compared to the 0001 crystal plane. Histograms of the reaction rates on these different LDH crystal planes illustrate the spatial distribution of reactivity of a single catalyst particle. In another study the investigation of $TiO_2$ crystals using single-molecule, single-particle fluorescence imaging during the reduction of a boron-dipyrromethene compound by Majima and co-workers has led to the localization of photo-catalytically active sites. These sites are found to be located in higher amounts at the 101 crystal plane compared to the 001 plane. This is illustrated in Figure 2.2a.[9,18] Both landmark studies clearly indicate that the orientation of crystal planes influences the reactivity of the catalytic crystals. It is thus important for the fundamental understanding of such materials to gather more knowledge on the effect of crystal facets on catalyst performance.

Secondly, it is known that zoning of active sites within a porous solid can occur and one might wonder what the implications of such phenomena for concentration gradients of reactants or products are. A case study that investigates this intriguing issue involved individual zeolite Beta crystals. Using confocal fluorescence microscopy a gradient in coke formation was observed due to an inhomogeneous aluminum distribution within the catalyst crystal.[19] A higher amount of aluminum sites on the external surface of the crystals leads to a more hydrophilic surface that contains a higher amount of Brønsted acid sites compared to the internal part of the crystals. The higher the hydrophilicity of the reagent, the better its ability to penetrate towards the interior of the zeolite crystal, which leads to a high coke formation in the internal parts of the crystal.

Related to the naturally occuring aluminum zoning in zeolite Beta crystals, such a phenomenon could also be introduced artificially by the synthesis of large coffin-shaped ZSM-5 crystals with an external silicalite-1 layer. The product distribution within these zeolite crystals was studied using UV-Vis micro-spectroscopy and confocal fluorescence microscopy.[20] The inner aluminum-containing ZSM-5 crystallite was found to be still accessible towards reactant and product molecules through the aluminum-free external silicalite-1 layer. However, during the methanol-to-olefins reaction a significant decrease in the formation of extended graphite-like coke species compared to conventional ZSM-5 crystals was observed. This decrease is due to the egg-yolk distribution of active aluminum species and the consequent inactivity of the silicalite-1 layer towards coke formation. Tuning the structure of zeolite crystals could thus provide elegant new ways towards optimized catalytic systems.

Zoning of active sites was observed as well for the titanosilicate molecular sieve ETS-10 by Jeong *et al*.[10] It is known that within this material $TiO_3^{2-}$ quantum wires are present, which give ETS-10 its promising application as a component for *e.g.* solar cells. ETS-10 crystals were studied with laser scanning confocal polarized micro-Raman, which can reveal the location and structure of the quantum wires. More specifically, the microscopy experiments showed that the quantum wires are not evenly distributed within the material and that their length and length homogeneity vary within the crystal. An hourglass pattern was observed for their distribution, as shown in Figure 2.2b. The density of the quantum wires decreases from the center to the edge and from the middle to the corner along that edge. Since this density correlates with the crystallinity of the sample, important new information on the crystals becomes available. The crystallinity was found to increase in the direction of the crystal growth.

The surface active sites of the ETS-10 material were revealed in more detail in work from the Majima group by the application of fluorescence imaging during the photocatalytic oxidation of the dye 3'-(*p*-aminophenyl) fluorescein (APF).[21] APF molecules are preferentially adsorbed on the exterior of ETS-10 crystals, since they are too large to enter the crystal pores. After treatment of the ETS-10 crystals with HF, the fluorescence intensities measured for ETS-10 crystals were not only higher, but additionally spanned a broader intensity range. The photocatalytic activity of the crystals thus displayed an increased *inter*particle heterogeneity upon HF treatment. By examining individual crystals it was found that a highly fluorescent signal was detected at a crack-like defect as well as near the crystal edge. The partial local removal of Ti atoms in ETS-10 results in the generation of titanols as well as in the formation of larger micropores. Such defects can act as highly active sites for adsorption and oxidation of APF molecules.

**Accessibility**

Accessibility of structured porous oxide materials is a crucial factor that directly influences their spatiotemporal reactivity. The intrinsic structure of as-synthesized porous oxides gives rise to diffusion limitations that affect the spatial reactivity of the materials.

An in-depth examination of micron-sized coffin-shaped zeolite ZSM-5 crystals by different micro-spectroscopic techniques has led to a better understanding of their structure, micropore orientation, Brønsted acidity, activity and diffusion boundaries. *Intra*particle heterogeneities in terms of reactivity have been revealed by Kox and colleagues using UV-Vis micro-spectroscopy, confocal fluorescence microscopy, coherent anti-stokes Raman scattering and synchrotron-based IR microscopy in combination with the styrene and thiophene oligomerization probe

reactions. These Brønsted acid-catalyzed probe reactions lead to the formation of carbocationic reaction products, which can be monitored in time in different parts of the crystal bodies. Micro-spectroscopy experiments during both oligomerization reactions, exemplified in Figure 2.2c for styrene oligomerization, clearly showed that differences in micropore orientation in distinct parts of the zeolite material cause different product distributions in the edges and the body of the crystal. Furthermore, the product molecules were selectively aligned within the straight pores of the ZSM-5 crystals.[22-24] The use of a template burning approach, which yields fluorescent products that encounter diffusion barriers within the crystals, was used to elucidate the complex *inter*growth structure of the zeolite crystals.[25]

A further rationalization of the micropore distribution and the related molecular diffusion barriers of large ZSM-5 crystals was achieved by Electron Backscatter Diffraction.[26] This technique confirmed the differences in pore orientation in the edges of the zeolite crystals compared to the main body, as visualized in Figure 2.2c. Differences in pore orientation introduce *inter*growth structures, which clearly impact the reactivity of the different domains in such a crystal. It was found that such *inter*growth structures are not only present in the previously described coffin-shaped ZSM-5 zeolite. Further analysis of differently sized and shaped ZSM-5 zeolites and different metal-containing microporous aluminophosphates (MeAPO-5) was performed to investigate their internal structure in microscopic detail. All examined micron-sized crystals were found to display *inter*growth structures consisting of different subunits, revealing their wide-spread occurrence. Crystals with different length-to-width aspect ratios were examined for the large ZSM-5 crystals and four types of *inter*growth structures were revealed that were dependent on this aspect ratio. The interfaces between the subunits that build up the overall crystal structure cause distinct molecular diffusion barriers. This observation provides clear proof for the existence of *inter*particle heterogeneities between different zeolite crystals, leading to distinct molecular diffusion barriers.[26]

With respect to the visualization of defects and diffusion barriers within structured porous oxides, dye molecules can be used to visualize such molecular boundaries. Seebacher *et al.* brought up the idea of combining confocal fluorescence microscopy and large fluorescent dyes, such as 4-(4-diethylaminostyryl)-1-methyl-pyridinium-iodide (DAMPI) or oxazine-1, to study defect structures within zeolite ZSM-5 crystals.[27] This approach has since then been successfully applied by other groups as well for structural studies of porous oxides. Since the dyes are too large to enter the micropores of zeolitic material, all spots in which the dyes can be occluded into a material indicate larger defect voids. Such experiments have been applied to investigate the structure of both untreated and

intentionally damaged micron-sized coffin-shaped ZSM-5 crystals.[13] From these experiments it was clear that DAMPI molecules could only penetrate into the damaged regions of the crystals, thus revealing the presence of larger internal zeolite voids (Figure 2.2d).

The shape and accessibility of the network within porous oxides can also influence the organization of molecules within the material. An investigation of alignment of probe molecules with different molecular sizes within zeolite L crystals was performed by Brasselet and co-workers using two-photon fluorescence polarimetric microscopy.[28] With this approach it was found that fluorescent molecules display a considerably higher degree of disorder when they are more flexible or smaller. Higher concentrations of molecules led to a higher degree of disorder due to steric interactions between the molecular species in densely packed regions.

Second-harmonic generation (SHG) microscopy can shed further light on diffusion and organisation of organic molecules in porous materials, since it is a surface-specific technique. Van der Veen *et al.* have studied several porous materials, among which micron-sized SAPO-5 and ZSM-5 crystals, during the uptake of *p*-nitroaniline (PNA).[29-30] Only head-to-tail arranged PNA molecules are visualized with SHG microscopy. It was found that for both types of crystals ordering of PNA molecules at the external parts of the crystal took place, which gives rise to SHG. The interior of the ZSM-5 crystals did not display SHG signal although the pores were filled with PNA, thus indicating disordered PNA molecules. Interestingly, for the SAPO-5 crystals, which display a one-dimension pore system, both the interior and external parts of the crystal give rise to head-to-tail organisation of PNA molecules.

Distinct active sites within a catalyst body can display differences in accessibility and adsorption strength towards reacting molecules. An elegant investigation of the molecular diffusion of fluorescent terrylene diimide derived molecules in a hexagonally ordered mesoporous silica film was executed using fluorescence microscopy for high-resolution tracking by Bräuchle and co-workers.[14,31-32] The channel system in different parts of the mesoporous silica film was found to display very large varieties in shape and tortuosity, schematically shown in Figure 2.2e. This leads to a broad distribution in both the diffusion coefficients and the time that molecules spend immobilized at an adsorption site. These results indicate the large *intra*particle heterogeneities, both in the mesopore structure and strength of the adsorption sites. Such differences will largely impact the spatial and consequently the overall reactivity of catalytic materials. Even more in-depth insight into the growth of silica nanochannels was obtained by monitoring their real-time formation and growth.[33] Using fluorescence polarization imaging and atomic force microscopy the formation of lamellar structures that are the precursors of the final hexagonal layers could be examined in great detail.

The photocatalytic activity and accessibility of individual porous $TiO_2$ nanotubes was investigated using a similar approach.[34] Such tubes contain straight macropores (100-150 nm) as well as mesopores (5-10 nm) and it is known that a variety of reactive oxygen species, which react with organic molecules, can be formed on $TiO_2$ surfaces. Aminophenyl fluorescein (APF) molecules for example can, in the presence of reactive oxygen species, be converted into fluorescein and these molecules can subsequently be monitored in a spatiotemporal way. It was found that both the formation of fluorescein in macro- and mesopores could be visualized. Counting rates of single fluorescein molecules were found to be an order of magnitude higher within the macropores compared to the mesopores, due to kinetic restrictions for the transport of reagents in the smaller mesopores. The exact positions at which fluorescein molecules were generated could be determined from the measurements as well and were found to be heterogeneously distributed, even for isolated nanotubes. A possible explanation for the spatial variations in reactivity of the nanotubes could be the presence of surface defects.

It is well known that mesoporous silica materials can be modified by *post*-synthesis functionalization. 3-aminopropyltriethoxysilane (APTES), for example, can be grafted on the surface of mesoporous silica and makes the material susceptible towards reaction with a variety of functional groups. This process has been studied by a combination of nitrogen physisorption and confocal laser scanning microscopy (CLSM) by Gartmann *et al*.[35] They have found that the presence of water during the grafting process strongly influences the deposition of APTES: an increasing contribution of larger pores is observed in that case. This indicates that the amino groups are less uniformly distributed in the material. By examining individual crystals using CLSM after fluorescent labeling, it was found that amino groups were accumulated at the pore entrances. This is due to the increased interaction of APTES with the surface in the presence of water, which leads to preferential grafting of the most accessible sites.

Another important factor in the reactivity of porous oxides is the volume that is effectively used to perform reactions. A detailed fluorescence microscopy study of a Ti-MCM-41 catalyst particle during the epoxidation of a fluorescent reporter molecule has revealed a gradient in the amount of fluorescent products along the crystal diameter.[36] In these experiments the formation of fluorescent reporter molecules only took place in the outer 300 nanometers of the catalyst crystals, which had an average total width of 2 μm. These remarkable observations indicate an inefficient use of the overall catalyst volume, which must be pronounced in many other catalytic materials as well.

Evolution of concentration profiles in porous materials can be monitored in great detail using interference microscopy. By such studies, pioneered by Kärger and co-workers, profound insight into the catalyst

volume of individual catalyst particles that is effectively used during reactions can be obtained. An interference microscopy study of *e.g.* ferrierite zeolite crystals during desorption of methanol, has shown that there is a transport resistance at the surface of the crystals, which leads to a delayed desorption of methanol.[37-38] The proposed model that explains this transport resistance is the presence of a thin layer at the surface of the crystal in wich mass transport is very slow. Reasons for the occurrence of such a layer could be sterical obstructions caused by an increase in structural defects near the surface of the crystals.

The relatively low efficiency in the use of catalyst body volume can be significantly improved by increasing the accessibility of the material and thus decreasing *intra*particle diffusion limitations. This can lead to the presence of different pore sizes within porous oxides, since well-established *post*-synthesis treatments, such as dealumination or desilication, can be applied to create meso- and macropores within initially microporous zeolites. Such so-called hierarchical zeolites will consequently display regions with higher and lower accessibility towards reactants as well as a spatial alteration of their reactivity.[39] However, *post*-synthesis treatments can also create new types of heterogeneities within catalyst batches and within individual catalyst particles.

Alkaline treatment of porous oxidic materials is one clear example of a procedure that can lead to an increased accessibility of catalytic solids. As examplified for micron-sized zeolite SSZ-13 crystals by Sommer *et al.* (Figure 2.2f), the reactivity of the crystals towards the oligomerization of styrene derivatives increased upon alkaline treatment and revealed differences in reactivity in distinct parts of the crystals.[15] Furthermore, differences were observed in the reactivity of distinct crystals after alkaline treatment. This is indicative of an *inter*particle heterogeneity in the susceptibility of individual SSZ-13 crystals towards the alkaline etching procedure, which consequently influences the reactivity of individual crystals within the catalyst batch. Another study by Kox and colleagues has shown similar results. By comparison of purely microporous micron-sized boat-shaped ZSM-5 crystals and their desilicated derivatives upon reaction with styrene, it was found that desilication leads to the formation of mesopores.[40] UV-Vis micro-spectroscopy measurements of the product distribution in the parent and desilicated crystals showed that the introduction of mesopores leads to an enhanced selectivity towards dimeric styrene products. Furthermore, the mesopore formation increases the accessibility of the crystals, which results in a more evenly distributed product formation within the crystals. In a recent study, Karwacki *et al.* have evaluated large coffin-shaped ZSM-5 crystals upon steam treatment, which results in dealumination, and a similar enhancement of the accessibility of the zeolite material has been noticed.[41] However, the tip regions of the crystals, in which the straight pores are open to the surface,

were found to be hardly affected, illustrating the spatial variations in the effects of zeolite steam treatments.

The size of individual particulates within a structured porous oxide greatly influences the reactivity of the material. Since the external-surface-to-catalyst-volume ratio changes upon alterations of the catalyst particle size, the contribution of the surface reactions in comparison to reactions within the catalyst material will change. A clear example of this phenomenon is observed for micron-sized ZSM-5 crystals in comparison to conventional ZSM-5 crystals with dimensions of a few hundred nanometers. For both types of crystals the oligomerization reaction of 4-fluorostyrene was followed in time using UV-Vis micro-spectroscopy.[22,42] It was observed that the formation of the cyclic dimeric reaction product was much more pronounced upon reaction of the nanometer-sized crystallites, which could be rationalized by the fact that the cyclic dimer is formed at the external surface of the ZSM-5 material, which is more dominant for small sized zeolite crystals.

## 4. Supported metal (oxide) nanoparticles

### Active sites

One of the most detailed insights into spatial heterogeneities of supported metal (oxide) nanoparticles originates from the research work of Chen and co-workers using single-molecule fluorescence microscopy.[43] By investigating single turnovers of the gold nanoparticle-catalyzed conversion of resazurin to fluorescent resorufin, the activity of individual gold particles has been investigated. Flashes of light were detected for every single product molecule adsorbed on individual gold nanoparticles, as illustrated in Figure 2.3a. Both the kinetics of product formation and product dissociation could be elegantly followed in time for a series of catalyst particles. In about 1% of all turnover events, multiple on-levels were observed. This is due to the formation of a new product molecule before dissociation of the previous one, which is an example of *intra*particle reactivity heterogeneity.[49] Individual gold nanoparticles of 6 nm in size show different activities and by statistical analysis of the single-particle turnover trajectories as a function of substrate concentrations it was possible to determine kinetic parameters of individual Au nanoparticles.

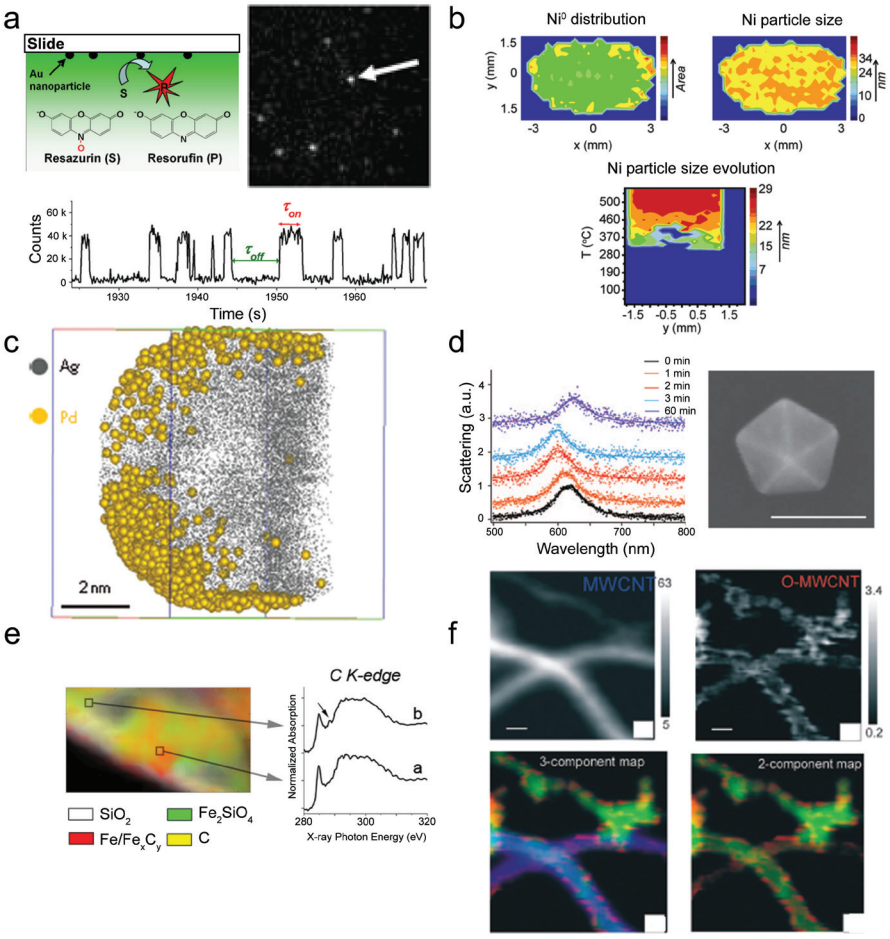


**Figure 2.3.** Selected examples from literature on the presence of spatiotemporal heterogeneities within supported metal (oxide) nanoparticles. **(a)** Single catalyst turnover activity of gold nanoparticles reveals on and off-levels that differ per particle, thus revealing the presence of distinct surface site types[43]; **(b)** $Ni/Al_2O_3$ catalyst bodies contain Ni nanoparticles differing in size and amount along the pellet[44]; **(c)** Ag/Pd core/shell catalyst particles with a thin Pd layer show significantly higher activity towards hydrogen production than particles with a thicker Pd shell[45]; **(d)** Gold decahedron nanoparticles, studied with surface plasmon spectroscopy, display a blue shift due to electron injection from ascorbic acid and subsequently a red shift due to oxidation of ascorbic acid[46]; **(e)** Analysis of a silica-supported iron-based Fischer-Tropsch catalyst under working conditions reveals the preferential presence of carbidic carbon (yellow) in iron-rich areas (green and red)[47]; **(f)** $RuO_2$ on multi-walled carbon nanotubes shows a non-homogeneous distribution of $RuO_2$ (blue) over the carbon material (green).[48]

The *inter*particle heterogeneities in terms of activity for different Au nanoparticles have been explained by the presence of two types of surface sites with different catalytic properties. The first surface site type, which displays a lower activity, has a higher substrate binding affinity (type-a). The second surface site, with a lower substrate binding affinity, has a higher activity (type-b). Each Au nanoparticle seems to predominantly possess type-a behavior at low substrate concentration, whereas type-b behavior dominates at higher substrate concentration. The exact substrate concentration at which the transition from type-a to type-b occurs differs for each Au nanoparticle and spans a range of two orders of magnitude, which is a clear indication of the large heterogeneity within the nanoparticle batch. Unfortunately, the origin of these type-a and type-b surface sites has not yet been determined and would provide insight into its relationship with specific crystal facets of the Au nanoparticles. This requires that *e.g.* transmission electron microscopy would be combined under identical experimental conditions with fluorescence microscopy. In a related study from the same group the connection between Au particle size and activity has been examined and both product formation and dissociation rates were found to depend on the size of the gold particles.[50] Small particle sizes, *e.g.* 6 nm, displayed a higher substrate binding activity, which led to an increased catalytic conversion. However, the product binding activity was found to increase as well with smaller particle size, which resulted in a lower product dissociation.

Sakamoto *et al.* have shown that Au clusters with a diameter of about 1 nm display different properties compared to large nanoparticles or bulk material.[51] More specifically, the photocatalytic activity of the $Au_n$ (n = amount of Au atoms) clusters was tested and it was found that the initial fluorescence of the clusters could be both reversibly and irreversibly quenched in the presence of $O_2$. Oxygen adsorption can take place on negatively charged $Au_n$ clusters by a (partial) charge transfer. Since quenching was partially reversible, this quenching must proceed through a weak interaction. The binding energy of $O_2$ on $Au_n$ clusters with an odd number of atoms was found to be much smaller than that of even-numbered $Au_n$ clusters. This means that the observed fluorescent species in the experiment would be odd-numbered $Au_n$ clusters, in which the quenching is much less pronounced. To validate this observation, other electron acceptors, such as nitrobenzene, have been examined. The reduction potentials of these molecules were comparable to that of $O_2$ and the compounds were found to quench the fluorescence as well. The electron transfer is thus thought to be one of the reasons for the fluorescence quenching properties of $O_2$.

As explained previously for the structured porous oxide catalysts, zoning of active sites can occur in metal (oxide) catalysts as well and affects the spatial reactivity of a catalytic material. The macro-distribution

of metal nanoparticles within catalyst pellets for example is known to impact catalyst activity, selectivity and stability. By using UV-Vis, Raman and IR micro-spectroscopy as well as magnetic resonance imaging it has been possible to map in great detail the distribution of Co, Mo, Pd and Ni within mm-sized alumina extrudates.[52] More specifically, it was possible to vary the overall distribution of these transition metal elements within an extrudate by altering the pH of the aqueous impregnation solution as well as by using additives, such as citrate, chloride and amines.[53] Depending on the type of Ni complex used for catalyst impregnation and by varying the temperature, different macro-distributions of Ni metal and Ni carbide particles were obtained within the catalyst body. Interestingly, in the case of supported $Ni/Al_2O_3$ catalyst bodies it was even possible to obtain insight into the genesis and particle size distribution of metallic Ni within catalyst bodies. This could be done with tomographic energy dispersive diffraction imaging in three dimensions, as depicted in Figure 2.3b.[44] As can be seen in this figure, a higher amount of Ni nanoparticles was deposited at the external parts of the catalyst pellet, leading to zoning in the amount of Ni along the axis of the pellet. The size of the Ni particles differed from spot to spot and varied between 24 and 34 nm when the material was calcined at 773 K.

A zoning of active sites has been observed by Xu and colleagues for single-walled carbon nanotubes as well.[54] Super-resolution single-molecule fluorescence microscopy in combination with resazurin as fluorescent probe molecule was used to probe individual electro-catalysis events. It was found that the fluorescent bursts during electro-catalysis occur at discrete sites, *e.g.* defect sites or nanotube ends, suggesting that only part of the particle is actively involved in the catalytic process.

Within metal (oxide) nanoparticle catalysts core/shell metal particle systems, comparable to the core/shell silicalite-1/ZSM-5 example described for the porous oxides, have been developed as well. In a breakthrough investigation by Tsang and co-workers atom probe tomography has been used to elucidate the structure of individual Ag/Pd core/shell catalysts. These catalyst particles, as illustrated in Figure 2.3c, contain a shell of 1 to 10 layers of Pd atoms, which accommodates terrace sites that, promoted by the Ag core, greatly enhance catalytic activity in the production of hydrogen by formic acid decomposition.[45] A significantly higher activity towards hydrogen production was observed in case of a thin (1-2 atomic layers) Pd shell, which indicates that the electronic promotion effect of the Ag core is only influential over a few atomic distances.

Moreover, a study of Au/Pd core/shell nanoparticles on a $SiO_x/Si$ support provided additional clear evidence that the thickness of the Pd shell influences the behavior of the catalyst particle.[55] Particles with a thicker Pd shell were found to show a higher tendency of Au/Pd *inter*diffusion and

the formation of palladium silicide. Furthermore, the metal nanoparticles were studied with dark-field microscopy during hydrogen uptake under realistic reaction conditions. It was found that differently shaped particles displayed distinct hydrogen uptake trajectories. Triangular plates and icosahedra showed a qualitatively different hydrogen uptake than decahedra in the same catalyst batch. It was observed that the thickness of the Pd shell was uniformly thicker for the decahedra compared to the triangles and icosahedra and that such variations led to differences in hydrogen uptake behavior of the nanoparticles.

Mulvaney and co-workers, by using a combination of dark-field microscopy and surface plasmon spectroscopy, have been able to monitor the rates of the two consecutive steps comprising a redox reaction at the single particle level for gold nanoparticles.[46] More specifically, they have investigated an individual ~ 100 nm-sized Au decahedron particle during the oxidation of ascorbic acid by oxygen dissolved in water. In the first 3 minutes of the reaction a sudden blue shift of the surface plasmon band of Au was noticed, as shown in Figure 2.3d. This shift of approximately 20 nm could be explained in terms of an electron injection of 4,600 electrons per second from the ascorbate anions into the individual Au nanoparticle. In a second step, a gradual red shift was observed (Figure 2.3d) and after 60 minutes the initial surface plasmon band had returned to its starting position, which corresponds to a consumption of 65 oxygen molecules per second. As these surface plasmon phenomena could be cyclically measured, this approach offers potential for investigating the influence of particle size and shape on other reactions catalyzed by Au.

Scanning transmission X-ray microscopy (STXM) and micro-beam X-ray absorption fine structure spectroscopy (μ-XAFS) have been developed in recent years to reveal spatial heterogeneities within supported metal (oxide) catalyst materials. STXM, for example, has been performed on individual silica supported iron-based Fischer-Tropsch catalyst particles by de Smit *et al*. (Figure 2.3e). This has led to the generation of nanoscopic maps of the phase changes of an individual catalyst particle.[47] These maps indicated *intra*particle heterogeneities, as it was found that the active iron phase was inhomogeneously distributed within the silica binder. The spatial inhomogeneities were found to depend on the treatment as well as on the applied reaction conditions. Furthermore, the location of carbon species during the reaction has been accurately mapped and a preferential presence of carbidic carbon in iron-rich areas is observed, while patches of aliphatic carbon are found in the iron-poor areas of the catalyst material.

In another elegant STXM experiment the electronic structure of individual ruthenium oxide coated multi-walled carbon nanotubes has been investigated.[48] An increase in surface oxidation of the carbon nanotubes has been observed after $RuO_2$ coating, which is indicative of a

strong interaction between $RuO_2$ and the carbon nanotubes. Also here the nanoscopic maps demonstrate pronounced *intra*particle heterogeneities, as the $RuO_2$ coating is non-homogeneously spread over the carbon nanotubes. This phenomenon is shown in Figure 2.3f. A first-of-its-kind μ-XAFS investigation has recently been performed by Tada and colleagues. These authors have studied a practical $NiO_x/Ce_2Zr_2O_y$ catalyst and proper data analysis revealed the presence of catalytically active and inactive phases within an individual catalyst particle.[56]

## 5. Conclusions

The micro- and nano-spectroscopic studies discussed in this chapter allow to conclude that the occurrence of spatiotemporal heterogeneities at the level of an individual catalyst particle as well as between different catalyst particles is more rule than exception. One might wonder what kind of consequences these observations imply for catalyst research in general. First of all, it is clear that new chemical information becomes available on the required structure of active sites, including their distribution and embedding within their matrix. These insights enable more deliberate approaches for catalyst preparation. Furthermore, the observed heterogeneities should be taken into account in future theoretical and engineering modeling studies. Ultimately these considerations will lead to a more complete rational design, in which scientific knowledge and advanced synthesis tools allow the construction of intricate catalyst materials with full control over the activity, selectivity and stability of the active sites.

### Acknowledgement

Agnieszka Ruppert (Technical University Lodz, Poland) is acknowledged for the design of Figure 2.1.

### References

[1] *Handbook of Heterogeneous Catalysis*; 2nd ed.; G. Ertl, H. Knözinger, F. Schüth, J. Weitkamp, Eds. Wiley-VCH: Weinheim **2008**.
[2] J. Hagen *Industrial Catalysis: A Practical Approach* Wiley-VCH: Weinheim **1999**.
[3] F. Tao; M. Salmeron *Science* **2011**, *331*, 171-173.
[4] *In Situ Spectroscopy of Catalysts*; B. M. Weckhuysen, Ed. American Scientific Publishers: Stevenson Ranch **2004**.
[5] B. M. Weckhuysen *Nature Chem.* **2009**, *1*, 690-692.
[6] G. A. Somorjai; Y. Li *Introduction to surface chemistry and catalysis*; 2nd ed. John Wiley & Sons, Inc.: Hoboken **2010**.
[7] G. Ertl *Angew. Chem. Int. Ed.* **2008**, *47*, 3524-3535.
[8] K. L. Yeung; N. Yao *J. Nanosci. Nanotechnol.* **2004**, *4*, 647-690.

[9] T. Tachikawa; S. Yamashita; T. Majima *J. Am. Chem. Soc.* **2011**, *133*, 7197-7204.
[10] N. C. Jeong; H. Lim; H. Cheong; K. B. Yoon *Angew. Chem. Int. Ed.* **2011**, *50*, 8697-8701.
[11] B. M. Weckhuysen *Angew. Chem. Int. Ed.* **2009**, *48*, 4910-4943.
[12] E. Stavitski; M. H. F. Kox; B. M. Weckhuysen *Chem. Eur. J.* **2007**, *13*, 7057-7065.
[13] M. B. J. Roeffaers; R. Ameloot; M. Baruah; H. Uji-i; M. Bulut; G. De Cremer; U. Müller; P. A. Jacobs; J. Hofkens; B. F. Sels; D. E. De Vos *J. Am. Chem. Soc.* **2008**, *130*, 5763-5772.
[14] A. Zürner; J. Kirstein; M. Döblinger; C. Bräuchle; T. Bein *Nature* **2007**, *450*, 705-709.
[15] L. Sommer; S. Svelle; K. P. Lillerud; M. Stöcker; B. M. Weckhuysen; U. Olsbye *Langmuir* **2010**, *26*, 16510-16516.
[16] M. B. J. Roeffaers; B. F. Sels; H. Uji-i; F. C. De Schryver; P. A. Jacobs; D. E. De Vos; J. Hofkens *Nature* **2006**, *439*, 572-575.
[17] G. De Cremer; B. F. Sels; D. E. De Vos; J. Hofkens; M. B. J. Roeffaers *Chem. Soc. Rev.* **2010**, *39*, 4703-4717.
[18] T. Tachikawa; N. Wang; S. Yamashita; S.-C. Cui; T. Majima *Angew. Chem. Int. Ed.* **2010**, *49*, 8593-8597.
[19] A. N. Parvulescu; D. Mores; E. Stavitski; C. M. Teodorescu; P. C. A. Bruijnincx; R. J. M. Klein Gebbink; B. M. Weckhuysen *J. Am. Chem. Soc.* **2010**, *132*, 10429-10439.
[20] D. Mores; E. Stavitski; S. P. Verkleij; A. Lombard; A. Cabiac; L. Rouleau; J. Patarin; A. Simon-Masseron; B. M. Weckhuysen *Phys. Chem. Chem. Phys.* **2011**, *13*, 15985-15994.
[21] T. Tachikawa; S. Yamashita; T. Majima *Angew. Chem. Int. Ed.* **2010**, *49*, 432-435.
[22] M. H. F. Kox; E. Stavitski; B. M. Weckhuysen *Angew. Chem. Int. Ed.* **2007**, *46*, 3652-3655.
[23] M. H. F. Kox; K. F. Domke; J. P. R. Day; G. Rago; E. Stavitski; M. Bonn; B. M. Weckhuysen *Angew. Chem. Int. Ed.* **2009**, *48*, 8990-8994.
[24] E. Stavitski; M. H. F. Kox; I. Swart; F. M. F. de Groot; B. M. Weckhuysen *Angew. Chem. Int. Ed.* **2008**, *47*, 3543-3547.
[25] L. Karwacki; E. Stavitski; M. H. F. Kox; J. Kornatowski; B. M. Weckhuysen *Angew. Chem. Int. Ed.* **2007**, *46*, 7228-7231.
[26] L. Karwacki; M. H. F. Kox; D. A. M. de Winter; M. R. Drury; J. D. Meeldijk; E. Stavitski; W. Schmidt; M. Mertens; P. Cubillas; N. John; A. Chan; N. Kahn; S. R. Bare; M. Anderson; J. Kornatowski; B. M. Weckhuysen *Nature Mater.* **2009**, *8*, 959-965.
[27] C. Seebacher; J. Rau; F.-W. Deeg; C. Bräuchle; S. Altmaier; R. Jäger; P. Behrens *Adv. Mater.* **2001**, *13*, 1374-1377.
[28] A. Gasecka; L.-Q. Dieu; D. Brühwiler; S. Brasselet *J. Phys. Chem. B* **2010**, *114*, 4192-4198.
[29] M. A. van der Veen; J. Van Noyen; B. F. Sels; P. A. Jacobs; T. Verbiest; D. E. De Vos *Phys. Chem. Chem. Phys.* **2010**, *12*, 10688-10692.
[30] M. A. van der Veen; B. F. Sels; D. E. De Vos; T. Verbiest *J. Am. Chem. Soc.* **2010**, *132*, 6630-6631.
[31] J. Kirstein; B. Platschek; C. Jung; R. Brown; T. Bein; C. Bräuchle *Nature Mater.* **2007**, *6*, 303-310.
[32] J. Michaelis; C. Bräuchle *Chem. Soc. Rev.* **2010**, *39*, 4731-4740.
[33] C. Jung; P. Schwaderer; M. Dethlefsen; R. Köhn; J. Michaelis; C. Bräuchle *Nat. Nanotechnol.* **2011**, *6*, 87-92.
[34] T. Tachikawa; T. Majima *Langmuir* **2009**, *25*, 7791-7802.
[35] N. Gartmann; C. Schütze; H. Ritter; D. Brühwiller *J. Phys. Chem. Lett.* **2010**, *1*, 379-382.
[36] G. De Cremer; M. B. J. Roeffaers; E. Bartholomeeusen; K. Lin; P. Dedecker; P. P. Pescarmona; P. A. Jacobs; D. E. De Vos; J. Hofkens; B. F. Sels *Angew. Chem. Int. Ed.* **2010**, *49*, 908-911.

[37] L. Heinke; C. Chmelik; P. Kortunov; D. M. Ruthven; D. B. Shah; S. Vasenkov; J. Kärger *Chem. Eng. Technol.* **2007**, *30*, 995-102.
[38] C. Chmelik; J. Kärger *Chem. Soc. Rev.* **2010**, *39*, 4864-4884.
[39] J. Pérez-Ramírez; C. H. Christensen; K. Egeblad; C. H. Christensen; J. C. Groen *Chem. Soc. Rev.* **2008**, *37*, 2530-2542.
[40] M. H. F. Kox; E. Stavitski; J. C. Groen; J. Pérez-Ramírez; F. Kapteijn; B. M. Weckhuysen *Chem. Eur. J.* **2008**, *14*, 1718-1725.
[41] L. R. Aramburo; L. Karwacki; P. Cubillas; S. Asahina; D. A. M. de Winter; M. R. Drury; I. L. C. Buurmans; E. Stavitski; D. Mores; M. Daturi; P. Bazin; P. Dumas; F. Thibault-Starzyk; J. A. Post; M. W. Anderson; O. Terasaki; B. M. Weckhuysen *Chem. Eur. J.* **2011**, DOI: 10.1002/chem.201101361.
[42] I. L. C. Buurmans; E. A. Pidko; J. M. de Groot; E. Stavitski; R. A. van Santen; B. M. Weckhuysen *Phys. Chem. Chem. Phys.* **2010**, *12*, 7032-7040.
[43] P. Chen; X. Zhou; H. Shen; N. M. Andoy; E. Choudhary; K.-S. Han; G. Liu; W. Meng *Chem. Soc. Rev.* **2010**, *39*, 4560-4570.
[44] L. Espinosa-Alonso; M. G. O'Brien; S. D. M. Jacques; A. M. Beale; K. P. de Jong; P. Barnes; B. M. Weckhuysen *J. Am. Chem. Soc.* **2009**, *131*, 16932-16938.
[45] K. Tedsree; T. Li; S. Jones; C. W. A. Chan; K. M. K. Yu; P. A. J. Bagot; E. A. Marquis; G. D. W. Smith; S. C. E. Tsang *Nat. Nanotechnol.* **2011**, *6*, 302-307.
[46] C. Novo; A. M. Funston; P. Mulvaney *Nat. Nanotechnol.* **2008**, *3*, 598-602.
[47] E. de Smit; I. Swart; J. F. Creemer; G. H. Hoveling; M. K. Gilles; T. Tyliszczak; P. J. Kooyman; H. W. Zandbergen; C. Morin; B. M. Weckhuysen; F. M. F. de Groot *Nature* **2008**, *456*, 222-226.
[48] J. Zhou; J. Wang; H. Fang; C. Wu; J. N. Cutler; T. K. Sham *Chem. Commun.* **2010**, *46*, 2778-2780.
[49] W. Xu; J. S. Kong; Y. T. E. Yeh; P. Chen *Nature Mater.* **2008**, *7*, 992-996.
[50] X. Zhou; W. Xu; G. Liu; D. Panda; P. Chen *J. Am. Chem. Soc.* **2010**, *132*, 138-146.
[51] M. Sakamoto; T. Tachikawa; M. Fujitsuka; T. Majima *J. Am. Chem. Soc.* **2009**, *131*, 6-7.
[52] L. Espinosa-Alonso; A. M. Beale; B. M. Weckhuysen *Acc. Chem. Res.* **2010**, *43*, 1279-1288.
[53] L. Espinosa-Alonso; A. A. Lysova; P. de Peinder; K. P. de Jong; I. V. Koptyug; B. M. Weckhuysen *J. Am. Chem. Soc.* **2009**, *131*, 6525-6534.
[54] W. Xu; H. Shen; Y. J. Kim; X. Zhou; G. Liu; J. Park; P. Chen *Nano Lett.* **2009**, *9*, 3968-3973.
[55] M. L. Tang; N. Liu; J. A. Dionne; A. P. Alivisatos *J. Am. Chem. Soc.* **2011**, *133*, 13220-13223.
[56] M. Tada; N. Ishiguro; T. Uruga; H. Tanida; Y. Terada; S.-i. Nagamatsu; Y. Iwasawa; S.-i. Ohkoshi *Phys. Chem. Chem. Phys.* **2011**, *13*, 14910-14913.

# Chapter 3

## Styrene Oligomerization as a Molecular Probe Reaction for Zeolitic Brønsted Acidity: A UV-Vis Micro-Spectroscopy and DFT Study


### Abstract

A series of H-ZSM-5 samples with different framework silicon-to-aluminum (Si/Al) ratios was studied by analyzing the kinetics and reaction mechanism of the oligomerization of 4-fluorostyrene as molecular probe reaction for Brønsted acidity. The formation of carbocationic species was followed by UV-Vis micro-spectroscopy. Three carbocationic products were observed, namely a cyclic dimer, a conjugated linear dimer and a larger, more conjugated carbocation. Rate constants for the formation of all three products show a maximum at a Si/Al ratio of 25. Oligomerization of 4-fluorostyrene within the larger supercages of zeolite H-Y leads solely to cyclic dimers. The experimental observations were rationalized by DFT calculations, which show that the selectivity of the styrene oligomerization is controlled by the steric properties of the *intra*zeolite micropore voids. Two reaction pathways were considered for the formation of the conjugated linear carbocation. The conventional mechanism involves a hydride transfer between two dimeric hydrocarbons in the zeolite pores. Here, an alternative monomolecular path is proposed, in which the hydride transfer takes place between a hydrogen atom of a styrene dimer and a zeolitic proton, yielding a conjugated carbocation and molecular $H_2$. Computed free energies indicate that the preference for a particular reaction mechanism is determined by the local shape of the zeolite micropores.



This work is based on the following manuscript: I. L. C. Buurmans, E. A. Pidko, J. M. de Groot, E. Stavitski , R. A. van Santen and B. M. Weckhuysen, *Phys. Chem. Chem. Phys.* **2010**, 12, 7032-7040.

## 1. Introduction

Zeolites are crystalline aluminosilicates that constitute an important group of solids, which can be used as heterogeneous catalysts for a wide variety of reactions.[1-2] The well-defined microporous structures of these materials along with pronounced acidities define the main area of their application, which is acid catalysis. Numerous characterization studies have been performed to reveal the relationship between the molecular structure of zeolitic materials, their catalytic activity and Brønsted or Lewis acidity.[3-7] A wide variety of acid-catalyzed hydrocarbon transformations can be promoted by zeolites.[8-9] These include important chemical reactions, such as isomerization, oligomerization and cracking of hydrocarbons.[1,10] Since the 1960s zeolites have been succesfully applied for the catalytic cracking of oil.[8-9] It is generally believed that carbocations are the important reaction intermediates or transition states for these processes.[8-9]

Zeolite acidity depends, among other factors, on the framework aluminum concentration. Indeed, by introducing more aluminum atoms in the framework (*i.e.* at lower silicon-to-aluminum (Si/Al) molar ratios), the density of acid sites in the material increases. On the other hand, the strength of the individual acid sites increases when the sites become more isolated.[11-12] This behavior is generally known as the next nearest neighbor effect.[8,13] For that reason the effective acidity of Brønsted acid sites in H-ZSM-5, as calculated by aluminum topological density calculations, is expected to show a maximum around a Si/Al ratio of 9.5.[14] Furthermore, for the reactivity of zeolites the accessibility of the acid sites plays an important role. By creating mesopores and extra-framework aluminum species upon steaming or acid leaching treatments of the zeolite-based catalysts, enhancement of reactivity is observed.[15] The partial destruction of the crystalline structure improves the accessibility of the intrazeolite active sites towards large molecules. This favorably affects the catalytic reactivity of the resulting mesoporous zeolite.[2,16] Elucidating the relationship between acidity, accessibility and reactivity is of great importance for both the fundamental understanding of zeolites in catalysis and for the optimization of their catalytic performance.

A wide variety of techniques for the characterization of zeolite acidity is available.[1,9,17-19] Among the most commonly used techniques are IR spectroscopy in combination with various probe molecules[20-22], activity analysis in hydrocarbon cracking[23-24], temperature-programmed desorption (TPD) of basic probe molecules such as ammonia[25-26] or amines[27] and solid-state NMR spectroscopy.[28] For example, IR spectroscopy in combination with pyridine, lutidine and collidine as molecular probes provides an accessibility index of the different types of acid sites within zeolite materials.[22]

UV-Vis spectroscopy constitutes another suitable tool to study

the reactivity and acidity of zeolite materials. By monitoring the acid catalyzed transformation of a probe molecule, namely the oligomerization of 4-fluorostyrene, with UV-Vis micro-spectroscopy, the formation of carbocationic reaction intermediates can be monitored.[29-31] Substituted styrenes are suitable probe molecules because the various oligomerization products have different UV-Vis spectroscopic signatures and therefore can be studied *in situ*. Furthermore, depending on the Brønsted acid strength and spatial properties of the microporous structure of the catalyst, formation of specific carbocationic products is expected. This allows the direct investigation of the Brønsted acidity by analyzing the reaction products formed upon styrene oligomerization. Fluorine-substituted styrene is an attractive candidate, as it shows a moderate reactivity towards acid-catalyzed oligomerization, thus allowing time-resolution of the reaction steps and determination of reaction rate constants for the formation of particular carbocations.[29-31]

In this chapter, the reactivity of a series of H-ZSM-5 crystallites with different Si/Al ratios is investigated by UV-Vis micro-spectroscopy to establish a relationship between Brønsted acidity and styrene oligomerization reactivity. The product formation within H-ZSM-5 is compared to that in zeolite H-Y. Density functional theory (DFT) calculations were used to create a molecular-level picture of the experimental observations.

## 2. Experimental procedures

UV-Vis micro-spectroscopy studies were performed using an Olympus BX41M upright research microscope provided with a 10x 0.3 NA objective lens. Illumination of the sample was done using a 75W tungsten lamp. The microscopy setup was equipped with a 50/50 double-viewport tube, which accommodated a charge-coupled device (CCD) video camera (ColorView IIIu, Soft Imaging System GmbH) and an optical fiber mount. The microscope was connected to a CCD UV-Vis spectrometer (AvaSpec-2048TEC, Avantes) by a 200-µm-core fiber. UV-Vis micro-spectroscopy measurements were carried out using an *in situ* cell (Linkam Scientific Instruments FTIR 600) equipped with a temperature controller (Linkam Scientific Instruments TMS 94). Both the UV-Vis microscopy setup and the *in situ* cell are depicted in Figure 3.1.

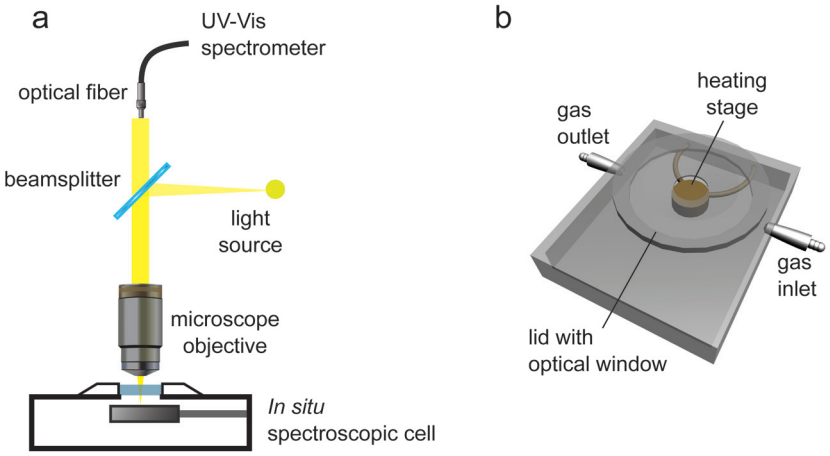


**Figure 3.1. (a)** Schematic representation of the UV-Vis microscope and **(b)** the *in situ* spectroscopic cell.

The acidity of H-ZSM-5 materials was studied using a probe molecule that shows a spectral change when exposed to Brønsted acid sites. 4-fluorostyrene (Acros Organics, 97%) was chosen for that purpose since only sufficiently strong Brønsted acid sites are able to protonate the molecule, which subsequently undergoes an oligomerization reaction that can be studied by the changes in the UV-Vis absorption bands.[30] With confocal fluorescence microscopy measurements on H-ZSM-5 crystals it was shown that the styrene oligomerization reaction can take place in the micropores of the zeolite.[29-31]

Zeolite ZSM-5 samples (CBV2314, Si/Al = 11.5; ACZeo-ZN030, Si/Al = 15; ACZeo-ZH030, Si/Al = 15; CBV5524G, Si/Al = 25; CBV8014, Si/Al = 40 and CBV28014, Si/Al = 140) and zeolite Y samples (ACZeo-Y307, Si/Al = 3.5; ACZeo-Y411, Si/Al = 5.5; ACZeo-Y530, Si/Al = 15; ACZeo-Y655, Si/Al = 27.5; CBV760, Si/Al = 30 and CBV780, Si/Al = 40) were obtained from Albemarle Corporation and Zeolyst International in either $NH_4^+$- or $H^+$-form. Prior to first use all $NH_4^+$-samples were heat-treated at 723 K for 24 h. Preceding all measurements samples were heat-treated in air at 723 K for 2 h to remove any adsorbed species.

All experiments were performed on 5 mg of zeolite powder, compressed to a pellet at a pressure of 5 ton $cm^{-2}$ on a Perkin-Elmer 15.011 laboratory press. After heating the pellet to the desired temperature for 10 min, 10 µl of 4-fluorostyrene was added and UV-Vis absorption spectra were taken every 5 s using an acquisition time of 20 ms and averaging the signal 100 times.

$N_2$-physisorption isotherms were recorded using a Micromeritics Tristar 3000 setup operating at 77 K. Prior to physisorption measurements, all samples were dried overnight at 573 K under a $N_2$ flow. The Brunauer-Emmett-Teller (BET) surface area was determined and rounded off to the nearest half dozen. In order to obtain the micropore volume and external surface area (rounded off to the nearest half dozen) of the samples the t-plot method was applied to the obtained physisorption isotherms. The results of the structural characterization of the H-ZSM-5 materials used in this study are summarized in Table 3.1.

**Table 3.1.** Overview of the investigated H-ZSM-5 materials.

| Sample name | Si/Al molar ratio | t-plot external surface area ($m^2$ $g^{-1}$) | t-plot micropore volume ($cm^3$ $g^{-1}$) | BET surface area ($cm^3$ $g^{-1}$) |
|---|---|---|---|---|
| ZSM5-1 | 11.5 | 120 | 0.13 | 370 |
| ZSM5-2 | 15 | 165 | 0.13 | 420 |
| ZSM5-3 | 15 | 160 | 0.11 | 380 |
| ZSM5-4 | 25 | 200 | 0.11 | 405 |
| ZSM5-5 | 40 | 205 | 0.11 | 415 |
| ZSM5-6 | 140 | 110 | 0.12 | 380 |

Quantum chemical calculations were performed using the Vienna Ab Initio Simulation Package (VASP) within density functional theory (DFT).[32] The gradient-corrected Perdew-Burke-Ernzerhof (PBE) exchange-correlation functional was used. [33] Electron-ion interactions were described with the projected-augmented wave (PAW) method[34-35] and for valence electrons a plane wave basis set was applied. The energy cut-off was set to 400 eV. The Brillouin zone sampling was restricted to Γ-point.[36] In a first step the cell parameters were optimized for the periodic models of full-silica zeolite crystals. The acquired parameters were used in all further calculations. Such computational settings were previously shown to be adequate for an accurate description of catalytic reactivity of zeolites.[37-41] For all structures full geometry optimizations were performed with the fixed cell parameters using a conjugated gradient algorithm. At the initial step of optimization all atoms of the unit cell were allowed to relax. Convergence at this stage was assumed to be attained when the energy difference between the optimization steps was below $10^{-4}$ eV. At the next step, the local structures of the adsorption complexes were refined by geometry optimization in which only the positions of the atoms of the hydrocarbon species and the Brønsted acid site were relaxed until the forces on each atom were below 0.02 eV/Å. According to our test calculations such an approximation allows substantial reduction of the computational costs associated with the optimization of the zeolite models

and at the same time leads to rather accurate results. Even though further relaxation of the structures containing a hydrocarbon species confined in zeolite ZSM-5 with the threshold of 0.02 eV/Å applied to all atoms of the model may require up to 100 additional steps, the associated total energy change did not exceed 5 kJ $mol^{-1}$. A modest Gaussian smearing was applied to band occupations around the Fermi level and the total energies were extrapolated to $\sigma \rightarrow 0$.

The used model for the H-ZSM-5 zeolite was a complete periodically repeated MFI unit cell. All calculations were performed using the orthorhombic structure of ZSM-5.[42] Unsubstituted styrene was used as a model reagent compound. The parameters of the all-silica MFI orthorhombic structure ($Si_{96}O_{192}$) after optimization of volume and shape were as follows: a = 20.119 Å, b = 19.767 Å, c = 13.161 Å. This compares perfectly with the respective experimental XRD data (a = 20.090 Å, b = 19.738 Å, c = 13.142 Å).[42] By replacing one of the 96 unit cell silicon atoms by an aluminum atom, an MFI lattice with a Si/Al ratio of 95 was obtained. The aluminum atom was positioned at the T2 crystallographic site, which creates an acid site at the intersection of the straight channel and the sinusoidal pore. A hydrogen atom, which introduced a Brønsted acid site, was implemented into the structure to obtain a neutral framework.

Similar to previous studies[37-38] the periodic model of the zeolite H-Y structure used for DFT calculations was a rhombohedral faujasite unit cell ($Si_{48}O_{96}$). The following optimized parameters of the all-silica zeolite Y rhombohedral unit cell were calculated: a = b = c = 17.5125 Å, α = β = γ = 60.00°. 14 silicon atoms were replaced by aluminum atoms, which were uniformly distributed over the unit cell according to the Löwenstein-rule. This resulted in a Si/Al ratio of 2.43. Furthermore, 14 hydrogen atoms, which act as Brønsted acid sites were implemented in the structure to achieve a neutral framework. To test the impact of the framework Al density on the stability of the carbocationic species in faujasite, selected products of the styrene dimerization confined in a low-aluminum faujasite matrix denoted as USY (Si/Al = 47) were also considered. In this case a single Al atom was introduced at the 6-membered ring of the supercage (SII site). The DFT-computed formation energies of various linear dimeric styrene species did not differ more than 5 kJ $mol^{-1}$ in H-Y compared to USY matrices. Therefore we limit the discussion of the results obtained to the more realistic H-Y model that is furthermore unbiased by the arbitrarily chosen positioning of framework Al atoms.

Gibbs free energies were computed within the ideal gas approximation at a pressure of 1 atm and a temperature of 373 K using the results of frequency analysis performed by means of the finite difference method as implemented in VASP. Using this method, harmonic normal modes were computed. Small displacements (0.02 Å) of atoms

from the extraframework species were used for the estimation of the numerical Hessian matrix. The other zeolitic atoms were kept fixed to their equilibrium positions. For the gas-phase the $H_2$ contributions to the partition functions from translational, rotational and vibrational motions were taken into account, whereas only vibrational degrees of freedom were considered for the species in the zeolite channel.

The energies of formation as calculated with DFT were further corrected for dispersion interactions by adding the contributions from van der Waals *inter*molecular bonds between the confined hydrocarbon species and the zeolite lattice. The *inter*atomic interactions involved were estimated by computing an additional *inter*atomic Lennard-Jones potential for the DFT-optimized structures as defined in the CVFF[43-44] force field with the approach as proposed by Demuth *et al.*[39] and Vos *et al*.[40] using the GULP program.[45] The CVFF force field is known to be very accurate for the description of various phenomena associated with the formation and dynamics of hydrocarbon species within the zeolite pores.[46-47] Previous studies indicated that the addition of the empirical corrections to the results obtained at the PBE level result in both thermodynamic and kinetic parameters very close to those obtained at the higher *ab initio* level.[41,48]

## 3. Results and discussion

To the series of H-ZSM-5 zeolite samples with different Si/Al ratios (Table 3.1) 4-fluorostyrene was added at 333 K. The reaction was monitored using *in situ* UV-Vis micro-spectroscopy. Figure 3.2 shows that, upon reaction, three major absorption bands were formed at 520 nm, 560 nm and 610 nm and that their intensities increased in time. According to Scheme 3.1 (product **7**) and Table 3.2, the absorption band at 520 nm corresponds to the formation of a cyclic dimeric carbocation. Absorption at a wavelength of 490 nm is reported for the comparable compound 4-methoxystyrene upon exposure to acidic zeolites.[49-50] The band is slightly shifted due to the presence of the electron withdrawing fluorine atom in the case of 4-fluorostyrene. The additional absorption bands around 560 nm and 610 nm are due to the presence of a conjugated linear dimeric carbocation (Scheme 3.1 (product **5**) and Table 3.2) and a larger, more conjugated carbocation, respectively.[29,49,51]

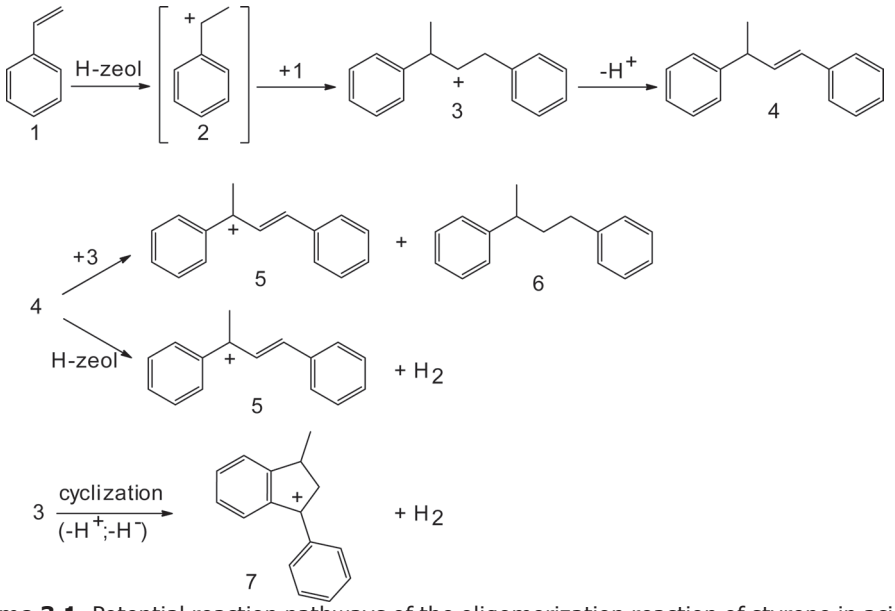


**Scheme 3.1.** Potential reaction pathways of the oligomerization reaction of styrene in acidic zeolites.[49,51] Upon protonation of styrene (**1**) by a Brønsted acid site of the zeolite, the initial benzylic carbocation (**2**) is formed. Dimerization with another styrene monomer (**1**) can take place to yield the linear dimeric 1,3-bisphenyl-1-butylium cation (**3**), which can undergo cyclization to the cyclic dimeric 3-methyl-phenylindanyl (indanyl) carbocation (**7**) or undergo a hydride shift to form the conjugated linear dimeric 1,3-bisphenyl-2-buten-1-ylium (allylic) carbocation (**5**). A bimolecular pathway for this reaction and a direct hydride transfer from the zeolite framework to the linear dimer are both considered. Further oligomerization will yield larger, more conjugated reaction products.

From gas chromatography (GC) analysis it is known that styrene is converted into a mixture of a linear and a cyclic dimer when using a variety of both liquid and solid acids.[52] The formation of dimeric products upon exposure of 4-methoxystyrene dissolved in isooctane to H-Y and H-ZSM-5 samples has been demonstrated by UV-Vis spectroscopy.[50] The extracted styrene products were analyzed using GC, gas chromatography coupled mass spectrometry (GC-MS), gas chromatography coupled infrared spectroscopy (GC-IR), proton nuclear magnetic resonance ($^{1}$H-NMR) and carbon nuclear magnetic resonance ($^{13}$C-NMR). *In situ* IR spectroscopy of acidic zeolites during reaction with 4-methoxystyrene demonstrates that dimers are the major components in the mixture of organic products.[49] Furthermore, the experimentally obtained UV-Vis and IR spectra were supported with theoretical calculations at the Hartree-Fock and Becke 3-parameter, Lee-Yang-Parr (B3LYP) levels to simulate the spectra.[53] By preparing the conjugated linear dimeric carbocation (**5**) in solution it was possible to measure its characteristic $^{13}$C-NMR signals and compare these to a $^{13}$C-NMR spectrum predicted by theoretical calculations.[53] In addition,

an *in situ* synchrotron-based IR micro-spectroscopy study, supported by model DFT calculations on 4-fluorostyrene oligomerization in H-ZSM-5 crystals has clearly indicated the formation of conjugated linear dimeric carbocations (**5**) within the straight channels of the zeolite.[54]

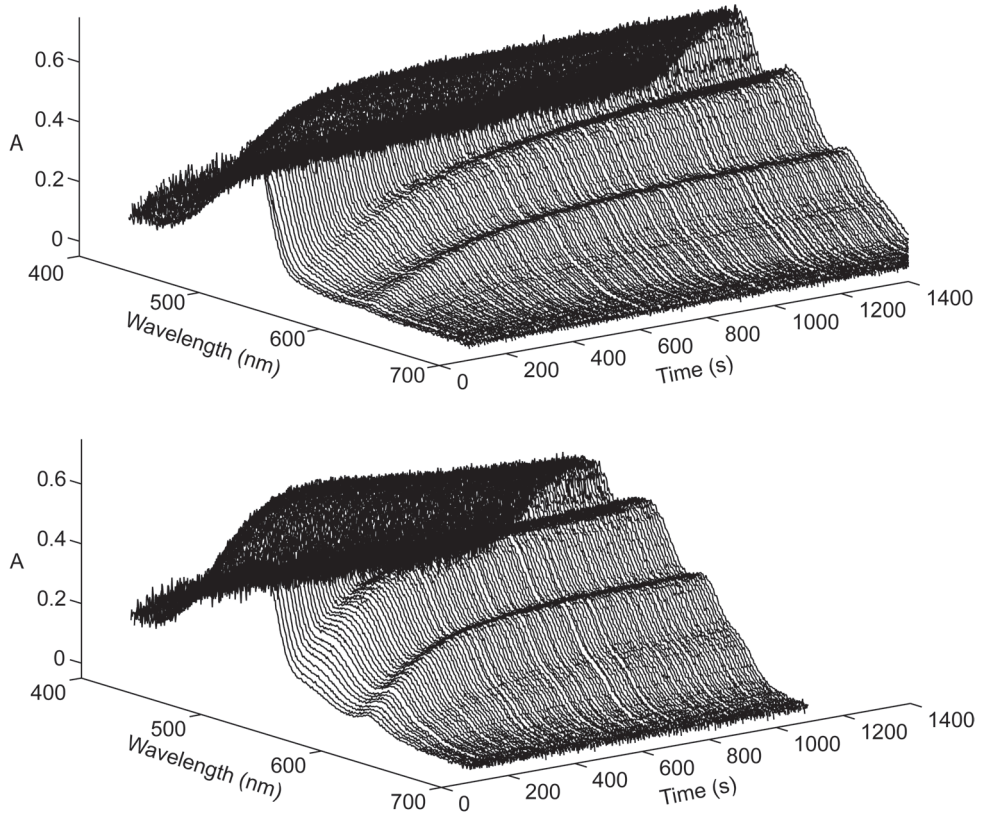


**Figure 3.2. (top)** Examples of the evolution of the UV-Vis absorption bands in time for ZSM5-1 (Si/Al ratio 11.5) and **(bottom)** ZSM5-4 (Si/Al ratio 25) upon exposure to 4-fluorostyrene at 333 K.

**Table 3.2.** Assignment of the UV-Vis absorption bands of 4-methoxystyrene products upon exposure to zeolites.

| Sample | UV-Vis absorption bands (nm) | Band assignment | Ref. |
|---|---|---|---|
| H-ZSM-5 | 360; 580 | benzylic and allylic carbocation | [50-51] |
| H-Y | 360; 490; 580 | benzylic; indanyl and allylic carbocation | [49-51] |

The development of the absorption bands in time was followed to determine the reactivity of H-ZSM-5 samples with different Si/Al ratios. Since the absorption bands overlap significantly, a deconvolution of the different bands in the UV-Vis spectra was performed and seven Gaussian functions, shown in Table 3.3 and Figure 3.3, were resolved.

The Gaussian functions at 494, 522, 565, 613 and 643 nm determine the shape of the UV-Vis absorption spectra. The Gaussian at 450 nm forms a broad background, while the Gaussian function at 664 nm has only a very small contribution to the overall shape. The positions and widths of the Gaussian bands are independent of the H-ZSM-5 sample used. The consistency of the deconvolution indicates that the results as proposed here have physical meaning. Furthermore, the fact that a consistent interpretation can be given is another strong point of the deconvolution.

**Table 3.3.** Overview of the positions and widths of the Gaussian functions used to deconvolute the UV-Vis absorption spectra of the investigated H-ZSM-5 samples.

| Sample | Si/Al ratio | Position and width (between brackets) of Gaussians |
|---|---|---|
| ZSM5-1 | 11.5 | 450 (100), 494 (29), 522 (19.5), 565 (28.5), 613 (20), 643 (13), 664 (13) |
| ZSM5-2 | 15 | 450 (100), 494 (29), 521 (19.5), 564 (28), 613 (20), 643 (13), 664 (13) |
| ZSM5-3 | 15 | 450 (100), 494 (29), 521 (19.5), 563 (28), 613 (20), 643 (13), 664 (13) |
| ZSM5-4 | 25 | 450 (100), 494 (29), 523 (19.5), 566 (28.5), 614 (20), 643 (13), 664 (13) |
| ZSM5-5 | 40 | 450 (100), 494 (29), 523 (19.5), 566 (28), 614 (20), 643 (13), 664 (13) |
| ZSM5-6 | 140 | 450 (100), 494 (29), 522 (19.5), 565 (28), 614 (20), 643 (13), 664 (13) |

The normalized development of the five Gaussian functions that determine the shape of the UV-Vis absorption spectra was plotted in time. Two sets of Gaussians with distinct development in time turned out to be present: Gaussian functions at 494 nm and 522 nm showed the same time dependent behavior, while the Gaussians at 565, 613 and 643 nm formed the other type. The two Gaussian functions at 494 nm and 522 nm together determine the shape of the product band of the cyclic dimeric carbocation. The three Gaussian functions at 565, 613 and 643 nm determine the shape of the product bands of the conjugated linear dimeric and the larger carbocation. The fact that the Gaussian functions of the conjugated linear dimeric and the larger, more conjugated carbocation show the same development in time indicates that the larger carbocation is indeed formed upon further oligomerization of the linear dimeric carbocation. This is in good agreement with the reaction mechanism as shown in Scheme 3.1.

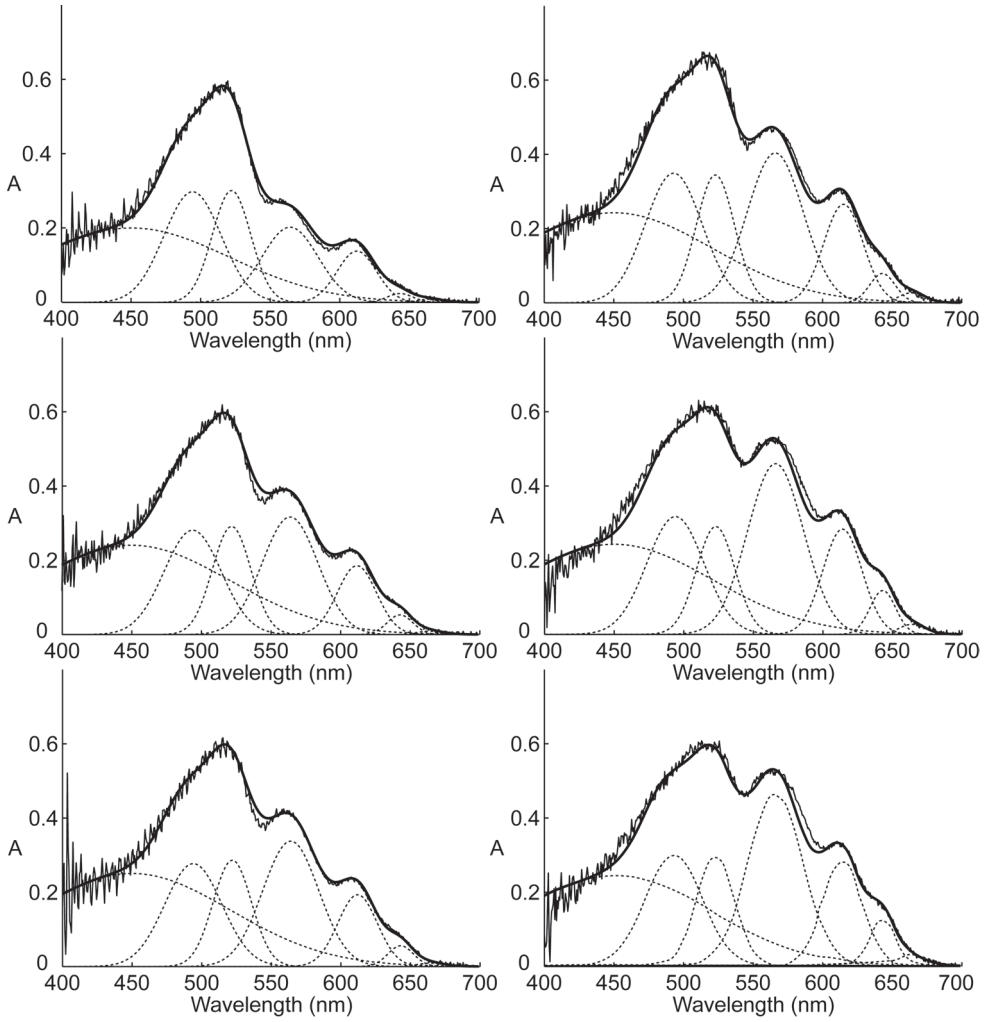


**Figure 3.3.** Examples of the deconvolution procedure for UV-Vis absorption spectra of H-ZSM-5. **(left)** ZSM5-1 (Si/Al ratio 11.5) and **(right)** ZSM5-4 (Si/Al ratio 25) were exposed to 4-fluorostyrene at 333 K. The displayed spectra were taken after **(top)** 250 s; **(middle)** 500 s and **(bottom)** 600 s and deconvoluted (solid line) with a linear combination of seven Gaussian functions (dashed lines).

From both types of Gaussians one function was chosen as a representative of the set: using second-order kinetics a fit was made for the development of the Gaussians at 522 and 565 nm in time. This procedure is depicted in Figure 3.4 for the Gaussian function at 565 nm. The second-order kinetic equation used was $d = m_0/(1+m_0kt)$, where $d$ is the transient dimer concentration, $m_0$ is the initial concentration of

reagent and *k* is the reaction rate constant for a bimolecular conversion.

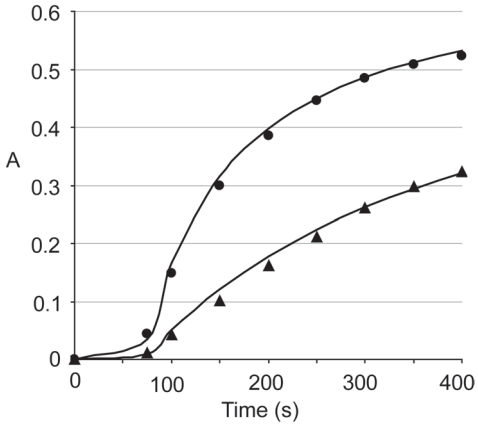


**Figure 3.4.** Absorption of the Gaussian band at 565 nm as a function of reaction time for ZSM5-1 (triangles) and ZSM5-4 (dots). The lines represent the fitting curves as fitted with second-order kinetics.

From the fitting curves as determined for the Gaussians at 522 and 565 nm reaction rate constants were obtained for samples with different Si/Al ratios. Both Gaussian functions indicated the same result: a maximum in reactivity (rate constant) is obtained for the H-ZSM-5 sample with a Si/Al ratio of 25 (Figure 3.5).

Since neither the external surface area of this zeolite sample, nor its micropore volume (see Table 3.1) shows a maximum in comparison to the other zeolite samples, the higher reactivity can be attributed to an optimum in Brønsted acidity for the oligomerization of styrene. As mentioned previously, from aluminum topological density calculations it is known that the expected maximum in Brønsted acidity is reached at a Si/Al ratio of 9.5.[14] The theoretical maximum is at a lower Si/Al ratio than observed here, since the oligomerization of styrene requires one protonated and one unprotonated styrene monomer in close proximity to each other. At low Si/Al ratios the chance of finding unprotonated styrene molecules is small due to the abundance of acid sites, which slows down the reaction. In a statistical study on the aluminum distribution in ZSM-5 the probability of finding a second aluminum atom within a sphere with a radius of 1 nm around a given aluminum atom was calculated.[55] This probability is 1 in a framework with a Si/Al ratio of 12, while the probability is 0.9 for a Si/Al ratio of 24. Since styrenes are quite large molecules, the latter distribution is more beneficial for the styrene oligomerization reaction.

Additional measurements on the oligomerization reaction of 4-fluorostyrene were performed on a zeolite H-Y sample with a Si/Al ratio of 15. The obtained UV-Vis spectrum for this reaction at 333 K, as depicted in Figure 3.6, shows only one absorption band at a wavelength of 520 nm. This band corresponds to the formation of the cyclic dimeric

carbocation. Additionally, zeolite H-Y samples with different Si/Al ratios (3.5; 5.5; 15; 27.5; 30 and 40) were studied during the oligomerization reaction of 4-fluorostyrene. For all samples only formation of the cyclic dimer was found, as all spectra displayed an absorption maximum at 520 nm.

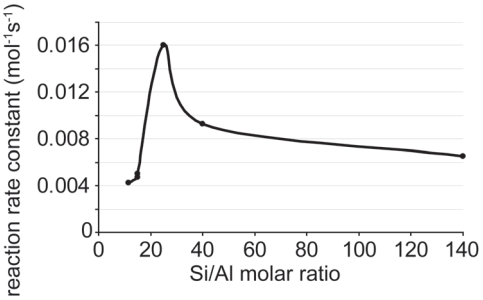


**Figure 3.5.** Reaction rate constants for the reaction of 4-fluorostyrene with H-ZSM-5 samples at 333 K as determined for the Gaussian function at 565 nm. A maximum in reactivity is obtained for a Si/Al ratio of 25. The shown reaction rate constants are an average of two measurements.

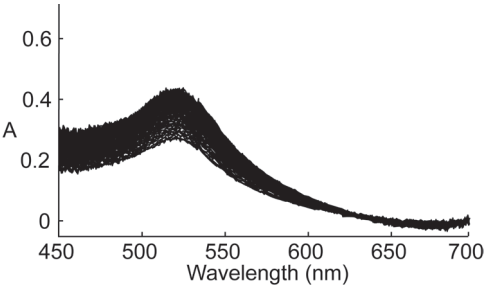


**Figure 3.6.** Example of the evolution of the UV-Vis absorption band in time for zeolite H-Y (Si/Al ratio 15) upon exposure to 4-fluorostyrene at 333 K.

Thermodynamics of the oligomerization reaction of styrene in the pores of zeolites H-ZSM-5 and H-Y were further investigated by periodic DFT calculations. For H-ZSM-5 calculations on the formation of carbocations were performed for a Brønsted acid site at the intersection of the straight channel and the sinusoidal pore. For zeolite H-Y formation energies of the carbocations in a supercage were calculated. Formation of the linear dimeric carbocation (**5**) and the cyclic dimeric carbocation (**7**) confined within H-ZSM-5 (Figures 3.7 and 3.8, respectively) and H-Y (Figure 3.9) matrices was assumed to proceed via the mechanism proposed by Corma and García.[49] The corresponding reaction steps are shown in Scheme 3.1, whereas the computed energies of formation are listed in Table 3.4. According to Corma and García[49] the formation of species **5** involves a hydride transfer between species **4** and **3** confined in the microporous matrix. Whereas such a bimolecular reaction could proceed within the large supercages of H-Y, the favorable arrangement of the two bulky hydrocarbon species **3** and **4** tightly fitted into the pore system of H-ZSM-5 seems unrealistic. Therefore, an additional monomolecular reaction pathway was considered for the formation of the conjugated linear dimeric carbocations. It involves recombination of a hydridic H species at the tertiary carbon atom of **4** with an adjacent

acidic proton of the zeolite, resulting in **5** and molecular $H_2$. Although one expects such a dehydrogenation path to be energetically less favorable than the conventional hydride transfer, the substantial entropy gain due to the formation of mobile $H_2$ molecules may favor this path.

The optimized structure of **5** in H-ZSM-5 (Figure 3.7) shows *circa* 40 short (below 3.2 Å) *inter*molecular interactions between oxygen atoms of the zeolite framework and H species of the carbocation. For the respective structure in the supercage of H-Y (Figure 3.9a) there are only 13 of those *inter*molecular contacts, which correspond to van der Waals (vdW) or dispersion interactions. This suggests an important role of these rather weak but numerous contacts in the stabilization of various bulky hydrocarbon species in zeolitic voids, especially in H-ZSM-5 zeolites. However, it is known that DFT calculations fail in their description of such bonds.[56] Applying empirical or higher-level *ab initio* corrections to the DFT-optimized structures usually yields rather accurate adsorption and reaction energies.[39-40,48] For that reason the van der Waals correction was implemented into the calculations to achieve a more accurate qualitative picture of the stabilities of various hydrocarbon species in zeolites, especially when formed in the pore system of H-ZSM-5.

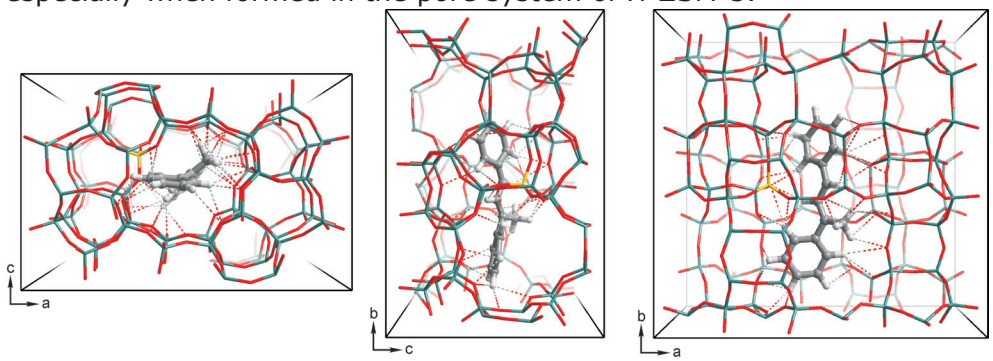


**Figure 3.7.** Optimized structure of **5** in H-ZSM-5 (views along b, a, and c crystallographic axes). Dashed lines indicate CH•••Oz *inter*molecular contacts below 3.2 Å.

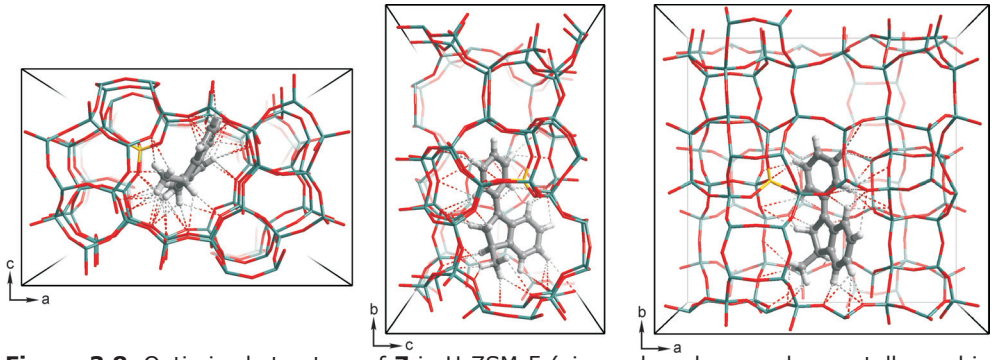


**Figure 3.8.** Optimized structure of **7** in H-ZSM-5 (views along b, a, and c crystallographic axes). Dashed lines indicate CH•••Oz *inter*molecular contacts below 3.2 Å.

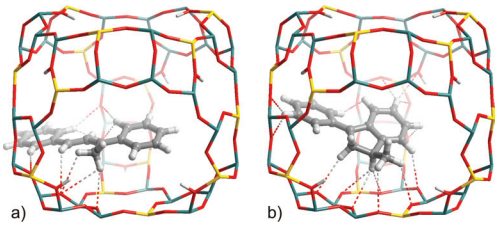


**Figure 3.9.** Optimized structure of **(a) 5** and **(b) 7** in zeolite H-Y. Dashed lines indicate CH•••Oz *inter*molecular contacts below 3.2 Å.

When the impact of vdW interactions is neglected ($\Delta E^{PBE}$), the formation of the linear dimeric carbocation (**1** → **3**) that is the precursor for both the cyclic and the conjugated linear carbocation is substantially favored in the larger pores of zeolite H-Y as compared to the respective process in the pores of H-ZSM-5 ($\Delta E^{PBE}$ values equal -89 and +2 kJ mol$^{-1}$, respectively). After correcting for the van der Waals interactions between the carbocations and the zeolite framework, the formation of **3** becomes equally strongly exothermic for both zeolites. The computed $\Delta E^{PBE+vdW}$ values equal -218 kJ mol$^{-1}$ and -216 kJ mol$^{-1}$ for H-Y and H-ZSM-5, respectively. The larger contribution of vdW interactions in the former case is due to the much tighter fit of the dimeric species in the straight pores of H-ZSM-5.

**Table 3.4.** Pure electronic ($\Delta E^{PBE}$, kJ mol$^{-1}$) and corrected for van der Waals interactions ($\Delta E^{PBE+vdW}$, kJ mol$^{-1}$) DFT computed energies of the reactions shown in Scheme 3.1.

| | H-ZSM-5 | | H-Y | |
|---|---|---|---|---|
| | $\Delta E^{PBE}$ | $\Delta E^{PBE+vdW}$ | $\Delta E^{PBE}$ | $\Delta E^{PBE+vdW}$ |
| **1** → **2** | +8 | -126 | -11 | -89 |
| **2** → **3** | -6 | -90 | -78 | -129 |
| **3** → **4** | -5 | -7 | -19 | -16 |
| **4** + **3** → **5** + **6** | -35 | -62 | -62 | -67 |
| **4** → **5** + $H_2$ | +56 | +35 | +60 | +47 |
| **3** → **7** + $H_2$ | +22 | +46 | -20 | -38 |

The $CH_2$ group in the resulting carbocation (**3**) is rather acidic. Thus, at the next step one of its H atoms is being transferred to the zeolite, yielding the conjugated alkene (**4**) adsorbed to a zeolitic Brønsted acid site. The driving force for this reaction step is the formation of a delocalized π-system in the neutral species **4** and the energy gain associated with the formation of a π-complex between the adsorbed alkene and the zeolitic Brønsted acid site. As follows from Table 3.4, this transformation is slightly exothermic for both framework types, indicating an almost equal stability of **3** and **4**. Since the number of $CH_x$ species and the number of stabilizing CH•••Oz contacts remains constant during this reaction, the vdW-corrected reaction energies are very close to the DFT-computed ones.

The subsequent transformation of **4** into the conjugated linear carbocation **5** requires a hydride transfer from the tertiary carbon atom of **4**. The generally accepted path for such a process involves species **3** as the H-acceptor. A specific arrangement of species **3** and **4** in close proximity to each other within the zeolite pores is required for the *inter*molecular hydride transfer. Although both the computed enthalpies suggest that this reaction is favorable, such a process seems sterically very challenging, especially in the case of H-ZSM-5. Therefore we consider an alternative path, in which an acidic proton of the zeolite plays the role of H-acceptor. In this case, the hydridic H-atom from the tertiary carbon of **4** directly recombines with the zeolitic proton, resulting in the conjugated carbocation **5** and a dihydrogen molecule. The corresponding reaction energies are *circa* 100 kJ $mol^{-1}$ higher when compared to the conventional path (Table 3.4). However, since the alternative reaction pathway involves formation of a gaseous $H_2$ species, one expects the finite temperature and entropic contribution to be substantial in this case. To verify this, we estimated Gibbs free energy changes at 373 K ($\Delta G°^{,vdW}_{373K}$) for the conventional bimolecular (**4** + **3** → **5** + **6**) and the direct (**4** → **5** + $H_2$) hydride transfer reaction in zeolites H-ZSM-5 and H-Y. The vdW-corrected $\Delta G°^{,vdW}_{373K}$ values for the former path equal –33 and –68 kJ $mol^{-1}$, whereas the free energy changes for the direct hydride transfer equal –64 and –45 kJ $mol^{-1}$, respectively for H-ZSM-5 and H-Y zeolites. These data convincingly show that the direct hydride transfer (**4** → **5** + $H_2$) is substantially favored within the narrow pores of H-ZSM-5, whereas in the larger H-Y supercage the bimolecular reaction (**4** + **3** → **5** + **6**) is the preferred reaction path.

The formation of the conjugated linear carbocation (**5**) in zeolites is in competition with the formation of the cyclic carbocation (**7**). A comparison of the overall formation energies of the linear species **5** and the cyclic product **7** from species **3** via the direct H-transfer (reactions **3** → **5** + $H_2$ and **3** → **7** + $H_2$, respectively) indicates that in the case of H-Y the formation of the cyclic carbocation (**3** → **7** + $H_2$, $\Delta E^{PBE+vdW}$ = –38 kJ $mol^{-1}$) is strongly favored over the formation of the linear product (**3** → **5** + $H_2$, $\Delta E^{PBE+vdW}$ = +31 kJ $mol^{-1}$). The situation is reversed when the transformations take place within H-ZSM-5. Although in this case both reactions are endothermic (**3** → **5** + $H_2$, $\Delta E^{PBE+vdW}$ = +28 kJ $mol^{-1}$ and **3** → **7** + $H_2$, $\Delta E^{PBE+vdW}$ = +46 kJ $mol^{-1}$), the specific spatial constraints of the H-ZSM-5 microporous environment disfavor the formation of the cyclic species **7**. When vdW interactions are taken into account the linear carbocation **5** is more stable by 18 kJ $mol^{-1}$ than cyclic species **7**. Since the equilibrium between **5** and **7** does not involve a change in the number of species, the finite temperature and the entropy corrections do not change the qualitative picture described above.

These findings are in line with the experimental observations. Indeed, the UV-Vis spectra upon styrene oligomerization in H-Y evidence

formation of only the cyclic carbocation (**7**), whereas within H-ZSM-5, also the formation of the conjugated linear carbocation (**5**) is observed. The major factors that influence the product distribution are the spatial constraints of the microporous environment and accordingly different degrees of stabilization of different hydrocarbon species by vdW contacts (Table 3.4). For that reason we propose that in the case of H-ZSM-5 formation of cyclic species **7** takes place at the more open sites near the edges of the zeolite microcrystals. This reasoning can be supported by the fact that the formation of the cyclic carbocation is hardly observed when the reaction is performed on large (20 x 20 x 100 μm) coffin-shaped H-ZSM-5 crystals.[31] Due to the fact that in these zeolite crystals the external surface area is very small compared to the micropore area, only a very small amount of cyclic product is formed. In the nanometer-sized (200-600 nm crystallites) H-ZSM-5 materials described in this chapter the external surface area is much larger, which enhances the formation of the cyclic product.

## 4. Conclusions

It has been demonstrated that the acid-catalyzed oligomerization of 4-fluorostyrene is a suitable probe reaction to monitor Brønsted acidity of porous solid materials with UV-Vis micro-spectroscopy. The different reaction rate constants obtained for the three products formed within the pore system of various H-ZSM-5 materials with distinct Si/Al ratios all show the same trend, *i.e.* an optimum in reactivity / acidity is found for a H-ZSM-5 sample with a Si/Al ratio of 25. The developed method was extended to the examination of zeolite H-Y samples. From these measurements it is clear that only the cyclic dimer is formed in the supercages of zeolite H-Y materials.

The results obtained with UV-Vis micro-spectroscopy were further rationalized by DFT calculations, which show that the oligomerization reaction of 4-fluorostyrene in the pores of H-ZSM-5 and H-Y displays differences in formation energy for the linear dimer and the cyclic dimer. These energy differences explain the distinct product distributions in the two framework types. In the pores of H-ZSM-5 both the linear and cyclic product can be formed with reasonable energies. The formation of the linear dimer is energetically slightly favored. The direct hydride transfer pathway is favored over the bimolecular hydride transfer pathway since it involves the formation of a gaseous $H_2$ species that causes a gain in entropy. In the cages of H-Y the formation of the cyclic dimer is energetically strongly favored over the formation of the linear dimer. These calculations support the observations made with UV-Vis, which indicate that only the cyclic dimer is formed in the supercages of H-Y,

while the H-ZSM-5 channels accommodate both the cyclic and the linear dimer.

**Acknowledgements**

Eli Stavitski (Utrecht University, The Netherlands) is acknowledged for designing both the software for acquisition and processing of the UV-Vis micro-spectroscopy measurements. Evgeny Pidko and Rutger van Santen (Technical University Eindhoven, The Netherlands) are thanked for the DFT calculations and related discussions.

**References**

[1] A. Corma *Chem. Rev.* **1995**, *95*, 559-614.
[2] A. Corma *Chem. Rev.* **1997**, *97*, 2373-2419.
[3] A. Bhan; E. Iglesia *Acc. Chem. Res.* **2008**, *41*, 559-567.
[4] M. Bevilacqua; T. Montanari; E. Finocchio; G. Busca *Catal. Today* **2006**, *116*, 132-142.
[5] K. J. Balkus, Jr.; A. K. Khanmamedova; R. Woo *J. Mol. Catal. A: Chem.* **1998**, *134*, 137-143.
[6] S. C. Loureiro Dias; J. L. de Macedo; J. Alves Dias *Phys. Chem. Chem. Phys.* **2003**, *5*, 5574-5579.
[7] D. Fărcaşiu; R. Leu; A. Corma *J. Phys. Chem. B* **2002**, *106*, 928-932.
[8] R. von Balmoos; D. H. Harris; J. S. Magee In *Handbook of Heterogeneous Catalysis*; 1st ed.; G. Ertl, H. Knözinger, J. Weitkamp, Eds.; Wiley-VCH: Weinheim **1997**; *4*, 1955-1983.
[9] W. E. Farneth; R. J. Gorte *Chem. Rev.* **1995**, *95*, 615-635.
[10] W. Vermeiren; J.-P. Gilson *Top. Catal.* **2009**, *52*, 1131-1161.
[11] R. Beaumont; D. Barthomeuf *J. Catal.* **1972**, *26*, 218-225.
[12] D. Barthomeuf *J. Phys. Chem.* **1979**, *83*, 249-256.
[13] R. J. Mikovsky; J. F. Marshall *J. Catal.* **1976**, *44*, 170-173.
[14] D. Barthomeuf *Mater. Chem. Phys.* **1987**, *17*, 49-71.
[15] W.-C. Cheng; E. T. Habib; K. Rajagopalan; T. G. Roberie; R. F. Wormsbecher; M. S. Ziebarth In *Handbook of Heterogeneous Catalysis*; 2nd ed.; G. Ertl, H. Knözinger, F. Schüth, J. Weitkamp, Eds.; Wiley-VCH: Weinheim **2008**; *6*, 2741-2778.
[16] J. Pérez-Ramírez; C. H. Christensen; K. Egeblad; C. H. Christensen; J. C. Groen *Chem. Soc. Rev.* **2008**, *37*, 2530-2542.
[17] *In Situ Spectroscopy in Heterogeneous Catalysis*; J. F. Haw, Ed.; Wiley-VCH: Weinheim **2002**.
[18] *In Situ Spectroscopy of Catalysts*; B. M. Weckhuysen, Ed.; American Scientific Publishers: Stevenson Ranch **2004**.
[19] H. G. Karge In *Handbook of Heterogeneous Catalysis*; 1st ed.; G. Ertl, H. Knözinger, F. Schüth, J. Weitkamp, Eds.; Wiley-VCH: Weinheim **2008**; *2*, 1096-1135.
[20] G. T. Haller *Catal. Rev. Sci. Eng.* **1981**, *23*, 477-504.
[21] J. W. Ward *J. Catal.* **1970**, *17*, 355-358.
[22] F. Thibault-Starzyk; I. Stan; S. Abelló; A. Bonilla; K. Thomas; C. Fernandez; J.-P. Gilson; J. Pérez-Ramírez *J. Catal.* **2009**, *264*, 11-14.
[23] J. A. Martens; P. A. Jacobs *Zeolites* **1986**, *6*, 334-348.
[24] J. W. Ward *J. Catal.* **1968**, *11*, 259-260.
[25] L. Forni *Catal. Rev. Sci. Eng.* **1973**, *8*, 65-115.
[26] A. Auroux; Y. S. Yin; J. C. Vedrine; L. Benoist *Appl. Catal.* **1988**, *36*, 323-330.

[27] D. J. Parrillo; C. Lee; R. J. Gorte *Appl. Catal. A. - Gen.* **1994**, *110*, 67-74.
[28] M. Hunger; D. Freude; H. Pfeifer *J. Chem. Soc., Faraday Trans.* **1991**, *87*, 657-662.
[29] M. H. F. Kox; E. Stavitski; B. M. Weckhuysen *Angew. Chem. Int. Ed.* **2007**, *46*, 3652-3655.
[30] M. H. F. Kox; E. Stavitski; J. C. Groen; J. Pérez-Ramírez; F. Kapteijn; B. M. Weckhuysen *Chem. Eur. J.* **2008**, *14*, 1718-1725.
[31] E. Stavitski; M. H. F. Kox; B. M. Weckhuysen *Chem. Eur. J.* **2007**, *13*, 7057-7065.
[32] G. Kresse; J. Furthmuller *Phys. Rev. B* **1996**, *54*, 11169-11186.
[33] J. P. Perdew; K. Burke; M. Ernzerhof *Phys. Rev. Lett.* **1996**, *77*, 3865-3868.
[34] G. Kresse; D. Joubert *Phys. Rev. B* **1999**, *59*, 1758-1775.
[35] P. E. Blochl *Phys. Rev. B* **1994**, *50*, 17953-17979.
[36] H. J. Monkhorst; J. D. Pack *Phys. Rev. B* **1976**, *13*, 5188-5192.
[37] P. Mignon; E. A. Pidko; R. A. van Santen; P. Geerlings; R. A. Schoonheydt *Chem. Eur. J.* **2008**, *14*, 5168-5177.
[38] E. A. Pidko; P. Mignon; P. Geerlings; R. A. Schoonheydt; R. A. van Santen *J. Phys. Chem. C* **2008**, *112*, 5510-5519.
[39] T. Demuth; L. Benco; J. Hafner; H. Toulhoat; F. Hutschka *J. Chem. Phys.* **2001**, *114*, 3703-3712.
[40] A. M. Vos; X. Rozanska; R. A. Schoonheydt; R. A. van Santen; F. Hutschka; J. Hafner *J. Am. Chem. Soc.* **2001**, *123*, 2799-2809.
[41] S. Svelle; C. Tuma; X. Rozanska; T. Kerber; J. Sauer *J. Am. Chem. Soc.* **2009**, *131*, 816-825.
[42] C. Baerlocher; L. B. McCusker, Database of Zeolite Structures: http://www.iza-structure.org/databases/.
[43] D. H. Kitson; A. T. Hagler *Biochemistry* **1988**, *27*, 7176-7180.
[44] P. Dauber-Osguthorpe; V. A. Roberts; D. J. Osguthorpe; J. Wolff; M. Genest; A. T. Hagler *Proteins: Struct., Funct., Genet.* **1988**, *4*, 31-47.
[45] J. D. Gale *Z. Kristallogr.* **2005**, *220*, 552-554.
[46] T. J. Hou; L. L. Zhu; X. J. Xu *J. Phys. Chem. B* **2000**, *104*, 9356-9364.
[47] H. Jobic; H. Ramanan; S. M. Auerbach; M. Tsapatsis; P. Fouquet *Microporous Mesoporous Mater.* **2006**, *90*, 307-313.
[48] E. A. Pidko; R. A. van Santen In *Zeolites and Catalysis: Synthesis, Reactions and Applications*; J. Cejka, A. Corma, S. I. Zones, Eds.; Wiley-VCH: Weinheim **2010**; *1*, 301-333.
[49] A. Corma; H. García *J. Chem. Soc., Dalton Trans.* **2000**, 1381-1394.
[50] F. L. Cozens; R. Bogdanova; M. Régimbald; H. García; V. Martí; J. C. Scaiano *J. Phys. Chem. B* **1997**, *101*, 6921-6928.
[51] V. Fornés; H. García; V. Martí; L. Fernández *Tetrahedron* **1998**, *54*, 3827 - 3832.
[52] A. R. Taylor; G. W. Keen; E. J. Eisenbraun *J. Org. Chem.* **1976**, *42*, 3477-3480.
[53] L. Fernández; V. Martí; H. García *Phys. Chem. Chem. Phys.* **1999**, *1*, 3689-3695.
[54] E. Stavitski; M. H. F. Kox; I. Swart; F. M. F. de Groot; B. M. Weckhuysen *Angew. Chem. Int. Ed.* **2008**, *47*, 3543-3547.
[55] M. J. Rice; A. K. Chakraborty; A. T. Bell *J. Catal.* **1999**, *186*, 222-227.
[56] Y. Zhao; D. G. Truhlar *J. Chem. Theory Comput.* **2005**, *1*, 415-432.

# Chapter 4

## Staining of Fluid Catalytic Cracking Catalysts using the Styrene Oligomerization Probe Reaction: Localizing Brønsted Acidity within a Single Catalyst Particle


### Abstract

A time-resolved *in situ* micro-spectroscopic approach has been used to investigate the Brønsted acidic properties of Fluid Catalytic Cracking (FCC) catalysts at the single particle level by applying an acid-catalyzed probe reaction, namely the oligomerization of styrene. The reactivity of individual FCC components (zeolite, clay, alumina and silica) was first monitored by UV-Vis micro-spectroscopy and showed that alumina and silica do not contain acid sites that are strong enough to catalyze the conversion of 4-fluorostyrene into carbocationic species. Zeolites (H-ZSM-5 and H-Y) and clay on the other hand show reactivity, which indicates that sufficiently strong Brønsted acid sites are present in these materials. By applying the same approach to individual FCC catalyst particles it has been found that the fingerprint of the zeolitic UV-Vis spectra is clearly recognizable, indicating a high reactivity of the zeolite domains compared to the other components. This almost exclusive zeolitic activity is confirmed by the fact that hardly any reactivity is observed for FCC particles that do not contain zeolite. Confocal fluorescence microscopy images of FCC catalyst particles and slices thereof reveal micron-sized domains with a highly fluorescent signal upon reaction. The high activity in these domains can be explained by the presence of zeolite particulates, which are inhomogeneously distributed throughout the FCC catalyst particles. When the approach was extended to the evaluation of laboratory deactivated FCC catalyst particles in a statistical approach, a clear trend of decreasing fluorescence intensity and thus reactivity of the zeolite domains was observed upon increasing severity of the deactivation. By comparing the average fluorescence intensities obtained with two styrenes that differ in reactivity, it has been found that the Brønsted acid site strength within FCC catalyst particles containing ZSM-5 is more uniform than within those containing zeolite Y.



This work is based on the following manuscript: I. L. C. Buurmans, J. Ruiz-Martínez, S. L. van Leeuwen, D. van der Beek, J. A. Bergwerff, W. V. Knowles, E. T. C. Vogt and B. M. Weckhuysen, *submitted for publication.*

## 1. Introduction

The acidity of heterogeneous catalysts, such as zeolites, is a very important research topic since such catalysts are widely used in a large range of industrial processes.[1-2] For that reason many studies have been performed with different techniques to investigate the acidic properties of zeolitic catalyst materials.[3-7] Usually those studies are performed using bulk characterization techniques. By doing so average information of the catalytic material is obtained and potential spatial heterogeneities cannot be satisfactorily monitored.

Micro-spectroscopic techniques have proven to be very accurate tools to follow chemical reactions at the level of a single catalyst particle.[8-14] In previous research the reactivity of *e.g.* large zeolite crystals has been studied in a space- and time-resolved manner using different probe reactions. The developed combination of these micro-spectroscopic techniques and suitable probe reactions has led to a better insight into the spatial reactivity of large zeolite ZSM-5 crystals. One such a probe reaction, which has been extensively studied, is the acid-catalyzed oligomerization reaction of styrene.[15-18] In addition, detailed information about the subunits that build up such a zeolite crystal and the influence of those subunits on the diffusivity and activity of the overall zeolite crystals could be obtained by a comparable approach.[19] However, the size of these zeolite crystals is very large. For that reason they should be considered as valuable model systems more than as industrially applied materials.

Nevertheless, the application of micro-spectroscopic techniques is not limited to ideal, large zeolite crystals. In this chapter the same approach has been used to investigate FCC catalyst particles. FCC is a very important industrial process for the production of transportation fuels from oil fractions and is the major gasoline-producing source in refineries[20-23] As already described in Chapter 1, FCC catalyst particles are complex mixtures of a zeolite component (either zeolite Y or ZSM-5) and several matrix components, *i.e.* clay, silica and alumina.[22,24] All combined this results in catalyst particles with a very inhomogeneous distribution of materials. Since cracking is initiated by the protonation of oil molecules, the acidity of the individual catalyst components is of great importance for the overall activity of the catalyst particles. Furthermore, all components present in the FCC particles have their own porous structure, which will influence the diffusion of oil molecules in the interior of the catalyst bodies.

Here, it will be shown that by combining micro-spectroscopy with a suitable probe reaction, the most reactive parts of an individual catalyst particle can be visualized. Inspired by the staining approaches used frequently in life sciences for the visualization of distinct parts of cells, a probe reaction was chosen that can selectively visualize Brønsted acid sites within catalytic materials. The selected probe reaction is the

Brønsted acid-catalyzed oligomerization reaction of styrene, which has been described in more detail in Chapter 3. A combination of UV-Vis micro-spectroscopy and confocal fluorescence microscopy allows the investigation of both the Brønsted acidity and the internal structure of individual FCC catalyst particles. It will be shown that the zeolite component in the catalyst particles is the most active compound in the oligomerization reaction of styrene. For that reason confocal fluorescence microscopy allows selective visualization of the zeolitic domains. By statistically evaluating the fluorescence intensities within several catalyst particles, an averaged fluorescence intensity value can be obtained that assesses the zeolitic Brønsted acidity. Furthermore, three different types of laboratory deactivated catalyst particles, namely steamed (ST), two-step cyclic deactivated (CD) and Mitchell impregnated-steam deactivated (MI) samples, have been analyzed in the same manner. The averaged fluorescence intensities for the different samples reveal a clear decrease upon deactivation, which indicates a reduction of their Brønsted acidity. These experiments therefore do not only provide valuable insight into the zeolite reactivity within catalyst particles, but also illustrate the applicability of confocal fluorescence microscopy as a technique to evaluate Brønsted acidity within a series of catalyst samples at the individual particle level.

## 2. Experimental procedures

4-fluorostyrene (Acros Organics, 97%) and 4-methoxystyrene (Acros Organics, 96%) were used as received. Zeolite H-Y (Si/Al = 15, BET surface area = 720 $m^2\ g^{-1}$), silica (BET surface area = 147 $m^2\ g^{-1}$), high-crystalline alumina (BET surface area = 34 $m^2\ g^{-1}$), low-crystalline alumina (BET surface area = 374 $m^2\ g^{-1}$) and clay (BET surface area = 20 $m^2\ g^{-1}$) were provided by Albemarle Corporation. H-ZSM-5 (Si/Al = 11.5, BET surface area = 370 $m^2\ g^{-1}$) was obtained from Zeolyst International. Silica and both types of alumina were dried at 373 K for 30 min. All materials were heat-treated at 723 K for 2 h prior to use to remove any adsorbed species. FCC catalyst particles were provided by Albemarle Corporation as well and used as received. The FCC catalyst batches used were FCC 2 (containing zeolite Y); FCC 6 (containing ZSM-5) and FCC 5 (without zeolite). Only the CD-deactivated catalyst particles were calcined before use at 973 K for 2 h.

UV-Vis micro-spectroscopic experiments were performed using an *in situ* cell (Linkam Scientific Instruments FTIR 600) equipped with a temperature controller (Linkam Scientific Instruments TMS94) for heating of the samples. More details on the microscopy setup can be found in the experimental procedures section of Chapter 3. The FCC components or particles were placed on the heating element of the *in situ* cell and

heated to the desired temperature for 10 min, after which 10 µl of styrene was added and UV-Vis absorption spectra were taken every 5 s using an acquistion time of 20 ms and averaging the signal 100 times.

The confocal fluorescence microscopy studies were performed using a Nikon Eclipse 90i upright microscope with a 100x 0.73 NA and a 50x 0.55 NA dry objective lens. A schematic representation of the microscope is depicted in Figure 4.1. Confocal fluorescence microscopy images were collected by a Nikon A1-SHR A1 R scan head connected to a Melles Griot laser light source with an emission wavelength of 561 nm (yellow diode-pumped solid-state laser, < 50 mW). The emission was detected by a A1-DU4 4 detector unit in the 570-620 nm wavelength range. Samples for confocal fluorescence microscopy were prepared by heating FCC catalyst particles in the *in situ* cell at 423 K for 3 min. Subsequently, 15 µl of styrene was added and the heating was stopped after 15 s.

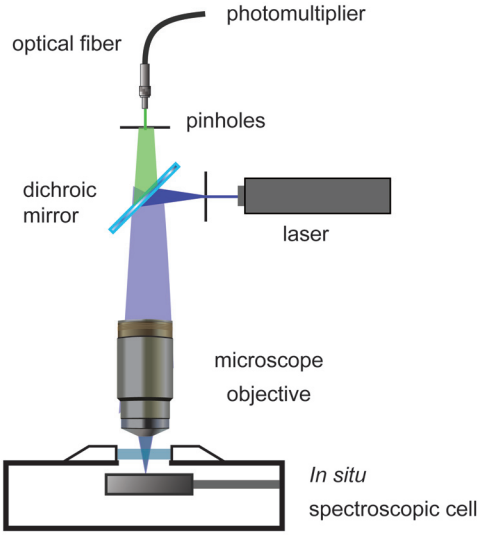


**Figure 4.1.** Schematic representation of the confocal fluorescence microscope.

Ultramicrotomy was conducted using a Leica EMUC6 microtome and a diatome diamond knife. FCC catalyst particles, after reaction with 4-fluorostyrene at 423 K, were embedded in Permapox 2240 A/B and hardened out at room temperature for 3 h. Slices of 10 µm thick were cut with a speed of 0.40 mm/s.

Deactivation of FCC catalyst particles was performed using three different methods, namely steaming, two-step cyclic deactivation and Mitchell impregnation-steam deactivation. Deactivation of fresh FCC catalyst particles was preceded in all cases by sieving (between 38/125 µm). Steam deactivation occurred by first preheating / drying in air to 873

K for 1 h followed by treatment at 1061 K for 20 h in 100% steam. Two-step cyclic deactivation was performed on an Imtech Cyclic Deactivation unit (CDU) with 20 cycles of alternating cracking-regeneration (step 1) followed by 120 cycles of alternating oxidation-reduction (step 2) to achieve 7500 ppmwt Ni and 3000 ppmwt V on the catalyst. Each sieved catalyst was preheated / dried to 873 K for 1 h prior to loading in the CDU. A single cycle in step 1 consisted of fluidizing the catalyst in $N_2$ to crack a vacuum gas oil (VGO) spiked with metal naphthenates at 773 K for 5 min, stripping hydrocarbons from the catalyst pores with $N_2$ for ~ 7 min while heating from 773 to 923 K, and regenerating the catalyst at 923 K for 30 min in an $O_2/N_2$ mixture (40:60 mol%). A single cycle in step 2, conducted continuously at 1043 K in steam, consisted of oxidation in $H_2O/O_2/N_2$ (40:25:35 mol%) for 2 min, stripping in $H_2O/N_2$ (40:60 mol%) for 1.5 min, reduction in $H_2O/H_2/N_2$ (40:25:35 mol%) for 7 min, and stripping in $H_2O/N_2$ (40:60 mol%) for 1.5 min. Temperatures in the CDU were measured in the fluidized catalyst bed by a thermocouple.Mitchell impregnation-steam deactivation[25] is a two-part method: first, incipient wetness impregnation of metal naphthenates dissolved in hexane (7500 ppmwt atomic Ni, 3000 ppmwt atomic V as measured by X-ray fluorescence spectroscopy) was performed. Subsequently, the samples were dried in air, after which a multistep calcination was performed, heating in air (2 h each at 473, 673 and 873 K). Secondly, a steam deactivation as described above was performed for 10 h.

Ammonia release from the FCC catalyst particles was investigated by temperature-programmed desorption (TPD) under He flow (25 ml $min^{-1}$) using a Micromeritics AutoChem II equipped with a thermal conductivity detector. 0.2 g of catalyst was loaded and dried at 873 K for 1 h, after which the sample was cooled down to 373 K. Afterwards, pulses of ammonia were introduced up to saturation of the sample. The temperature-programmed desorption was performed up to 873 K, with a heating ramp of 5 K $min^{-1}$.

## 3. Results and discussion

From previous research, partially described in Chapter 3, it is known that the acid-catalyzed oligomerization reaction of 4-fluorostyrene can be used as a probe reaction to monitor the Brønsted acidity of solid materials.[15-16,26] The formation of absorption bands assigned to three carbocationic reaction products ($\lambda_{abs}$= 520 nm, cyclic dimeric carbocation; $\lambda_{abs}$= 560 nm, linear dimeric carbocation and $\lambda_{abs}$= 610 nm, larger carbocation) can be studied with UV-Vis micro-spectroscopy when the conversion of 4-fluorostyrene is followed in time.[26] The potential reaction pathways are described in more detail in Scheme 3.1. Addition of 4-fluorostyrene

to zeolite H-ZSM-5 samples at 333 K shows the formation of all three carbocations, as displayed in Figure 4.2a. Zeolite H-Y, as depicted in Figure 4.2b, only catalyzes the conversion of styrene into the cyclic dimer, which gives rise to an absorption band at 520 nm. The investigation of both zeolites with a combination of UV-Vis micro-spectroscopy and DFT calculations has been discussed in more detail in Chapter 3.

Of the FCC matrix components, at temperatures up to 423 K, only clay is active and catalyzes the formation of the cyclic dimer (Figure 4.2c). This finding indicates that different pore systems can stabilize different carbocations. The same observations were made in Chapter 3, in which a comparison was made between the carbocations formed in zeolites H-ZSM-5 and H-Y. DFT calculations support our observations that different pore systems facilitate the formation of distinct carbocations.[26]

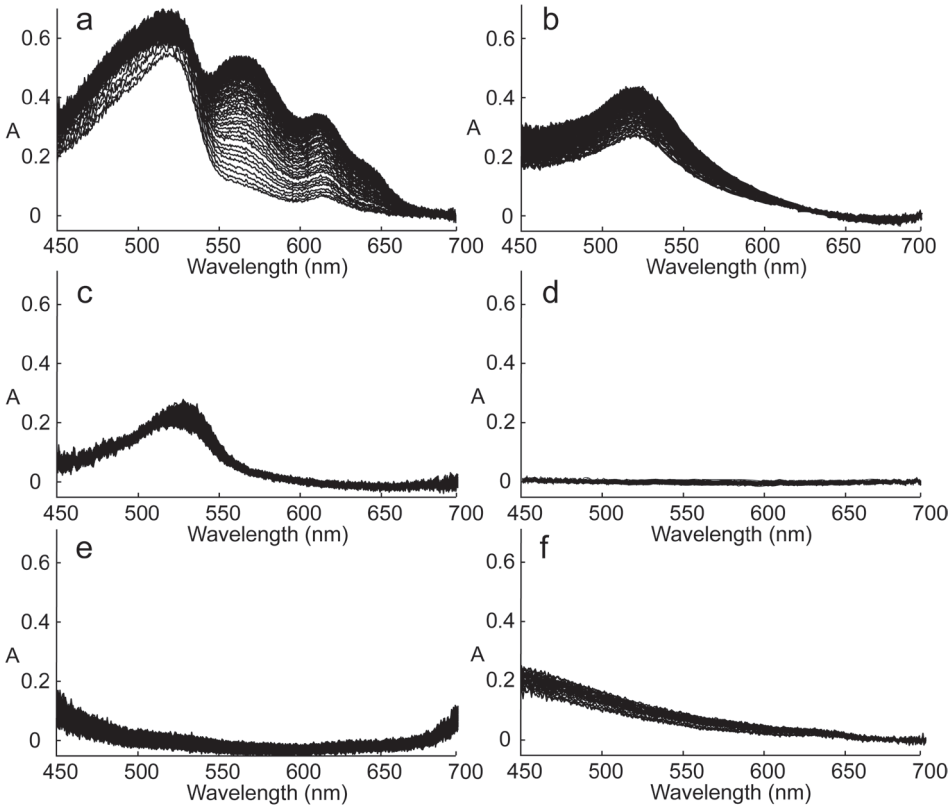


**Figure 4.2.** Evolution of the UV-Vis absorption bands in time for **(a)** zeolite H-ZSM-5 (Si/Al = 11.5); **(b)** zeolite H-Y (Si/Al = 15); **(c)** clay; **(d)** high-crystalline alumina; **(e)** low-crystalline alumina and **(f)** silica upon exposure to 4-fluorostyrene at 333 K.

Three different types of complete FCC catalyst particles were studied with UV-Vis micro-spectroscopy using the styrene oligomerization

as probe reaction. All FCC catalyst particles contained clay, alumina and silica. Two types additionally also incorporated either zeolite Y or ZSM-5, while one type did not contain any zeolite. When the FCC catalyst particles containing ZSM-5 or zeolite Y were exposed to 4-fluorostyrene at 333 K, a similar UV-Vis behavior was observed as for the separate zeolites. As illustrated in Figures 4.3a and b when compared with Figures 4.2a and b, the spectroscopic 'fingerprints' of the H-ZSM-5 and H-Y UV-Vis spectra are well recognizable in the spectra as obtained for the FCC catalyst particles. In contrast, the FCC particles that do not contain zeolite material show hardly any activity (Figure 4.3c). Even at a higher temperature, 423 K, only one band with very low absorption is observed at 520 nm, which indicates that a small amount of cyclic dimeric carbocations is formed due to the presence of clay. The FCC particles containing ZSM-5 show a different product ratio when the reaction is performed at 423 K. At this temperature mainly the linear dimer is formed.

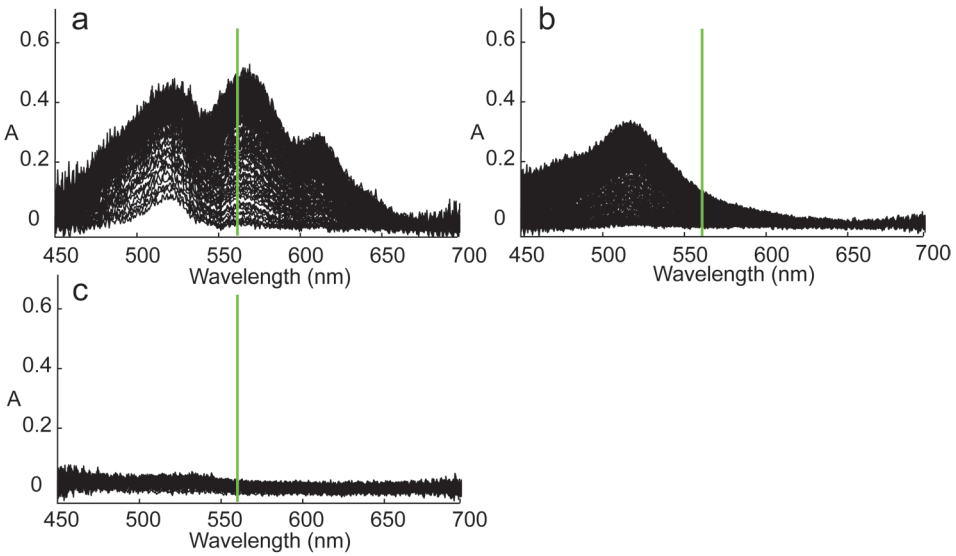


**Figure 4.3.** Evolution of the UV-Vis absorption bands in time for FCC catalyst particles containing **(a)** ZSM-5; **(b)** zeolite Y and **(c)** no zeolite upon exposure to 4-fluorostyrene at 333 K. The green lines represent the laser excitation wavelength of 561 nm, which is used during the confocal fluorescence microscopy experiments to excite the formed carbocations.

When the styrene oligomerization reaction is used as a probe reaction, it is possible to selectively excite the linear dimeric carbocation ($\lambda_{abs}$= 560 nm) with a laser of 561 nm. Since the linear dimeric carbocation is only formed in the pores of H-ZSM-5, this approach allows the selective visualization of the reactive zeolite domains. The confocal fluorescence microscopy images of FCC particles containing ZSM-5 indeed show that

domains with a highly fluorescent signal are inhomogeneously distributed over the sample. They are on average 1 – 5 µm in size and contain agglomerates of zeolite particulates, as can be seen in Figures 4.4a and b. Due to the inhomogeneity of the FCC particles and the consequent possibility of reflection of the fluorescent signal, only a small fraction of the fluorescence will reach the detector. As a result the fluorescence could only be accurately recorded up to a depth of 15 µm inside the particles. To overcome this problem and to study the internal activity in more detail, ultramicrotomy was performed on some FCC particles after reaction with 4-fluorostyrene to obtain slices with a thickness of 10 µm.

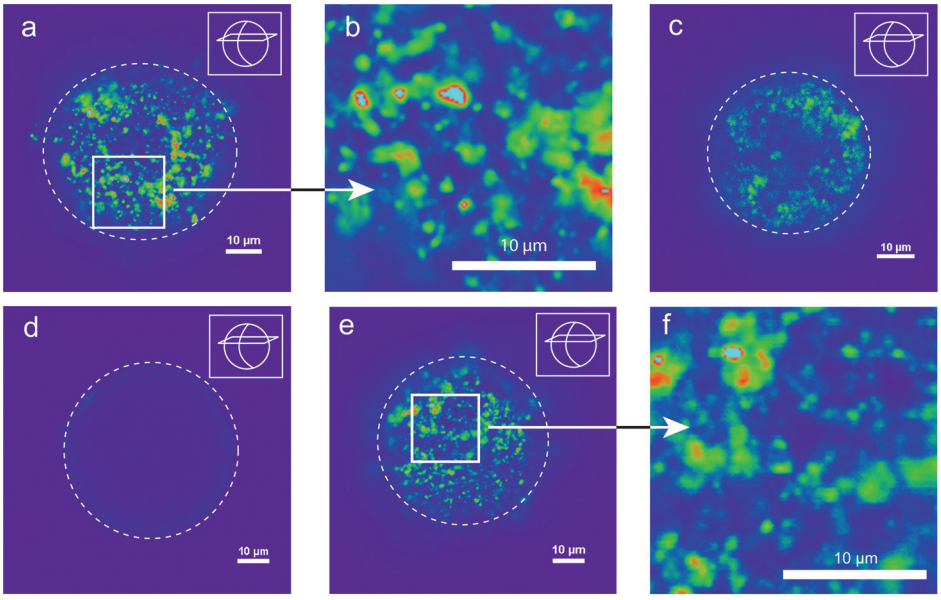


**Figure 4.4. (a)** Confocal fluorescence microscopy image of an FCC catalyst particle containing ZSM-5 upon reaction with 4-fluorostyrene (423 K, $\lambda_{ex}$ = 561 nm, detection = 570-620 nm, false color images). Image **(b)** shows a magnification of the highlighted area. **(c)** When the same reaction conditions are used to investigate an FCC catalyst particle containing zeolite Y, less distinct fluorescent domains are visible. **(d)** When no zeolite is present in the FCC particles hardly any fluorescence is detected. The detection sensitivity for the measurement of particles containing ZSM-5 is lower than for the other two samples in order to avoid overexposure. **(e)** Confocal fluorescence microscopy image and **(f)** the magnification thereof obtained upon reaction of FCC catalyst particles containing ZSM-5 with 4-fluorostyrene in gas phase at 423 K.

Figure 4.5 shows a confocal image of such a sliced FCC catalyst particle. From the comparison of the sliced FCC catalyst particles to the complete particles, it is clear that the internal reactivity is comparable to the reactivity of the more external parts of the catalyst. When FCC catalyst particles containing zeolite Y are investigated under the same

reaction conditions less fluorescence is detected, as depicted in Figure 4.4c. For that reason the zeolite domains are not as distinctly visible as for the FCC particles with ZSM-5. This is due to the fact that within zeolite Y only the cyclic dimer ($\lambda_{abs}$= 520 nm) is formed, which is less accurately excited with the 561 nm laser.[27] When no zeolite is present in the FCC catalyst particles, which is the case in Figure 4.4d, hardly any fluorescence is detected under the same conditions due to the lack of carbocation formation within the catalyst bodies.

The results so far have been obtained using liquid styrenes as reagents. However, additional reactions have been performed in the gas phase. In these experiments a nitrogen flow was used to evaporate 4-fluorostyrene, which was led over FCC catalyst particles containing ZSM-5 at 423 K. The increase in fluorescence was followed in time. The overall fluorescence increased during the first 15 min. After this time the fluorescence intensity was constant. The obtained fluorescent structure, as displayed in Figures 4.4e and f, is comparable to the one obtained for the liquid-phase reaction, which shows that the reactivity of the zeolite domains does not depend on the phase of the styrene reagent.

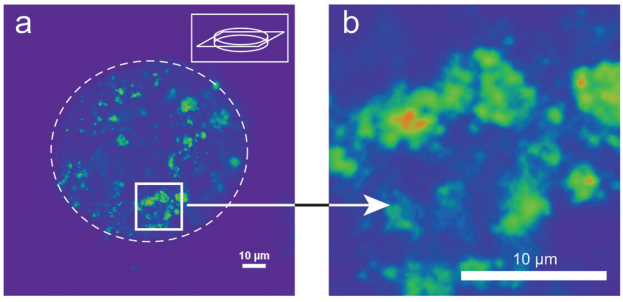


**Figure 4.5. (a)** Confocal fluorescence microscopy image of a 10 µm thick slice of an FCC catalyst particle containing ZSM-5 after reaction with 4-fluorostyrene (423 K, $\lambda_{ex}$ = 561 nm, detection = 570-620 nm, false color image). Image **(b)** shows a magnification of the highlighted area.

The fluorescence of both fresh and laboratory deactivated (ST, CD and MI) FCC catalyst particles was studied in more detail upon reaction with either 4-fluorostyrene or 4-methoxystyrene. In both cases the reaction was performed at 423 K. From previous research it is known that the oligomerization reactivity of styrenes depends on their substitution.[15] The strongly electron withdrawing fluorine group in 4-fluorostyrene leads to lower carbocation stability. The methoxy group, on the other hand, increases carbocation stability through the formation of a resonance structure. This difference is reflected in the reaction rate constants towards carbocation formation as obtained for the two different styrenes upon reaction with large H-ZSM-5 crystals. These values are 0.007 and 0.05 $mol^{-1}$ $s^{-1}$ for 4-fluorostyrene and 4-methoxystyrene, respectively.[15]

An example of a confocal fluorescence microscopy study of fresh and laboratory deactivated catalyst particles is depicted in Figure 4.6 for FCC catalyst particles containing zeolite ZSM-5 upon reaction with 4-fluorostyrene. A summary of the other confocal fluorescence microscopy experiments (FCC catalyst containing ZSM-5 upon reaction with 4-methoxystyrene and FCC catalyst containing zeolite Y upon reaction with either 4-fluorostyrene or 4-methoxystyrene) is given in Figure 4.7. When comparing the fresh and deactivated catalyst samples, it is clear that the fluorescence intensities after reaction decrease upon deactivation. This shows that the Brønsted acidity of the catalyst samples indeed decreases after deactivation. A statistical analysis of the fluorescence intensities of the zeolite domains was performed for all samples.[28] To perform this analysis for every sample an average of six catalyst particles that contained in total at least 100 fluorescent zeolite domains was taken.

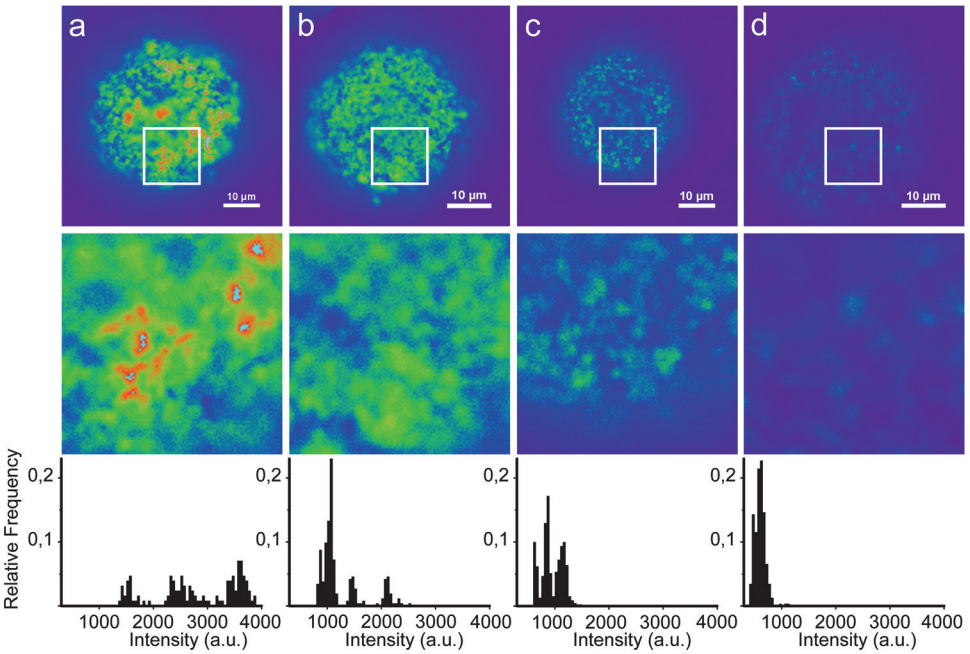


**Figure 4.6.** Confocal fluorescence microscopy images and magnifications thereof as obtained for FCC catalyst particles containing ZSM-5 in their **(a)** fresh; **(b)** steamed; **(c)** cyclic deactivated and **(d)** Mitchell impregnated-steam deactivated state, upon reaction with 4-fluorostyrene (423 K, $\lambda_{ex}$ = 561 nm, detection = 570-620 nm, false color images). A gradual decrease in fluorescence intensity upon the different deactivation methods is observed. When all fluorescent zeolite domains larger than 1 µm$^2$ within six different catalyst particles are analyzed, averaged fluorescence intensity histograms are obtained, as shown in the graphs below the images.

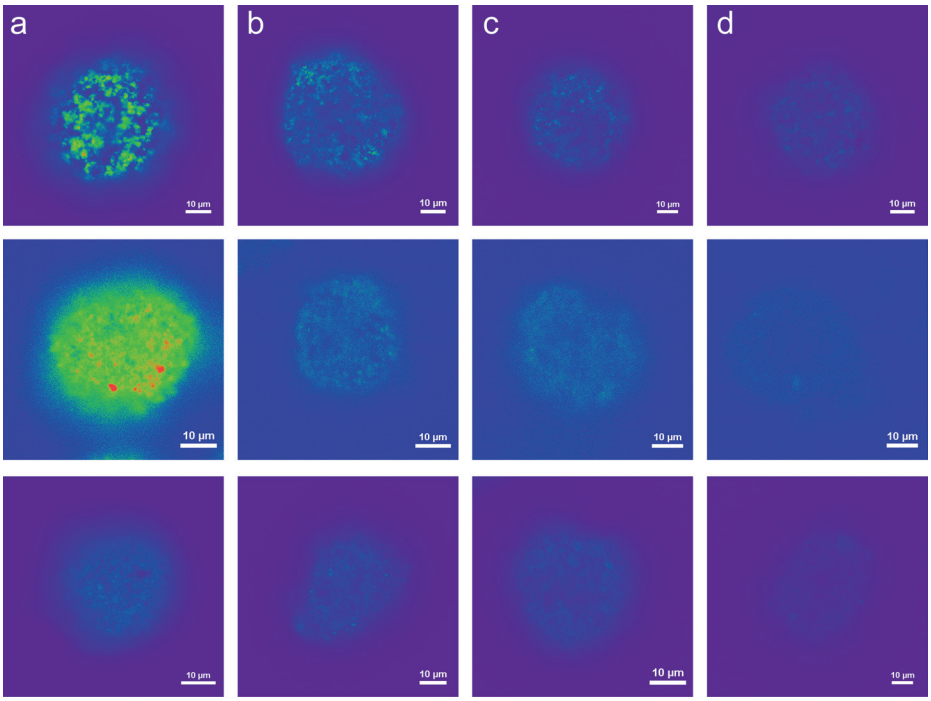


**Figure 4.7. (top)** Confocal fluorescence microscopy images as obtained for FCC catalyst particles containing ZSM-5 upon reaction with 4-methoxystyrene; **(middle)** FCC catalyst particles containing zeolite Y upon reaction with 4-fluorostyrene (all four figures boosted with the same factor because of very low fluorescence intensity) and **(bottom)** FCC catalyst particles containing zeolite Y upon reaction with 4-methoxystyrene in their **(a)** fresh; **(b)** steamed; **(c)** cyclic deactivated and **(d)** Mitchell impregnated-steam deactivated state (423 K, $\lambda_{ex}$ = 561 nm, detection = 570-620 nm, false color images). A gradual decrease in fluorescence intensity upon the different deactivation methods is observed.

The fluorescence intensity of the zeolite spots larger than 1 µm$^2$ in these six particles was analyzed and converted into fluorescence intensity histograms, as examplified in Figure 4.6. Fluorescent domains below 1 µm$^2$ were rejected, since in general over 90% of the zeolite domains is expected to be larger than this value.[23,29] To remove the fluorescence caused by the background and by residual fluorescence from zeolite domains in close proximity, an intensity threshold was set. This procedure is depicted in more detail in Figure 4.8.

By converting the fluorescence intensities of all remaining zeolite domains into fluorescence intensity histograms an overview of the population is obtained. From both the confocal fluorescence microscopy images and the fluorescence intensity histograms it is clear that the fluorescence intensity decreases when the severity of the deactivation process increases (fresh > ST > CD > MI). This can be explained by a

partial removal and deactivation of the acid sites in the zeolite domains upon steaming, cracking procedures and metal deposition. In the fresh catalyst sample fluorescence intensities with values up to 4000 (a.u.) are detected. Upon application of the different deactivation methods, these high fluorescence intensities are not observed. After the most severe deactivation methods, namely CD and MI, only intensity values lower than 1500 (a.u.) and 1000 (a.u.) remain, respectively. The statistical analysis was performed for both FCC catalyst particles containing zeolite Y and ZSM-5.

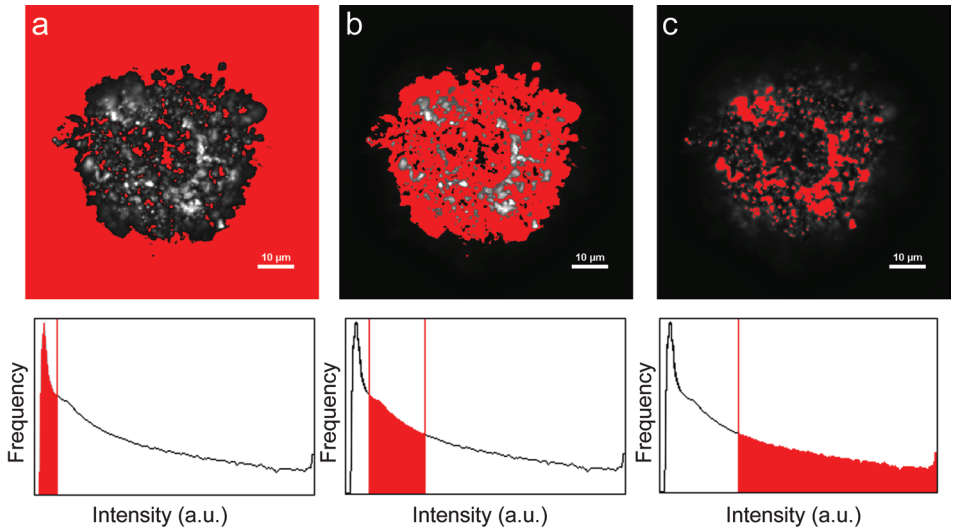


**Figure 4.8.** Confocal fluorescence microscopy images of an FCC catalyst particle containing ZSM-5 after reaction with 4-fluorostyrene at 423 K ($\lambda_{ex}$ = 561 nm, detection 570-620 nm). In the corresponding fluorescence intensity graphs below the images three different fluorescence intensity regions are highlighted in red. These same regions are highligted in red in the confocal fluorescence images as well. The fluorescence intensity profiles show three distinct regions: **(a)** background fluorescence; **(b)** residual fluorescence and **(c)** zeolitic fluorescence. The threshold used for further statistical analysis was set at the value at which all background and residual fluorescence contributions were rejected.

As a final step the fluorescence intensity histograms were used to calculate average fluorescence intensity values, which are shown in Figure 4.9. Upon deactivation a decreasing fluorescence intensity trend is observed for both styrenes and both FCC particles containing zeolite Y and ZSM-5. Comparison of the results obtained with 4-methoxystyrene and 4-fluorostyrene provides insight into the types of acid sites present in both catalyst samples. As indicated previously, 4-fluorostyrene, due to a lower carbocation stability, is a less reactive styrene compared to 4-methoxystyrene.[15] To obtain comparable reactivities towards both styrenes, stronger Brønsted acid sites are needed in the case of

4-fluorostyrene. As can be seen in Figure 4.9, the catalyst particles containing ZSM-5 show similar fluorescence intensities and thus comparable reactivity towards both styrenes. Apparently all Brønsted acid sites are strong enough to catalyze the conversion of both 4-methoxystyrene and 4-fluorostyrene. On the other hand, the catalyst particles containing zeolite Y display lower fluorescence intensity values upon reaction with the more-demanding 4-fluorostyrene. Seemingly not every Brønsted acid site within the catalyst particles containing zeolite Y has sufficient strength to convert 4-fluorostyrene into fluorescent carbocations. For that reason only a fraction of the Brønsted acid sites, which are visualized with the less demanding 4-methoxystyrene, is monitored upon reaction with 4-fluorostyrene. This finding indicates that the Brønsted acid sites within the catalyst particles containing zeolite Y display a higher diversity in strength compared to the Brønsted acid sites within catalyst particles containing ZSM-5.

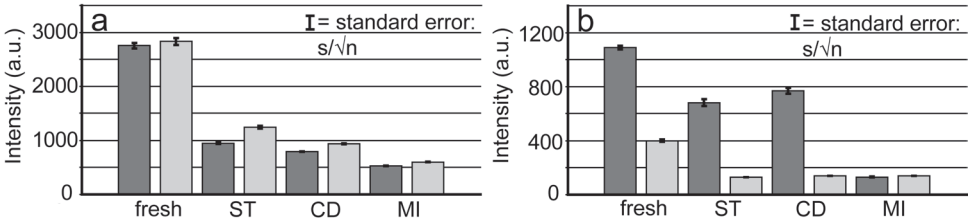


**Figure 4.9.** Fluorescence mean intensities and their corresponding standard errors for FCC catalyst particles containing **(a)** ZSM-5 and **(b)** zeolite Y in their different life stages as calculated from the fluorescence intensity histograms. Fluorescence intensities after reaction with 4-methoxystyrene (dark gray) and 4-fluorostyrene (light gray) are listed.

When the acidity of FCC catalyst particles containing ZSM-5 and zeolite Y is compared using temperature-programmed desorption (TPD) of ammonia, similar results are obtained, as depicted in Figure 4.10. Ammonia desorption at two different temperatures is observed for both types of FCC catalysts: around 470 K and 670 K. The ammonia desorbing at higher temperatures is indicative for the presence of strong Brønsted acid sites. For the FCC catalyst containing zeolite Y the curve is not very well resolved in the two different temperature domains, which is characteristic for the overlap of several components desorbing in a relatively wide temperature range. The desorption in the FCC catalyst containing ZSM-5 shows a better defined pattern with increasing temperature, which corresponds well with the more homogeneous Brønsted acidity strength observed by confocal fluorescence microscopy experiments. Ammonia TPD measurements in literature for individual zeolitic materials also indicate a wider distribution in acid site strength for zeolite H-Y compared to H-ZSM-5.[30-32]

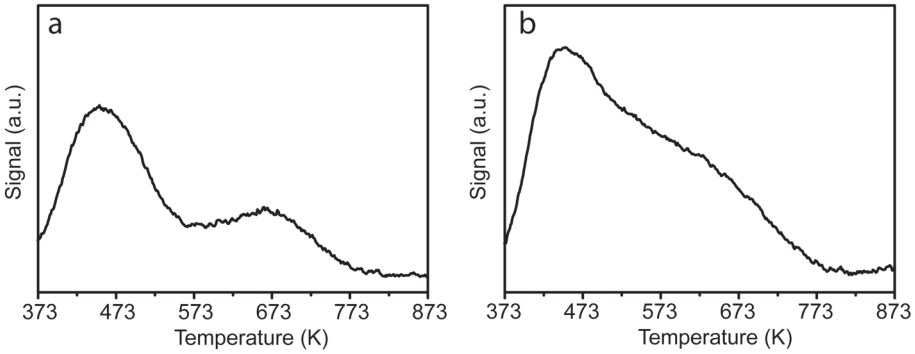


**Figure 4.10.** Temperature-programmed desorption plots of ammonia for fresh FCC catalyst particles containing **(a)** ZSM-5 and **(b)** zeolite Y.

## 4. Conclusions

Micro-spectroscopy provides direct insight into the Brønsted acidity and spatial reactivity of FCC catalyst particles. The liquid-phase oligomerization reaction of styrene is a suitable tool to study the Brønsted acidity of separate FCC components (zeolite, clay, high-crystalline alumina, low-crystalline alumina and silica) and individual FCC catalyst particles (containing ZSM-5, zeolite Y or no zeolite) using UV-Vis micro-spectroscopy. Only the zeolite and clay components in the FCC particles catalyze the oligomerization reaction towards carbocationic reaction products. When the individual FCC catalyst particles are studied, the characteristic UV-Vis absorption bands of the zeolite components are evidently present in the overall spectra. In contrast, hardly any reactivity is observed when no zeolite is present in the catalyst particles.

By exciting the formed carbocations in the different catalyst particles using a 561 nm laser, it is possible to obtain confocal fluorescence microscopy images that reflect the reactivity of the zeolite component within the catalyst bodies. In the images obtained by this life sciences inspired staining approach, micron-sized domains with a highly fluorescent signal are inhomogeneously distributed within the particles containing ZSM-5 and zeolite Y. When no zeolite is present in the FCC catalyst, hardly any fluorescence is observed. Additional experiments using styrene in the gas-phase show that the same reactive zeolite domains are visualized in that case, which proves that the results do not depend on the phase of the styrene reagent.

Investigation of laboratory deactivated catalyst particles using the same probe reaction and confocal fluorescence microscopy approach clearly shows that the fluorescence decreases when the severity of the

deactivation process increases. Fluorescence intensity histograms of the investigated catalyst particles were used to perform a statistical evaluation of the population. The decrease in fluorescence can be explained in terms of partial removal and deactivation of the acid sites in the zeolite domains due to steaming, coke formation and metal deposition. The use of two different styrenes, namely 4-methoxystyrene and the more demanding 4-fluorostyrene has shown that the Brønsted acid site strength within FCC catalyst particles containing ZSM-5 is more uniform than within those containing zeolite Y. These results are confirmed by ammonia TPD experiments.

## Acknowledgements

Eli Stavitski (Utrecht University, The Netherlands) is acknowledged for designing both the software for acquisition and processing of the UV-Vis micro-spectroscopy measurements. Kees van Leerdam and Caroline van der Meij (Akzo Nobel Chemicals bv., The Netherlands) are thanked for ultramicrotomy procedures.

## References and notes

[1] A. Corma *Chem. Rev.* **1995**, *95*, 559-614.
[2] A. Corma *Chem. Rev.* **1997**, *97*, 2373-2419.
[3] A. Bhan; E. Iglesia *Acc. Chem. Res.* **2008**, *41*, 559-567.
[4] M. Bevilacqua; T. Montanari; E. Finocchio; G. Busca *Catal. Today* **2006**, *116*, 132-142.
[5] K. J. Balkus, Jr.; A. K. Khanmamedova; R. Woo *J. Mol. Catal. A: Chem.* **1998**, *134*, 137-143.
[6] S. C. Loureiro Dias; J. L. de Macedo; J. Alves Dias *Phys. Chem. Chem. Phys.* **2003**, *5*, 5574-5579.
[7] D. Fărcaşiu; R. Leu; A. Corma *J. Phys. Chem. B* **2002**, *106*, 928-932.
[8] R. A. Schoonheydt *Angew. Chem. Int. Ed.* **2008**, *47*, 9188-9191.
[9] M. B. J. Roeffaers; J. Hofkens; G. De Cremer; F. C. De Schryver; P. A. Jacobs; D. E. De Vos; B. F. Sels *Catal. Today* **2007**, *126*, 44-53.
[10] B. M. Weckhuysen *Angew. Chem. Int. Ed.* **2009**, *48*, 4910-4943.
[11] M. B. J. Roeffaers; G. De Cremer; H. Uji-i; B. Muls; B. F. Sels; P. A. Jacobs; F. C. De Schryver; D. E. De Vos; J. Hofkens *Proc. Natl. Acad. Sci. U.S.A.* **2007**, *104*, 12603-12609.
[12] R. A. Schoonheydt *Chem. Soc. Rev.* **2010**, *39*, 5051-5066.
[13] E. Stavitski; B. M. Weckhuysen *Chem. Soc. Rev.* **2010**, *39*, 4615-4625.
[14] G. De Cremer; B. F. Sels; D. E. De Vos; J. Hofkens; M. B. J. Roeffaers *Chem. Soc. Rev.* **2010**, *39*, 4703-4717.
[15] M. H. F. Kox; E. Stavitski; B. M. Weckhuysen *Angew. Chem. Int. Ed.* **2007**, *46*, 3652-3655.
[16] M. H. F. Kox; E. Stavitski; J. C. Groen; J. Pérez-Ramírez; F. Kapteijn; B. M. Weckhuysen *Chem. Eur. J.* **2008**, *14*, 1718-1725.
[17] E. Stavitski; M. H. F. Kox; B. M. Weckhuysen *Chem. Eur. J.* **2007**, *13*, 7057-7065.
[18] E. Stavitski; M. H. F. Kox; I. Swart; F. M. F. de Groot; B. M. Weckhuysen *Angew. Chem. Int. Ed.* **2008**, *47*, 3543-3547.
[19] L. Karwacki; M. H. F. Kox; D. A. M. de Winter; M. R. Drury; J. D. Meeldijk; E.

Stavitski; W. Schmidt; M. Mertens; P. Cubillas; N. John; A. Chan; N. Kahn; S. R. Bare; M. Anderson; J. Kornatowski; B. M. Weckhuysen *Nature Mater.* **2009**, *8*, 959-965.
[20] M. Rigutto In *Zeolites and Catalysis: Synthesis, Reactions and Applications*; J. Čejka, A. Corma, S. I. Zones, Eds.; Wiley-VCH: Weinheim **2010**; *2*, 547-584.
[21] W. Vermeiren; J.-P. Gilson *Top. Catal.* **2009**, *52*, 1131-1161.
[22] W.-C. Cheng; E. T. Habib; K. Rajagopalan; T. G. Roberie; R. F. Wormsbecher; M. S. Ziebarth In *Handbook of Heterogeneous Catalysis*; 2nd ed.; G. Ertl, H. Knözinger, F. Schüth, J. Weitkamp, Eds.; Wiley-VCH: Weinheim **2008**; *6*, 2741-2778.
[23] S. Bhatia *Catalytic Applications of Zeolites in Industrial Processes* CRC Press, Inc.: Boca Raton **1989**.
[24] H. F. Rase *Handbook of Commercial Catalysts*; CRC Press, Inc.: Boca Raton **2000**, 362-391.
[25] B. R. Mitchell *Ind. Eng. Chem. Prod. Res. Dev.* **1980**, *19*, 209-213.
[26] I. L. C. Buurmans; E. A. Pidko; J. M. de Groot; E. Stavitski; R. A. van Santen; B. M. Weckhuysen *Phys. Chem. Chem. Phys.* **2010**, *12*, 7032-7040.
[27] *An attempt was made to study the fluorescence using a 514 nm laser excitation wavelength. However, less fluorescence signal was obtained due to the lower power of the laser light.*
[28] I. L. C. Buurmans; J. Ruiz-Martínez; W. V. Knowles; D. van der Beek; J. A. Bergwerff; E. T. C. Vogt; B. M. Weckhuysen*, Nature Chem.* **2011**, DOI: 10.1038/NCHEM.1148.
[29] *Internal data Albemarle Catalysts*.
[30] C. V. Hidalgo; H. Itoh; T. Hattori; M. Niwa; Y. Murakami *J. Catal.* **1984**, *85*, 362-369.
[31] K. Suzuki; T. Noda; N. Katada; M. Niwa *J. Catal.* **2007**, *250*, 151-160.
[32] N.-Y. Topsøe; K. Pedersen; E. G. Derouane *J. Catal.* **1981**, *70*, 41-52.

# Chapter 5

## Connection between Local Structure and Brønsted Acidity in Fluid Catalytic Cracking Catalyst Particles as Revealed by Integrated Laser and Electron Microscopy


### Abstract

An integrated fluorescence and transmission electron microscopy approach has been applied to visualize the different components (zeolite, clay, silica and alumina) in fresh and steamed FCC catalyst particles with nanometer resolution after reaction with 4-fluorostyrene. It was found that the FCC components were inhomogeneously distributed within the catalyst particles. Distinct regions, which could be divided into three subtypes, were defined: mainly containing zeolite (type I), mostly containing matrix components (type II) and a mixture of both (type I/II). The type I component was found to give rise to the highest fluorescence signal, which is in line with the previous observations that fluorescent styrene products are preferably formed within the Brønsted acidic zeolite component. Both the zeolite and clay component were additionally identified using electron diffraction. It was observed that upon steaming hardly any clay platelets were present. Mostly zeolite crystallites and amorphous material could be identified and the large regions of clay regularly found in the fresh FCC particles were lost. The electron diffraction pattern of zeolite-rich regions indicated that the diffraction maxima of zeolite Y remain after steaming. Additionally, complete diffraction rings were present in the diffraction pattern, which are attributed to the presence of γ-$Al_2O_3$ crystallites that are formed upon zeolite dealumination.



This work is based on the following manuscript: M. A. Karreman, I. L. C. Buurmans, J. W. Geus, A. V. Agronskaia, J. Ruiz-Martínez, H. C. Gerritsen and B. M. Weckhuysen, *submitted for publication.*


Matthia Karreman and Inge Buurmans contributed equally to this work and therefore this Chapter is part of both PhD theses.

## 1. Introduction

In Chapter 4 it has been shown that the oligomerization reaction of 4-fluorostyrene leads to a selective formation of fluorescent products within the Brønsted acidic zeolite domains of FCC catalyst particles. Confocal fluorescence microscopy thus allowed the visualization of the zeolite distribution and its Brønsted acidity within individual catalyst particles. Not only fresh catalyst particles, but also their deactivated derivatives could be investigated and it was shown that the Brønsted acidity of the zeolite decreases upon deactivation.

However, confocal fluorescence microscopy has limited spatial resolution and can only be applied to image the fluorescent domains within FCC catalyst particles. Electron microscopy, on the other hand, allows for high resolution imaging of structural details of the sample without the use of probe molecules. In previous FCC research some studies have been performed using either scanning electron microscopy (SEM) [1] or transmission electron microscopy (TEM)[2] for a structural study of individual catalyst particles. Furthermore, atomic force microscopy (AFM) has been exploited to study the topography of such FCC catalyst particles. [3-5] Integrated laser and electron microscope (iLEM)[6] is a newly developed characterization tool, which was recently introduced in life science research. [7,8] The iLEM combines the strength of fluorescence microscopy (FM) and TEM in one setup, thus allowing a fast survey of fluorescent domains and subsequent investigation of the regions of interest with superior spatial resolution.

In this chapter the application of iLEM to investigate both the fluorescent zeolite domains and the less fluorescent matrix components in nanoscopic detail is described.

## 2. Experimental procedures

Steam deactivation of the fresh catalyst particles was performed by Albemarle Corporation and is described in the experimental procedures section of Chapter 4.

The FCC catalyst batches used were FCC 2 (containing zeolite Y) and FCC 5 (without zeolite). The oligomerization reaction of 4-fluorostyrene on both fresh and steamed FCC catalyst particles containing zeolite Y and on FCC catalyst particles without zeolite component was performed in an *in situ* reaction cell (Linkam Scientific Instruments FTIR 600) equipped with a temperature controller (Linkam Scientific Instruments TMS 94). The FCC particles were placed on the heating element of the *in situ* cell and heated to 423 K for 5 min, after which 4-fluorostyrene was added and the heating was stopped after 10 s.

FCC catalyst particles, after reaction with 4-fluorostyrene or without performing any reaction, were heated for 2 h at 423 K under vacuum ($10^{-7}$ mbar). Subsequently, a 7 : 3 volume ratio of methyl methacrylate (Fischer Emergo, 99%, stabilized) and butyl methacrylate (Fischer Emergo, 99%) was added at 333 K, still under vacuum. The mixture of resin and FCC catalyst material was transferred into gelatin capsules (Agar Scientific) and hardened out at 333 K for 48 h. Wet sectioning was performed using a Leica EMUC6 microtome and a diamond knife (Diatome HI 6985 histo size 6 mm 45 grade) under a 6 degrees angle with a cutting speed of 50 mm/s in water. Samples were placed on either a TEM grid with a carbon film (Agar Scientific, 400 mesh copper grids with carbon film) or with a silicon monoxide film (Agar Scientific, Formvar 400 mesh copper grids with silicon monoxide film).

Samples of the separate zeolite Y and clay component suitable for TEM imaging were prepared by dispensing the materials in ethanol and sonicating in an ultrasonic bath for 2-4 min. A droplet of the dispersions was added to a TEM grid and, after evaporation of the ethanol, analyzed.

The majority of the imaging has been performed with the integrated Laser and Electron Microscope (iLEM). The iLEM is built up by a Tecnai 12 120 kV transmission electron microscope (FEI Company) that is equipped with a custom designed laser scanning fluorescence microscope mounted on one of its side ports. All TEM images were recorded at 80 kV with a bottom mount TEMCam-F214 (Tietz Video and Image processing systems) charge-coupled device (CCD) camera. A 488 nm laser (Bluephoton, Omicron Laserage Laserprodukte GmbH) was used for excitation of the sample and fluorescence was detected by an avalanche photo diode detector with a long pass 520 nm filter. Operation of the fluorescence microscope of the iLEM was performed by custom software written in LabView 8.0.

The selected area diffraction patterns and Figure 5.5d were imaged with a Field Emission Gun Tecnai 20 (FEI company) operating at 200 kV, equipped with a SIS MegaView II CCD camera. The analysis of the diffraction patterns was performed in iTEM. For image processing Photoshop CS4 was employed. To overlay the fluorescence image and the TEM image the γ-value of the fluorescence image was adjusted. In all figures, the TEM and FM images were scaled for optimal contrast by employing linear adjustments of the levels of the entire image.

## 3. Results and discussion

FCC catalyst particles were investigated after performing the Brønsted acid catalyzed oligomerization reaction of 4-fluorostyrene. The confocal fluorescence microscopy and UV-Vis micro-spectroscopy studies described

in Chapter 4 have shown that fluorescent products of such Brønsted acid catalyzed probe reactions are mainly formed within the Brønsted acidic zeolite component, thus allowing its selective visualization.[9] By investigating the FCC catalyst particles with iLEM, the fluorescence intensities and the local structure of the catalyst particle could be correlated.

The experimental approach and the iLEM setup are schematically shown in Figure 5.1. Upon reaction with 4-fluorostyrene, the spherical FCC catalyst particles (Ø 70 µm) were embedded in a resin (Figures 5.1a and b). Thin slices of 90 nm, suitable for TEM imaging, were cut from the specimen block and placed on a TEM grid (Figures 5.1c and d). The iLEM embodies a custom designed scanning FM, which is mounted in one of the side ports of a conventional TEM and therefore allows subsequent imaging with the FM (Figure 5.1e) and TEM (Figure 5.1f).

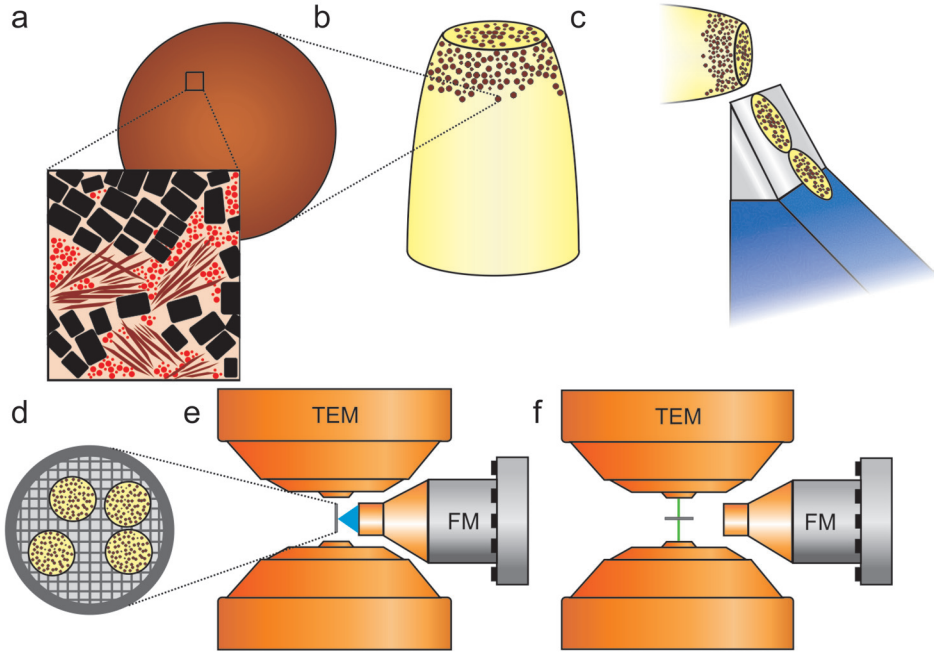


**Figure 5.1.** Schematic representation of the experimental approach and the iLEM setup. **(a)** An FCC catalyst particle and a structural detail containing zeolite Y crystallites (black, rectangles), clay platelets (brown, elongated structures) and amorphous material (red, dotted structures) are displayed. **(b)** The FCC particles are embedded in a resin (yellow) after reaction with 4-fluorostyrene at 423 K. **(c)** 90 nm thick sections of the FCC material are obtained by ultramicrotomy and **(d)** placed on a TEM grid. Panels **(e)** and **(f)** show a schematic inside view of a part of the iLEM. A detail of the fluorescence microscope (FM) is displayed, on the right, positioned in between the two poles of the objective lens of the TEM. The laser beam is perpendicular to the path of the electron beam (e). For FM imaging of the sliced particles, the grid is rotated 90° to face the laser beam (in blue). (f) After regions of interest are identified, the FM is partially retracted and the grid is tilted to its 0° position to allow for TEM imaging.

The fluorescence microscopy and TEM images were compared to obtain more insight into the fluorescence intensity and local structure within the catalyst particles, as depicted in Figure 5.2. First, FM imaging was performed (Figure 5.2a). Areas of the FCC particle showing bright and dim fluorescence were identified and could be relocated in the TEM (Figure 5.2b). Subsequently, the local structure of these areas was investigated in further detail at higher magnification (Figures 5.2c and d). A pictorial representation of the different structural features encountered in the TEM images is shown in the inset of Figure 5.1a.

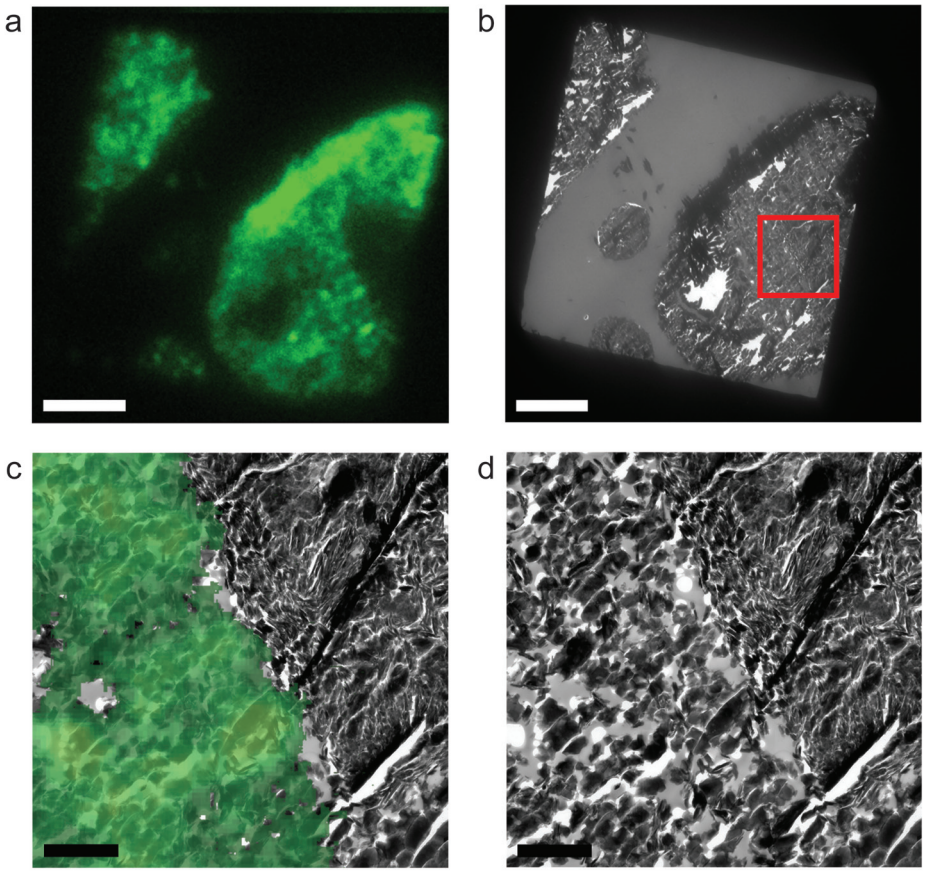


**Figure 5.2.** iLEM analysis of a sectioned FCC catalyst particle. **(a)** Fluorescence image; **(b)** TEM image, taken from the same region. The area highlighted in figure (b) with the red square is shown at higher magnification in panel **(c)**, an overlay of a TEM and fluorescence image, and **(d)**, only the TEM image. Scale bars represent 10 μm in (a) and (b) and 2 μm in (c) and (d).

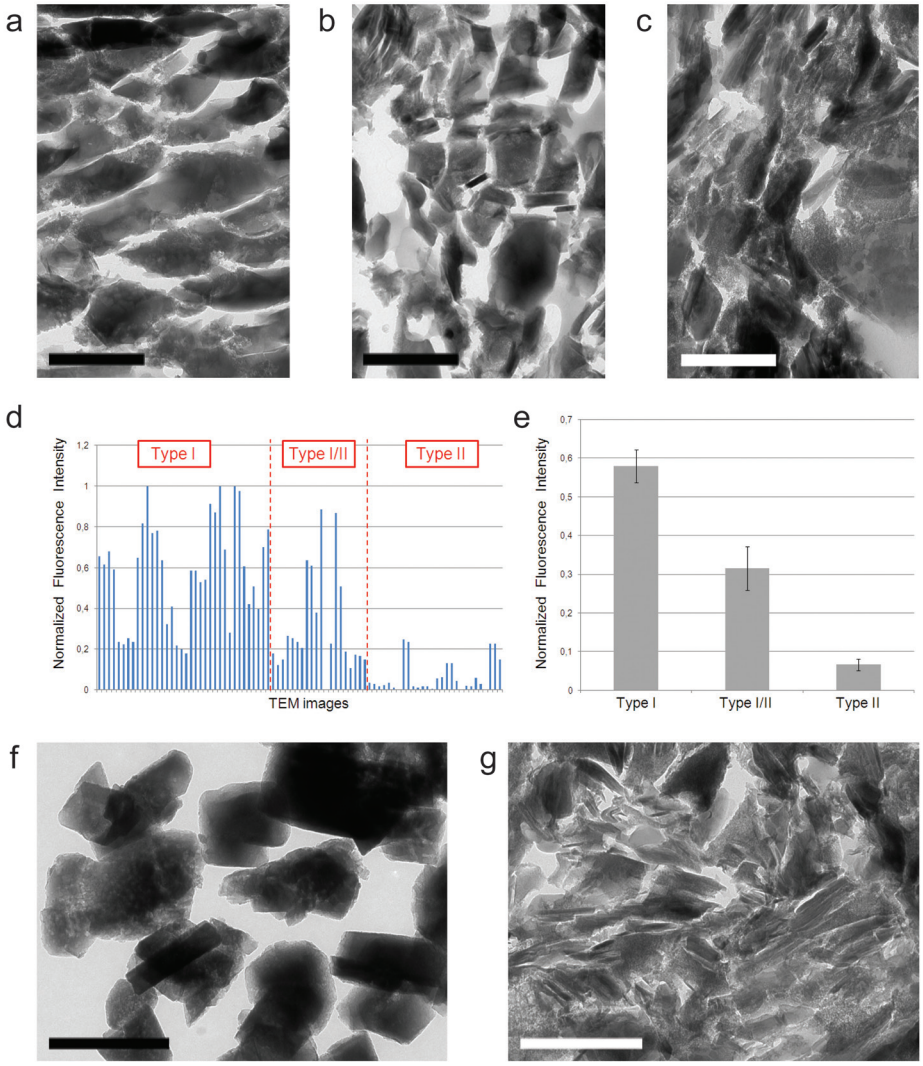


**Figure 5.3.** Representative TEM images from each structural subgroup within the FCC catalyst particles: **(a)** type I **(b)** type I/II and **(c)** type II. **(d)** The TEM images of the 84 investigated areas of different FCC catalyst particles were ordered into the three structural subtypes and the fluorescence intensity was measured. The graph indicates the normalized fluorescence intensity measured for each area (TEM images). Note the variation in fluorescence measured for areas sorted in type I/II. **(e)** Average fluorescence intensities of all images sorted into the three structural subtypes and their corresponding standard errors (error bars). **(f)** Reference TEM images of separate zeolite Y crystallites and **(g)** sections of FCC catalyst particles with only clay platelets and amorphous components, without zeolites. Scale bars all represent 500 nm.

The correlation between structure and fluorescence intensity, which is indicative of Brønsted acidity, was investigated by studying distinct areas in the FCC catalyst particles. Hereto, the local structure (TEM) and fluorescence intensity (FM) were studied thoroughly by performing a statistical analysis of 84 different regions in distinct sections of FCC particles. Two structurally distinct subtypes were defined, type I and II, as well as an intermediate type I/II, which shows a structural mixture of elements of both subtypes (Figures 5.3a, b and c).

TEM images of the 84 different regions were first sorted into the different subgroups I, I/II and II, based solely on structural characteristics. Subsequently, for each of the regions the local fluorescence intensity was measured. Areas in which bright fluorescent signal was measured were always sorted into structural subtype I or I/II. Likewise, the areas showing the lowest fluorescence intensity were always classified as structural types II or I/II (Figure 5.3d).

This observation implies that structurally different areas within FCC particles display distinct levels of fluorescence signal. Subtypes I and II disclose a large difference in structure and fluorescence intensities, whereas subtype I/II reveals a mixture of types I and II in terms of local structure and more widely varying fluorescence intensity. Statistically, there is a significant difference between the fluorescence intensities measured for the regions sorted in the subtypes I, I/II and II ($p<<0.05$, t-test).

Once a correlation between structural subtypes and distinct levels of fluorescence intensity was established, the next step was to identify the components which are characteristic for each subtype. As exemplified in Figure 5.3a, type I contains almost exclusively structures with dimensions of a few hundred nanometers that display structural features of zeolite Y crystals. To validate that these structures are indeed zeolite crystals, TEM images of the pure zeolite Y crystals were acquired (Figure 5.3f), and their structure was compared to that of the material found in type I. The electron dense component found in type I regions within the slices of FCC catalyst particles could be clearly recognized as zeolite Y crystals. Furthermore, electron diffraction patterns of the type I components confirm that they are indeed zeolite Y crystals. The high fluorescence intensities in the type I areas can be explained by the presence of Brønsted acidity within the zeolite component, which leads to the formation of fluorescent styrene products. The subtype II, with the lowest fluorescence intensity, shows a mixture of mostly matrix components. In type II plate-like particles and amorphous material could be recognized. The platelet component was assumed to be the clay present in the binder material. To support this hypothesis, TEM images of regions recognized as type II were compared to images of different FCC particles, composed solely of clay and amorphous silica and alumina and lacking the zeolitic component

(Figure 5.3g). Indeed, there is a very strong structural resemblance between the type II structure and the FCC particles containing just the binder material / matrix components. Comparison of electron diffraction patterns of FCC catalyst particles without zeolite component and type II regions further confirm the presence of clay platelets in type II regions. The low fluorescent signal is as expected, since the matrix components do not display significant Brønsted acidity. From the presence of distinct materials in the different subtypes it can be concluded that the different materials are inhomogeneously distributed within the catalyst particles.

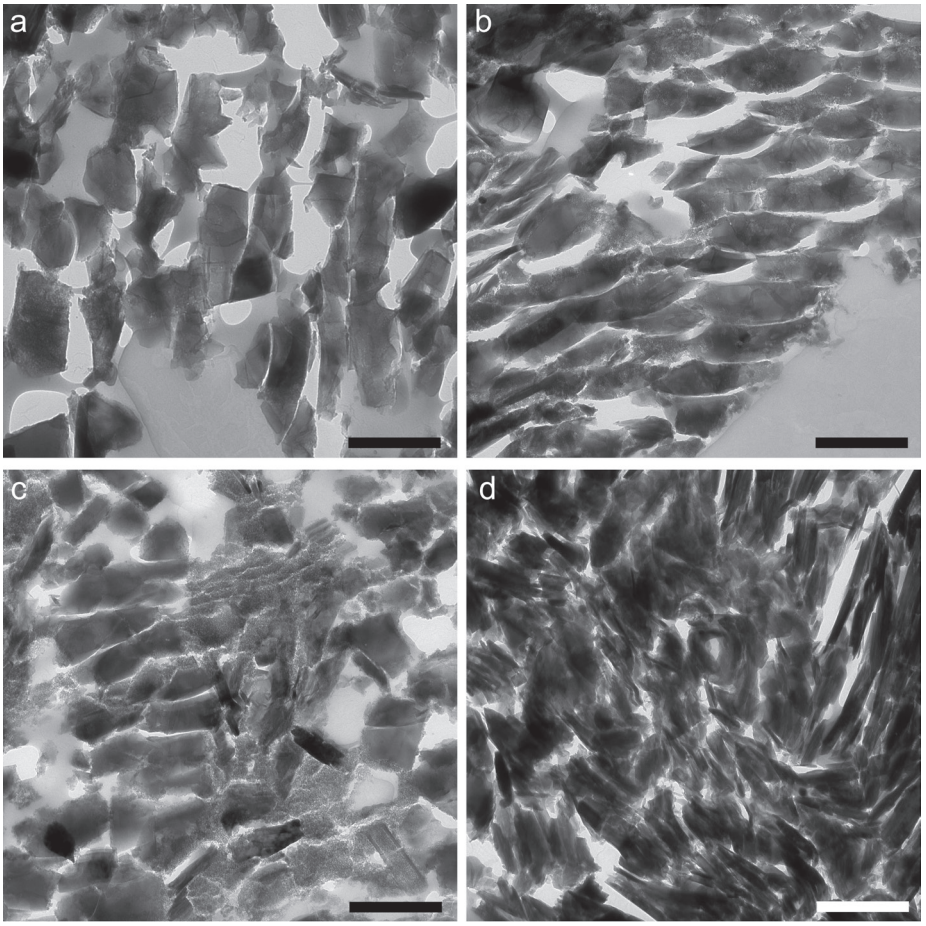


**Figure 5.4.** Representative TEM images from structural subtypes I and II categorized as 'open' and 'closed'. **(a)** Type I, open; **(b)** type I, closed; **(c)** type II, open and **(d)** type II, closed. Scale bars all represent 500 nm.

When looking at the distribution of material within the different subtypes, the spacing between the components seems to be larger in type I. This was investigated in further detail by dividing the images of both subtypes into images with significant spacing between the components ('open') and more densely packed ('closed') structures upon visual inspection. Examples of both the open and closed structures for type I and type II are shown in Figure 5.4. It was found that in type I about 70% of the 32 images could be categorized into the open structure. In type II this was about 45% of the 33 images. These findings roughly indicate that the type II structure seems to be less accessible than type I.

To prove the sensitivity of the iLEM approach towards structural and fluorescence changes, additional iLEM measurements were performed for FCC catalyst particles upon hydrothermal deactivation. Such a steam deactivation occurs in an industrial FCC unit as well and it leads to structural and chemical changes of the different components of FCC catalyst particles. Here, the steam deactivation was performed at 1061 K for 20 h in 100% steam. It is known that zeolite structures can be partially damaged due to the extraction of aluminum atoms from the framework upon steaming.[10,11] A decrease in framework aluminum content will consequently create new *extra*-framework aluminum species and this will lower the amount of Brønsted acid sites in the zeolitic material. This is reflected in a decrease in the reactivity towards the formation of fluorescent products,[9] as previously described in Chapter 4. In agreement with this loss of zeolitic Brønsted acidity, iLEM fluorescence microscopy images of steamed FCC particles showed much lower fluorescence intensity compared to fresh FCC particles. These results are exemplified in Figure 5.5a, displaying an FM image of a section of the steamed particles. A TEM overview of the same region is shown in Figure 5.5b. Furthermore, the steam treatment affected the structure of the zeolite crystals (Figures 5.5c and d). In the obtained TEM images the crystals appeared to be more damaged. Electron diffraction measurements of the steamed FCC particles revealed that the diffraction maxima of zeolite Y remain, but an additional presence of complete diffraction rings was observed, as displayed in Figure 5.5e. These diffraction rings confirm the presence of small γ-$Al_2O_3$ crystallites, which are formed upon dealumination of the zeolite.

Further structural characterization of these FCC catalyst particles showed that hardly any clay platelets were present after the steam treatment. Mostly zeolite crystallites and amorphous material could be identified and the large regions of clay regularly found in the fresh FCC particles were lost. From literature it is known that temperature and steam induced transformations of clay structures into amorphous material can take place.[12-14]

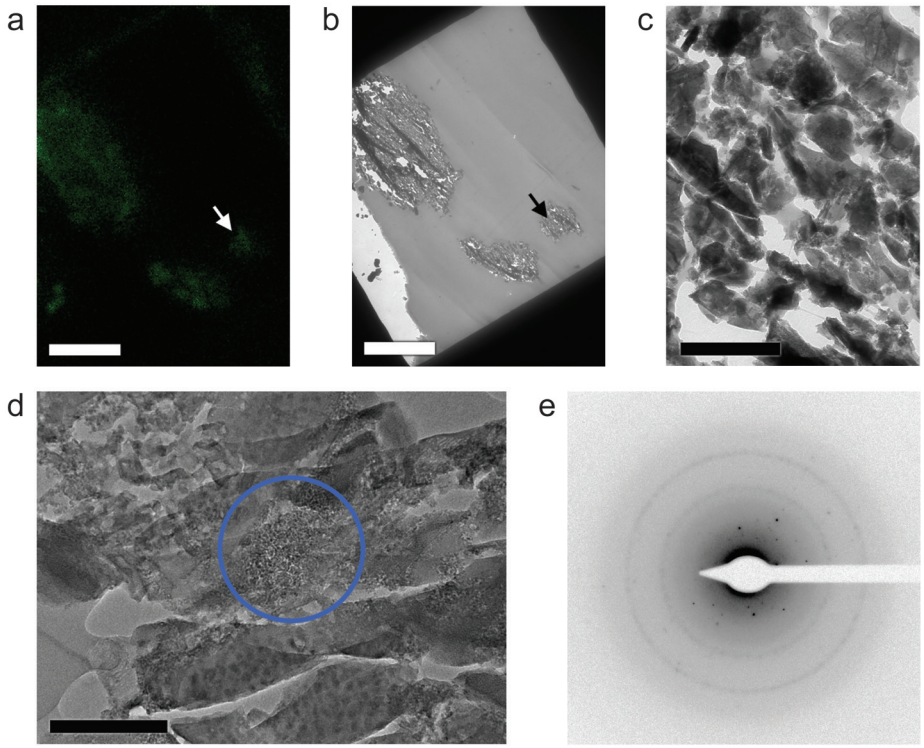


**Figure 5.5.** Analysis of FCC catalyst particles after steam deactivation. iLEM shows very low fluorescence signal, indicating reduced Brønsted acidity. **(a)** Fluorescence image of a region of sectioned steamed FCC particles, fluorescence intensity boosted with a factor 6 compared to Figure 5.2a; **(b)** TEM image, taken from the same region. Panel **(c)** displays a higher magnification of the area indicated in (a) and (b) with an arrow. **(d)** High magnification TEM image of a steamed FCC particle. **(e)** A selected area diffraction pattern (inverted) of the region indicated in (d) with the blue circle. Here the diffraction spots characteristic for zeolite Y are found as well as diffraction rings indicating the presence of γ-$Al_2O_3$ crystallites. Scale bars represent 10 μm in (a) and (b), 500 nm in (c) and 200 nm in (d).

## 4. Conclusions

The integrated laser and electron microscopy (iLEM) approach has been successfully applied in the characterization of FCC catalyst particles upon reaction with 4-fluorostyrene. The nanometer resolution of the characterization tool has revealed the structure of the active zeolitic component and its presence was confirmed with electron diffraction measurements. The zeolite-rich areas (type I) within the FCC particles were found to be most fluorescent, thus validating the results of Chapter 4, in which it was shown that the zeolite is the most Brønsted acidic

component within FCC catalysts. Furthermore, the structure of the matrix components clay, silica and alumina could be examined at the nanometer scale. The matrix-rich areas (type II) did not display significant fluorescent signal, which can be explained by the lack of strong Brønsted acid sites in these components. The fact that different structural types can be found in the FCC catalyst particles indicates that the FCC components are inhomogeneously distributed throughout the particles. Type I regions in general displayed a more open structure than type II areas.

Moreover, this approach provides sensitivity to changes in activity, structure and chemical properties of the catalytic material. By investigating FCC catalyst particles after steam treatment it was shown that hardly any clay platelets remained. Electron diffraction patterns in zeolitic regions in the catalyst particles revealed that the zeolite Y structure was still present. Additionally, small γ-$Al_2O_3$ crystallites were formed upon dealumination of the zeolite by steam.

## Acknowledgements

Caroline van der Meij and Kees van Leerdam (Akzo Nobel Chemicals bv., The Netherlands) are acknowledged for ultramicrotomy procedures. Cliff Johnston (Purdue University, United States of America) and Robert Schoonheydt (K. U. Leuven, Belgium) are thanked for fruitful discussions.

## References

[1] O. Bayraktar; E. L. Kugler *Catal. Lett.* **2003**, *90*, 155-160.
[2] R. A. Beyerlein; G. A. Tamborski; C. L. Marshall; B. L. Meyers; J. B. Hall; B. J. Huggins *ACS Symp. Ser.* **1991**, *452*, 109-143.
[3] M. L. Occelli; S. A. C. Gould; G. D. Stucky *Stud. Surf. Sci. Catal.* **1994**, *84*, 485-492.
[4] M. L. Occelli; S. A. C. Gould *Stud. Surf. Sci. Catal.* **2004**, *149*, 71-104.
[5] M. L. Occelli; S. A. C. Gould *Chemtech* **1994**, *24*, 24-27.
[6] A. V. Agronskaia; J. A. Valentijn; L. F. van Driel; C. T. W. M. Schneijdenberg; B. M. Humbel; P. M. P. van Bergen en Henegouwen; A. J. Verkleij; A. J. Koster; H. C. Gerritsen *J. Struct. Biol.* **2008**, *164*, 183-189.
[7] M. A. Karreman; A. V. Agronskaia; A. J. Verkleij; F. F. M. Cremers; H. C. Gerritsen; B. M. Humbel *Biol. Cell* **2009**, *101*, 287-299.
[8] M. A. Karreman; E. G. van Donselaar; H. C. Gerritsen; C. T. Verrips; A. J. Verkleij *Traffic* **2011**, *12*, 806-814.
[9] I. L. C. Buurmans; J. Ruiz-Martínez; W. V. Knowles; D. van der Beek; J. A. Bergwerff; E. T. C. Vogt; B. M. Weckhuysen*, Nature Chem.* **2011**, DOI: 10.1038/NCHEM.1148.
[10] S. van Donk; A. H. Janssen; J. H. Bitter; K. P. de Jong *Catal. Rev. Sci. Eng.* **2003**, *45*, 297-319.
[11] Y. Tao; H. Kanoh; L. Abrams; K. Kaneko *Chem. Rev.* **2006**, *106*, 896-910.
[12] G. Artioli *Nucl. Instrum. Meth. B* **1997**, *133*, 45-49.
[13] J. Sanz; A. Madani; J. M. Serratosa; J. S. Moya; S. Aza *J. Am. Ceram. Soc.* **1988**, *71*, C418-C421.
[14] B. Sonuparlak; M. Sarikaya; I. A. Aksay *J. Am. Ceram. Soc.* **1987**, *70*, 837-842.

# Chapter 6

## Staining of Fluid Catalytic Cracking Catalysts using the Thiophene Oligomerization Probe Reaction: Localizing Brønsted Acidity within a Single Catalyst Particle


### Abstract

A study of the reactivity and localization of thiophene derivatives has been conducted within FCC catalyst particles. To enable this the reactivity of the separate FCC components was followed by UV-Vis micro-spectroscopy. From these experiments it is clear that thiophenes selectively react on the Brønsted acid sites within the zeolite component. The oligomeric carbocation distribution within zeolites H-Y and H-ZSM-5 is different due to their distinct pore structures. Moreover, different reactivities have been observed for thiophene derivatives when the electron withdrawing / donating properties or the molecular sizes were varied. Furthermore, the results demonstrate that the formed carbocations are coke intermediates and the FCC particles containing zeolite Y promote this coke formation to a higher extent than those containing ZSM-5, *i.e.* the large supercages of zeolite Y allow the accommodation of bulky coke species. On the other hand, FCC particles containing ZSM-5 stabilize the carbocations within the narrower straight pores, diminishing coke formation. Confocal fluorescence microscopy images reveal inhomogeneously distributed micron-sized domains with high fluorescence within the FCC particles, which are attributed to the oligomeric carbocations formed on Brønsted acid sites within the zeolitic FCC component. This finding proves the suitability of the thiophene oligomerization reaction as a staining reaction for Brønsted acidity. The reactivity of different thiophenes has also been studied by this approach and the fluorescence intensity data reveal the same reactivity trends as the UV-Vis micro-spectroscopy studies.



This work is based on the following manuscript: J. Ruiz-Martínez, I. L. C. Buurmans, W. V. Knowles, D. van der Beek, J. A. Bergwerff, E. T. C. Vogt and B. M. Weckhuysen, *submitted for publication.*

## 1. Introduction

In Chapters 3 to 5 it has been shown that the oligomerization of styrene is a suitable probe reaction to enable the visualization of Brønsted acidity. Details of the styrene product formation within zeolites H-Y and H-ZSM-5 were obtained by UV-Vis micro-spectroscopy. For the FCC catalyst particles it was proven that only upon presence of zeolite Y or ZSM-5 within the particles reactivity towards the styrene oligomerization occured. Brønsted acid site maps of individual FCC catalyst particles were acquired using confocal fluorescence microscopy and revealed an inhomogeneous distribution of micron-sized zeolite particulates within the FCC catalyst particles. Changes in Brønsted acidity upon laboratory deactivation of FCC catalyst particles were studied using the same approach.

Here, we introduce another probe reaction for Brønsted acidity as a validation of our previous results. The oligomerization reaction of thiophene is selected for this purpose as a second staining approach. As previous research on large coffin-shaped ZSM-5 crystals has shown, the reactivity of thiophenes can be studied in a spatially resolved way using micro-spectroscopy.[1] The use of different thiophene derivatives provides evidence that the Brønsted acid site catalyzed formation of the initial carbocation is the rate-limiting step in the thiophene oligomerization. The thiophene product formation was monitored using UV-Vis micro-spectroscopy and confocal fluorescence microscopy.

## 2. Experimental procedures

Thiophene (Merck, > 99%), 2-bromothiophene (Aldrich, 97%), 2-chlorothiophene (Aldrich, 98%), 2-methylthiophene (Aldrich, 98%), 2-ethylthiophene (Aldrich, 97%), 3-methylthiophene (Fluka, ≥ 98 %), 1-benzothiophene (Merck, for synthesis) and dibenzothiophene (Merck, for synthesis) were used as received. Zeolites H-Y (Si/Al = 15, BET surface area = 720 $m^2\ g^{-1}$) and H-ZSM-5 (Si/Al = 15, BET surface area = 379 $m^2\ g^{-1}$), silica (BET surface area = 147 $m^2\ g^{-1}$), high-crystalline alumina (BET surface area = 34 $m^2\ g^{-1}$), low-crystalline alumina (BET surface area = 374 $m^2\ g^{-1}$) and clay (BET surface area = 20 $m^2\ g^{-1}$) were provided by Albemarle Corporation. Silica and both types of alumina were dried at 373 K for 30 min. All materials were heat-treated at 723 K for 2 h prior to use to remove any adsorbed species. FCC catalyst particles were provided by Albemarle Corporation as well and used as received. The FCC catalyst batches used were FCC 3 (containing zeolite Y); FCC 4 (containing ZSM-5) and FCC 5 (without zeolite).

UV-Vis micro-spectroscopic experiments were performed using an *in situ* cell (Linkam Scientific Instruments FTIR 600) equipped with a

temperature controller (Linkam Scientific Instruments TMS94) for heating of the samples. More details on the microscopy setup can be found in the experimental procedures section of Chapter 3. All UV-Vis experiments were performed on 50 mg of material, compressed to a pellet at a pressure of 5 ton $cm^{-2}$ on a Perkin-Elmer 15.011 laboratory press. The pellets of FCC components or particles were placed on the heating element of the *in situ* cell and heated to 333 K (FCC components) or 473 K (FCC catalyst particles) for 10 min, after which 15 µl of thiophene was added and UV-Vis spectra were taken every 3 s using an acquisition time of 50 ms and averaging the signal 50 times.

The confocal fluorescence microscopy studies were performed using a Nikon Eclipse LV150 microscope with a 50x 0.55 NA dry objective lens. Confocal fluorescence microscopy images were collected by Nikon D-Eclipse C1 head connected to a Melles Griot laser light source with an emission wavelength of 561 nm (yellow diode-pumped solid-state laser, < 50 mW). The fluorescence signal was detected with a photomultiplier tube in the 575-635 nm detection range. Samples for confocal fluorescence microscopy experiments were prepared by heating FCC catalyst particles in the *in situ* cell at 473 K for 10 min. Subsequently, 15 µl of thiophene was added and the heating was stopped after 10 s.

## 3. Results and discussion

The reaction mechanism of the oligomerization of thiophene, a weak base, on acidic solids has been discussed previously in literature and is depicted in Scheme 6.1.[1-4] During the oligomerization reaction carbocationic oligomers are formed. The ability of these carbocationic species to absorb and emit light in the visible region allows their study using optical micro-spectroscopic approaches.

The reactivity of the individual FCC components was studied in a first step using UV-Vis micro-spectroscopy and the resulting UV-Vis absorption spectra are shown in Figure 6.1. For both zeolites H-ZSM-5 and H-Y the appearance of absorption bands can be observed in the UV-Vis spectra. The H-ZSM-5 spectra display two predominant bands at 482 and 554 nm, while for zeolite H-Y the main absorption bands are located at 511 and 578 nm. These findings are comparable to those observed during the oligomerization of styrenes within zeolite H-Y and H-ZSM-5 described in Chapter 3: different pore structures lead to the formation of distinct carbocationic reaction products. The products were not identified, but they can be ascribed to the formation of carbocationic reaction intermediates on Brønsted acid sites, following the mechanism described in Scheme 6.1.

The attribution of the absorption bands to specific carbocations is beyond the goal of this study. UV-Vis measurements give limited

chemical information and the assignment of a band to unique species can be speculative. The proton-assisted thiophene oligomerization reactions are very complex and they may be associated with several *intra*- and *inter*molecular hydrogen transfers. This implies that two completely distinct oligomers may have the same double bond conjugated system and thus they may have comparable absorption bands.[5] However, some chemical information about the products formed within H-ZSM-5 compared to H-Y can be obtained from the UV-Vis spectra. The bands in zeolite H-ZSM-5 are shifted to lower wavelengths with respect to zeolite Y (482 versus 511 nm and 554 versus 578 nm). It is generally accepted that organic molecules that contain a larger conjugated π-system appear at higher absorption wavelengths.[6] Since H-ZSM-5 is built up by a narrower pore system than zeolite H-Y, it is reasonable to suggest that larger carbocations are formed in the supercages of zeolite H-Y. In agreement with our UV-Vis results, Chica *et al.* found an increase in the size of thiophene oligomers with increasing channel volume of the zeolitic material (H-ZSM-5 < H-Beta < H-Y).[7]

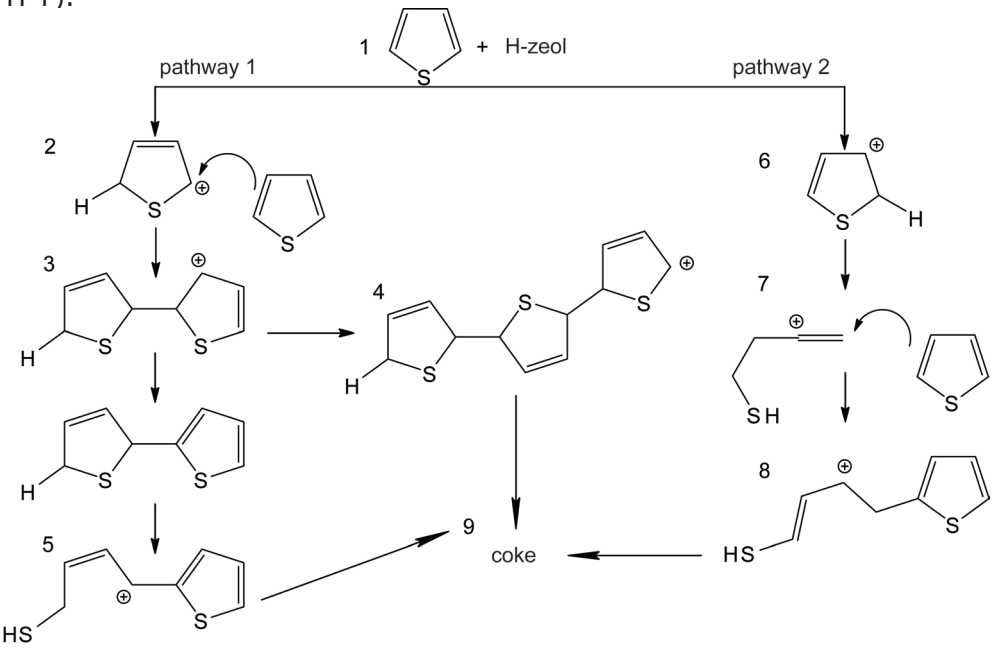


**Scheme 6.1.** Potential reaction pathways of the oligomerization reaction of thiophene on Brønsted acid sites. In the first step in both possible pathways, interaction of a thiophene monomer (**1**) with a Brønsted acid site leads to the formation of a protonated monomer with carbocationic character (**2** or **6**). In pathway 1, the carbocation reacts with another monomer to form a dimeric carbocation (**3**), which can either further oligomerize to produce a trimer (**4**), or a ring-opened dimer via C-S bond cleavage (**5**). In pathway 2, the initial carbocation (**6**) undergoes ring-opening (**7**) and subsequently reacts with another thiophene monomer to form species **8**. Further reactions in both pathways can lead to the formation of coke-like species (**9**).

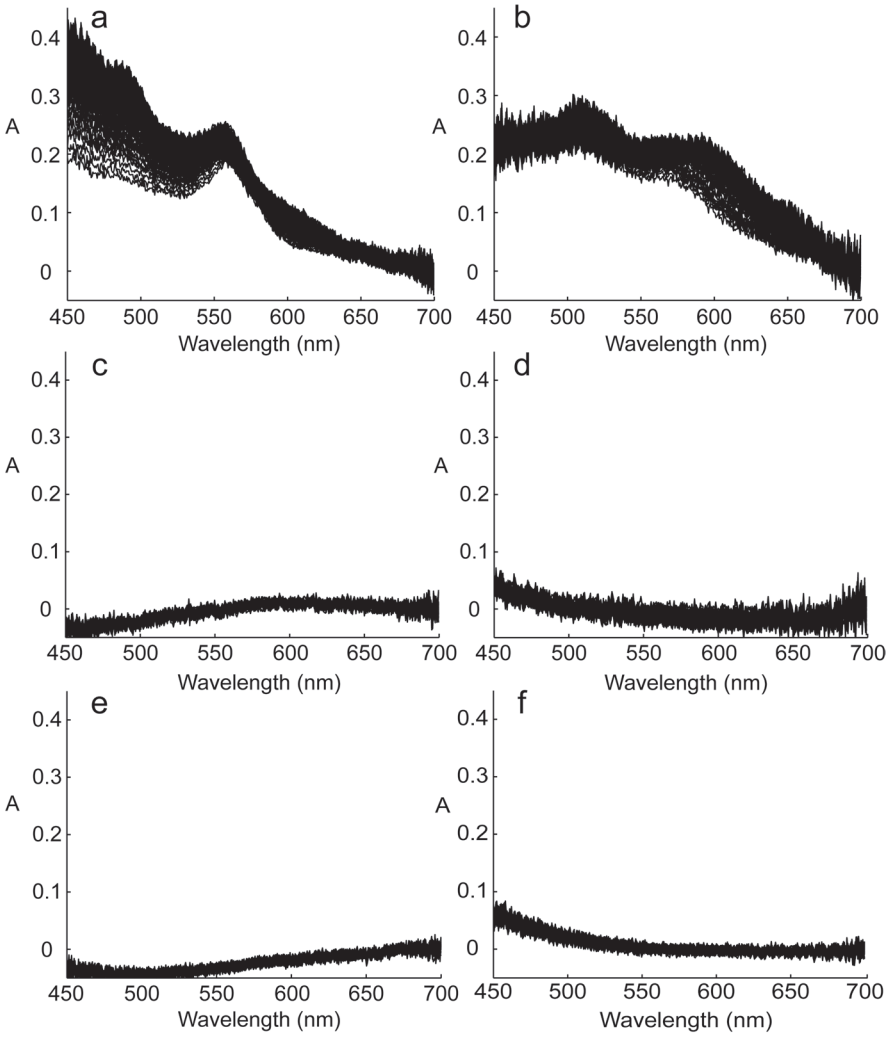


**Figure 6.1.** Evolution of the UV-Vis absorption bands in time for **(a)** H-ZSM-5 (Si/Al = 15); **(b)** zeolite H-Y (Si/Al = 15); **(c)** clay; **(d)** high-crystalline alumina; **(e)** low-crystalline alumina and **(f)** silica upon exposure to thiophene at 333 K.

From the UV-Vis absorption spectra of the FCC matrix components (clay, high-crystalline alumina, low-crystalline alumina and silica) it is clear that none of them shows reactivity towards the thiophene oligomerization reaction. This same observation is described in Chapter 4 for the styrene conversion, where only the clay component displays moderate reactivity. Thus, for both oligomerization reactions sufficiently strong Brønsted acidity is needed, which is lacking within the FCC matrix components.

Three different types of FCC catalyst particles (containing either zeolite ZSM-5 or Y or without zeolite) were also studied by UV-Vis micro-spectroscopy, as depicted in Figure 6.2. The reaction temperature was changed to 473 K for these experiments because of the low reactivity of the particles at 333 K. As expected from the UV-Vis analysis of the individual matrix components, the reactivity of the catalyst without zeolite was negligible. For the FCC catalyst particles containing ZSM-5, the formation of the different carbocations was extremely fast and no changes in the evolution of the different species could be observed. The absorption spectra of the FCC catalyst particles containing zeolite Y show a similar rapid formation of the absorption bands, as well as an increase in the background absorption in time. The rise of the background indicates the formation of more polyaromatic molecules, denoted in this study as coke-like species.[8]

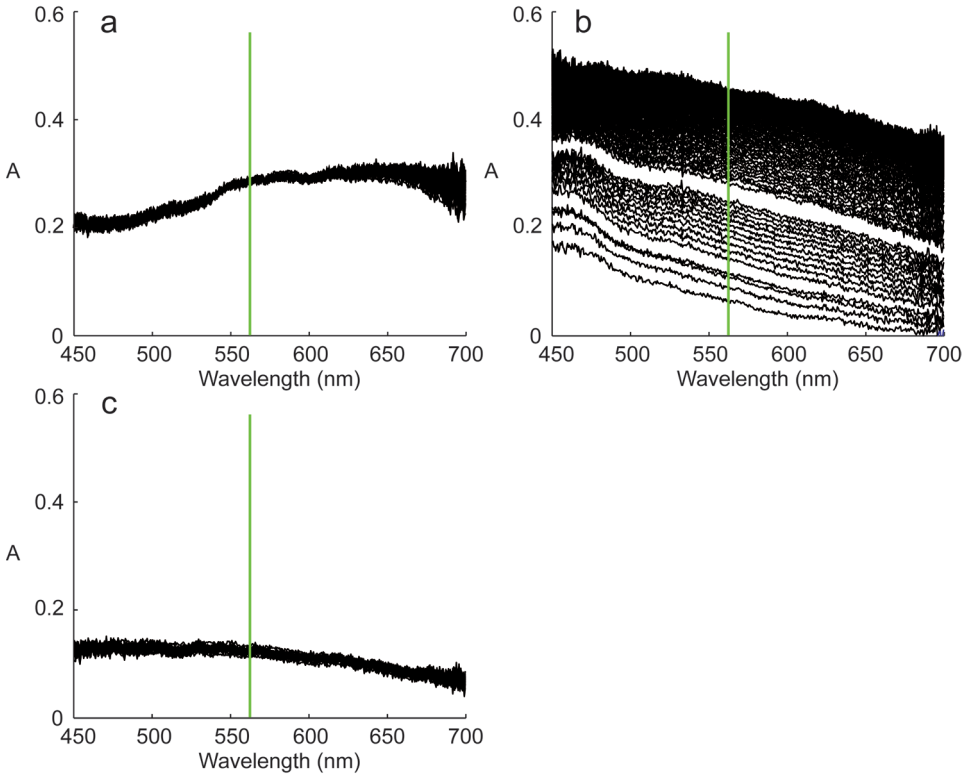


**Figure 6.2.** Evolution of the UV-Vis absorption bands in time for FCC catalyst particles containing **(a)** ZSM-5; **(b)** zeolite Y and **(c)** no zeolite upon exposure to thiophene at 473 K. The green lines represent the laser excitation wavelength of 561 nm, which is used during the confocal fluorescence microscopy experiments to excite the formed carbocations.

The reactivity of a series of substituted thiophene molecules was also studied. In both catalyst particles containing ZSM-5 and zeolite Y the same trends were observed. Typical UV-Vis absorption spectra for the catalyst particles containing zeolite Y are plotted in Figure 6.3. For the halogen-substituted thiophenes, 3-bromothiophene and 3-chlorothiophene, the absorbance was lower compared to that of thiophene and decreasing as the electronegativity of the substituent increases. This can be seen in Figures 6.3a, b and c. The presence of the halogen atom destabilizes the formation of the initial carbocation by an electron-withdrawing inductive effect, hence reducing the reactivity towards oligomer formation (Scheme 6.1).

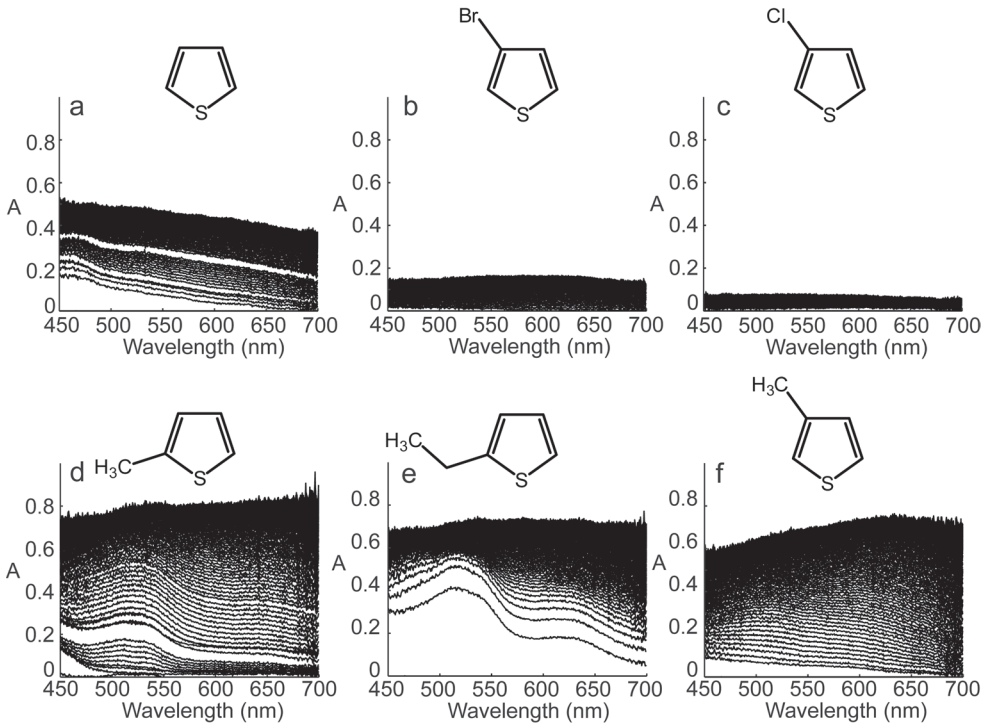


**Figure 6.3.** Evolution of the UV-Vis absorption bands in time for FCC catalyst particles containing zeolite Y upon exposure at 473 K to **(a)** thiophene; **(b)** 3-bromothiophene; **(c)** 3-chlorothiophene; **(d)** 2-methythiophene; **(e)** 2-ethylthiophene and **(f)** 3-methylthiophene.

The use of alkyl substituents, methyl and ethyl groups, which are well known to be electron donating groups (also called activating groups), stabilizes the formation of the initial carbocations. The corresponding UV-Vis absorption spectra (Figures 6.3d, e and f) indeed reveal an increase in the absorbance, which can be translated into a higher reactivity towards the formation of carbocationic oligomers when alkylated thiophene reagents

are used. The stability of the initial carbocation has been identified as the rate-determining step for similar oligomerization reactions, such as the dimerization of styrenes.[9-10] Our study of different thiophenes pinpoints the same, *i.e.* the stabilization of the initial protonated thiophene carbocations **2** and **6** (Scheme 6.1) rather than the dimerization step forms the rate-determining step in their oligomerization.

The reactivity of bulkier thiophene-like molecules, such as 1-benzothiophene and dibenzothiophene, was also investigated. As summarized in Figure 6.4, the reactivity is lower for bulkier thiophenes. Two factors could account for these reactivity differences. Firstly, the bulky thiophene molecules may encounter diffusion limitations, which subsequently hinder the formation of larger oligomers, resulting in a moderate product formation. This would explain the lower reactivity of the FCC catalyst particles containing ZSM-5 compared to the particles containing zeolite Y. Secondly, the formation of the initial carbocation could be less favored for thiophene derivatives with larger molecular sizes, thus lowering the overall reactivity. The same reactivity trends were observed in the hydrodesulphurization of 1-benzothiophene and dibenzothiophene in oil feedstocks.[11-13] In line with the results obtained for the other substituted thiophenes, the UV-Vis spectra of the bulky thiophenes reveal an increase in the background absorption, which can be ascribed to the formation of coke-like species.

Given the variety of the products formed, *i.e.* oligomers and coke-like species, a more detailed analysis of the time-resolved spectra was performed. By doing so, more insight into the catalytic reactivity of the different thiophene compounds in the two distinct FCC catalyst materials can be obtained. As a showcase the reaction of 2-methylthiophene on both FCC catalyst particles containing ZSM-5 and zeolite Y was selected. The intensities of both the band associated with the formation of oligomeric carbocations at 515 nm and the background rise due to the presence of coke-like species were plotted in time. These results are displayed in Figure 6.5. Different behavior was observed for the two catalyst types: the catalyst particles containing zeolite Y are more reactive towards the formation of coke-like species. The carbocationic product band at 515 nm displays a maximum in intensity, after which the intensity decreases to zero. Conversely, the carbocation intensity for the catalyst particles containing ZSM-5 increases in time and reaches a pseudoplateau, with a slightly negative slope.

Based on these results, a reaction mechanism of the distinct species formed during the conversion of 2-methylthiophene can be attempted: upon reaction, initially carbocationic oligomers, displaying an absorption band at 515 nm, are formed within the zeolite pores. For the catalyst particles containing zeolite Y, the formation of coke-like species starts after the formation of the carbocation and its highest formation

rate matches with the maximum concentration of carbocations. These findings, together with the observed disappearance of the carbocationic species over time, provide evidence that carbocations are indeed coke intermediates and this coke is accommodated in the large supercages. On the contrary, the carbocations are more stable within the narrower ZSM-5 cylindrical pores and the zeolite structure prevents the condensation reactions,[14-15] which results in limited coke formation. This effect is due to guest-host interactions between the organic carbocations and the zeolite pore structure, as described in literature.[16-18]

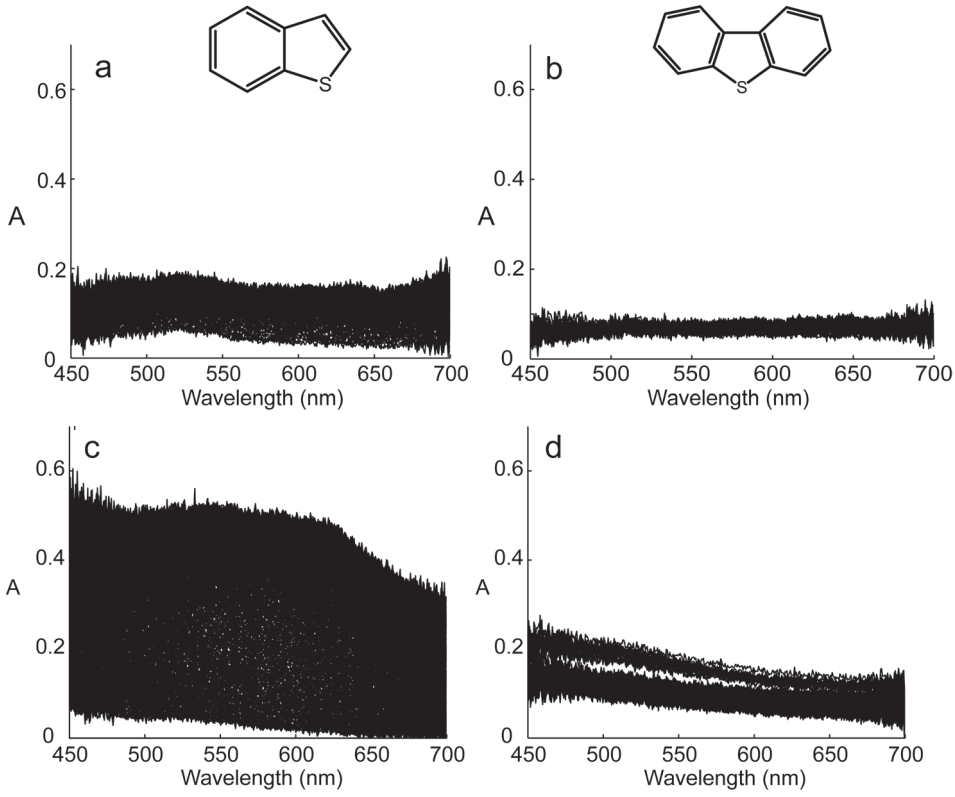


**Figure 6.4.** Evolution of the UV-Vis absorption bands in time for FCC catalyst particles containing **(a** and **b)** ZSM-5 and **(c** and **d)** zeolite Y upon exposure at 473 K to 1-benzothiophene and dibenzothiophene, respectively.

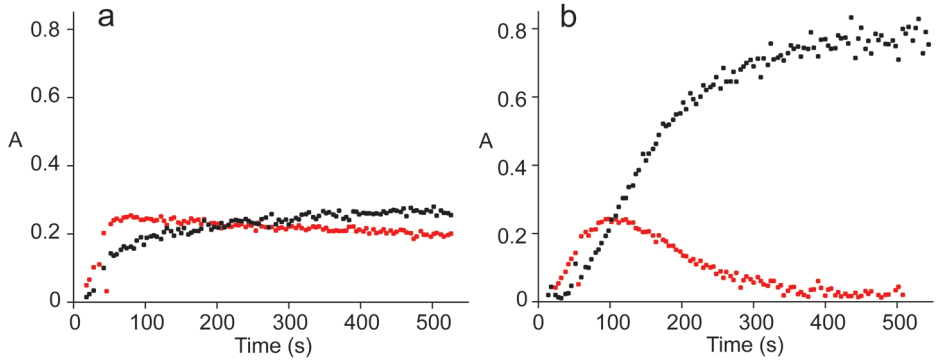


**Figure 6.5.** Time evolution of the intensity of the carbocationic 515 nm band (red) and the background absorption due to coke formation (black) for FCC particles containing **(a)** ZSM-5 and **(b)** zeolite Y during 2-methylthiophene conversion at 473 K.

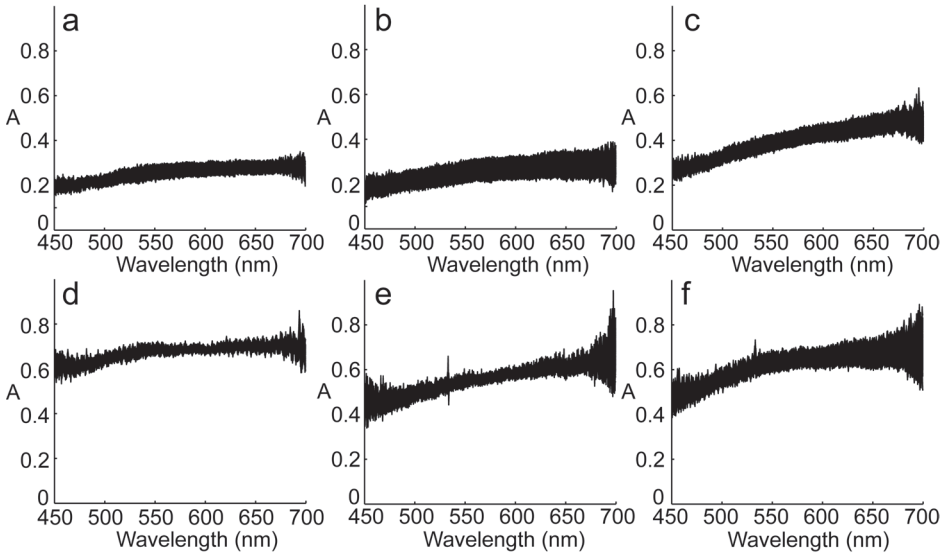


**Figure 6.6.** Evolution of the UV-Vis absorption bands in time for FCC catalyst particles containing **(top)** ZSM-5 and **(bottom)** zeolite Y upon reaction with **(a** and **d)** 1-benzothiophene; **(b** and **e)** thiophene and **(c** and **f)** 2-methylthiophene at 823 K.

To investigate the influence of the temperature on the reactivity of different thiophene molecules, time-resolved UV-Vis experiments were performed at 823 K. This temperature was selected to simulate the temperature conditions in an industrial FCC unit. The UV-Vis absorption spectra, plotted in Figure 6.6, reveal a fast background increase that remains constant in time. In addition, no absorption bands ascribed to the formation of carbocationic species were observed. These findings

point out that at such an elevated temperature, the formed carbocations are directly converted into coke-like species. The zeolitic pore structure influences the formation of coke to a large extent.[19] The absorption intensity is higher for the catalyst containing zeolite Y, independent of the type of thiophene derivative used. This observation clearly indicates that the large supercages of zeolite Y facilitate the formation of bulkier coke species to a higher extent than the somewhat smaller linear pores encountered in the internal structure of ZSM-5.

Confocal fluorescence microscopy experiments were conducted to map the location of the different carbocationic oligomers within FCC catalyst particles containing either ZSM-5, zeolite Y or without any zeolite component. Since the thiophene oligomerization reaction is Brønsted acid catalyzed, these maps at the same time reveal the distribution of Brønsted acid sites within the catalyst body. Figure 6.7 shows the fluorescence images of the different catalyst materials upon reaction with thiophene. In order to make a fair comparison, both the intensity of the laser and the sensitivity of the detector were kept constant. In all measurements, white spots represent overexposure of the detector due to highly fluorescent areas, which was found to be an advantageous tool to compare the fluorescence in different samples. The overexposed samples were also measured at lower detector sensitivities, as depicted in Figures 6.7d and e. A heterogeneous distribution of the fluorescence within the catalyst particles was observed, and a lower coloration was apparent for the catalyst particles without zeolite. Additional confocal fluorescence microscopy measurements, decreasing the detector sensitivity, reveal that no fluorescence could be detected in that case for the particles without zeolite. At these same settings still an intense fluorescence signal was obtained for the catalyst particles that contain zeolite, unambiguously pointing out that the thiophene oligomerization reaction selectively occurs in the zeolite domains. These experiments thus show that thiophene is a suitable staining reaction for the visualization of zeolite domains within FCC catalyst particles. As additional proof, the reactivity of the matrix components (clay, alumina and silica) was monitored separately by confocal fluorescence microscopy and, as it was expected, the fluorescence of the zeolite component was significantly higher.

In the FCC catalyst particles containing either ZSM-5 or zeolite Y micron-sized domains displaying a high fluorescence intensity are inhomogeneously distributed within the catalyst body. These domains correspond to areas with a Brønsted acidity that is strong enough to catalyze the formation of fluorescent thiophene carbocations. The fluorescence domains are 1-5 μm in diameter, which is in agreement with the zeolite domain size.[20]

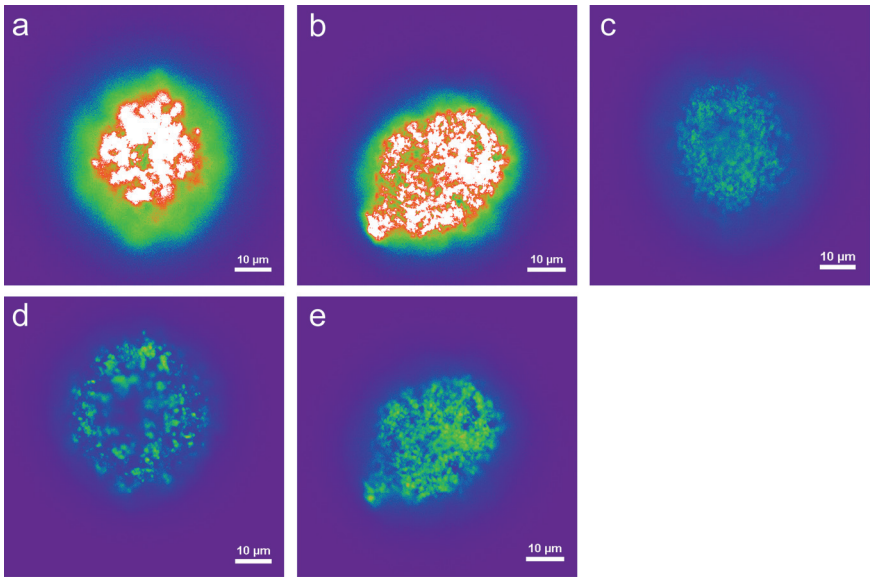


**Figure 6.7.** Confocal fluorescence microscopy images of FCC catalyst particles containing **(a)** ZSM-5; **(b)** zeolite Y and **(c)** no zeolite upon reaction with thiophene (473 K, $\lambda_{ex}$ = 561 nm, detection 575-635 nm, false color images). The sensitivity of the detector was kept constant (5.80 a.u.). White areas correspond to highly fluorescent areas that overexpose the detector. **(d)** and **(e)** are images of the same particles (a) and (b), measured at lower detector sensitivities (5.10 and 5.50 a.u., respectively).

The influence of substitution on the reactivity of thiophene molecules was also studied by confocal fluorescence microscopy. For both FCC catalyst particles containing ZSM-5 and zeolite Y similar trends were observed. The results for the FCC catalyst particles containing zeolite Y are depicted in Figure 6.8. For the halogen-substituted thiophenes, 3-bromothiophene and 3-chlorothiophene, the fluorescence intensity is lower compared to thiophene, decreasing as the electronegativity of the substituent increases (Figures 6.8a, b and c). This effect is comparable to the trends as obtained by the UV-Vis micro-spectroscopy measurements. The use of alkyl substituents, methyl and ethyl groups, leads to an increase in the formation of carbocationic oligomers, which is reflected in a boost in fluorescence intensity (Figures 6.8d to i).

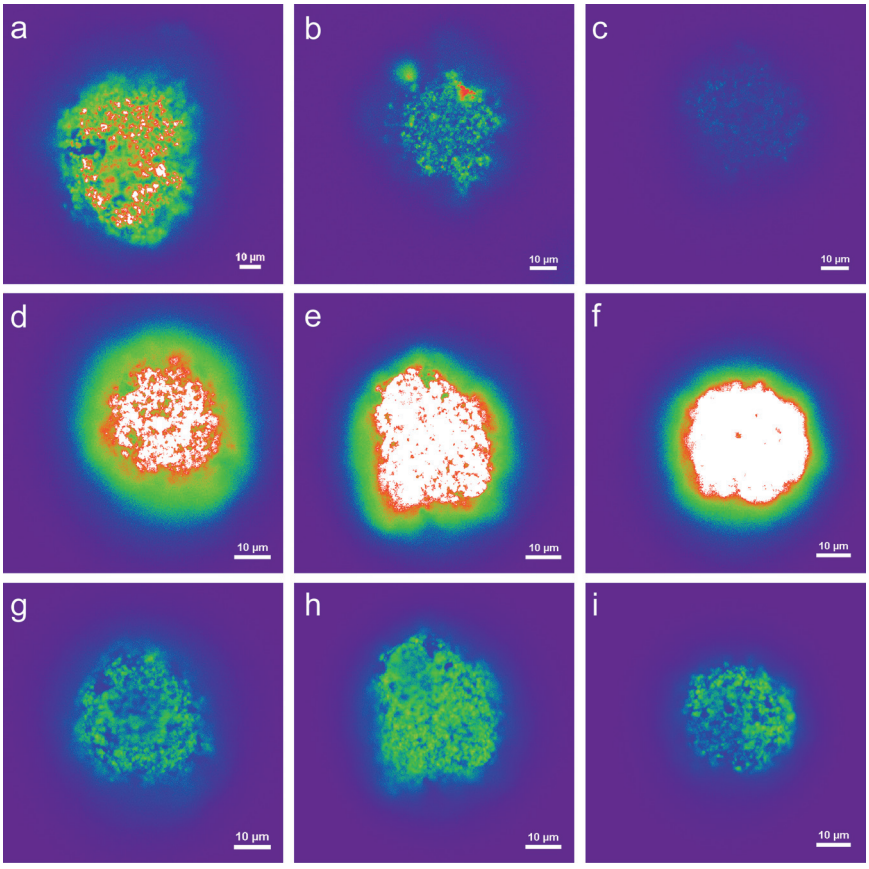


**Figure 6.8.** Confocal fluorescence microscopy images of FCC catalyst particles containing zeolite Y upon reaction with **(a)** thiophene; **(b)** 3-bromothiophene; **(c)** 3-chlorothiophene; **(d)** 2-methylthiophene; **(e)** 2-ethylthiophene and **(f)** 3-methylthiophene (473 K, $\lambda_{ex}$ = 561 nm, detection 575-635 nm, false color images). The sensitivity of the detector was kept constant (5.80 a.u.). For the alkyl substituted thiophenes, the fluorescence images display overexposed white areas. New confocal images were obtained for the catalyst particles (d); (e) and (f) at lower detector sensitivities, *i.e.* **(g)** 5.60 a.u.; **(h)** 5.45 a.u. and **(i)** 5.20 a.u., respectively.

Figure 6.9 displays the confocal fluorescence microscopy images of both FCC catalyst particles containing zeolite Y and ZSM-5 upon reaction with 1-benzothiophene and dibenzothiophene. The observed fluorescence intensities are also in agreement with the UV-Vis micro-spectroscopy experiments, *i.e.* the fluorescence intensity decreases for the more bulky thiophenes.

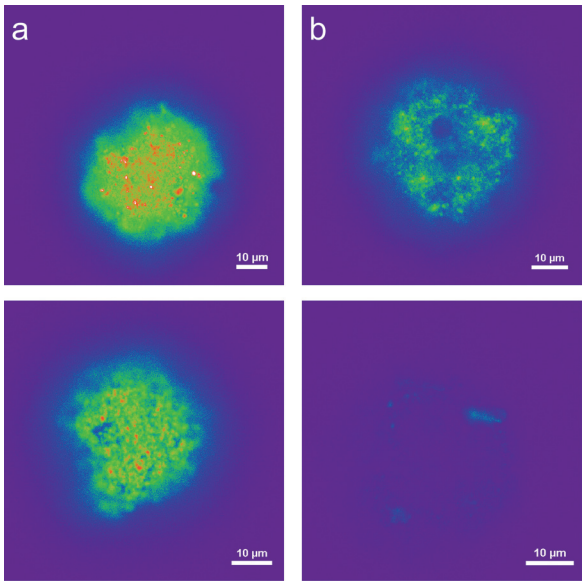


**Figure 6.9.** Confocal fluorescence microscopy images of FCC particles containing **(top)** ZSM-5 or **(bottom)** zeolite Y upon reaction with **(a)** 1-benzothiophene and **(b)** dibenzothiophene (473 K, $\lambda_{ex}$ = 561 nm, detection 575-635 nm, false color images).

## 4. Conclusions

UV-Vis micro-spectroscopy and confocal fluorescence microscopy have been used to study the reactivity and location of carbocationic products of the thiophene oligomerization reaction within FCC catalyst particles containing either ZSM-5 or zeolite Y. UV-Vis micro-spectroscopy experiments clearly show that thiophene and thiophene derivatives selectively react on the Brønsted acid sites of the zeolitic material, leading to the formation of light-absorbing carbocationic species within the zeolite domains. Different products are observed within the pores of ZSM-5 compared to zeolite Y. The matrix components of FCC catalyst particles do not show significant activity towards the formation of visible absorption bands.

Moreover, UV-Vis measurements reveal differences in reactivity of the FCC catalyst particles towards thiophenes with distinct substituents. Electron withdrawing substituents destabilize carbocation formation, which is apparent from a lower activity, whereas electron donating substituents boost the reactivity of thiophene derivatives. A more thorough analysis of the UV-Vis absorption spectra reveals the formation of coke-like species. Carbocationic thiophene products act as intermediates during the coke formation. Furthermore, the rate of coke formation depends on the zeolitic structure: the large supercages in zeolite Y facilitate a faster coke

formation compared to the more narrow pore structure of ZSM-5, which stabilizes the thiophene carbocations.

Confocal fluorescence microscopy images reveal inhomogeneously distributed micron-sized domains with high fluorescence intensity within the FCC particles. The fluorescence in these domains is attributed to the different thiophene oligomeric carbocations entrapped in the zeolitic material and thus reveals maps of the distribution of the Brønsted acidic zeolite material within FCC catalyst particles. The influence of the different thiophene substituents was also studied. The fluorescence intensity data reveal the same reactivity trends as the UV-Vis absorption spectra: electron withdrawing substituents lead to a lower oligomerization activity, while electron donating groups increase the reactivity.

## Acknowledgement

Eli Stavitski (Utrecht University, The Netherlands) is acknowledged for designing both the software for acquisition and processing of the UV-Vis micro-spectroscopy measurements.

## References and note

[1] M. H. F. Kox; K. F. Domke; J. P. R. Day; G. Rago; E. Stavitski; M. Bonn; B. M. Weckhuysen *Angew. Chem. Int. Ed.* **2009**, *48*, 8990-8994.
[2] G. Spoto; F. Geobaldo; S. Bordiga; C. Lamberti; D. Scarano; A. Zecchina *Top. Catal.* **1999**, *8*, 279-292.
[3] A. Chica; K. G. Strohmaier; E. Iglesia *Langmuir* **2004**, *20*, 10982-10991.
[4] M. H. F. Kox; A. Mijovilovich; J. J. H. B. Sättler; E. Stavitski; B. M. Weckhuysen *ChemCatChem* **2010**, *2*, 564-571.
[5] F. Geobaldo; G. T. Palomino; S. Bordiga; A. Zecchina; C. O. Areán *Phys. Chem. Chem. Phys.* **1999**, *1*, 561-569.
[6] J. V. Caspar; V. Ramamurthy; D. R. Corbin *J. Am. Chem. Soc.* **1991**, *113*, 600-610.
[7] A. Chica; K. G. Strohmaier; E. Iglesia *Appl. Catal. B. - Environ.* **2005**, *60*, 223-232.
[8] D. Mores; E. Stavitski; M. H. F. Kox; J. Kornatowski; U. Olsbye; B. M. Weckhuysen *Chem. Eur. J.* **2008**, *14*, 11320-11327.
[9] F. L. Cozens; R. Bogdanova; M. Régimbald; H. García; V. Martí; J. C. Scaiano *J. Phys. Chem. B* **1997**, *101*, 6921-6928.
[10] E. Stavitski; M. H. F. Kox; B. M. Weckhuysen *Chem. Eur. J.* **2007**, *13*, 7057-7065.
[11] R. Shafi; G. J. Hutchings *Catal. Today* **2000**, *59*, 423-442.
[12] M. J. Girgis; B. C. Gates *Ind. Eng. Chem. Res.* **1991**, *30*, 2021-2058.
[13] H. Wang; R. Prins *J. Catal.* **2009**, *264*, 31-43.
[14] J. F. Haw; J. B. Nicholas; T. Xu; L. W. Beck; D. B. Ferguson *Acc. Chem. Res.* **1996**, *29*, 259-267.
[15] M. L. Cano; A. Corma; V. Fornés; H. García *J. Phys. Chem.* **1995**, *99*, 4241-4246.
[16] E. Roduner; L.-M. Wu; R. Crockett; C. J. Rhodes *Catal. Lett.* **1992**, *14*, 373-379.
[17] F. R. Chen; J. J. Fripiat *J. Phys. Chem.* **1992**, *96*, 819-823.
[18] H. García; H. D. Roth *Chem. Rev.* **2002**, *102*, 3947-4007.
[19] M. Guisnet; P. Magnoux *Appl. Catal.* **1989**, *54*, 1-27.
[20] *Internal data Albemarle Catalysts*.

# Chapter 7

## Catalytic Activity in Individual Fluid Catalytic Cracking Catalyst Particles Imaged throughout Different Life Stages by Selective Staining


### Abstract

Confocal fluorescence microscopy in combination with the thiophene oligomerization probe reaction has been applied as a tool to study the Brønsted acidity of fresh and laboratory deactivated FCC catalyst particles. The structure of zeolite particulates is visualized for two series of FCC catalyst particles containing zeolite Y. The experiments reveal a gradual reactivity decrease upon deactivation of the catalyst samples. Subsequent addition of the non-reactive bulky dye Nile Blue A, which is too large to enter the zeolitic micropores, allows visualization of the FCC matrix components. Brønsted acidity maps have been constructed at the single particle level from fluorescence microscopy images. By applying a statistical methodology to a series of catalysts deactivated via industrial protocols, a correlation could be established between Brønsted acidity and cracking activity. As a further proof of the validity of our Brønsted acidity mapping method, a comparison was made with results obtained via well-established characterization techniques for structural and acidity evaluation. These techniques lack information at the individual particle level, but trends comparable to our confocal fluorescence microscopy approach have been obtained. To pinpoint the general applicability of the method, the statistical confocal fluorescence microscopy evaluation has been utilized to study an industrial equilibrium catalyst sample. For this sample both *intra*- and *inter*particle heterogeneities, which reflect the large variation in age and activity within such an industrial sample, can be clearly revealed using the statistical confocal fluorescence method.



This work is based on the following manuscript: I. L. C. Buurmans; J. Ruiz-Martínez; W. V. Knowles; D. van der Beek; J. A. Bergwerff; E. T. C. Vogt; B. M. Weckhuysen*, Nature Chem.* **2011**, DOI: 10.1038/NCHEM.1148.

Inge Buurmans and Javier Ruiz-Martínez contributed equally to this work.

## 1. Introduction

As proven in Chapters 3 to 6, the oligomerization reactions of styrene and thiophene can act as suitable probe reactions for the investigation and visualization of Brønsted acidity within individual FCC catalyst particles using micro-spectroscopic approaches. Confocal fluorescence microscopy studies reveal maps of the Brønsted acidic zeolite component within the catalyst particles, which is inhomogeneously distributed throughout the catalyst body. In this chapter the aforementioned approach is applied to provide a direct link between fluorescence intensity / Brønsted acidity at the single particle level and catalytic cracking activity of laboratory deactivated catalyst particles. Furthermore, a statistical analysis is employed for the investigation of an industrial equilibrium catalyst sample in comparison to the laboratory deactivated catalyst materials.

The use of fluorescence microscopy in combination with probe molecules is a powerful tool in life sciences research[1-5] and has recently been introduced in the field of heterogeneous catalysis [6-13], as outlined in Chapter 2. The ability to stain with fluorescent dyes that selectively bind to individual targets in cells and tissues permits the visualization of cellular components and distinct biological events.[14] Inspired by life sciences methods, in this chapter the staining approach was extended to enable the visualization of distinct components within FCC catalyst particles.

## 2. Experimental procedures

Thiophene (Merck, > 99%), Nile Blue chloride (Acros Organics, pure) and pyridine (Acros Organics, 99+%) were used as received. Zeolite H-Y (Si/Al = 5.5, BET surface area = 622 $m^2\ g^{-1}$), silica (BET surface area = 147 $m^2\ g^{-1}$), high-crystalline alumina (BET surface area = 34 $m^2\ g^{-1}$), low-crystalline alumina (BET surface area = 374 $m^2\ g^{-1}$) and clay (BET surface area = 20 $m^2\ g^{-1}$) were provided by Albemarle Corporation. Silica and both types of alumina were dried at 373 K for 30 min. All materials were heat-treated at 723 K for 2 h prior to use to remove any adsorbed species. FCC catalyst particles were provided by Albemarle Corporation as well and used as received. The FCC catalyst batches used were FCC 1 and FCC 2 (both containing zeolite Y), FCC 5 (without zeolite) and an equilibrium catalyst batch. The laboratory deactivation of the two catalyst batches was performed by Albemarle Corporation and is described in the experimental procedures section of Chapter 4. These catalyst samples were used as received. Only the CD-deactivated FCC catalyst and the equilibrium catalyst (Ecat) particles were calcined before use at 973 K for 2 h.

UV-Vis micro-spectroscopic experiments were performed using an *in situ* cell (Linkam Scientific Instruments FTIR 600) equipped with a temperature controller (Linkam Scientific Instruments TMS94) for heating of the samples. More details on the microscopy setup can be found in the experimental procedures section of Chapter 3. All UV-Vis experiments were performed on 50 mg of material, compressed to a pellet at a pressure of 5 ton $cm^{-2}$ on a Perkin-Elmer 15.011 laboratory press. The pellets of FCC components or particles were placed on the heating element of the *in situ* cell and heated to 373 K for 5 min, after which 15 µl of thiophene was added and UV-Vis absorption spectra were taken every 3 s using an acquisition time of 10 ms and averaging the signal 50 times.

Confocal fluorescence experiments were performed using a Nikon Eclipse 90i upright microscope with a 50x 0.55 NA dry objective lens. More details on the setup can be found in the experimental procedures section of Chapter 4. Three Melles Griot laser light sources with emission wavelengths of 488 nm (ion laser, 150 mW); 561 nm (yellow diode-pumped solid-state laser, < 50 mW) and 638 nm (diode laser, 150 mW) were used for excitation. The used emission detection ranges were 500-550 nm; 570-620 nm and 662-737 nm for the 488 nm; 561 nm and 638 nm laser, respectively. Samples for confocal fluorescence microscopy were prepared by placing FCC catalyst particles on the heating element of the *in situ* cell and heating them at 373 K for 5 min. Subsequently, 15 µl of thiophene was added and the heating was stopped after 10 s. Nile Blue A, dissolved in ethanol, was added to the catalyst particles at room temperature.

$N_2$-physisorption isotherms for the separate FCC components were recorded using a Micromeritics Tristar 3000 set-up operating at 77 K. Prior to physisorption measurements, all samples were degassed for 12 h at 573 K in a nitrogen flow. BET surface areas were determined using 10 $P/P_0$ points between 0.06 and 0.25. $N_2$-physisorption isotherms for the FCC catalyst particles were recorded at 77 K using a Micromeritics ASAP 2405. Prior to physisorption measurements, samples were heated in a calcination furnace at 773 K for 3 h (Ecat) or 1 h (all others) followed by vacuum treatment at 573 K until a degas rate < 20 millitorr over 120 s was achieved. BET surface areas were determined using five $P/P_0$ points between 0.06 and 0.22. Micropore volumes ($cm^3\,g^{-1}$) were determined by t-plot analysis for t between 3.3 and 5.4 Å to ensure inclusion of all five minimum required pressure points.

Pyridine adsorption on the FCC catalyst particles was performed by heating 0.5 g of catalyst in a round bottom flask under vacuum ($10^{-3}$ mbar) at 573 K for 2 h. Subsequently, 0.6 mL of pyridine were added to the catalyst through a septum. After pyridine addition the sample was dried at room temperature in air for 3 h, after which the physisorbed pyridine was removed by heating at 363 K for 15 min. Self-supported catalyst

wafers of ground FCC catalyst particles (20 mg) after pyridine adsorption were pressed at a pressure of 5 ton $cm^{-2}$ applied for 3 min. The catalyst wafer was placed inside a holder for transmission IR measurements. FT-IR spectra were recorded on a Perkin-Elmer 2000 FT-IR instrument. For each spectrum 128 scans were recorded with a resolution of 4 $cm^{-1}$.

Ammonia release from the FCC catalyst particles was investigated by temperature-programmed desorption (TPD) under He flow (25 mL $min^{-1}$) using a Micromeritics AutoChem II equipped with a TCD detector. 0.2 g of catalyst was loaded and dried at 873 K for 1 h, after which the sample was cooled down to 373 K. Subsequently, pulses of ammonia were introduced up to saturation of the sample. The temperature-programmed desorption was performed up to 873 K, with a heating ramp of 5 K $min^{-1}$.

X-ray powder diffraction patterns of the ground FCC catalyst particles were acquired using a Bruker-AXS D8 Advance powder X-ray diffractometer. The diffractometer was equipped with an automatic divergence slit, a Våntec-1 detector, and a cobalt K-alpha 1,2 ($\lambda$ = 1.79026 Å) source. Diffraction patterns were collected between 4-70 2θ with an increment of 0.017 (2θ) and an acquisition time of 2 s per step for the fresh, ST and CD samples, and 4 s per step for the MI and Ecat samples. Structureless Le Bail extractions were performed on the measured diffraction patterns (4-20 2θ) using Rietica LHPM package in order to determine the unit cell sizes. The background correction was done using a $5^{th}$ order polynomial. The peak profile parameters were calculated using a Pseudo-Voigt function. A cubic unit cell of space group *Fd3m*, corresponding to an ultrastable dehydrated dealuminated zeolite Y, was used for the initial unit cell size.[15] Calculated unit cell sizes were 24.893 Å (fresh; $R_{wp}$ = 2.1), 24.341 Å (ST; $R_{wp}$ = 1.1) and 24.382 Å (CD; $R_{wp}$ = 1.9) for the FCC 1 sample, and 24.554 Å (fresh; $R_{wp}$ = 9.5), 24.335 Å (ST; $R_{wp}$ = 6.5), 24.307 Å (CD; $R_{wp}$ = 6.3) and 24.147 Å (MI; $R_{wp}$ = 4.6) for the FCC 2 sample. The unit cell was 24.291 Å ($R_{wp}$ = 4.1) for the Ecat sample.

Performance testing of the FCC catalyst particles was conducted on an Imtech Fluid Simulation Test (FST) apparatus. The small-scale single batch cracking unit simulates the product yield of a commercial FCC reactor (without regeneration) by injecting a small sample mass of gas oil into a narrow closed-end cylinder containing a single charge (< 10 g) of fluidized catalyst. After drying in air at 473 K for 1 h, catalysts were transferred into the reactor and fluidized with 30 $cm^3$ $N_2$. A thermocouple embedded in the middle of the fluidized catalyst bed monitors the average bed temperature and is controlled by an electrical clamshell furnace at pseudo-isothermal reactor conditions of 811 K. Kuwait vacuum gas oil feed (20.8 API gravity, 2.8 wt% total sulfur, 1040 ppmwt total nitrogen, 250 ppmwt basic nitrogen, 0.26 wt% Conradson carbon) was injected down flow into the reactor to a fixed axial position of 3.175 mm from the bottom of the 1.6 cm internal diameter reactor at a constant feed rate of

0.2 g $s^{-1}$ for 60 s.

For comparison of activity measurements between catalysts, the ratio of catalyst mass to feed mass (catalyst-to-oil ratio, CTO) was controlled between 3-6 w/w by holding the feed rate constant and varying the catalyst amount, giving catalyst-to-feed contact times in the order of 0.8 s. The catalyst was stripped in $N_2$ afterwards for 1000 s to remove any remaining hydrocarbons before catalyst collection. Reaction products were cooled to 263 K in a glycol bath to condense the heavier compounds before disengagement of gaseous products. Mass recovery of gaseous products was determined by volumetric water displacement and of total liquid products by weighing. Product yield structure determination occurred by gas chromatography: gas products ($H_2$, C1-C6) were measured by an MTI Analytical Instruments QUAD; speciation of the total liquid products occured via simulated distillation (ASTM D-2887) on an Agilent 6890. Carbon deposited on the spent catalyst as a by-product of the cracking process was measured *ex situ* by IR measurements (LECO CS-400) of $CO_2$ generated from combustion.

## 3. Results and discussion

A systematic confocal fluorescence study was designed to differentiate between discrete materials in the FCC catalyst particles. The methodology involves the use of two different dyes, as illustrated in Figure 7.1a. In the first step, the Brønsted acid site catalyzed thiophene oligomerization reaction, which yields fluorescent carbocations[16] was selected to specifically stain the zeolitic particulates. Details on the reaction pathways of the Brønsted acid-catalyzed thiophene oligomerization [17] can be found in the results and discussion section of Chapter 6. The visualization of the carbocationic thiophene products after reaction at 373 K was accomplished by illumination with either a 488 nm or a 561 nm laser, which cause fluorescence of the species that absorb light at those wavelengths. The reaction temperature was set to accurately initiate the thiophene oligomerization reaction and is sufficient to ensure the formation of fluorescent probe molecules on Brønsted acid sites. High reaction temperatures were avoided to prevent side reactions, such as coke formation of the initial thiophene oligomerization products. In Chapter 6 it was indeed shown that coke formation is more pronounced at elevated reaction temperatures. Such side reactions would interfere with the Brønsted acidity mapping for which our method is tailored.

Secondly, by using a non-reactive dye, Nile Blue A, which is too large to enter the zeolite micropores, the FCC matrix can be stained. Nile Blue A shows a high fluorescence when excited with a 638 nm laser. The combined application of thiophene and Nile Blue A reveals *intra*particle

heterogeneities, namely differences in the position and size of zeolitic domains within the matrix of a single FCC particle. This is illustrated in Figures 7.1b to e, which compare two distinct types of FCC particles, namely with and without zeolite Y. For the particle containing zeolite Y, Figures 7.1b and c show highly fluorescent green domains, which can be attributed to the presence of thiophene carbocations. The domains display an average size of 2-5 µm and are heterogeneously distributed over the red-colored FCC matrix. The absence of green fluorescence in Figures 7.1d and e indicates that the particle without zeolite Y has insufficient Brønsted acid strength to promote carbocationic thiophene product formation.

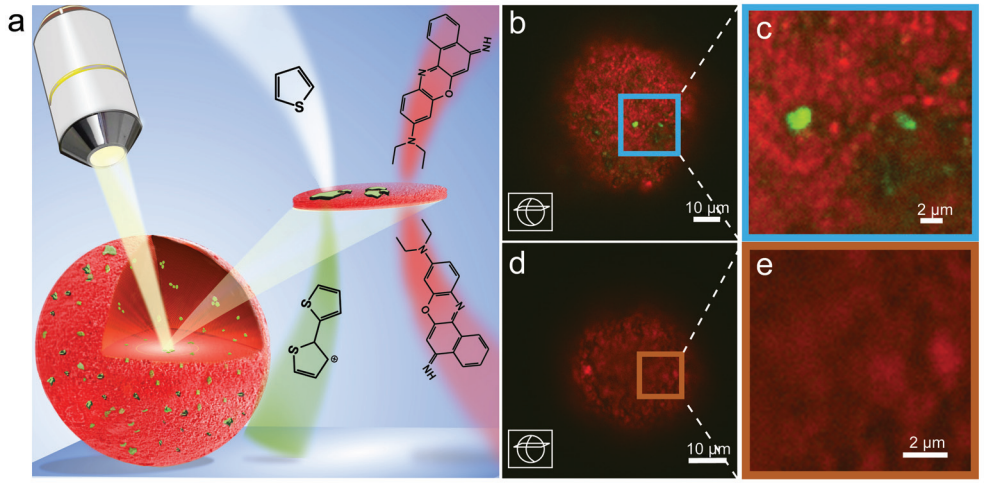


**Figure 7.1. (a)** Schematic representation of the research approach, in which confocal fluorescence microscopy is used to visualize distinct components of FCC catalyst particles after staining with two different probe molecules. **(b)** Confocal fluorescence microscopy image of an FCC catalyst particle containing zeolite Y and **(d)** Confocal fluorescence microscopy image of an FCC catalyst particle without zeolite component upon reaction with thiophene (green) at 373 K ($\lambda_{ex}$ = 488 nm, detection 500-550 nm) and subsequent staining with Nile Blue A (red) at 298 K ($\lambda_{ex}$ = 638 nm, detection 662-737 nm). Fluorescence intensities were all boosted with the same factor. Insertions **(c)** and **(e)** are magnifications of the highlighted areas.

The assumption that the thiophene reaction only occurs in the zeolite Y domains was confirmed in Chapter 6 using a detailed UV-Vis micro-spectroscopy study. In the UV-Vis spectra of zeolite H-Y, clear absorption bands attributed to the formation of thiophene carbocations are observed. Within the matrix, none of the components displayed activity towards the formation of light absorbing species.

Two batches of FCC catalysts, containing the same zeolite Y but manufactured in different catalyst production plants (further denoted as samples FCC 1 and FCC 2), were also studied using UV-Vis micro-spectroscopy, as depicted in Figure 7.2. In addition, they were compared

to an FCC catalyst sample in which the zeolitic part was replaced by clay (FCC 5). The results clearly show that the FCC catalyst particles without zeolite are inert to the formation of Brønsted acid-catalyzed thiophene products and no absorption bands are observed. In contrast, absorption bands arise in the spectra of zeolite-containing FCC particles, corresponding to products formed by the zeolitic domains. Comparable results are also described in Chapter 6 for a different batch of FCC catalyst particles containing zeolite Y.

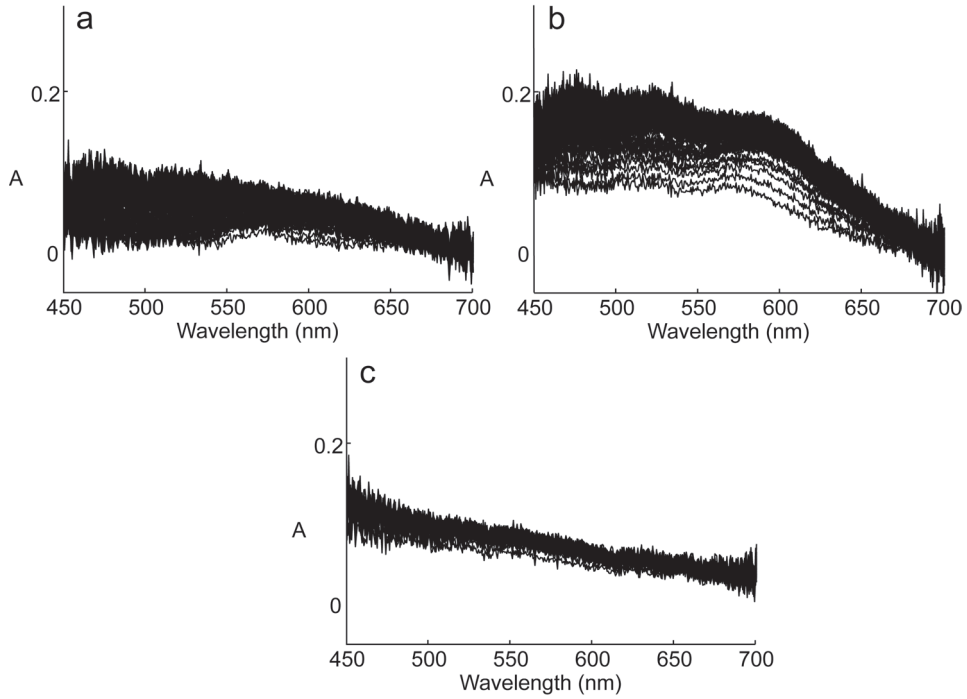


**Figure 7.2.** Examples of the evolution of the UV-Vis absorption bands in time for **(a)** FCC 1 (containing zeolite Y); **(b)** FCC 2 (containing zeolite Y) and **(c)** FCC 5 (without zeolite) upon exposure to thiophene at 373 K.

Owing to the successful visualization of the zeolite domains within the FCC particles, a 3D reconstruction of the fluorescence intensity is obtained. Since fluorescent products are formed at Brønsted acid sites only, such an image reveals a 3D-map of the Brønsted acidity within the catalyst body. It is known that deactivation in the cracking process is strongly linked to the loss of Brønsted acidity.[18-22] This opens the possibility of visualizing Brønsted acidity changes after different deactivation procedures using the thiophene probe reaction. For this purpose, the two catalyst batches under study, FCC 1 and FCC 2, were used as prepared (fresh) and after three industrially relevant deactivation methods: steaming (ST),[23] two-step

cyclic deactivation (CD)[24-25] and Mitchell impregnation-steam deactivation (MI).[26] These industrial laboratory protocols attempt to mimic catalyst behavior in an industrial cracking unit in terms of deactivation by coke formation, metals deposition and/or hydrothermal ageing. More details regarding the deactivation methods can be found in the experimental procedures section of Chapter 4. Fluorescence was detected in the 570-620 nm wavelength range after excitation with a 561 nm laser. When the fluorescence intensities of the different FCC 1 catalyst samples upon exposure to thiophene were studied, it is evident from Figure 7.3 that less fluorescence is detected for deactivated catalyst samples following the trend: fresh > ST > CD > MI. Since sufficiently strong Brønsted acid sites are needed for the formation of fluorescent carbocations, this means that the amount of strong acid sites has decreased upon deactivation. The same sequence in fluorescence intensity has been measured for the FCC 2 catalyst batch, as depicted in Figure 7.4.

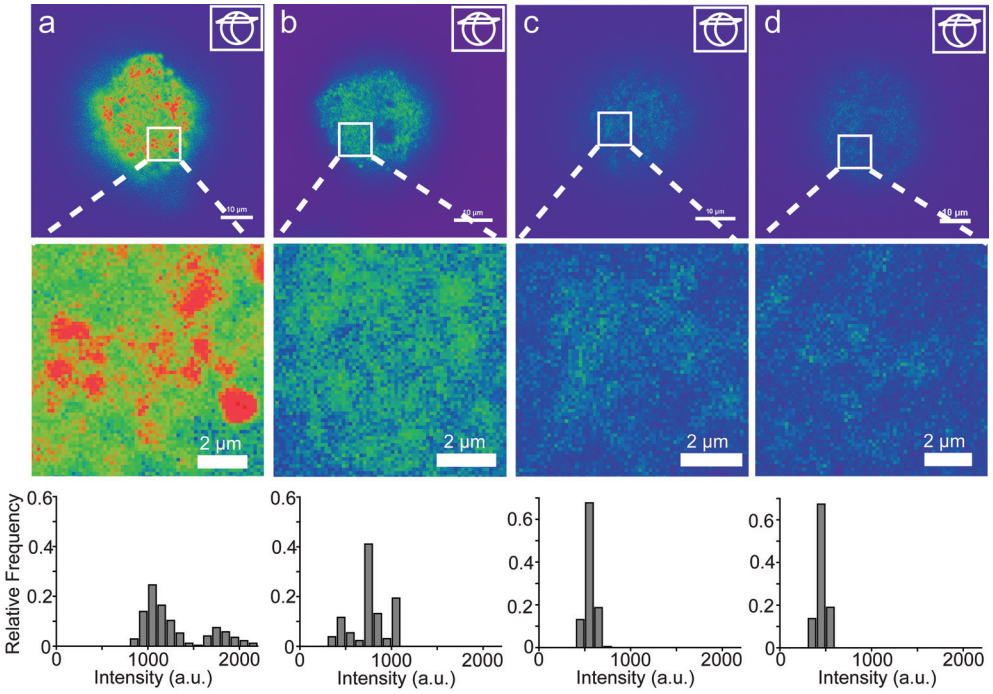


**Figure 7.3. (top)** Confocal fluorescence microscopy images of individual FCC 1 catalyst particles after reaction with thiophene at 373 K ($\lambda_{ex}$ = 561 nm, detection 570-620 nm, false color images, intensities all boosted with the same factor) in different stages of deactivation: **(a)** fresh; **(b)** steamed; **(c)** two-step cyclic deactivated and **(d)** Mitchell impregnated-steam deactivated. **(middle)** Magnifications of the highlighted areas disclose zeolitic domains in the micron size range with decreasing intensity upon deactivation. **(bottom)** Fluorescence intensity histograms as determined for the zeolite domains in the four different samples.

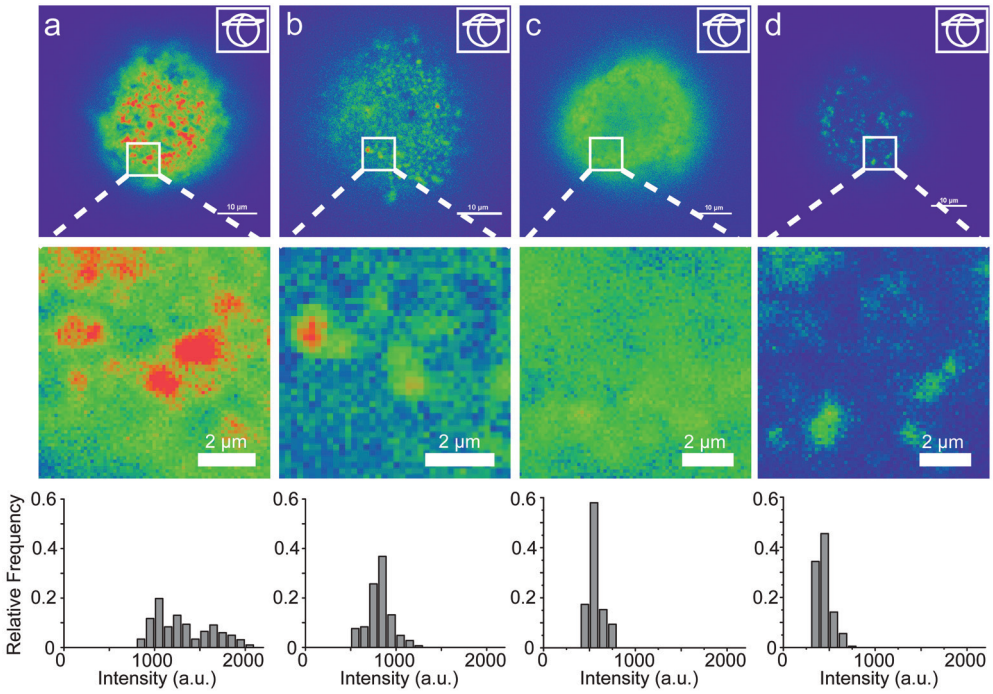


**Figure 7.4. (top)** Confocal fluorescence microscopy images of individual FCC 2 catalyst particles after reaction with thiophene at 373 K ($\lambda_{ex}$ = 561 nm, detection 570-620 nm, false color images, intensities all boosted with the same factor) in different stages of deactivation: **(a)** fresh; **(b)** steamed; **(c)** two-step cyclic deactivated and **(d)** Mitchell impregnated-steam deactivated. **(middle)** Magnifications of the highlighted areas disclose zeolitic domains in the micron size range with decreasing intensity upon deactivation. **(bottom)** Fluorescence intensity histograms as determined for the zeolite domains in the four different samples.

It is important to mention that deactivation can also influence the accessibility of the catalyst matrix towards probe molecules. In order to rule out this factor as the main cause for the fluorescence intensity changes, all samples were investigated with confocal fluorescence microscopy after addition of Nile Blue A. The distribution of Nile Blue A, as shown in Figure 7.5, is comparable for all investigated samples. This finding confirms that the catalyst particles are still accessible towards probe molecules in the used size range after deactivation.

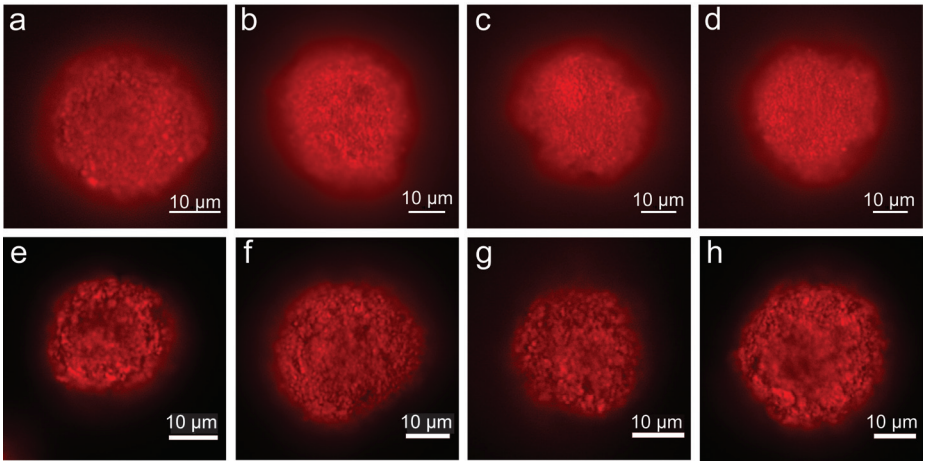


**Figure 7.5.** Confocal fluorescence microscopy images of **(top)** FCC 1 and **(bottom)** FCC 2 catalyst particles in their **(a** and **e)** fresh; **(b** and **f)** steamed; **(c** and **g)** two-step cyclic deactivated and **(d** and **h)** Mitchell impregnated-steam deactivated state after staining with Nile Blue A at room temperature ($\lambda_{ex}$ = 638 nm, detection 662-737 nm).

The fluorescent signal of the different samples upon reaction with thiophene was studied in detail by performing a statistical analysis of six to eight catalyst particles per sample. A more quantitative insight into the fluorescence intensities was acquired, as the average fluorescence intensity of all zeolite spots within the population was calculated. To resolve the *intra*particle heterogeneity, a fluorescence intensity threshold was set to remove the FCC matrix fluorescence and the residual fluorescence of zeolite particles in close proximity. Domains that are too close together cannot be resolved with fluorescence microscopy. This phenomenon is well-described in literature for the field of fluorescence imaging of nanoscopic events.[27-28] The threshold setting was done in a similar way as described for the styrene oligomerization analysis in Chapter 4. Again all fluorescent areas smaller than 1 µm$^2$ were rejected, because over 90% of the zeolitic domains is expected to be larger than this value.[29-30] An averaged intensity of at least 150 zeolite spots in different catalyst particles was determined for every sample.

The fluorescence intensity histograms, showing a population distribution with a clear maximum for all samples (Figures 7.3 and 7.4, bottom), were used to determine the average fluorescence intensities for the different samples. The results of this analysis are given in Figure 7.6a and indicate a decrease in Brønsted acidity upon deactivation. To validate our method, a parallel statistical evaluation was performed. In this analysis the mean fluorescence intensity per individual FCC particle was used to determine the average fluorescence intensity of the sample. The results of this approach are summarized in Figure 7.6b and show

comparable fluorescence intensity values, which follow the same trends as those described in Figure 7.6a. The only difference is that the standard errors are significantly larger due to the smaller amount of data points (n = 6 particles vs. n = 150 domains).

By comparing the fluorescence intensity values of the FCC 1 and FCC 2 catalyst batches depicted in Figures 7.6a and b, the reliability of the analysis method was tested. The fluorescence images and average fluorescence intensities of both catalyst batches reveal the same trend in average fluorescence intensity decrease. The average fluorescence intensity values across the two catalyst types display a maximum difference of 7 %. These observations indicate that our characterization method is very valuable for comparing and evaluating different types of FCC catalyst particles that have experienced distinct deactivation protocols.

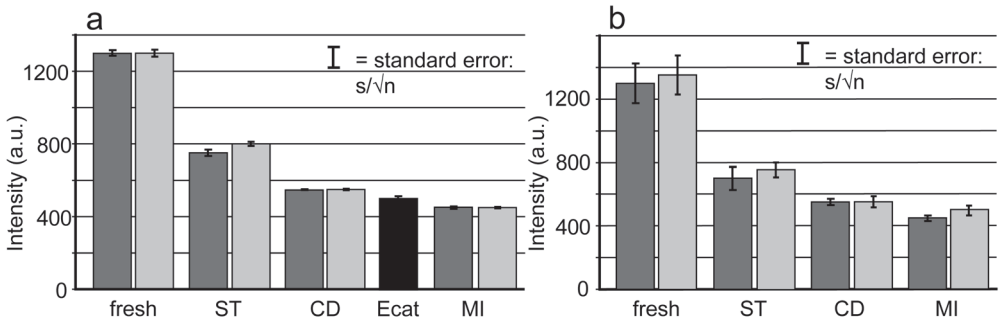


**Figure 7.6. (a)** Fluorescence mean intensities and their corresponding standard errors, as determined from the statistical analysis of at least 150 zeolitic domains in the confocal fluorescence measurements of FCC catalyst particles: FCC 1 (dark gray), FCC 2 (light gray) and Ecat (black). **(b)** Alternative calculation of the fluorescence mean intensities of the FCC 1 (dark gray) and FCC 2 (light gray) populations. The averages are obtained by first averaging all fluorescent (zeolite) domains above the threshold intensity value and larger than 1 $\mu m^2$ within one FCC catalyst particle. Afterwards, the average fluorescence intensity values obtained for six to eight FCC catalyst particles were averaged and the standard errors were determined.

The question now arises whether mapping of the Brønsted acidity within FCC catalyst particles can be linked to catalytic cracking reactivity. To investigate this issue, a comparison was made between the Brønsted acidity data deduced from the confocal fluorescence microscopy measurements and cracking activity data obtained in laboratory Fluid Simulation Tests (FST) on the different deactivated catalysts for the conversion of vacuum gas oil (VGO). Due to its high activity, the fresh catalyst could not be tested in such an approach. The obtained structure-performance relationship is illustrated in Figures 7.7 and 7.8 for the FCC 1 and FCC 2 catalyst materials, respectively.

The deactivated catalyst materials spanned a range of activities.

The ST samples, treated under harsh hydrothermal conditions, were the most active. The CD catalysts, subjected to mild hydrothermal deactivation *in tandem* with metals and coke deposition during cyclic VGO cracking and regeneration, were slightly less active. The MI samples, exposed to moderate hydrothermal conditions after metals impregnation, showed the lowest conversion. The metals used for CD and MI protocols, nickel and vanadium, promote catalyst deactivation primarily through coke formation and Brønsted acid site destruction. Nominal metal concentrations were kept uniform between CD and MI samples. Therefore, dissimilar conversions between the samples, as reflected in a significantly higher coke formation for the MI samples (Figure 7.9), hint at fundamental differences in the chemical nature and impact of these metals on the overall catalyst. Both the catalytic activity (Figures 7.7a and 7.8a) and the selectivity towards gasoline, the desired product (Figures 7.7b and 7.8b), is diminished as a consequence of catalyst deactivation.

When the cracking activity data are compared to the Brønsted acidity changes monitored with our statistical confocal fluorescence analysis, the same trend is observed, illustrating a decreasing cracking activity and Brønsted acidity with increasing deactivation severity. Since the deactivation techniques employed cause partial loss of the number of Brønsted acid sites and changes in the overall structure of the zeolite, one expects that the effective amount of active sites available for cracking reactions also decreases. This decrease can be investigated in fine detail using our statistical confocal fluorescence microscopy approach, which greatly helps to explain the observed activity differences in the cracking tests.

To corroborate our approach, additional bulk characterization of the FCC catalyst particles was performed. For this purpose, a selection of the methods listed in Table 1.1 of Chapter 1 (page 17) has been applied to investigate the ensemble properties of the FCC catalyst samples. More specifically, nitrogen physisorption, IR spectroscopy after pyridine adsorption, temperature-programmed desorption of ammonia and X-ray powder diffraction studies were conducted. The results, as summarized in Figures 7.7c to f and 7.8c to f, clearly confirm our confocal fluorescence microscopy data and the observed acidity trends. Nitrogen physisorption shows a significant loss of micropore volume across samples, which can be explained by a partial destruction of the zeolite within the catalyst (Figures 7.7c and 7.8c). From literature it is known that the cracking activity decreases upon loss of zeolite structure.[31-32] Pyridine adsorption followed by IR spectroscopy is a well-established technique to reveal acidity in solid materials.[33] As shown in Figures 7.7d and 7.8d, the IR spectroscopy measurements performed on the FCC catalyst particles reveal a gradual decrease in the Brønsted acidity upon deactivation. Temperature-programmed desorption (TPD) of ammonia, depicted in

Figures 7.7e and 7.8e, reveals an analogous decrease in the overall acidity (total area below the curves), with a loss of strong acidity (peak at 650 K) for the deactivated samples. X-ray powder diffraction (XRD) patterns (Figures 7.7f and 7.8f) of the FCC catalyst materials indicate a loss in the crystallinity for the deactivated samples, as clearly seen from the increased background contribution. A Le Bail extraction of the measured XRD patterns reveals a decrease in unit cell size upon deactivation, which is indicative of a loss of framework aluminum atoms from the zeolite. As a consequence the quantity of Brønsted acid sites is diminished. The calculated unit cell sizes for the different samples are listed in the experimental procedures section.

All obtained results show that the confocal fluorescence microscopy approach is very useful in assessing Brønsted acidity upon different deactivation stages and forms a bridge with the catalytic activity. The samples studied so far have been deactivated and tested under controlled laboratory conditions to mimic their behavior in a real FCC unit. As a showcase, the same approach was applied to an equilibrium catalyst (Ecat) taken from a commercial FCC unit. As described in Chapter 1, due to constant deactivation in the refiner's FCC unit, degrading catalyst activity is compensated by the continual addition of fresh catalyst to maintain stable activity levels. The resulting Ecat is a mixture of particles with different residence time histories, which therefore display diverse activity levels. Bulk characterization techniques, shown in Figure 7.7, provide average information about the Ecat behavior and indicate that the Ecat cracking activity level is in between the activity of the CD and MI samples. This is in good agreement with the acidity trends obtained with pyridine IR spectroscopy and ammonia TPD. The XRD pattern of the Ecat indicates that a significant amount of crystallinity is preserved during the FCC process. A decrease in unit cell size compared to the CD sample illustrates a lower amount of framework aluminum.

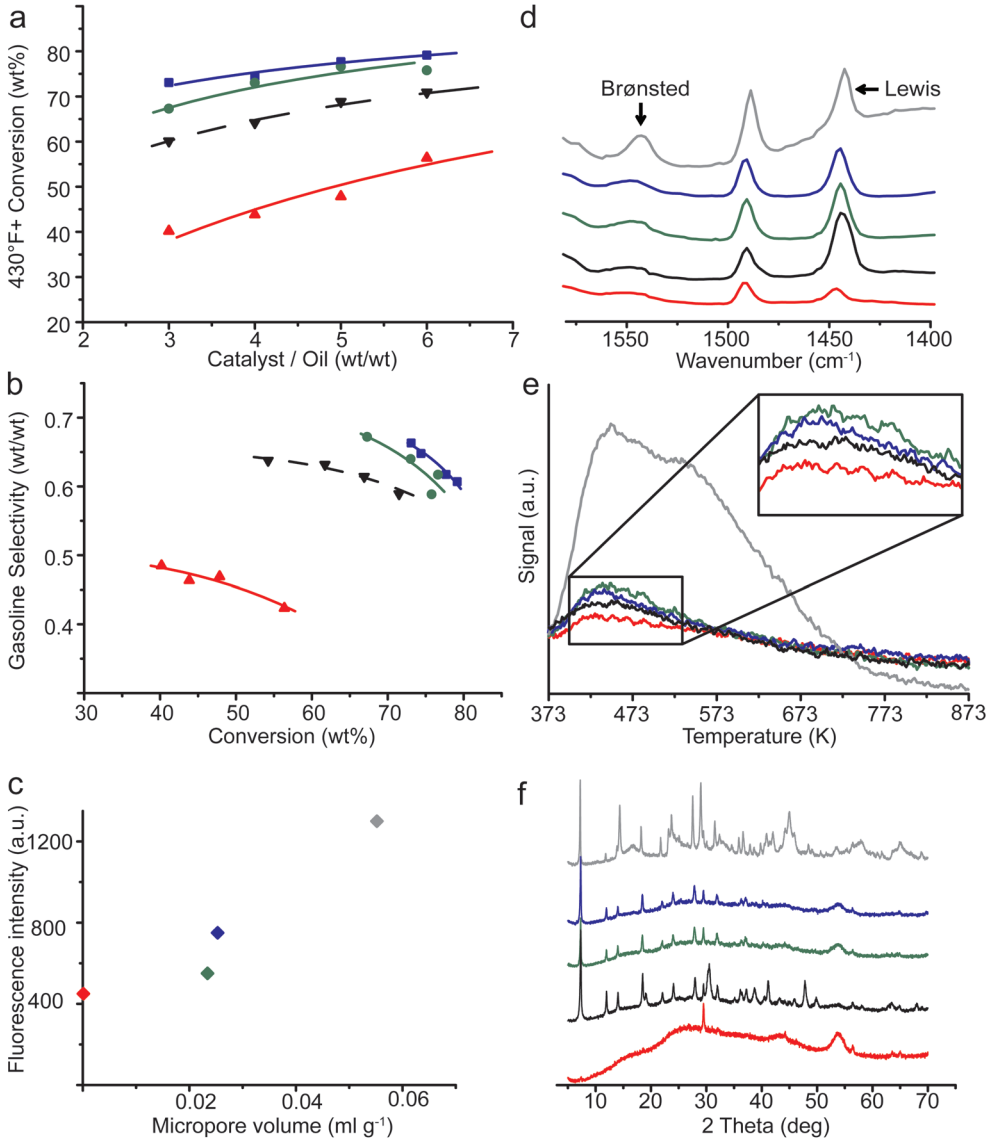


**Figure 7.7.** Bulk characterization techniques for the FCC 1 catalyst particles in their fresh (gray), steamed (blue), two-step cyclic deactivated (green) and Mitchell impregnated-steam deactivated (red) state. Black represents the performance of the equilibrium catalyst. **(a)** Activity data; **(b)** gasoline selectivity; **(c)** average fluorescence intensity values, obtained from thiophene oligomerization on the catalyst particles as a function of the micropore volume determined by nitrogen physisorption; **(d)** transmission IR-spectra after pyridine adsorption. The vibrations due to adsorption of pyridine on both Brønsted and Lewis acid sites within the catalyst samples are visible; **(e)** temperature-programmed desorption plots of ammonia and **(f)** X-ray diffraction powder patterns.

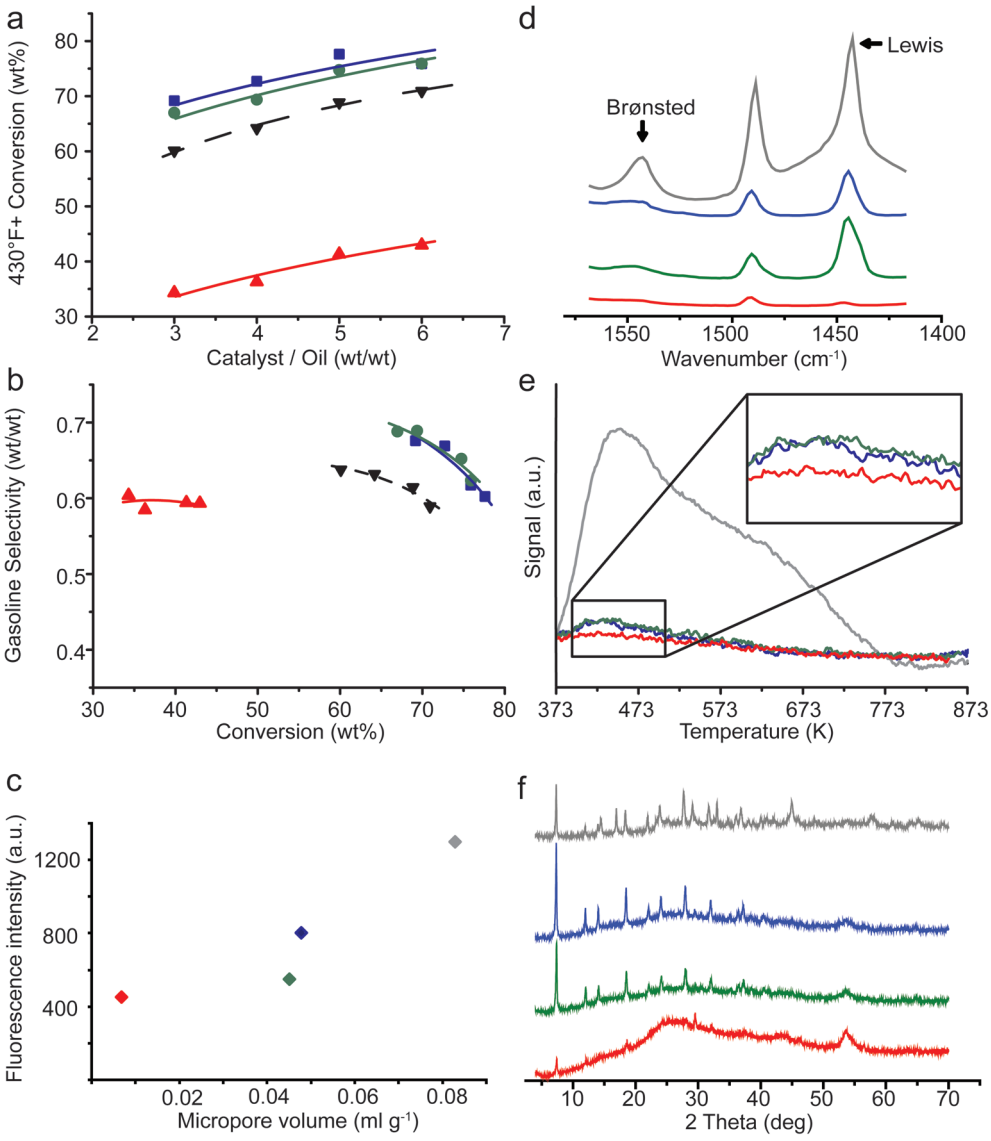


**Figure 7.8.** Bulk characterization techniques for the FCC 2 catalyst particles in their fresh (gray), steamed (blue), two-step cyclic deactivated (green) and Mitchell impregnated-steam deactivated (red) state. Black represents the performance of the equilibrium catalyst. **(a)** Activity data; **(b)** gasoline selectivity; **(c)** average fluorescence intensity values, obtained from thiophene oligomerization on the catalyst particles as a function of the micropore volume determined by nitrogen physisorption; **(d)** transmission IR-spectra after pyridine adsorption. The vibrations due to adsorption of pyridine on both Brønsted and Lewis acid sites within the catalyst samples are visible; **(e)** temperature-programmed desorption plots of ammonia and **(f)** X-ray diffraction powder patterns.

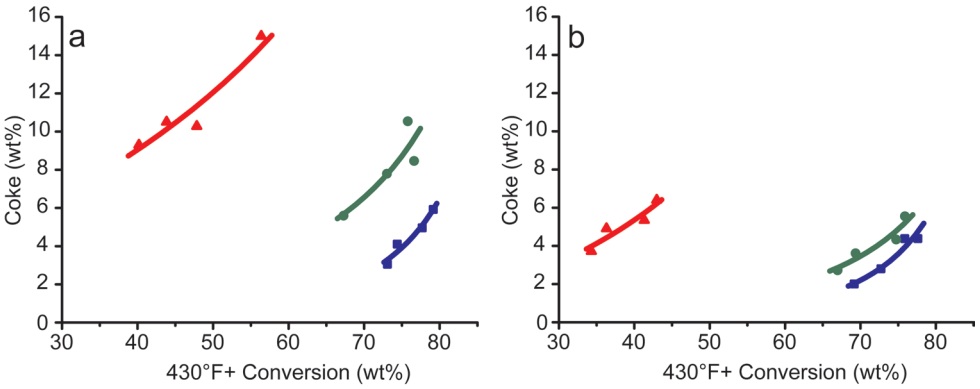


**Figure 7.9.** Coke selectivity of **(a)** FCC 1 and **(b)** FCC 2 catalyst particles in their steamed (blue), two-step cyclic deactivated (green) and Mitchell impregnated-steam deactivated (red) state.

The average fluorescence intensities obtained with our method (Figure 7.6) predicts the Brønsted acidity and thus the cracking activity of the Ecat, which is indeed in between those of CD and MI samples (Figure 7.7a). This analysis confirms the Brønsted acidity trends as obtained with the bulk characterization techniques. These bulk characterization methods, however, lack an important part of the information, since they average the individual contributions of catalyst particles, resulting in an overall value of, for example, catalyst performance and Brønsted acidity. It is here that the real strength of the newly developed approach becomes evident. This is illustrated in Figure 7.10, which summarizes the average fluorescence intensities for seven individual FCC 1 catalyst particles in their fresh state and as a function of the different deactivation protocols (ST, CD and MI). It can be observed that even in the fresh FCC catalyst particles a wide range of fluorescence intensities is present, indicating that the catalyst particles already differ in their Brønsted acidity directly after preparation. Possible explanations could be either that the amount of zeolite domains within each FCC catalyst particle is different or that the zeolitic material, from which the FCC catalyst particles are composed, possesses intrinsic heterogeneities in its Brønsted acid sites. A steam deactivation protocol decreases the average fluorescence intensities of the seven catalyst particles and the variation of the fluorescence intensities is less pronounced than in the case of the fresh catalyst. Both the shift to lower average fluorescence intensity and the decrease in variance further proceed when considering the CD and MI catalyst particles. Seemingly, harsher deactivation protocols lead to the creation of a more uniform batch of catalyst particles in terms of Brønsted acidity.

Interestingly, the developed approach allows one to assess the

Brønsted acidity of individual FCC particles in the Ecat batch as well. Figure 7.10 reveals that the range of fluorescence intensities observed for the Ecat sample covers a wider range than those of CD and MI combined, reflecting a larger *inter*particle heterogeneity in terms of age and acidity within an industrial Ecat. One might wonder why the Ecat sample, which is a mixture of fresh and aged catalyst particles, does not seem to contain one or more FCC particles with an average fluorescence intensity approaching that of the fresh catalyst sample. The reason is that fresh FCC particles are directly fed into the regenerator, resulting in an immediate lowering of their Brønsted acidity due to the exposure to steam in the regenerator. In other words, part of the Ecat sample should display more resemblance to the ST sample than to the fresh catalyst material. Summarizing, the results in Figure 7.10 clearly show the added value of analyzing catalyst batches at the individual particle level.

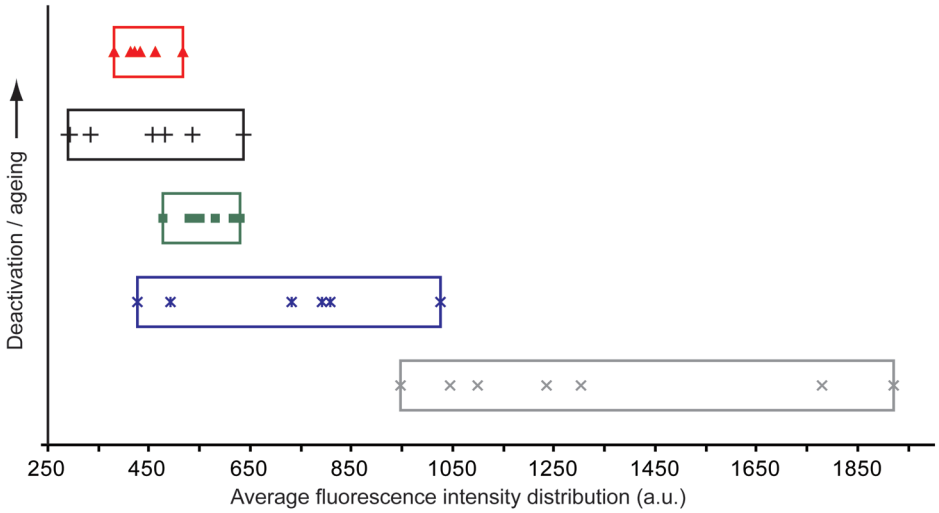


**Figure 7.10.** Average fluorescence intensity ranges that cover the intensities of all seven individual FCC 1 catalyst particles in their fresh (gray); steamed (blue); two-step cyclic deactivated (green) and Mitchell impregnated-steam deactivated (red) state. Black represents the average fluorescence intensities as determined for the seven Ecat particles.

## 4. Conclusions

Confocal fluorescence microscopy allows the visualization of specific catalyst components within individual FCC catalyst particles by selective staining, particularly the active zeolitic phase. Thiophene oligomerization, a Brønsted acid-catalyzed reaction, has proven to be the bridge necessary to translate confocal fluorescence microscopy images into Brønsted acidity

maps. The novel characterization method shows sensitivity towards different industrially relevant deactivation protocols and can serve as a powerful tool in the effort to develop enhanced laboratory deactivation procedures that even more closely simulate commercial practice. Proper statistical analysis of the confocal fluorescence microscopy data has led to a direct link between fluorescence intensity / Brønsted acidity at the single particle level and catalytic cracking activity of laboratory deactivated bulk catalysts. Furthermore, our method can determine the age distribution of a catalyst employed in a real FCC unit in terms of *inter*particle Brønsted acidity differences.

## Acknowledgements

The following people are acknowledged: Fouad Soulimani (Utrecht University, The Netherlands) for help with the IR measurements, Marjan Versluijs-Helder (Utrecht University, The Netherlands) for the XRD measurements, Upakul Deka (Utrecht University, The Netherlands) for the calculations of the unit cell sizes, Eli Stavitski (Utrecht University, The Netherlands) for the design of both the software for acquisition and processing of the UV-Vis spectroscopy measurements, Julie Francis (Albemarle Corporation, United States of America) for fruitful discussions and Agnieszka Ruppert (Technical University Lodz, Poland) for the design of Figure 7.1.

## References and note

[1] J. Zhang; R. E. Campbell; A. Y. Ting; R. Y. Tsien *Nature Rev. Mol. Cell Biol.* **2002**, *3*, 906-918.
[2] P. O. Krutzik; G. P. Nolan *Nat. Methods* **2006**, *3*, 361-368.
[3] B. R. Martin; B. N. G. Giepmans; S. R. Adams; R. Y. Tsien *Nat. Biotechnol.* **2005**, *23*, 1308-1314.
[4] J. Rajagopal; W. J. Anderson; S. Kume; O. I. Martinez; D. A. Melton *Science* **2003**, *299*, 363.
[5] Z. Darzynkiewicz; E. Bedner; X. Li; W. Gorczyca; M. R. Melamed *Exp. Cell Res.* **1999**, *249*, 1-12.
[6] L. Karwacki; M. H. F. Kox; D. A. M. de Winter; M. R. Drury; J. D. Meeldijk; E. Stavitski; W. Schmidt; M. Mertens; P. Cubillas; N. John; A. Chan; N. Kahn; S. R. Bare; M. Anderson; J. Kornatowski; B. M. Weckhuysen *Nature Mater.* **2009**, *8*, 959-965.
[7] M. B. J. Roeffaers; B. F. Sels; H. Uji-i; F. C. De Schryver; P. A. Jacobs; D. E. De Vos; J. Hofkens *Nature* **2006**, *439*, 572-575.
[8] W. Xu; J. S. Kong; Y. T. E. Yeh; P. Chen *Nature Mater.* **2008**, *7*, 992-996.
[9] K. Naito; T. Tachikawa; M. Fujitsuka; T. Majima *J. Am. Chem. Soc.* **2009**, *131*, 934-936.
[10] G. De Cremer; B. F. Sels; D. E. De Vos; J. Hofkens; M. B. J. Roeffaers *Chem. Soc. Rev.* **2010**, *39*, 4703-4717.
[11] P. Chen; X. Zhou; H. Shen; N. M. Andoy; E. Choudhary; K.-S. Han; G. Liu; W. Meng *Chem. Soc. Rev.* **2010**, *39*, 4560-4570.

[12] T. Tachikawa; T. Majima *Chem. Soc. Rev.* **2010**, *39*, 4802-4819.
[13] B. M. Weckhuysen *Angew. Chem. Int. Ed.* **2009**, *48*, 4910-4943.
[14] W. Denk; J. H. Strickler; W. W. Webb *Science* **1990**, *248*, 73-76.
[15] J. B. Parise; D. R. Corbin; L. Abrams; D. E. Cox *Acta Crystallogr.* **1984**, *C40*, 1493-1497.
[16] M. H. F. Kox; A. Mijovilovich; J. J. H. B. Sättler; E. Stavitski; B. M. Weckhuysen *ChemCatChem* **2010**, *2*, 564-571.
[17] M. H. F. Kox; K. F. Domke; J. P. R. Day; G. Rago; E. Stavitski; M. Bonn; B. M. Weckhuysen *Angew. Chem. Int. Ed.* **2009**, *48*, 8990-8994.
[18] R. von Balmoos; D. H. Harris; J. S. Magee In *Handbook of Heterogeneous Catalysis*; 1st ed.; G. Ertl, H. Knözinger, J. Weitkamp, Eds.; Wiley-VCH: Weinheim **1997**; *4*, 1955-1983.
[19] W. Vermeiren; J.-P. Gilson *Top. Catal.* **2009**, *52*, 1131-1161.
[20] M. Rigutto In *Zeolites and Catalysis: Synthesis, Reactions and Applications*; 1st ed.; J. Čejka, A. Corma, S. I. Zones, Eds.; Wiley-VCH: Weinheim **2010**; *2*, 547-584.
[21] J. M. Newsam *Science* **1986**, *231*, 1093-1099.
[22] A. Corma *Chem. Rev.* **1995**, *95*, 559-614.
[23] E. Rautiainen; R. Pimenta; M. Ludvig; C. Pouwels *Catal. Today* **2009**, *140*, 179-186.
[24] M. Bendiksen; E. Tangstad; T. Myrstad *Appl. Catal. A. - Gen.* **1995**, *129*, 21-31.
[25] A. C. Psarras; E. F. Iliopoulou; K. Kostaras; A. A. Lappas; C. Pouwels *Microporous Mesoporous Mater.* **2009**, *120*, 141-146.
[26] B. R. Mitchell *Ind. Eng. Chem. Prod. Res. Dev.* **1980**, *19*, 209-213.
[27] M. J. Rust; M. Bates; X. Zhuang *Nat. Methods* **2006**, *3*, 793-795.
[28] E. Betzig; J. K. Trautman *Science* **1992**, *257*, 189-195.
[29] *Internal data Albemarle Catalysts*.
[30] S. Bhatia *Catalytic Applications of Zeolites in Industrial Processes* CRC Press, Inc.: Boca Raton **1989**.
[31] N. Y. Chen; T. O. Mitchell; D. H. Olson; B. P. Pelrine *Ind. Eng. Chem. Prod. Res. Dev.* **1977**, *16*, 247-252.
[32] D. Chen; S. Sharma; N. Cardona-Martinez; J. A. Dumesic; V. A. Bell; G. D. Hodge; R. J. Madon *J. Catal.* **1992**, *136*, 392-402.
[33] W. E. Farneth; R. J. Gorte *Chem. Rev.* **1995**, *95*, 615-635.

# Chapter 8

## Structure and Acidity of Individual Fluid Catalytic Cracking Catalyst Particles Studied by Synchrotron-Based Infrared Micro-Spectroscopy


### Abstract

A synchrotron-based infrared micro-spectroscopy study has been conducted to investigate the structure as well as the Brønsted and Lewis acidity of FCC catalyst particles at the individual particle level. Both fresh and laboratory deactivated catalyst particles, as well as an equilibrium catalyst taken from an industrial cracking unit have been studied. From the infrared spectra of the fresh and laboratory deactivated samples it was clear that the zeolite component experiences partial collapse upon deactivation. Furthermore, it was found that characteristic bands, caused by the presence of clay material, are lost upon deactivation. Previously conducted bulk transmission infrared measurements after pyridine adsorption already indicated a loss of Brønsted and Lewis acidity upon deactivation. Furthermore, the equilibrium catalyst was found to display an acidity in between those of the laboratory deactivated samples. The study described in this chapter reveals the same acidity trends, but additionally provides information about the distribution of the Brønsted and Lewis acidity within individual catalyst particles, revealing a larger variety in Brønsted acidity for the equilibrium catalyst material. This observation can be attributed to the wide age distribution within industrial equilibrium catalysts and directly shows the added value of micro-spectroscopy approaches in the investigation of *inter*particle heterogeneities.



This work is based on the following manuscript: I. L. C. Buurmans, F. Soulimani, J. Ruiz-Martínez, H. E. van der Bij and B. M. Weckhuysen, *submitted for publication*.


Inge Buurmans and Fouad Soulimani contributed equally to this work.

## 1. Introduction

The micro-spectroscopic studies in combination with suitable probe reactions described in Chapters 4 to 7 all aim to monitor the Brønsted acidity of FCC catalyst materials at the individual particle level. Since acidity is such an important property of catalytic materials for a wide variety of reactions, a large range of bulk techniques for the characterization of acidity is available.[1-14] These approaches have been described in more detail in the introduction of Chapter 3.

A very useful development for the investigation of Brønsted and Lewis acidity in catalytic materials is the application of synchrotron-based IR micro-spectroscopy in combination with pyridine adsorption. Pyridine adsorption is frequently used for acidity studies, since the interaction with both types of acid sites gives rise to different C-C stretch vibration frequencies.[15-16] IR light from a synchrotron source is about 100-1000 times brighter compared to a conventional IR source, thus allowing the use of a smaller aperture in order to obtain spatial information of the catalyst samples under investigation.[17-19] Furthermore, the brightness of the IR light is sufficient to enable measurements in transmission mode, which facilitates the investigation of the acidity of the full internal volume of catalyst bodies, instead of obtaining only information about the acidity of the external surface of such materials.

In this chapter the structure and acidity of individual fresh and laboratory deactivated catalyst particles as well as equilibrium catalyst (Ecat) particles is examined using synchrotron-based IR micro-spectroscopy. This approach allows an evaluation of structural changes of individual FCC catalyst particles upon deactivation. By infrared microscopy measurements after pyridine adsorption, an assessment of the Brønsted and Lewis acidity at the individual particle level within the different catalyst batches is enabled. Furthermore, the study provides a validation of the results obtained in Chapters 4 to 7.

## 2. Experimental procedures

Pyridine (Acros Organics, 99+%, for spectroscopy) was used as received. FCC catalyst particles were provided by Albemarle Corporation and used as received. The FCC catalyst batches used were FCC 2 (containing zeolite Y) and a second Ecat batch. Only the two-step cyclic deactivated (CD) and Ecat sample were calcined before use at 973 K for 2 h. The laboratory deactivation procedures of the catalyst material were performed by Albemarle Corporation and are described in the experimental procedures section of Chapter 4. Pyridine adsorption on the FCC catalyst particles was performed as described in the experimental procedures section of

Chapter 7. The bulk infrared measurements described in this chapter are the ones previously reported in Chapter 7.

Fourier transform infrared (FT-IR) microscopy experiments of individual catalyst particles were performed at beamline U10B at the National Synchrotron Light Source of Brookhaven National Laboratory (Upton, NY, United States). A Thermo Nicolet Continuμm IR microscope with a 32x Schwarzschild objective, connected to a Thermo Nicolet Magna 860 FT-IR spectrometer equipped with an MCT-detector was used. Synchrotron-IR light was used as the infrared light source. The FCC catalyst particles with and without adsorbed pyridine were placed on a 1 mm thick $CaF_2$ slide and IR spectra were collected in transmission mode in the 4000-1000 $cm^{-1}$ wavenumber range with a spectral resolution of 4 $cm^{-1}$. An IR beam (aperture) size of 20 x 20 μm was used and 128 scans per spectrum were taken. The average particle size of all particles under study was 75 μm.

Peak areas of the Brønsted and Lewis acid site vibrations were determined in the 1560-1531 $cm^{-1}$ and 1452-1434 $cm^{-1}$ range, respectively. Integrals were calculated for the baseline corrected spectra using the Perkin-Elmer Spectrum software.

## 3. Results and discussion

Transmission synchrotron-based IR spectra of a representative set of individual FCC catalyst particles in the spectral range 4000-1100 $cm^{-1}$ are shown in Figure 8.1. It is clear that the spectra have a complex band structure and in view of the characteristic hydroxyl region of the different components (clay, zeolite Y, alumina and silica) present in the catalyst particles the focus is on the 3800-3400 $cm^{-1}$ range. Figure 8.1a shows that in the spectra of the fresh catalyst sample characteristic OH stretch vibrations are observed at 3698, 3667 (as a shoulder), 3653, 3620 and 3600 (weak band) $cm^{-1}$. The four vibrations with the highest wavenumbers are characteristic for clay mineral,[20] while the 3600 $cm^{-1}$ could be due to the non-acidic hydroxyl group of dealuminated zeolite Y.[21] The broad absorption in the 3500-3000 $cm^{-1}$ region is explained in terms of hydrogen-bonded hydroxyl groups. The latter groups originate from the presence of water, but can also be explained in terms of hydrogen-bridged OH-groups of zeolite Y and the matrix components alumina and silica.[22] One might expect to observe the spectral signatures of Brønsted acid groups of zeolite Y (occurring at 3630, 3610 , 3555 and 3525 $cm^{-1}$),[23] but as the zeolite component most probably consist of dealuminated zeolite Y the IR spectra are weak in intensity.[21]

Upon deactivation of the catalyst samples the characteristic hydroxyl groups of the clay mineral disappear. This is illustrated in *e.g.* Figure 8.1b

for the steamed FCC catalyst particles. These spectra imply that the clay mineral is destroyed during the steam treatment and this observation is in line with those of Chapter 5 on the basis of the iLEM experiments: only in the fresh catalyst sample the characteristic plate-like clay structure could be recognized in the acquired TEM images. Interestingly, the IR spectra in Figure 8.1b also indicate the formation of a characteristic vibration around 3740 $cm^{-1}$, which is due to terminal hydroxyl groups. This band is an indication for structural changes taking place during the dealumination and related collapse of zeolite Y during *e.g.* steam treatment, since it is attributed to the formation of amorphous silica.[24] Summarizing the results so far, the OH stretch region of the measured IR spectra indicates that during deactivation the structures of the clay mineral as well as the zeolite component are affected. A partial collapse of the zeolite material within FCC catalyst particles upon deactivation was previously observed in Chapter 7 with X-ray powder diffraction.

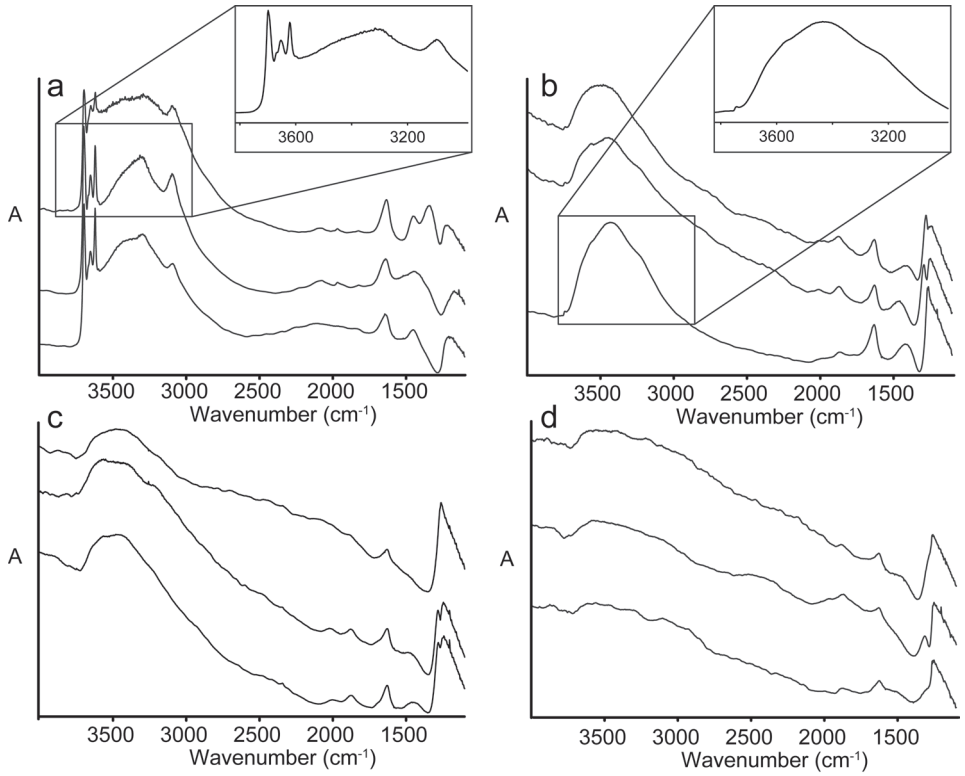


**Figure 8.1.** Transmission IR spectra of individual **(a)** fresh; **(b)** steamed; **(c)** two-step cyclic deactivated and **(d)** Mitchell impregnated-steam deactivated catalyst particles.

In a next step, the acidic properties of the FCC materials under

investigation were studied. Figure 8.2 shows a selection of IR spectra of individual FCC catalyst particles in their fresh and laboratory deactivated state. These spectra have been collected after pyridine adsorption and the informative spectral region 1620-1400 $cm^{-1}$ is depicted. All samples display three bands in the selected wavenumber range. The band with a maximum at 1545 $cm^{-1}$ corresponds to pyridine adsorbed on Brønsted acid sites as pyridinium ions. At 1490 $cm^{-1}$ a band which is caused by a mixture of Brønsted and Lewis acid site adsorbed pyridine is observed.[15-16] Furthermore, Lewis acid sites are visible due to the pyridine C-C stretch vibration at 1445 $cm^{-1}$. The spectra indicate that the highest amount of both Brønsted and Lewis acid sites is observed for the fresh catalyst particles. Upon hydrothermal treatment, coke formation and/or metal deposition part of the acid sites is either removed or deactivated. This is clearly reflected in the intensities of the pyridine vibrations observed for the deactivated samples.

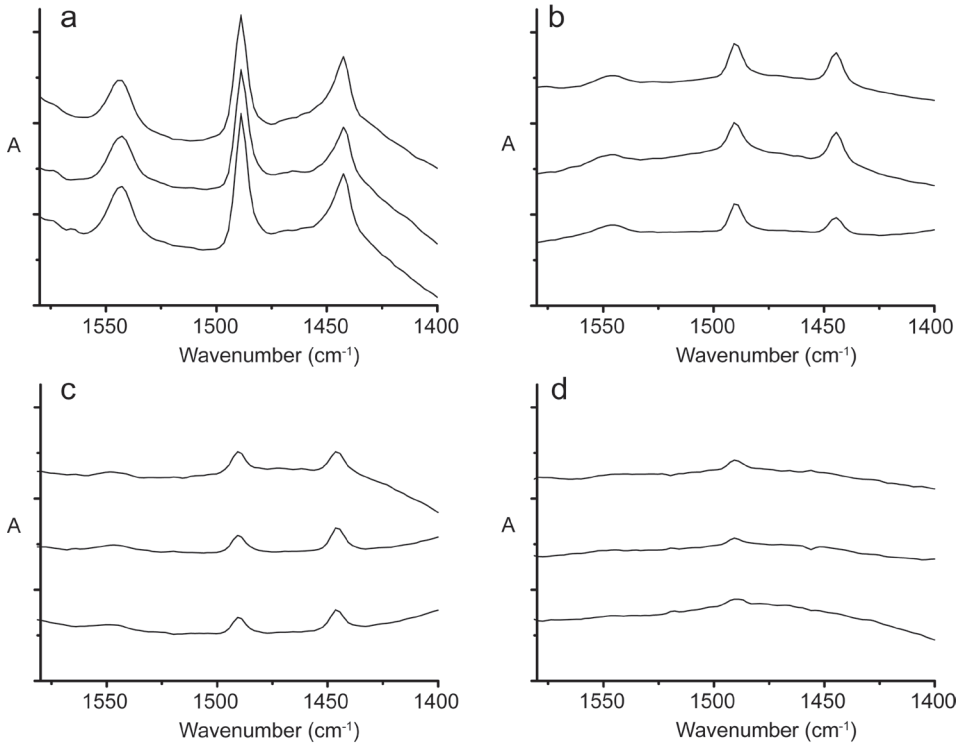


**Figure 8.2.** Transmission IR spectra of individual **(a)** fresh; **(b)** steamed; **(c)** two-step cyclic deactivated and **(d)** Mitchell impregnated-steam deactivated catalyst particles after pyridine adsorption.

Previously, bulk transmission IR measurements of the same catalyst samples (denoted as FCC 2) were performed,[25] as reported in Chapter 7. The normalized acid site peak areas for these bulk IR measurements are summarized in Table 8.1 and reveal a comparable decreasing Brønsted and Lewis acidity trend upon deactivation. However, these measurements provide insight into the average acidity of the catalyst. The approach described here enables evaluation of the acidity of individual catalyst particles. By investigating a series of 15 FCC catalyst particles for every sample, insight into the Brønsted and Lewis acidic properties of individual catalyst particles is obtained, while evaluating at the same time the acidity differences within the catalyst batch.

The peak areas of the C-C stretch vibrations of pyridine adsorbed on Brønsted (1560-1531 $cm^{-1}$) and Lewis (1452-1434 $cm^{-1}$) acid sites were determined for individual catalyst particles. Furthermore, the size of every catalyst particle was taken into account, since for all spectroscopic techniques the peak intensities are proportional to the path length of the light. More intense IR absorption bands are thus expected for larger catalyst particles. For that reason all calculated peak areas were corrected using the catalyst particle diameter: all peak areas were normalized on the size of the largest catalyst particle (100 μm). The normalized 15-particle averaged Brønsted and Lewis acid site peak areas are listed in Table 8.1 as well. The results confirm the trend obtained with bulk IR measurements: both Brønsted and Lewis acidity decrease upon increase in the severity of the catalyst deactivation procedure.

**Table 8.1.** Normalized peak areas for the Brønsted and Lewis acid site bands of pyridine ring C-C stretch vibrations in fresh, steamed (ST), two-step cyclic deactivated (CD) and Mitchell impregnated-steam deactivated (MI) catalyst particles. The Brønsted and Lewis acid site peak areas were determined between 1560-1531 $cm^{-1}$ and 1452-1434 $cm^{-1}$, respectively. Both bulk transmission IR measurements, performed on self supported catalyst wafers and IR micro-spectroscopy measurements of individual catalyst particles, were evaluated. The averages for the micro-spectroscopy experiments were obtained by investigating the transmission IR-spectra of 15 different catalyst particles per sample. All peak areas were particle size corrected by normalization using the diameter of the catalyst particle before averaging the peak areas.

| Sample | Bulk Brønsted acid site peak area | Bulk Lewis acid site peak area | Ensemble-averaged Brønsted acid site peak area | Ensemble-averaged Lewis acid site peak area |
|---|---|---|---|---|
| Fresh | 1.00 | 1.00 | 1.00 | 1.00 |
| ST | 0.22 | 0.42 | 0.30 | 0.48 |
| CD | 0.27 | 0.65 | 0.14 | 0.38 |
| MI | 0.050 | 0.017 | 0.048 | 0.018 |

Since the catalyst circulating in a commercial FCC unit is continuously fed with fresh catalyst particles that replace some of the spent

catalyst coming from the regenerator unit, the resulting Ecat displays a large age distribution among its individual catalyst particles. Due to the different amount of cracking-regeneration cycles that the particles have undergone, they display diverse activity levels. It is expected that this diversity is also reflected in the Brønsted and Lewis acidic properties of the catalyst particles. Transmission IR-spectra of a representative set of individual Ecat particles are shown in Figure 8.3.

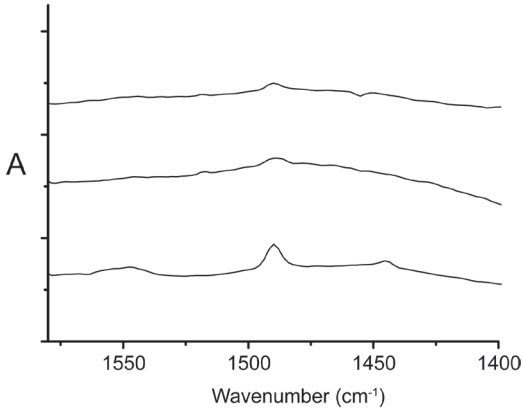


**Figure 8.3.** Transmission IR spectra of individual Ecat particles after pyridine adsorption.

The normalized Brønsted and Lewis acid site band areas for both the bulk transmission IR measurements (0.059 and 0.11, respectively) and the normalized ensemble-averaged transmission IR measurements (0.16 and 0.12, respectively) indicate an acidity between the CD and MI samples. In order to obtain more insight into the acidity differences between individual catalyst particles, the Brønsted and Lewis acid site peak areas of the individual particles of every sample are displayed in Figure 8.4. As can be seen in this figure, the diversity in Brønsted acid peak area of the Ecat sample covers a wider range compared to the CD and MI samples, reflecting the large acidity differences due to age variations within the Ecat batch. However, this observation does not hold for the Lewis acidity of the samples. The Lewis acid site differences between individual catalyst particles in the CD batch are much broader than those within the Ecat sample. This observation indicates that the cyclic deactivation method overestimates the variation in Lewis acidity.

In the research described in Chapter 7 the reactivity and acidity trends within a different Ecat batch and within the laboratory deactivated catalyst samples were evaluated using ammonia TPD and bulk pyridine IR measurements. The observed acidity trends are comparable to those obtained here, since they indicate as well that the acidity of the Ecat is in between those of the CD and MI samples. Furthermore, the acidity of

the Ecat and the laboratory deactivated catalysts was analyzed at the individual particle level by a confocal fluorescence microscopy approach. The Brønsted acid site catalyzed oligomerization of thiophene was applied as a probe reaction, leading to fluorescent products. Investigation of the fluorescence intensities of individual catalyst particles enables evaluation of their Brønsted acidity. Using this approach, large heterogeneities in the Brønsted acidity of the Ecat particles were observed. The heterogeneity of the Brønsted acidity within the Ecat batch spanned a wider range than those of the CD and MI samples combined. This is in line with the pyridine IR experiments reported here.

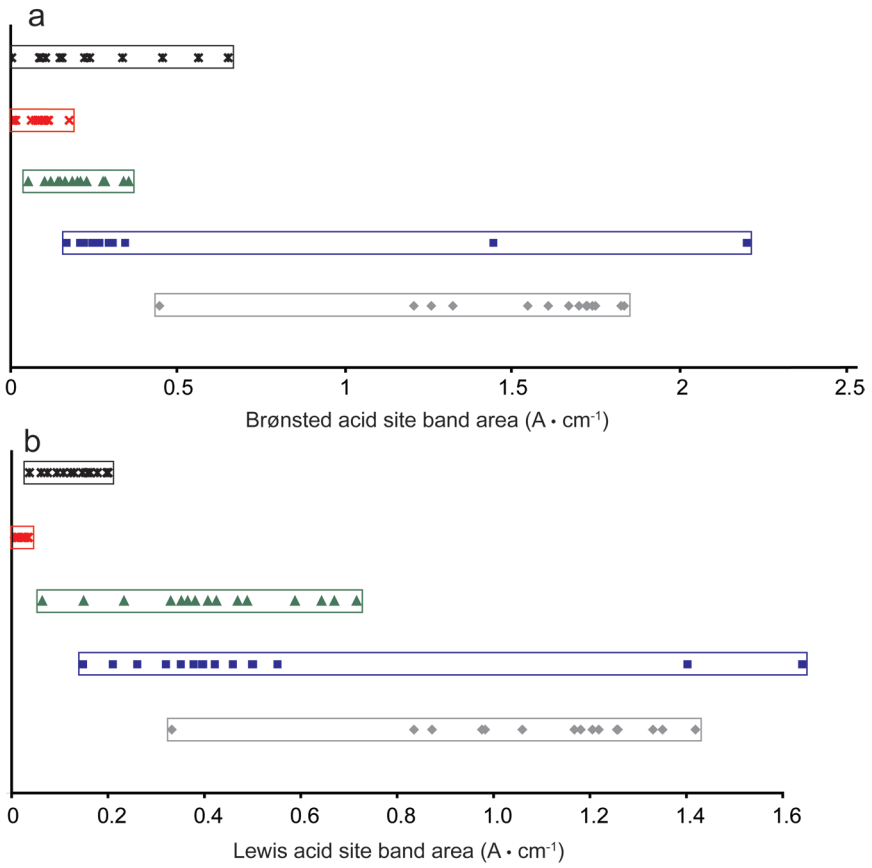


**Figure 8.4. (a)** Brønsted and **(b)** Lewis acid site peak areas for the individual FCC catalyst particles within the fresh (gray); steamed (blue); two-step cyclic deactivated (green); Mitchell impregnation-steam deactivated (red) and Ecat (black) catalyst particle batches. All displayed band areas are corrected for the size of the catalyst particles. The total distribution ranges of the peak areas per catalyst sample are depicted as rectangles.

## 4. Conclusions

Synchrotron-based IR micro-spectroscopy is a powerful tool to acquire more insight into the structural changes of FCC catalyst particles upon deactivation. It was found that both the zeolite and the clay structure present in the fresh catalyst particles were affected upon deactivation. The zeolite material was found to partially collapse and dealuminate, while the clay structure was destroyed upon deactivation treatment. IR micro-spectroscopy measurements after pyridine adsorption can be used to evaluate both Brønsted and Lewis acidity within individual FCC catalyst particles. By investigating a population of 15 catalyst particles per sample, comparable acidity trends are obtained as with bulk pyridine IR experiments. The approach described in this chapter thus confirms the structural and Brønsted acidity trends obtained with the micro-spectroscopic studies described in Chapters 4 to 7. This fact provides solid validation for the use of the styrene and thiophene oligomerization reactions as probes for Brønsted acidity.

Additionally insight into the heterogeneities within a catalyst batch can be deduced with the IR micro-spectroscopic approach applied here. The conducted experiments reveal large *inter*particle heterogeneities in Brønsted and Lewis acidity within the different catalyst batches. The Brønsted acidity differences within the Ecat batch are significantly larger than those in the CD and MI samples, which reflects the large age differences within a commercial Ecat material. This observation underpins the importance of micro-spectroscopic approaches for catalyst research to understand and evaluate the performance of catalyst materials at the individual particle level.

### Acknowledgements

Randy Smith, Eli Stavitski and Lisa Miller (National Synchrotron Light Source, United States of America) are acknowledged for their assistance with the IR measurements. The NSLS is supported by the U.S. Department of Energy, Office of Science, Office of Basic Energy Sciences, under contract DE-AC02-98CH10886.

### References

[1] A. Corma *Chem. Rev.* **1995**, *95*, 559-614.
[2] W. E. Farneth; R. J. Gorte *Chem. Rev.* **1995**, *95*, 615-635.
[3] *In Situ Spectroscopy in Heterogeneous Catalysis*; 1st ed.; J. F. Haw, Ed.; Wiley-VCH: Weinheim **2002**.
[4] *In Situ Spectroscopy of Catalysts*; 1st ed.; B. M. Weckhuysen, Ed.; American Scientific Publishers: Stevenson Ranch **2004**.
[5] H. G. Karge In *Handbook of Heterogeneous Catalysis*; 2nd ed.; G. Ertl, H. Knözinger,

F. Schüth, J. Weitkamp, Eds.; Wiley-VCH: Weinheim **2008**; *2*, 1096-1135.
[6] L. Forni *Catal. Rev. Sci. Eng.* **1973**, *8*, 65-115.
[7] D. J. Parrillo; C. Lee; R. J. Gorte *Appl. Catal. A. - Gen.* **1994**, *110*, 67-74.
[8] A. Auroux; Y. S. Yin; J. C. Vedrine; L. Benoist *Appl. Catal.* **1988**, *36*, 323-330.
[9] J. A. Martens; P. A. Jacobs *Zeolites* **1986**, *6*, 334-348.
[10] J. W. Ward *J. Catal.* **1968**, *11*, 259-260.
[11] M. Hunger; D. Freude; H. Pfeifer *J. Chem. Soc., Faraday Trans.* **1991**, *87*, 657-662.
[12] G. T. Haller *Catal. Rev. Sci. Eng.* **1981**, *23*, 477-504.
[13] J. W. Ward *J. Catal.* **1970**, *17*, 355-358.
[14] F. Thibault-Starzyk; I. Stan; S. Abelló; A. Bonilla; K. Thomas; C. Fernandez; J.-P. Gilson; J. Pérez-Ramírez *J. Catal.* **2009**, *264*, 11-14.
[15] G. Busca *Catal. Today* **1998**, *41*, 191-206.
[16] E. P. Parry *J. Catal.* **1963**, *2*, 371-379.
[17] L. M. Miller; R. J. Smith *Vib. Spectrosc.* **2005**, *38*, 237-240.
[18] W. D. Duncan; G. P. Williams *Appl. Opt.* **1983**, *22*, 2914-2923.
[19] G. L. Carr; J. A. Reffner; G. P. Williams *Rev. Sci. Instrum.* **1995**, *66*, 1490-1492.
[20] V. C. Farmer *Spectrochim. Acta, Part A* **2000**, *56*, 927-930.
[21] O. Cairon; K. Thomas; T. Chevreau *Microporous Mesoporous Mater.* **2001**, *46*, 327-340.
[22] J. N. Kondo; R. Nishitani; E. Yoda; T. Yokoi; T. Tatsuni; K. Domen *Phys. Chem. Chem. Phys.* **2010**, *12*, 11576-11586.
[23] B. Gil; K. Mierzyńska; M. Szczerbińska; J. Datka *Microporous Mesoporous Mater.* **2007**, *99*, 328-333.
[24] T. Chevreau; A. Chambellan; J. C. Lavalley; E. Catherine; M. Marzin; A. Janin; J. F. Hémidy; S. Khabtou *Zeolites* **1990**, *10*, 226-234.
[25] I. L. C. Buurmans; J. Ruiz-Martínez; W. V. Knowles; D. van der Beek; J. A. Bergwerff; E. T. C. Vogt; B. M. Weckhuysen*, Nature Chem.* **2011**, DOI: 10.1038/NCHEM.1148.

# Chapter 9

## a. Summary and Conclusions

The aim of this PhD thesis was to unravel the internal structure as well as the reactivity and acidity properties of Fluid Catalytic Cracking (FCC) catalyst particles at the individual particle level. To do so a range of micro-spectroscopic techniques was explored that allows an investigation of the catalyst spheres with micro- or nanometer precision in either two or three dimensions. The techniques applied were UV-Vis micro-spectroscopy, confocal fluorescence microscopy, integrated laser and electron microscopy and infrared micro-spectroscopy.

In **Chapter 2** a perspective on the fast developing field of micro- and nano-spectroscopy was presented by recent research efforts described in literature. This review showed that both in structured porous oxide catalysts and in catalytic materials containing supported metal (oxide) nanoparticles different types of spatiotemporal heterogeneities are present. These heterogeneities were divided into two classes: heterogeneities in active sites and accessibility. It was demonstrated that micro- and nano-spectroscopic approaches can provide valuable new insights into such heterogeneities, both at the *intra-* and *inter*particle level in heterogeneous catalysts.

The results described in **Chapter 3** comprise a combination of UV-Vis micro-spectroscopy and density functional theory (DFT) calculations to investigate the products of the styrene oligomerization reaction in zeolites H-Y and H-ZSM-5. This reaction was used, also in Chapters 4 and 5, as a probe reaction for Brønsted acidity. It was found that the formation of carbocationic oligomeric products could be followed in time and that they could be identified using UV-Vis micro-spectroscopy. Furthermore, the rate of formation within different H-ZSM-5 samples was found to depend on the silicon-to-aluminum ratio within the zeolitic material. Different products were formed within the framework of H-Y compared to H-ZSM-5: within zeolite H-Y only cyclic dimers were observed, while the H-ZSM-5 samples were found to convert styrene monomers into a mixture of cyclic and linear dimers as well as larger, more conjugated oligomers. DFT calculations of the possible reaction pathways led to a rationalization of the experimental observations. The steric properties of the zeolitic micropores were found to greatly influence the distinct products formed.

The focus of **Chapter 4** was the use of the styrene oligomerization as a probe reaction for the investigation of FCC catalyst particles containing either ZSM-5 or zeolite Y. By studying all individual FCC components (zeolite, clay, alumina and silica) by UV-Vis micro-spectroscopy it was clear that only the zeolite and clay material can convert 4-fluorostyrene into carbocationic products. By applying the same approach to individual FCC catalyst particles the fingerprint of the zeolitic UV-Vis spectra was clearly recognizable, indicating a high reactivity of the zeolite domains compared to the other components. Particles that did not contain zeolite

were inactive towards the oligomerization reaction. Since the styrene monomers selectively react within the zeolite component, a comparable staining approach as frequently used in life sciences to visualize distinct cellular features could be applied in this research. Indeed, subsequent confocal fluorescence microscopy experiments of FCC catalyst particles revealed micron-sized domains with a highly fluorescent signal upon reaction. The high activity in these domains was explained by the presence of zeolite particulates, which were inhomogeneously distributed throughout the FCC catalyst bodies. When the approach was extended to the evaluation of laboratory deactivated FCC catalyst particles in a statistical approach, a clear trend of decreasing fluorescence intensity and thus reactivity of the zeolite domains was observed upon increasing severity of the deactivation. Furthermore, a comparison was made between the average fluorescence intensities obtained upon 4-fluorostyrene and 4-methoxystyrene oligomerization, two styrenes which differ in reactivity. By doing so, it was found that the Brønsted acid site strength within FCC catalyst particles containing ZSM-5 is more uniform than within those containing zeolite Y.

**Chapter 5** described a correlative approach that combines fluorescence microscopy and transmission electron microscopy (TEM) in one setup: integrated laser and electron microscopy (iLEM). By studying 90 nm thick slices of FCC catalyst particles after reaction with 4-fluorostyrene, fluorescence intensities and the local structure of the catalyst particles could be correlated. It was found that brightly fluorescent regions mainly contained zeolite crystals, while dimly fluorescent areas consisted mostly of the matrix components clay, silica and alumina. The individual zeolite crystals and clay platelets as well as amorphous material could be recognized within the sliced FCC catalyst particles. Furthermore, electron diffraction studies confirmed the identification of the zeolite and clay material. After steam treatment of the FCC sample hardly any clay platelets were present in the catalyst particles. Mostly zeolite crystallites, identified with electron diffraction, and amorphous materials could be recognized. The presence of small γ-$Al_2O_3$, which are formed upon dealumination of the zeolite, was confirmed with electron diffraction measurements.

In **Chapter 6** a second probe reaction for Brønsted acidity, the oligomerization of thiophene, was introduced. UV-Vis micro-spectroscopy experiments and confocal fluorescence microscopy measurements of FCC particles and their individual components showed that carbocationic thiophene reaction products were selectively formed within the zeolite component. Different products were found within zeolite H-Y compared to H-ZSM-5. Moreover, different reactivities were observed for thiophene derivatives when the electron withdrawing / donating properties or the molecular sizes were varied. Furthermore, the results demonstrated that at high temperatures the formed carbocations are coke intermediates. The

FCC particles containing zeolite Y promoted this coke formation to a higher extent than those containing ZSM-5. In line with the results obtained in Chapter 4, the inhomogeneously distributed micron-sized zeolite domains could be visualized using confocal fluorescence microscopy. These results confirmed that the thiophene oligomerization reaction is a suitable staining reaction for Brønsted acidity.

Bearing this knowledge in mind and knowing that deactivation in the industrial FCC process is strongly linked to the loss of Brønsted acidity, **Chapter 7** aimed to reveal a correlation between Brønsted acidity and catalytic cracking activity. Confocal fluorescence microscopy measurements confirmed a gradual fluorescence and thus Brønsted acidity decrease upon laboratory deactivation of the catalyst samples. Subsequent addition of the non-reactive bulky dye Nile Blue A, which is too large to enter the zeolitic micropores, allowed selective staining and visualization of the FCC matrix components. By applying a statistical methodology to the series of catalysts deactivated via industrial protocols, a correlation was established between Brønsted acidity and cracking activity data. A comparison with results obtained via well-established bulk characterization techniques (infrared spectroscopy after pyridine adsorption, temperature-programmed desorption of ammonia and X-ray powder diffraction) confirmed the acquired Brønsted acidity trends. Furthermore, investigation of an industrial equilibrium catalyst sample using the statistical confocal fluorescence microscopy approach indicated a large variety in Brønsted acidity between different particles within the catalyst batch. This broad Brønsted acidity distribution reflects the large age and activity variation within such an industrial sample.

**Chapter 8** described the application of synchrotron-based infrared micro-spectroscopy for the investigation of the structure and Brønsted as well as Lewis acidity within fresh, laboratory deactivated and equilibrium catalyst particles at the individual particle level. When deactivating the FCC catalyst particles, indications for a partial collapse of the zeolite structure were apparent in the IR spectra. The clay structure present in the fresh catalyst particles was found to be destroyed upon deactivation, as earlier shown by the iLEM experiments in Chapter 5. Previously conducted bulk transmission infrared measurements already indicated a loss of Brønsted and Lewis acidity upon deactivation. Furthermore, the equilibrium catalyst was found to display an acidity in between those of the laboratory deactivated samples. The study of fifteen individual particles per catalyst sample in this chapter confirmed this acidity trend, but additionally revealed a large variety in Brønsted acidity for the equilibrium catalyst material. This heterogeneity was, as mentioned previously, attributed to the wide age distribution within industrial equilibrium catalysts.

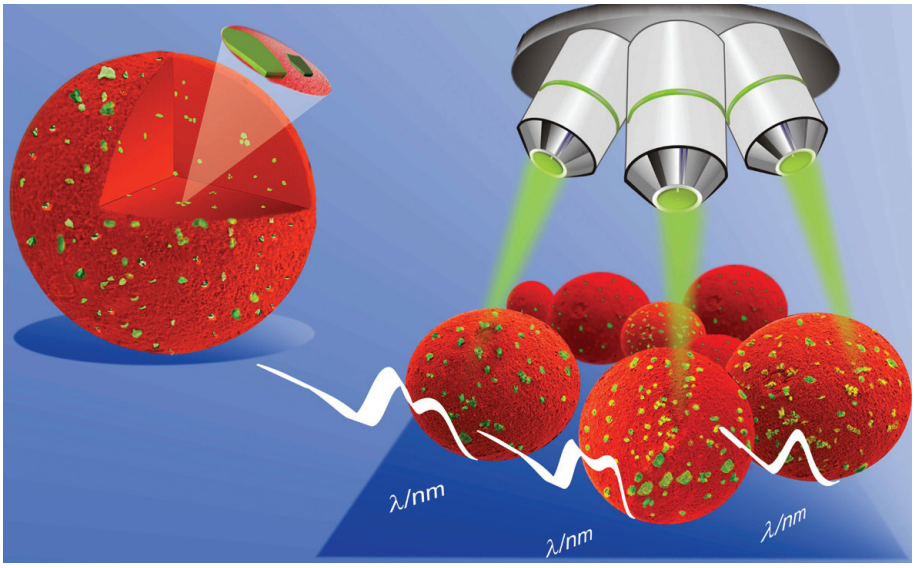


**Summarizing Figure.** Micro-spectroscopy, combined with selective staining approaches, can be applied for the investigation of both *intra*- and *inter*particle heterogeneities within individual FCC catalyst particles.

Summarizing, the micro-spectroscopic studies described in this PhD thesis have led to a more thorough understanding of individual FCC catalyst particles in terms of structure, reactivity, Brønsted / Lewis acidity and both *intra*- and *inter*particle heterogeneities. Several important conclusions can be drawn in terms of the methods used and the findings reported in this thesis.

The applied **methods** allow the investigation of the spatial heterogeneities within FCC catalyst materials at the individual particle level. Two different life sciences inspired staining reactions, namely the oligomerization of styrenes and of thiophenes, can be applied to probe the Brønsted acidity of FCC catalyst materials. Not only the Brønsted acidity of fresh catalyst particles, but also the changes in Brønsted acidity upon different laboratory deactivation methods can be satisfactorily evaluated using these staining reactions. The approach clearly shows the added value of micro-spectroscopic techniques: bulk characteristics, such as cracking activity, could be linked to the behavior of individual catalyst particles in terms of Brønsted acidity of their zeolite domains as observed at the microscopic level. Furthermore, the aforementioned probe reactions lead to the formation of products with distinct optical absorption characteristics that differ depending on the pore structure of the zeolitic material. The rate of product formation is indicative for the Brønsted acidity of the zeolite.

Decreases in the Brønsted acidity of the zeolite domains upon laboratory deactivation were found to occur in a homogeneous manner: zeolite domains in the internal parts of the catalyst particles were equally affected by deactivation treatments compared to zeolite domains at the external surface of the catalyst. Furthermore, the described approaches allow prediction of catalyst cracking performance, while at the same time evaluating the variations in Brønsted acidity among individual particles. The evaluation of individual equilibrium catalyst particles indicated a large variety in Brønsted acidity between different particles within the catalyst batch. None of the laboratory deactivation techniques investigated here accurately reflected these ***inter*particle heterogeneities** within industrial FCC materials. This conclusion indicates that enhanced laboratory deactivation techniques should be developed to more closely mimic equilibrium catalyst behavior.

The described studies indicate the presence of ***intra*particle heterogeneities** within FCC particles. Clearly, the micron-sized zeolite domains responsible for most of the cracking activity were found to be inhomogeneously distributed and partially agglomerated within the material. This observation implies that the efficiency of the catalyst could possibly be increased if the zeolite domains would be more evenly distributed throughout the particles. Confocal fluorescence microscopy would then be a very accurate tool to study this distribution, in combination with an evaluation of the catalytic performance of the new catalytic material.

**Future developments** in both FCC catalyst research and application of micro-spectroscopic methods are numerous. One interesting pathway would be the development of probes to selectively visualize Lewis acidity within FCC catalysts. Since Lewis acid sites are known to promote coke formation, their location and concentration are crucial factors in the development of better FCC catalyst materials.

Secondly, selective visualization of the location and distribution of the clay component would add valuable new information to the overall investigation of individual FCC catalyst particles. Since clay is one of the pre-cracking agents within FCC catalysts, visualization of its distribution would be beneficial for the understanding and optimization of catalytic performance.

The styrene and thiophene oligomerization reactions are accurate probe reactions for Brønsted acidity evaluation. However, these molecules do not mimic the molecular dimension of the species present in real oil feed, nor do they contain the metal contaminants present in oil fractions. For that reason the development of new probe reactions that more closely mimic molecules present in oil feed in size and chemical properties could shed more light on the cracking process in terms of diffusion and poisoning.

The fluorescence microscopy approach described in this thesis

intrinsically opens pathways for the application of *sub*-diffraction imaging techniques based on single-molecule fluorescence imaging. The fluorogenic reaction approach allows imaging of single fluorescent events within the zeolite domains. By doing so, turnover frequencies of individual active sites could be determined within the catalyst particles.

Furthermore, a logical next step would be to apply the developed methods and probe reactions to different catalytic systems. In industry a wide variety of zeolite-based as well as other acid catalyst materials is applied. Since most of these catalysts contain several ingredients, similar heterogeneities are expected to be present in such catalytic systems. Micro-spectroscopy could be applied for the investigation of their structure and acidity in future research.

**Acknowledgement**

Agnieszka Ruppert (Technical University Lodz, Poland) is acknowledged for the design of the summarizing Figure.

# Chapter 9

## b. Perspectives

As described in Chapters 4 to 8, several micro-spectroscopic techniques have been succesfully applied to visualize the reactive zeolite domains and the structural features within FCC catalyst particles. The combination of a Brønsted acid site probe reaction and a fluorescent dye that is too large to enter the zeolitic micropores has led to a selective staining approach. With this method both the zeolitic structure and the matrix components could be visualized using confocal fluorescence microscopy. Furthermore, a study of fresh, deactivated and equilibrium catalyst particles upon a Brønsted acid catalyzed probe reaction has proven the applicability of confocal fluorescence microscopy as a tool to study the changes in zeolite Brønsted acidity within individual catalyst particles.

Integrated laser and electron microscopy (iLEM) has confirmed the link between the different types of materials within FCC catalysts (zeolite, clay, silica and alumina) and their Brønsted acidity. iLEM enabled investigation of the FCC structure in nanoscopic detail, thus providing valuable new insights into the relationship between structure and Brønsted acidity for individual FCC particles and their components. Since only thin slices of catalyst materials can be investigated with this technique, limited insight into the overall porous network and related accessibility (*e.g.* open and closed structures) has been obtained with this approach.

The application of focused ion beam milling in combination with scanning electron microscopy (FIB-SEM) can yield valuable additional information on the structure and porosity of individual FCC catalyst particles. Previously such an approach has succesfully been applied to study the internal architecture and mesopores of large ZSM-5 crystals.[1,2] The FIB uses accelerated gallium ions to remove small volumes of material, a process called milling. The integration of a FIB onto a SEM allows to mill a cross section with the FIB which can be imaged *in situ* using the SEM. This approach thus intrinsically allows the acquisition of SEM images at different depths in a catalyst body by analyzing a series of cross-sections obtained after consecutive milling steps. By doing so, both the external and internal structure of individual FCC catalyst particles can be examined.

Furthermore, by sectioning particles that have previously been exposed to styrenes, confocal fluorescence microscopy measurements can be performed on deeper layers of the catalyst bodies. As described in Chapter 4, confocal fluorescence microscopy measurements of intact FCC catalysts only allow to record a satisfying image up to a depth of about 15 µm inside the particle. When focusing deeper, the fluorescence signal of the internal parts of the material will not reach the detector. A FIB treatment can be a way to overcome this issue.

In a first set of experiments FCC catalyst particles containing zeolite Y (the FCC 2 catalyst batch) were, after reaction with 4-fluorostyrene

at 423 K, sprinkled onto an aluminum stub with a carbon sticker. Four particles were selected and confocal fluorescence microscopy images were acquired. Subsequently, the sample was coated with 3.5 nm Pt/Pd. Secondary electron (SE) SEM images of the same particles were taken, as examplified in Figures 9.1a and e, for two different particles. After imaging the complete FCC catalyst particles, a section of about 7 µm thick was milled away with the FIB using an acceleration voltage of 30 kV and a current of 20 nA. A polishing step of the surface was performed afterwards using a current of 7 nA.

Afterwards the same four catalyst particles were examined using confocal fluorescence microscopy. From these experiments it was clear that the fluorescence of the styrene carbocations remained after exposure of the particles to the electron and ion beams and the vacuum conditions required in the FIB-SEM: high quality confocal fluorescence microscopy images of the particles could be acquired after the FIB treatment. By comparing the confocal fluorescence microscopy and backscattered electron (BSE) SEM images after sectioning, it turned out to be possible to make an accurate overlay of the two types of images, thus allowing a correlation between Brønsted acidity and local structure of the interior of FCC catalyst particles. An example of the SEM images and confocal fluorescence microscopy images as well as an overlay of the two is depicted in Figures 9.1b to d and Figures 9.1f to h for the two different FCC catalyst particles shown in Figures 9.1a and e, respectively. As is clear from these images, some regions in which the fluorescence signal is very low correspond to cavities in the SEM images, while other low fluorescent areas were found to contain very dense material. Two reasons could account for the fact that these dense material areas hardly fluoresce: they are either not accessible for styrene molecules or they do not contain any Brønsted acid sites that are strong enough to catalyze the oligomerization of 4-fluorostyrene into fluorescent products.

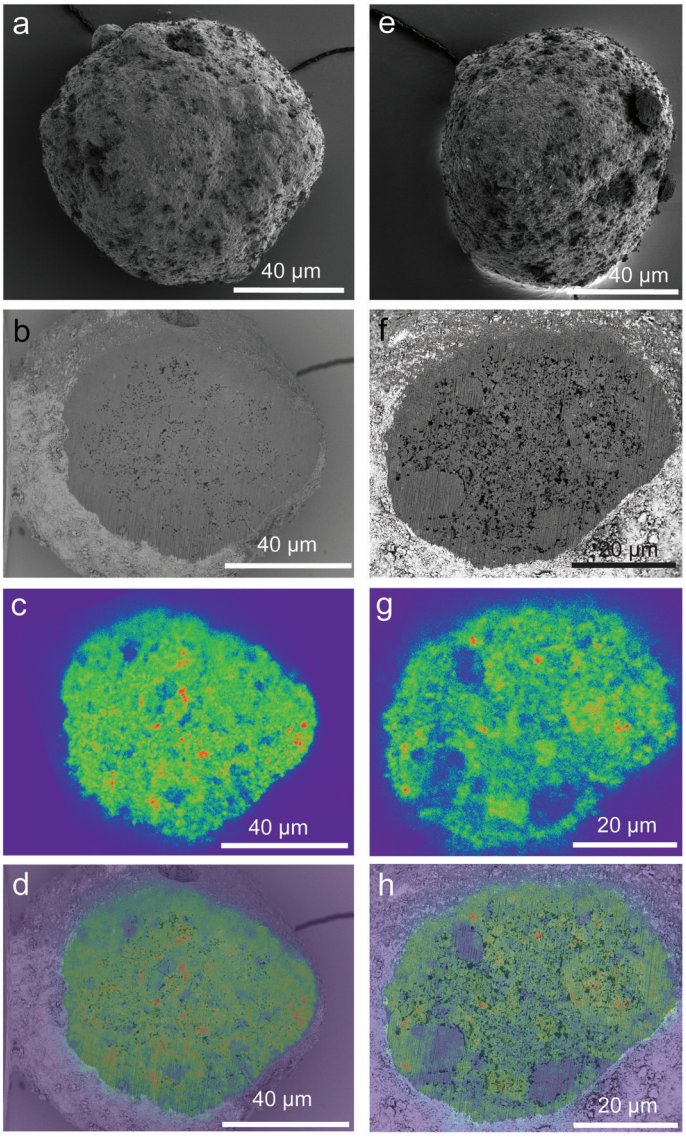


**Figure 9.1. (a)** SE SEM image of an FCC catalyst particle. **(b)** BSE SEM image; **(c)** confocal fluorescence microscopy image ($\lambda_{ex}$ = 561 nm, detection 570-620 nm, false color image) and **(d)** overlay of the BSE SEM image with the confocal fluorescence microscopy image for the particle depicted in (a) after milling away a 7 µm thick slice using the FIB. **(e)** SE SEM image of another FCC catalyst particle. **(f)**; **(g)** and **(h)** display the same series of images (BSE SEM; confocal fluorescence microscopy and overlay of the two) for the particle depicted in (e) after milling away a 7 µm thick slice using the FIB.

A more thorough evaluation of the SEM images additionally revealed that the catalyst particles display a very meso- and macroporous structure. However, the presence of a thin layer of less porous material was observed on the rim of the particle. To investigate the thickness and structure of this outer crust in more detail, ten more FCC catalyst particles from the same catalyst batch were sectioned using the FIB approach. The cross-sections of these fourteen FCC particles all revealed the presence of such an outer crust. These experiments thus indicate that the structure of the external layer of the catalyst particles differs from the internal structure. By measuring and imaging the rim of five of these particles in 70 spots in total, an average thickness of 2 µm of the external layer material was found. This is illustrated in Figures 9.2a and b for an FCC catalyst particle after FIB sectioning.

The specific type of FCC catalyst particles examined in this Perspectives Chapter has been designed to contain such a dense outer crust. The presence of a robust external layer guarantees attrition resistance of the catalyst during the cracking process. Different catalyst particles, lacking such a crust can be synthesized as well and display an increased accessibility towards larger oil molecules while losing some of their attrition resistance. For that reason the construction of FCC catalysts is always a trade-off between firmness of the catalyst particles and their accessibility / porosity.

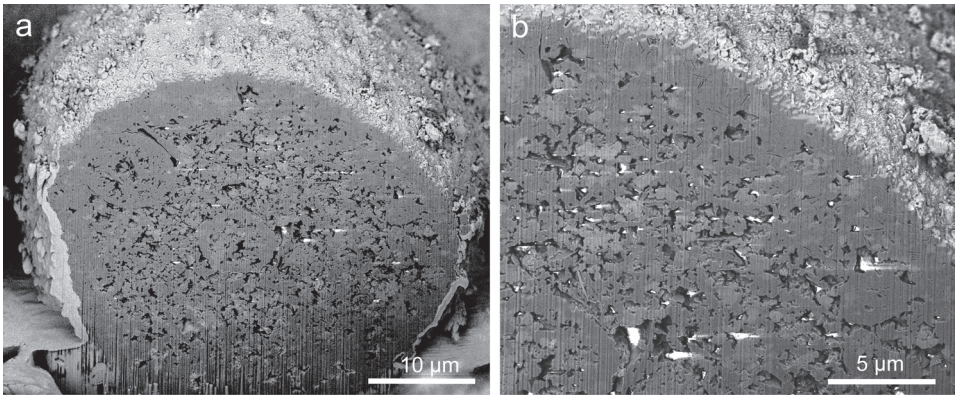


**Figure 9.2. (a)** BSE SEM image of an FCC catalyst after sectioning using the FIB. **(b)** Magnification of the image at the outer part of the catalyst body, which clearly reveals the presence of a crust of less porous material.

To obtain more insight into the pore structure of individual FCC catalyst bodies, FIB-SEM tomography was employed. Such an approach has previously been described in literature for the investigation of biological and geological samples.[3] After making an initial cross section, the FIB was used to remove thin consecutive slices and subsequently SEM images were recorded of the renewed cross sections. A total of 1000 slices with a thickness of 20 nm was milled and subsequently imaged. By doing so an overview of the structural features in different layers of the catalyst particle was obtained (Figure 9.3). Afterwards, image filters were applied to suppress noise and correct for a gradient in the brightness of the image from the top to the bottom. A threshold value in the gray-values was set to distinguish pores and material (Figure 9.4). The first 100 of these thresholded images could be stacked using the IMOD program, [4] as depicted in Figure 9.5 for the first three images. In Figure 9.6 the resulting three-dimensional map of the pore distribution in the FCC catalyst particle is displayed. The external surface of the reconstruction, depicted in yellow, was annotated manually.

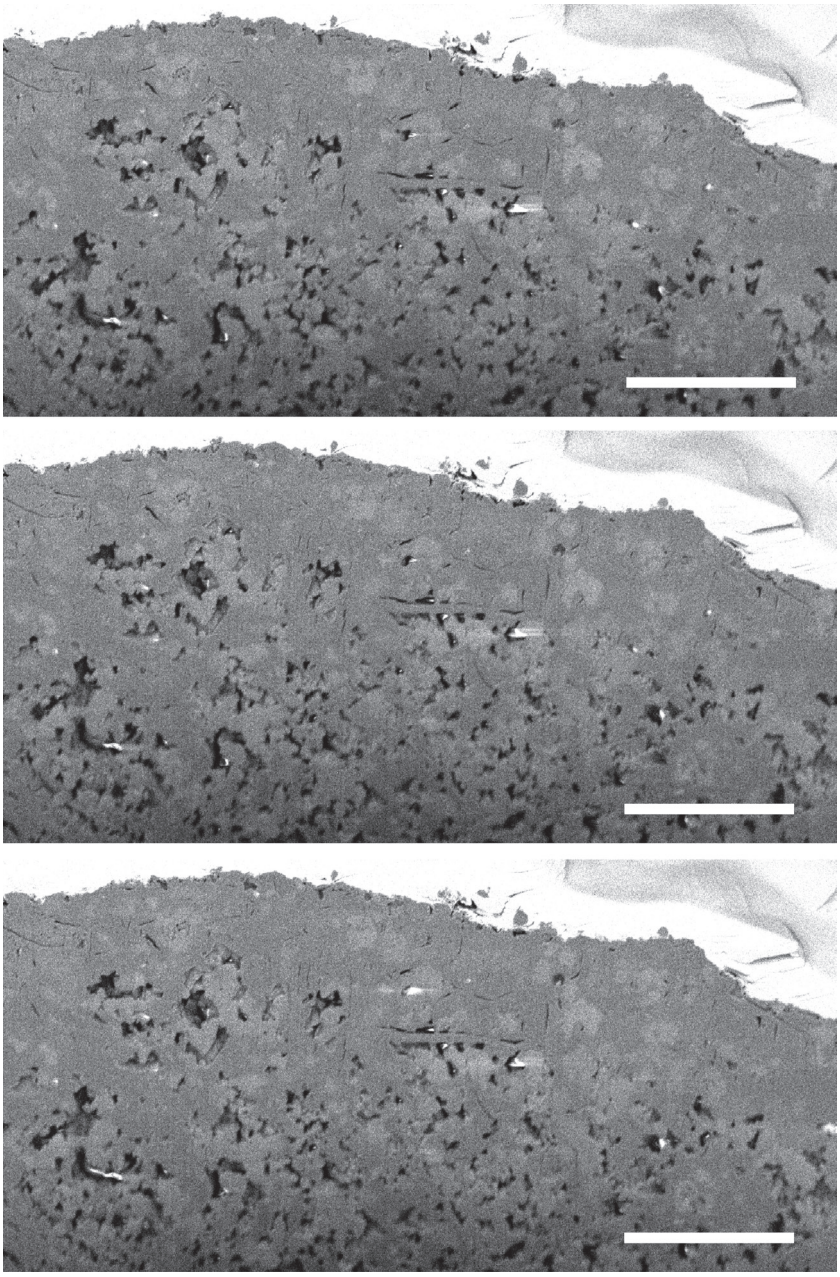

**Figure 9.3.** BSE SEM images of an FCC catalyst particle after consecutive sectioning steps of 20 nm. Scale bars represent 5 μm.

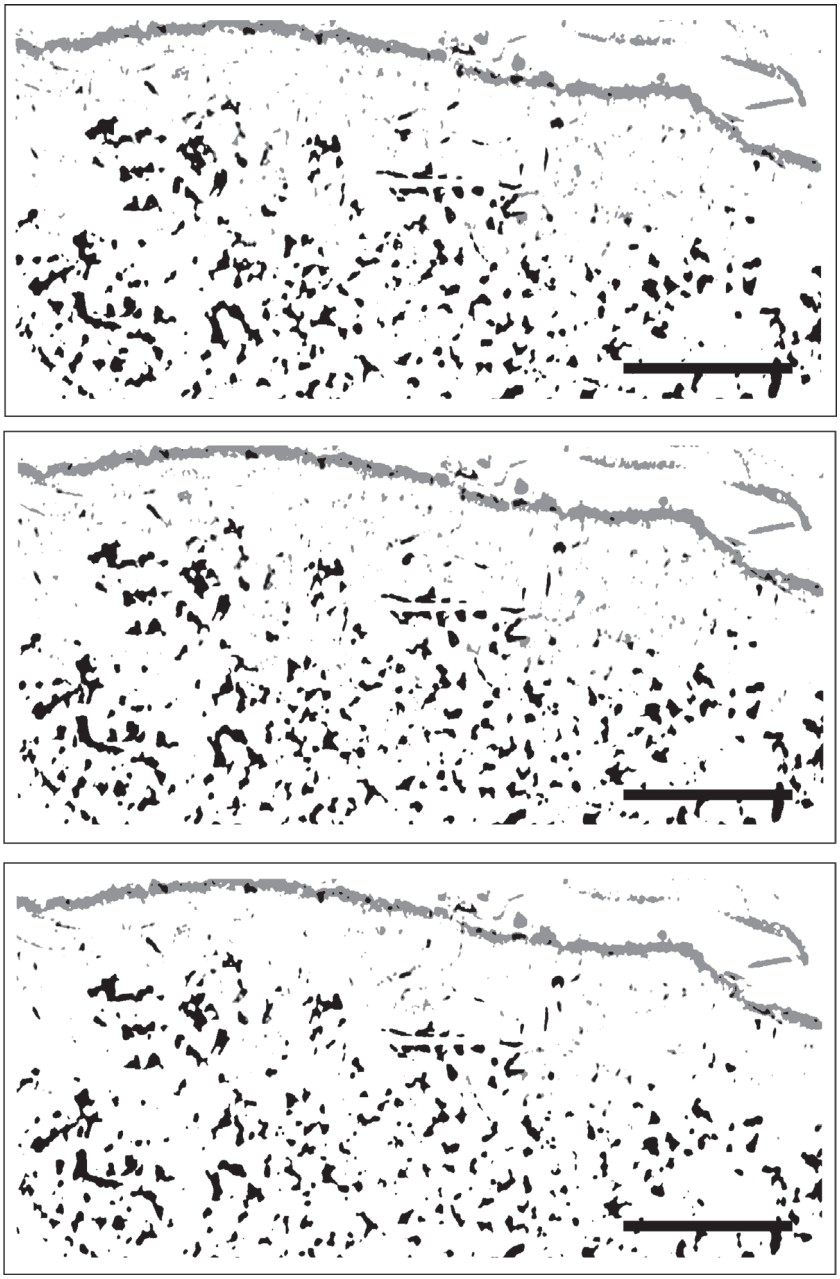

**Figure 9.4.** The three SEM images of figure 9.3 were filtered and thresholded: macropores are displayed in black, while material is displayed in white. Scale bars represent 5 µm.

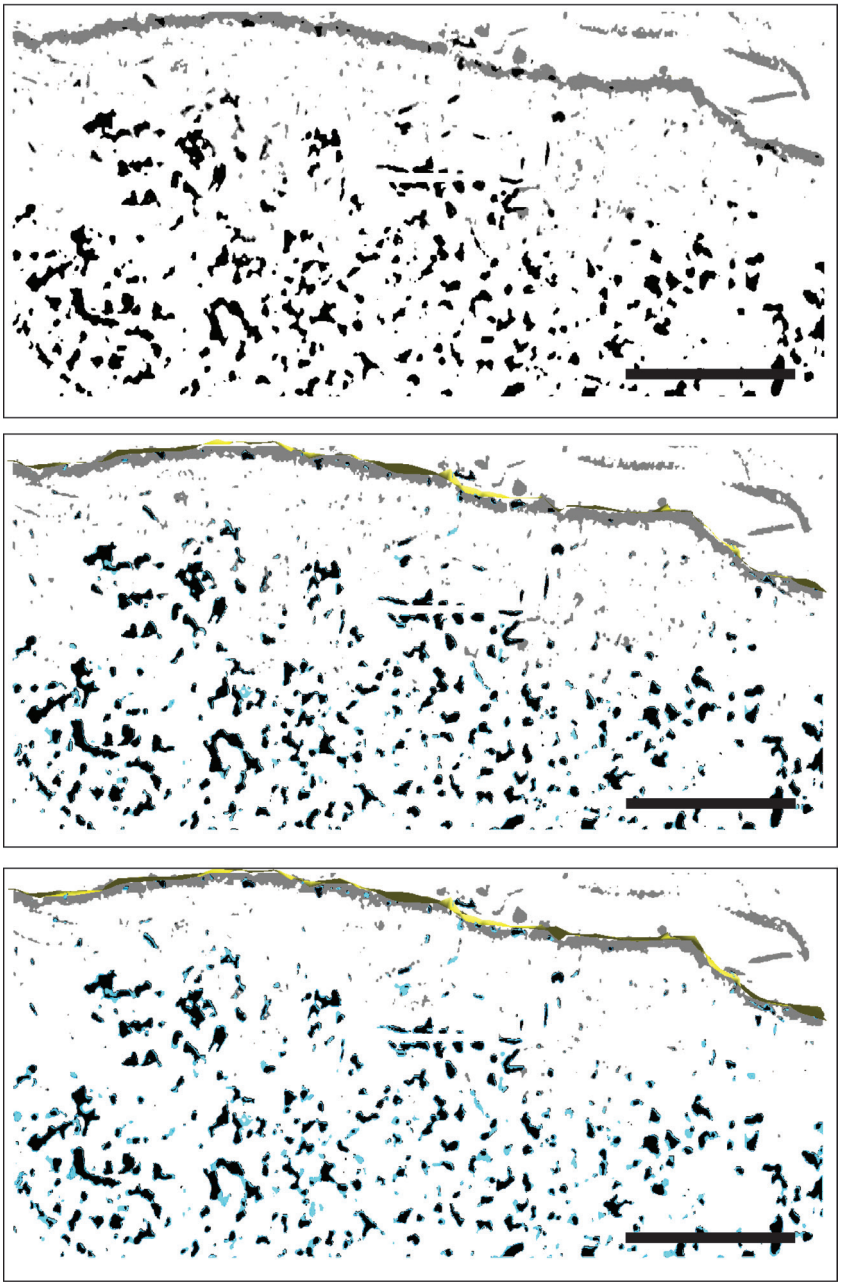

**Figure 9.5.** Overlaying the three thresholded SEM images of Figure 9.4 initiates the three-dimensional reconstruction of the macropores (blue). Scale bars represent 5 µm, the external surface is shown in yellow.

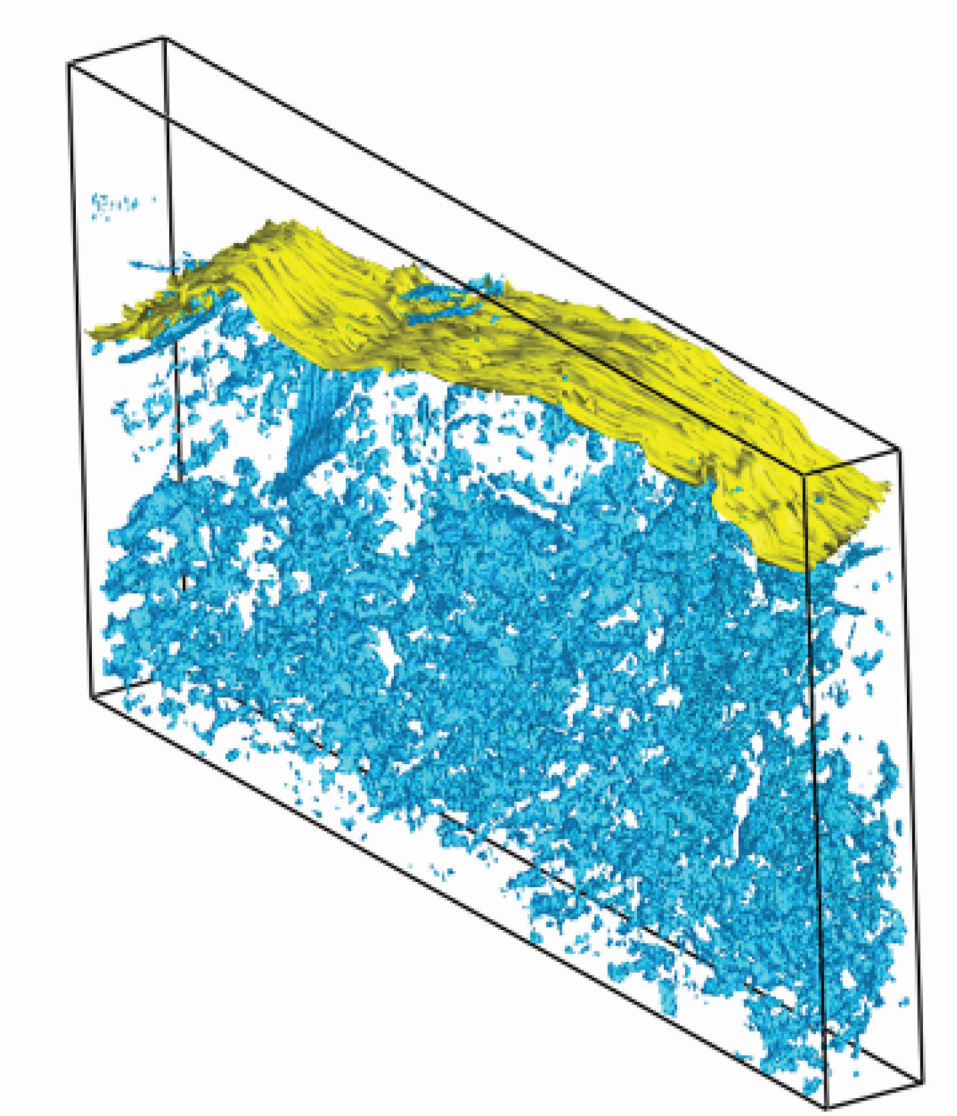

**Figure 9.6.** Three-dimensional reconstruction of the porous network in a volume of 24.6 x 12.1 x 2.0 μm of the FCC catalyst particle depicted in Figures 9.3 to 9.5. Macropores are displayed in blue, while the external surface is shown in yellow.

Figure 9.6 indicates the presence of the more dense crust in the FCC catalyst particle. In the original SEM images used to create the three-dimensional reconstruction, every pixel represents 15 nm. The smallest pores that are implemented into the three-dimensional reconstruction after thresholding and filtering are about 6 to 8 pixels in width. This results

in a final resolution of the reconstructed image of about 90-120 nm. In other words, macropores can be visualized in three dimensions within an FCC catalyst particle. In future experiments higher magnifications could be used for SEM imaging to improve the resolving power and distinguish features down to about 10 nm.

The three-dimensional pore reconstruction of Figure 9.6 shows that less macropores run through the outer few micrometers of the catalyst particle. Diffusion in the crust region thus has to occur to a larger extent via the smaller mesopores and micropores. The inner part of the catalyst particle displays a very macroporous network, which is indicative of lower diffusion limitations and higher accessibility of the material. Many of the pores and cavities visible in the interior are interconnected, thus facilitating molecular transport of large crude oil components within the FCC catalyst particles.

The analysis of the first FIB-SEM samples of FCC catalysts shows the clear potential for a structural investigation of such industrially applied catalyst materials. As these first experiments have already indicated, both the external and internal structure as well as the porous network of FCC catalysts can be visualized using FIB-SEM tomography. These experiments can yield valuable new insights into the porosity in different areas of the catalyst body and provide a link with Brønsted acidity when combined with fluorescence microscopy in a similar manner as the iLEM approach described in Chapter 5.

## Acknowledgements

Matthijs de Winter (Utrecht University, The Netherlands) is acknowledged for the FIB-SEM experiments and their analysis as well as for fruitful discussions that led to the creation of this Perspectives Chapter. Misjaël Lebbink (Utrecht University, The Netherlands) is acknowledged for his work on (semi-)automatic segmentation of the FIB-SEM tomography data. Jovana Zečević, Jan Andries Post and Martyn Drury (Utrecht University, The Netherlands) are thanked for useful discussions.

## References

[1] L. Karwacki; D. A. M. de Winter; L. R. Aramburo; M. N. Lebbink; J. A. Post; M. R. Drury; B. M. Weckhuysen *Angew. Chem. Int. Ed.* **2011**, *50*, 1294-1298.

[2] L. R. Aramburo; L. Karwacki; P. Cubillas; S. Asahina; D. A. M. de Winter; M. R. Drury; I. L. C. Buurmans; E. Stavitski; D. Mores; M. Daturi; P. Bazin; P. Dumas; F. Thibault-Starzyk; J. A. Post; M. W. Anderson; O. Terasaki; B. M. Weckhuysen *Chem. Eur. J.* **2011**, *Chem. Eur. J.* **2011**, DOI:10.1002/chem.201101361.

[3] D. A. M. de Winter; C. T. W. M. Schneijdenberg; M. N. Lebbink; B. Lich; A. J. Verkleij; M. R. Drury; B. M. Humbel *J. Microsc.* **2008**, *233*, 372-383.

[4] J. R. Kremer; D. N. Mastronarde; J. R. McIntosh *J. Struct. Biol.* **1996**, *116*, 71-76.

# Chapter 9

## c. Nederlandse Samenvatting: Onderzoeksbeschrijving en Belangrijkste Conclusies

Een belangrijk onderzoeksgebied binnen de chemie is het maken, op eigenschappen onderzoeken, optimaliseren, testen en gebruiksklaar maken van katalysatoren. De eenvoudigste definitie van een katalysator is "een stof die de snelheid van een chemische reactie beïnvloedt zonder daarbij zelf verbruikt te worden". Met andere woorden: door het toevoegen van een katalysator aan een reactiemengsel kan een reactie sneller verlopen. De katalysator kan in principe zijn werk blijven doen, doordat hij zelf niet opgebruikt wordt bij de reactie. Daarnaast kan een katalysator ervoor zorgen dat binnen een reactie bepaalde producten gemakkelijker gevormd worden dan andere, waardoor het proces selectiever verloopt. Op deze manier wordt er meer van het gewenste product gevormd. Omdat er minder energie nodig is voor de reactie en omdat de opbrengst van het gewenste product hoger is, is er vanuit de industrie veel interesse in het ontwikkelen van goede katalysatoren.

De in dit onderzoek beschreven katalysator is de FCC (Fluid Catalytic Cracking – gefluïdiseerd katalytisch kraken) katalysator. Dit katalysatormateriaal zorgt voor een groot deel (ongeveer 40-45%) van de wereldwijde productie van benzine uit ruwe olie. Oliemoleculen zijn hele grote moleculen die niet geschikt zijn voor de verbrandingsmotor van een auto. Om deze oliemoleculen om te zetten in kleinere benzine-achtige moleculen wordt het zogenaamde kraakproces gebruikt. In dit proces worden de oliemoleculen in kortere stukjes geknipt die wel geschikt zijn voor gebruik in motoren. Dit kraken kan zowel met als zonder katalysator uitgevoerd worden: bij hele hoge temperaturen (rond de 900°C) worden de oliemoleculen ook zonder katalysator in stukjes gebroken. Echter, door het toevoegen van een geschikte katalysator kan de reactie bij lagere temperaturen (ongeveer 550°C) plaatsvinden, wat dus een grote energiewinst oplevert. Verder zorgt de katalysator ervoor dat er een grotere hoeveelheid van de gewenste benzineproducten gevormd wordt en dat er minder bijproducten, zoals gassen, ontstaan.

De FCC katalysator bestaat uit poreuze bolletjes die gemiddeld 70 micrometer (iets minder dan een tiende millimeter) groot zijn. Ze zijn opgebouwd uit verschillende materialen: zeoliet, klei, aluminiumoxide en siliciumoxide. Al deze materialen hebben hun eigen structuur en samenstelling. Aan het oppervlak en in de holten van de materialen vinden de kraakreacties plaats. Het zeoliet, een gatenkaas-achtig mineraal met een zeer regelmatige poriestructuur, is de belangrijkste component in het kraakproces. In de poriën van het zeoliet bevinden zich de actieve ankerpunten waar het kraken gebeurt: de zure plaatsen. De zogenaamde Brønsted zure plaatsen, die vooral in het zeoliet voorkomen, zijn de ankerpunten die het meest actief zijn in het kraken en dus produceren van benzine. Wanneer een oliemolecuul in de buurt komt van een Brønsted zure plaats in het zeoliet dan draagt deze plaats zijn actieve groep over op het oliemolecuul. Na deze eerste stap vinden verschillende vervolgstappen

plaats, die uiteindelijk leiden tot het doorknippen van de keten in het oliemolecuul. De andere materialen (klei, aluminiumoxide en siliciumoxide) zorgen onder andere voor de stevigheid van de katalysatorbolletjes en voor het wegvangen en daardoor onschadelijk maken van metalen, die in de olie voorkomen. Zulke metalen kunnen het zeoliet kapot maken en zorgen voor een toename in de gevormde hoeveelheden ongewenste producten. Daarnaast kunnen de andere materialen de olie voorkraken: de oliemoleculen worden alvast in iets kortere ketens geknipt, die door het zeoliet gemakkelijker verder gekraakt kunnen worden.

In de industrie en in academische laboratoria is al veel onderzoek gedaan naar FCC katalysatoren. Meestal worden deze analyses uitgevoerd op bulkschaal: een groot aantal FCC deeltjes wordt tegelijk onderzocht, waardoor gemiddelde gegevens over het gedrag van de katalysator verkregen worden. Onder andere de katalytische prestaties, zure eigenschappen en stabiliteit van FCC katalysatoren zijn op deze manier onderzocht. Echter, zulke bulk-studies geven geen of beperkt inzicht in verschillen (heterogeniteiten) tussen verschillende katalysatordeeltjes (*inter*particulair) en binnen ieder afzonderlijk FCC katalysatordeeltje (*intra*particulair).

Het doel van het in dit proefschrift beschreven onderzoek was het ontrafelen van de interne structuur, reactiviteit en zure eigenschappen van FCC katalysatordeeltjes op individueel deeltjesniveau. Met verschillende zogenaamde micro-spectroscopische technieken zijn deze eigenschappen van individuele FCC deeltjes onderzocht.

Micro-spectroscopie combineert de kracht van microscopie en spectroscopie in één techniek. Iedere microscopische techniek gebruikt licht of electronen om, met behulp van lenzen en spiegels, een uitvergroot beeld te vormen van het te onderzoeken monster. Met een electronenmicroscoop kunnen meer gedetailleerde beelden verkregen worden dan met een lichtmicroscoop. Spectroscopie is het gebruik maken van licht, dat een interactie aangaat met het te onderzoeken materiaal om zo een beeld te krijgen van de eigenschappen van het monster. Veel moleculen bezitten de eigenschap dat ze een bepaalde kleur licht kunnen absorberen. Aan de hand van een analyse van de geabsorbeerde kleuren (of golflengten) van het licht kan een uitspraak gedaan worden over de vraag met welk molecuul men te maken heeft. Andere moleculen kunnen juist licht uit gaan zenden wanneer ze met een bepaalde golflengte bestraald worden. Dit fenomeen wordt fluorescentie genoemd. Door microscopie en spectroscopie te combineren worden dus microscopie-plaatjes van een materiaal verkregen die ook chemische informatie bevatten.

Veel van de in dit onderzoek beschreven observaties zijn gedaan met behulp van een bepaald soort micro-spectroscopie, namelijk confocale fluorescentie microscopie. Bij deze techniek wordt op de FCC bolletjes

eerst een reactie uitgevoerd: er wordt een vloeistof bij de deeltjes gevoegd waarvan de beginmoleculen in de FCC deeltjes omgezet kunnen worden in fluorescente productmoleculen. Deze producten kunnen gedetecteerd worden met de confocale fluorescentie microscoop doordat ze licht uit gaan zenden wanneer ze met een laser bestraald worden. De fluorescente detectie-moleculen ontstaan alleen als er Brønsted zure plaatsen in de FCC deeltjes aanwezig zijn. De microscoop registreert vervolgens waar fluorescent signaal waarneembaar is en waar niet. Doordat niet op alle plaatsen in de FCC deeltjes Brønsted zure plaatsen aanwezig zijn, zullen ook niet overal fluorescente moleculen ontstaan. Op deze manier kan er met confocale fluorescentie microscopie een beeld gecreëerd worden van de locatie van de Brønsted zure plaatsen. Die blijken voornamelijk aanwezig te zijn in het zeolietmateriaal. De klei, het aluminiumoxide en het siliciumoxide zijn niet zuur genoeg voor het ontstaan van fluorescente moleculen. Hierdoor wordt dus eigenlijk een plattegrond verkregen die aangeeft waar zich de zeolietdomeinen bevinden binnen een FCC deeltje en hoe groot ze zijn.

Het blijkt dat de meeste zeolietdomeinen een paar micrometer (een paar honderdste millimeter) groot zijn en dat ze niet homogeen verdeeld zijn in de FCC deeltjes. Er zijn plaatsen met veel zeolietmateriaal en plaatsen waar zich nauwelijks zeoliet bevindt. Met behulp van electronenmicroscopie is het vervolgens mogelijk om een nog gedetailleerder beeld te krijgen van de zeolietdomeinen en de kleidomeinen. Ook uit deze analyse blijkt dat er binnen FCC deeltjes regio's aanwezig zijn die rijk zijn aan ofwel zeoliet of klei of juist een mengsel van de twee materialen bevatten. *Intra*particulaire heterogeniteit is dus duidelijk aanwezig in de katalysatorbolletjes.

Niet alleen de vers gesynthetiseerde FCC deeltjes, maar ook FCC deeltjes die een deactiveringsbehandeling hebben ondergaan zijn in dit proefschrift onderzocht. Er zijn allerlei factoren waardoor FCC deeltjes een deel van hun kraakactiviteit kunnen verliezen. Een daarvan is, zoals eerder vermeld, de aanwezigheid van metalen in de olie. Deze maken de zeolietstructuur kapot. Daarnaast zorgt de vorming van ongewenste producten, die in de poriën van de katalysator achterblijven, voor een verminderde toegankelijkheid van de FCC deeltjes en voor blokkering van de Brønsted zure plaatsen. In de industrie probeert men dit soort deactiveringsprocessen te simuleren om zo meer te weten te komen over de aard en de gevolgen ervan. Zulke in de laboratoria van Albemarle Catalysts gedeactiveerde katalysatoren zijn met dezelfde technieken onderzocht. Door deze katalysatoren op het niveau van de individuele deeltjes te bekijken bleek dat de fluorescentie-intensiteit lager is dan die van verse katalysatormonsters. Dit kan verklaard worden door het feit dat een deel van de Brønsted zure plaatsen van de zeolietcomponent verdwijnt tijdens het deactiveren. De verwachting was dat daardoor ook de activiteit van de katalysator in het kraakproces af zou nemen.

Kraakactiviteit-gegevens van de verschillende monsters bevestigen deze hypothese.

Als laatste monster is een zogenaamde Ecat (equilibrium catalyst – evenwichtskatalysator) onderzocht. Een evenwichtskatalysator is een FCC materiaal dat afkomstig is uit een FCC kraakreactor en dus onder industriële reactiecondities zijn werk gedaan heeft. Tijdens het kraakproces worden de deeltjes hergebruikt: na een kraakronde wordt de FCC katalysator afgevoerd naar de regenerator. De in de poriën achtergebleven ongewenste moleculen worden hier weggebrand, waarna de FCC deeltjes geschikt zijn voor hergebruik en opnieuw in de kraakreactor gebracht worden. Er zijn echter in iedere kraakronde deeltjes die afvallen doordat ze te erg beschadigd en gedeactiveerd zijn. Om de activiteit van het katalysatormengsel constant te houden wordt ook in iedere kraak-regeneratieronde verse katalysator toegevoegd. Hierdoor is de resulterende evenwichtskatalysator een mengsel van jonge en oude deeltjes. Oude deeltjes zullen naar verwachting in het algemeen minder actief zijn dan jongere en minder Brønsted zuurheid vertonen. Ook dit verschijnsel is onderzocht met de micro-spectroscopische technieken door steekproefsgewijs verschillende katalysatordeeltjes binnen het monster te bekijken. Het blijkt inderdaad dat er een grote spreiding in Brønsted zuurheid is binnen zo'n Ecat monster. Deze spreiding (*inter*particulaire heterogeniteit) is aanzienlijk groter dan binnen de in het laboratorium gedeactiveerde monsters, waarin alle deeltjes aan dezelfde condities zijn blootgesteld.

Samenvattend heeft het in dit proefschrift beschreven onderzoek aangetoond dat micro-spectroscopische methoden met succes toegepast kunnen worden voor het onderzoeken van individuele FCC katalysatordeeltjes. Meer inzicht in de structuur, reactiviteit, zuurheid en heterogeniteit op *intra*- en *inter*particulair niveau kon zo verkregen worden. Over zowel de methoden als de bevindingen kunnen verschillende belangrijke conclusies getrokken worden.

De gebruikte **methoden** maken het onderzoek naar de plaatselijke heterogeniteiten in FCC materialen op individueel deeltjesniveau mogelijk. Verschillende reacties, die daar waar Brønsted zure plaatsen aanwezig zijn fluorescente producten opleveren, kunnen toegepast worden voor een evaluatie van de Brønsted zuurheid in FCC katalysatormaterialen. Zowel verse als laboratorium gedeactiveerde monsters konden op dezelfde manier geëvalueerd worden. Bulkeigenschappen zoals kraakactiviteit konden vervolgens worden gekoppeld aan de activiteit en Brønsted zuurheid van de zeolietdomeinen, waargenomen op microscopisch niveau.

De afname in Brønsted zuurheid van de zeolietdomeinen na deactivering bleek homogeen te verlopen: zeolietdomeinen binnenin de katalysatordeeltjes werden evenveel aangetast als zeolietdomeinen op

het externe oppervlak. Daarnaast maakte de beschreven aanpak het mogelijk om een voorspelling te doen over de kraakprestaties, terwijl tegelijkertijd de variaties in Brønsted zuurheid van de individuele deeltjes beoordeeld konden worden. De variatie in Brønsted zuurheid van individuele evenwichtskatalysatordeeltjes bleek groot te zijn. Geen van de laboratorium deactiveringsmethoden leverde een accurate weergave van deze ***inter*particulaire heterogeniteiten** op. Dit betekent dat meer geavanceerde deactiveringsmethoden ontwikkeld zouden moeten worden die het gedrag van een evenwichtskatalysator beter nabootsen.

Alle beschreven studies duiden op de aanwezigheid van ***intra*particulaire heterogeniteiten** in FCC deeltjes. De zeolietdomeinen, die verantwoordelijk zijn voor het grootste deel van de kraakactiviteit, zijn niet homogeen verdeeld en deels samengeklonterd in het materiaal. Wellicht kan de efficiëntie van de katalysator verbeterd worden als de zeolietdomeinen evenrediger over het katalysatorvolume verdeeld zouden zijn. Confocale fluorescentie microscopie zou ook voor dit onderzoek een geschikt hulpmiddel zijn. De verdeling van de zeolietdomeinen in zo'n nieuwe katalysator zou ermee bekeken kunnen worden, in combinatie met een evaluatie van het kraakgedrag van het nieuwe monster.

Er zijn vele **toekomstige ontwikkelingen** in zowel het FCC katalysator onderzoek als in de toepassing van micro-spectroscopische methoden mogelijk. Een interessante nieuwe onderzoeksrichting is het gebruik van andere detectie-moleculen, die specifiek Lewis zure plaatsen kunnen aanwijzen. Lewis zure plaatsen zorgen tijdens het kraken voor de vorming van ongewenste producten, die de toegankelijkheid van de FCC deeltjes verminderen en de Brønsted zure plaatsen blokkeren. Daarom zou de ontwikkeling van andere detectie-moleculen, die de locatie en concentratie van Lewis zure plaatsen in kaart kunnen brengen, een nieuwe stap kunnen zijn in het beter begrijpen van FCC katalysatoren.

Ten tweede kan het selectief zichtbaar maken van de kleicomponent in FCC deeltjes waardevolle nieuwe informatie opleveren. Klei is een van de materialen die in FCC katalysatoren een deel van het voorkraken van de olie op zich nemen. Daardoor is een beter zicht op de verdeling van deze component gunstig voor het optimaliseren van FCC katalysatormaterialen.

De in dit onderzoek gebruikte detectie-reacties blijken zeer geschikt te zijn voor het aantonen van Brønsted zuurheid. Echter, de moleculen die in deze detectie-reacties gebruikt worden zijn niet ontworpen om de moleculaire grootte of eigenschappen van echte oliemoleculen te simuleren. Daarom zou de ontwikkeling van nieuwe detectie-reacties waarvan de moleculen chemisch gezien beter lijken op die van moleculen in echte olie meer inzicht kunnen opleveren in het kraakproces.

De beschreven fluorogene reactieproducten openen nieuwe onderzoeksmogelijkheden in de richting van zogenaamde '*sub*-diffractie

weergave technieken'. Met deze technieken kan in nog meer detail naar fluorescente materialen gekeken worden door in te zoomen op de individuele actieve plaatsen in de zeolietdomeinen.

Daarnaast zou een logische vervolgstap zijn om de ontwikkelde methoden en detectie-reacties toe te passen op andere katalytische systemen. In de industrie is een breed assortiment aan katalysatoren beschikbaar dat zeoliet of andere zure materialen bevat. Aangezien zulke katalysatoren meestal verscheidene ingrediënten bevatten is de verwachting dat soortgelijke heterogeniteiten aanwezig zullen zijn in deze katalytische materialen. Micro-spectroscopie zou in toekomstig onderzoek toegepast kunnen worden om de structuur en zuurheid van zulke katalysatoren te onderzoeken.

# List of Abbreviations

| | |
|---|---|
| $\lambda_{abs}$ | absorption wavelength |
| $\lambda_{ex}$ | excitation wavelength |
| µ-XAFS | micro-beam X-ray absorption fine structure |
| AAS | atomic absorption spectroscopy |
| AFM | atomic force microscopy |
| AlPO | aluminophosphate |
| APF | *p*-aminophenyl fluorescein |
| API | American Petroleum Institute |
| APTES | 3-aminopropyltriethoxysilane |
| a.u. | arbitrary units |
| B3LYP | Becke 3-parameter, Lee-Yang-Parr |
| BET | Brunauer-Emmett-Teller |
| $^{13}$C-NMR | carbon-13 nuclear magnetic resonance |
| CCD | charge-coupled device |
| CD | two-step cyclic deactivation |
| CDU | cyclic deactivation unit |
| CLSM | confocal laser scanning microscopy |
| CTO | catalyst-to-oil ratio |
| CVFF | consistent valence force field |
| DAMPI | 4-(4-diethylaminostyryl)-1-methyl-pyridinium iodide |
| DCR | Davison circulating riser |
| DFT | density functional theory |
| Ecat | equilibrium catalyst |
| EPMA | electron probe microanalysis |
| EPR | electron paramagnetic resonance spectroscopy |
| ESCA | electron spectroscopy for chemical analysis |
| ETS-10 | Engelhard titanosilicate structure 10 |
| EXAFS | extended X-ray absorption fine structure |
| FAU | faujasite |
| FCC | Fluid Catalytic Cracking |
| FIB | focused ion beam |
| FST | fluid simulation test |
| FT | Fourier transform |
| GC | gas chromatography |
| GC-IR | gas chromatography coupled infrared spectroscopy |
| GC-MS | gas chromatography coupled mass spectrometry |
| GULP | general utility lattice program |
| $^{1}$H-NMR | proton nuclear magnetic resonance |
| H-Beta | protonic zeolite Beta |
| H-Y | protonic zeolite Y |

| | |
|---|---|
| H-ZSM-5 | protonic ZSM-5 |
| ICP-AES | inductively coupled plasma – atomic emission spectroscopy |
| iLEM | integrated laser and electron microscopy |
| IR | infrared |
| ITQ-40 | Instituto de Tecnología Química 40 |
| LDH | layered double hydroxide |
| MAS NMR | magic angle spinning nuclear magnetic resonance |
| MAT | microactivity test |
| MCT | mercury cadmium telluride |
| MFI | Mobil five |
| MI | Mitchell impregnation-steam deactivation |
| MS | mass spectrometry |
| $N_2$ physisorp. | nitrogen physisorption |
| NA | numerical aperture |
| NMR | nuclear magnetic resonance |
| PAW | projected augmented wave |
| PBE | Perdew-Burke-Ernzerhof |
| PNA | *p*-nitroaniline |
| Ref. | reference |
| SAPO-5 | silicon-substituted AlPO-5 |
| SEM | scanning electron microscopy |
| SEM-EDS | scanning electron microscopy – X-ray energy dispersive spectroscopy |
| SIMS | secondary ion mass spectrometry |
| ST | steam deactivation |
| STEM | scanning transmission electron microscopy |
| STXM | scanning transmission X-ray microscopy |
| TEM | transmission electron microscopy |
| TGA | thermo-gravimetric analysis |
| Ti-MCM-41 | titanium-substituted Mobil catalytic material 41 |
| TPD | temperature-programmed desorption |
| TPR | temperature-programmed reduction |
| USY | ultrastable zeolite Y |
| UV-Vis | ultraviolet-visible |
| VASP | Vienna *ab initio* simulation package |
| VdW | van der Waals |
| VGO | vacuum gas oil |
| VPI-5 | Virginia Polytechnic Institute 5 |
| XPS | X-ray photo-electron spectroscopy |
| XRD | X-ray powder diffraction |
| XRF | X-ray fluorescence spectroscopy |
| ZSM-5 | zeolite Socony Mobil 5 |

# List of Publications and Presentations

## Publications

I. L. C. Buurmans*, D. A. M. de Winter*, M. N. Lebbink, J. A. Post, M. R. Drury and B. M. Weckhuysen, *'New Insights into the Structure, Composition and Porosity of an Individual Cracking Catalyst Particle'*, in preparation.

I. L. C. Buurmans and B. M. Weckhuysen, *'Observation of Dynamic Processes in Heterogeneous Catalysis at the Individual Particle Level'*, in preparation.

M. A. Karreman*; I. L. C. Buurmans*; J. W. Geus; A. V. Agronskaia; J. Ruiz-Martínez; H. C. Gerritsen; B. M. Weckhuysen, *'Integrated Laser and Electron Microscopy Correlates Structure of Fluid Catalytic Cracking Particles to Brønsted Acidity'*, submitted for publication.

J. Ruiz-Martínez; I. L. C. Buurmans; W. V. Knowles; D. van der Beek; J. A. Bergwerff; E. T. C. Vogt; B. M. Weckhuysen, *'Staining of Individual Fluid Catalytic Cracking Catalyst Particles: Poisoning Studies with Thiophene-like Molecules'*, submitted for publication.

I. L. C. Buurmans*; F. Soulimani*; J. Ruiz-Martínez; H. E. van der Bij; B. M. Weckhuysen, *'Structure and Acidity of Individual Fluid Catalytic Cracking Catalyst Particles Studied by Synchrotron-Based Infrared Micro-Spectroscopy'*, submitted for publication.

I. L. C. Buurmans; J. Ruiz-Martínez; S. L. van Leeuwen; D. van der Beek; J. A. Bergwerff; W. V. Knowles; E. T. C. Vogt; B. M. Weckhuysen, *'Staining of Fluid Catalytic Cracking Catalysts: Localizing Brønsted Acidity within a Single Catalyst Particle'*, submitted for publication.

L. R. Aramburo; S. Wirick; P. S. Miedema; I. L. C. Buurmans; F. M. F. de Groot; B. M. Weckhuysen, *'Styrene Oligomerization as a Molecular Probe Reaction for Brønsted Acidity at the Nanoscale'*, submitted for publication.

P. C. A. Bruijnincx, I. L. C. Buurmans, Y. Huang, G. Juhász, M. Viciano-Chumillas, M. Quesada, J. Reedijk, M. Lutz, A. L. Spek, E. Münck, E. L. Bominaar, R. J. M. Klein Gebbink, *'Mono- and Dinuclear Iron Complexes of Bis(1-methylimidazol-2-yl)ketone (bik): Structure, Magnetic Properties and Catalytic Oxidation Studies'*, Inorg. Chem. **2011**, DOI: 10.1021/ic200332y.

I. L. C. Buurmans*; J. Ruiz-Martínez*; W. V. Knowles; D. van der Beek; J. A. Bergwerff; E. T. C. Vogt; B. M. Weckhuysen, *'Catalytic Activity in Individual Cracking Catalyst Particles Imaged throughout Different Life Stages by Selective Staining'*, Nature Chem. **2011**, DOI: 10.1038/NCHEM.1148.

L. R. Aramburo; L. Karwacki; P. Cubillas; S. Asahina; D. A. M. de Winter; M. R. Drury; I. L. C. Buurmans; E. Stavitski; D. Mores; M. Daturi; P. Bazin; P. Dumas; F. Thibault-Starzyk; J. A. Post; M. W. Anderson; O. Terasaki; B. M. Weckhuysen, *'Porosity, Acidity and Reactivity of Dealuminated Zeolite ZSM-5 at the Single Particle Level: Influence of Zeolite Architecture*' Chem. Eur. J. **2011**, DOI: 10.1002/chem.201101361.

I. L. C. Buurmans; E. A. Pidko; J. M. de Groot; E. Stavitski; R. A. van Santen; B. M. Weckhuysen, *'Styrene Oligomerization as a Molecular Probe Reaction for Zeolite Acidity: a UV-Vis Spectroscopy and DFT Study'*, Phys. Chem. Chem. Phys. **2010**, *12*, 7032-7040.

P. C. A. Bruijnincx; I. L. C. Buurmans; S. Gosiewska; M. A. H. Moelands; M. Lutz; A. L. Spek; G. van Koten, *'Iron(II) Complexes with Bio-Inspired N,N,O Ligands as Oxidation Catalysts: Olefin Epoxidation and Cis-Dihydroxylation'*, *Chem. Eur. J.* **2008**, *4*, 1228-1237.

* Indicates that both authors contributed equally to the work.

## Oral Presentations

I. L. C. Buurmans; J. Ruiz-Martínez; D. van der Beek; J. A. Bergwerff; W. V. Knowles; E. T. C. Vogt; B. M. Weckhuysen, *'Spatial Reactivity of Individual Fluid Catalytic Cracking Catalyst Particles throughout Different Life Stages'*, 22nd North American Catalysis Society Meeting, Detroit, Michigan, United States of America, June 2011.

I. L. C. Buurmans; J. Ruiz-Martínez; D. van der Beek; J. A. Bergwerff; W. V. Knowles; E. T. C. Vogt; B. M. Weckhuysen, *'Spatial Reactivity of Individual Fluid Catalytic Cracking Catalyst Particles throughout Different Life Stages'*, 34th British Zeolite Association Conference, Edinburgh, Scotland, United Kingdom, April 2011.

I. L. C. Buurmans; J. Ruiz-Martínez; B. M. Weckhuysen, *'Spatial Reactivity of Individual Fluid Catalytic Cracking Catalyst Particles throughout Different Life Stages'*, 12th Netherlands Chemistry and Catalysis Conference, Noordwijkerhout, The Netherlands, March 2011.

I. L. C. Buurmans; B. M. Weckhuysen, *'Spatial Reactivity of Individual Fluid Catalytic Cracking Catalyst Particles throughout Different Life Stages'*, 12th Workshop of the International Research Training Group on Structural Analysis, Spectroscopy and Reactivity of Porous Materials, Utrecht, The Netherlands, November 2010.

I. L. C. Buurmans; B. M. Weckhuysen, *'Visualization of Acidity and Internal Structure of a Fluid Catalytic Cracking Catalyst Particle using Micro-Spectroscopy'*, 11th Netherlands Chemistry and Catalysis Conference, Noordwijkerhout, The Netherlands, March 2010.

## Poster Presentation

I. L. C. Buurmans; J. Ruiz-Martínez; S. L. van Leeuwen; B. M. Weckhuysen, *'Catalyst Staining: Visualizing Acidity within an Individual Fluid Catalytic Cracking Catalyst Particle',* 16th International Zeolite Conference joint with the 7th International Mesostructured Materials Symposium, Sorrento, Italy, July 2010.

# Curriculum Vitae

Inge Buurmans was born on the 9th of October 1983 in Amstelveen, The Netherlands. In 2002, she obtained her Gymnasium diploma at the Willem de Zwijger College in Bussum. In October of that year she started her undergraduate studies in Chemistry at Utrecht University. During these studies she performed her master's thesis research in the group of Organic Chemistry and Catalysis at Utrecht University on the synthesis and catalytic performance of bio-mimetic iron oxide complexes. Furthermore, during an internship at Akzo Nobel Chemicals bv in Arnhem, she investigated the thermal and oxidative stability of chelating agents. After obtaining her Master of Science degree in Chemical Sciences (*cum laude*) from Utrecht University in 2007 she initiated her PhD research project, funded by Albemarle Catalysts, under the supervision of prof. dr. ir. Bert M. Weckhuysen in October of that year. This project focused on the investigation of the acidic properties and structure of Fluid Catalytic Cracking catalyst particles at the single particle level by the application of micro-spectroscopic approaches. The results obtained during that period are described in this thesis and were presented at several (inter)national conferences. In 2011 she received the prize for the best oral presentation given by a PhD student during the Netherlands Chemistry and Catalysis Conference in Noordwijkerhout. In the same year she won the third prize for the best oral presentation at the British Zeolite Association Conference in Edinburgh.

# Acknowledgements / Dankwoord

*Another day,*
*another week*
*another year won't bring another moment*
*like this.*

These last words of Horatius' poem exactly describe what it has been like to spend my four years as a PhD student in the Inorganic Chemistry and Catalysis group; whatever good things will come my way in the future, the experiences I have had during the past four years will never return. That is why I tried to cherish every moment of it.

I had the privilege of meeting many great people to work with and enjoy being a PhD student with and I want to take this opportunity to thank the most important people that made this period unforgettable.

Bert, I would like to thank you for everything. Thank you for the trust you had when putting the FCC project into my hands. At the moment you gave me two research proposals to choose from, I immediately knew that FCC was the topic I would love to spend some years on! Over the years I have learned a lot from working with you. Your creativity, your ability and optimism to see future research possibilities, the opportunities you gave me to extend / present / defend my research and to see something of the world really made me grow as a person and as a scientist. I will always remember the numerous conversations we had in your office on research, music, art and anything else in life that is important.

Javi, I really wonder what I would have done without you. On several occassions I told you that I owe so much to you! From the moment you entered the lab and we started working on the same topic, 'my' FCC project right away changed into 'ours' and I couldn't have wished for a better person to form a team with. Not only in terms of research, but also from a personal perspective it was wonderful to have you around. Working in the group wouldn't have been the same and wouldn't have been as pleasant without you. It is a real pity that our collaboration ends here, I will definitely miss it. I wish you all the best for your future and I am sure that we will stay in touch.

Davide, after being in the same labs for six years, it is now happening: we will both go our own ways. Whenever I needed you, you were there for discussions, advice, a little chat or just to listen to me in moments of despair. I am so happy that you found such a beautiful new career opportunity and I am sure that a great future awaits you. I know where to find you, even if your new job will lead you to the other side of

the world. I'm looking forward to an amazing party together to celebrate our success!

Fouad, what can I say? You are such a positive vibe in the group! Keep up the good work in the lab, it is fantastic to see that you are always willing to help anyone in any situation and always with a smile on your face. Especially during our beamtimes together I got to know you better as a person and I feel very fortunate that I have been given that opportunity. I will meet you soon for a tall cappuchino with caramel and some serious shopping to keep the memories of the Big Apple alive!

The whole nanorangers team: Marianne, Łukasz, Davide, Javi, Luis, Hendrik, Zoran and Qingyun, I would like to thank you for the nice atmosphere in the lab. There was always time for a discussion of each others work or for a little chat and this combination made my microscopy time very dynamic and enjoyable. Luis, I love you Spanish attitude and passion for everything and I am sure that in one year you will defend a wonderful thesis. Hendrik, I laughed so much with you. Your down-to-earth way of thinking is very refreshing.

Five students did a large amount of work for me: Jennifer, Ralph, Wouter, Sanne and Ramon, thank you all for being part of the project. You really helped me a lot on different topics of my thesis and it was very pleasant to work with you. Your enthusiasm, smart questions and hard work encouraged me and helped me to proceed. Jennifer, Chapter 3 is based on your experiments, which you performed and reported so neatly within those few weeks of bachelorthesis that I could straight away write them up. Sanne, Chapter 4 contains a lot of your data and analysis. For more than a year we worked together and you were a great addition to the FCC team.

Eelco, Will, David and Jaap, I would like to thank you for the fruitful discussions on my project and your involvement in the experiments, articles and my booklet. I very much enjoyed the collaboration with Albemarle and realise that without your help I would have never gotten the opportunity to work with those beautiful FCC catalysts nor perform such industry-intertwined research. I am honored, Eelco, that you will be part of my defense committee.

I spent quite some time in IR-beamtimes, working together with fantastic teams. Luis, Davide, Tom, Matt, Javi, Fouad and Hendrik, my good memories of synchrotron experiments definitely have to do with working with all of you.

During the last few months of my project I have visited the fifth floor of the Kruyt building numerous times to discuss different types of electron microscopy with two people. Matthijs and Matthia, thank you for the collaboration. I very much enjoyed working with both of you and feel that the techniques, which you have so willingly shared with me, have really pushed the FCC research forward. Matthia, it was a real pleasure to

get to know you better. I hope that we will keep contact and that our joint article will fit as nicely in your thesis as it does in mine.

My roommates over the years in two different buildings: Adri, Hirsa, Upakul, René, Peter M., Javi, Anne-Mette, Joe Z. and Selvedin, I want to thank you for making my time in the office so nice.

Coffee and lunch breaks were a really fun part of my working days thanks to a lot of people. I would like to specially thank Mariska, Harry, Davide, Javi, Niels, Adri, Piter, Bart, Tamara, Fouad, Peter M., Ilona, Rob, Joe S., Annelie and Carlo for the small talk that was always so welcome during a day full of science. Mariska, I am very happy that we met each other in the group and I am looking forward to a continuation of our after work meetings and dinners.

Dymph and Monique, thank you for all the small and bigger things you arranged for me. The group could not wish for better secretaries than you two!

Ad M., thank you for your help with the equipment in our lab and in the preparation for synchrotron trips. Your technical expertise helped me a lot over the years.

Elise, lief piepje, wat is het al lang geleden dat we samen twee kleine meisjes waren. Maar wat is er sindsdien weinig veranderd! Nog steeds even gek samen en nog steeds ben ik even gek op jou! Dankjewel voor je werkelijk onvoorwaardelijke vriendschap en steun in iedere denkbare situatie. Ik vind het geweldig dat je letterlijk achter me zult staan tijdens mijn verdediging.

Anna, mijn andere nimf, wat een voorrecht om je te kennen. Vanaf het allereerste moment dat we elkaar ontmoetten als bruggertjes op de middelbare school heb ik er nooit aan getwijfeld dat we in elkaars leven zouden blijven. Je bent een vriendin uit duizenden.

De hele 'podiumgroep', Anna, Michael, Sébastien, Imke, Ryan, Jennifer, Lieuwe, Stéphanie, Ties, Irene en Simon: dank voor alle etentjes, uitjes en vakanties samen. Het is nog steeds hetzelfde gevoel als toen we tieners op 't Willem waren en ik ben heel blij om ook allen die er later bij zijn gekomen tot mijn vrienden te kunnen rekenen.

Marieke, Edo, Tima en Timo, wat fijn dat we elkaar ontmoet hebben tijdens het studeren en nog steeds zo goed contact hebben. Ik hoop dat we nog heel lang samen gezellige activiteiten zullen ondernemen.

Mijn schoonfamilie en vooral Floris en Martine, dank voor het welkom in jullie gezin. Ondertussen alweer bijna negen jaar kom ik bij jullie over de vloer en het is fijn om te weten dat jullie er zijn.

Fleur en Maarten, mijn lieve zus en broer, dank jullie wel voor het feit dat we al zoveel jaren een hecht gezin vormen. Samen een gezellige dag / avond doorbrengen of een weekendje weg vieren is altijd een feest. Jullie zijn van kleins af aan bij mijn leven betrokken geweest en dat voelt heel fijn en vertrouwd. Dank ook voor het medeleven, de interesse en de lieve berichtjes in de drukke tijd van het schrijven van mijn proefschrift. Ben heel trots me jullie zus te mogen noemen.

Liefste papa en mama, waar moet ik beginnen? Ik kan me geen betere ouders wensen en voel me gezegend dat ik in ons gezin kon opgroeien. Jullie hebben me altijd gesteund bij alles wat ik wilde doen en altijd in mij geloofd. Als ik straks voor de commissie mijn proefschrift verdedig hoop ik dat jullie weten dat ik daar nooit gestaan zou hebben zonder jullie vertrouwen en niet-aflatende liefde.

Lo, de allerlaatste woorden in dit proefschrift zijn voor jou. Je weet hoe ongelooflijk belangrijk het voor me is dat ik bij jou thuis kan komen. Altijd ben je er voor mij en ik kan me mijn leven niet zonder jou voorstellen. Ook al is jouw aanwezigheid bijna vanzelfsprekend, toch realiseer ik me heel vaak wat een gigantisch geluk het is dat je al zoveel jaren mijn grote liefde, vriend en maatje bent. Dank voor alles!

Inge